Sustainable Isolation and Application of Cationic Cellulose Nanocrystals

vorgelegt von

M. Sc.
Esther Elisabeth Jaekel

an der Fakultät II - Mathematik und Naturwissenschaften
der Technischen Universität Berlin

zur Erlangung des akademischen Grades

Doktor der Naturwissenschaften
- Dr. rer. nat. -

genehmigte Dissertation

Promotionsausschuss:

Vorsitzender:	Prof. Dr. Reinhard Schomäcker
Gutachter:	Prof. Dr. Arne Thomas
Gutachter:	Prof. Dr. Dr. h.c. Markus Antonietti
Gutachterin:	Dr. habil. Carmen Freire

Tag der wissenschaftlichen Aussprache: 19. April 2023

Berlin 2023

II

To Flori,
who unknowingly initiated my colloid chemistry career when we were nine
and inspires me to walk off-trail –
while other kids chose cats and dogs for their project work,
you chose laundry detergents.

Acknowledgments

This thesis would not have been possible without the professional as well as moral support of many people. First of all, I would like to thank Markus for his valuable guidance, helpful discussions, and this special and inspiring place he has created at the MPIKG. I am also grateful to Prof. Arne Thomas for taking time and effort to be my thesis advisor and to Prof. Carmen Freire for agreeing to reviewing this dissertation as co-examiner. Thanks to my group leader Svitlana for her scientific guidance and for giving me the opportunity to grow into an independent researcher.

I would like to recognize the invaluable assistance of our lab technicians: Tina, thank you for supporting my lab work and keeping our lab running. Antje, thank you for helping me with countless measurements and analyses and for your kindness. Marlies, thank you for performing GPC for me. Uschi, Jessica, Katharina, Ines, thank you for always finding time to help me wipe floors or locate equipment, chemicals, and people. A big thanks also to all the other technical and administration staff of the MPIKG that make the institute work, sometimes without us being aware of it. I especially thank Tobi for helping me fix my machines. I also sincerely thank our librarians Annette and Silke for their competent service and helpful advice. I must also acknowledge the collaborators of projects in this thesis: Steven and Steffen, Rubina, Lukas and Yu, Sarah and Oleksandr. Thank you for doing excellent work and helping me with your expertise.

I am very grateful to have shared an office with only amazing people, Diana, Ivan, Kailey, Rui, and Halim, who created a space of kindness, trust, comfort, and support. Special thanks to Diana, for all your care and for sharing a piece of wisdom anytime I needed it. Rui, thank you for your kind and generous heart and for always sharing your snacks. I also want to thank my other colleagues for their company and sharing not only laughs, coffees and cakes, but also a little bit of their life with me. I especially thank Bradley and Agata for Freundschaft, emotional support, and professional advice.

To my friends: Thank you for bearing with my unreliable self and for listening to my complaints especially in the last few months. I especially want to thank Dominic for being on my side, no matter what, and for always believing in me to a sometimes unreasonable

extent. Laura, thank you for supporting me emotionally and sweetening my life for more than 22 years now.

My deepest gratitude goes to my parents Barbara and Uwe. I am very grateful to have grown up in such a loving, funny, and intelligent family. Thank you for your love, your support, and your trust in me to find my way in life. Thank you also for providing me with the greatest siblings imaginable. Judith, Finn, Meret, and Josh, thanks to each of you for being the way you are and always providing a welcome distraction in one way or the other.

Finally, thank you, Alessandro, for your care, your patience, your endless words of encouragement and your unconditional support and optimism – without you, I might have not finished this work.

Abstract

Cellulose is the most abundant biopolymer on Earth and as such an important soldier in battling the pollution of the environment with synthetic, fossil-based, and non-biodegradable plastics. As opposed to conventional plastics, cellulose cannot be dissolved in common solvents, but it requires the use of harmful chemicals to make it processable. The cellulose fiber is built up of highly ordered regions that alternate with small disordered regions. By chemically cutting the fiber in the disordered regions with a strong acid, rod-shaped semi-crystalline particles can be evolved, called cellulose nanocrystals (CNCs). Thanks to their small dimensions in the range of nanometers and their hydrophilic character, those cellulose particles are processable in water. Along with their natural origin and biodegradability, this makes CNCs a promising sustainable alternative for fossil-based compounds and materials. However, strong mineral acids such as sulfuric acid, which is most commonly used for the extraction of CNCs, are not safe to work with on a large scale and produce particles with a high negative surface charge that is not always desirable.

This work presents the development of a more sustainable extraction method to isolate CNCs from cellulose sources. The method uses a deep eutectic solvent based on ammonium formate and natural organic acids as extraction medium that also has a reactive function. Different media and reaction conditions are screened and the new material is characterized to investigate the underlying extraction mechanism. The treatment is found to produce cationic CNCs with an increased nitrogen content, pointing to a functionalization with amino groups. The CNCs exhibit a low degree of substitution, hence a low positive surface charge, which enables their straightforward application as Pickering stabilizer. To the best of the knowledge gathered in the course of this thesis, this is the first one-step treatment to introduce cationic functionalities and as such it is an important addition to the biomaterial toolbox and broadens the range of applications for nanocelluloses.

The second part of this work focuses on different applications in which CNCs may replace synthetic polymers or chemicals based on their properties. Firstly, CNCs are considered for membranes in gas separation applications due to their high crystallinity and their

ability to form self-standing, dense, and non-porous films. For this, CNCs are mixed with ionic liquids as functional additives. The resulting films exhibit an increased flexibility and gas permeability compared to the pure CNC film. Although no desirable selectivities for particular gases are observed, a tunable gas permeation behavior dependent on the cellulose source and the resulting CNC properties is revealed. Secondly, the gas barrier properties of CNCs are combined with their ability to stabilize Pickering emulsions in order to produce a CNC-rich emulsion of natural oils and waxes. It is demonstrated that the inclusion of linseed oil in CNC dispersions produces a hydrophobic paper coating with a decreased water vapor transmission rate. Lastly, more concentrated CNC-stabilized emulsions are demonstrated to be suitable for direct ink writing when co-stabilized by α-cyclodextrin. A synergy between the stabilizers leads to excellent printability and high shape fidelity and results in a platform ink that can be tuned by inclusion of compounds in both water and oil phase. This is demonstrated by the addition of alginate to the continuous phase, providing mechanical integrity to the printed object.

Zusammenfassung

Cellulose ist das am häufigsten vorkommende Biopolymer auf der Erde und als solches eine wertvolle Ressource im Kampf gegen Umweltverschmutzung durch synthetische, biologisch nicht abbaubare Kunststoffe und die Abhängigkeit von fossilen Rohstoffen. Um die Herstellung von Cellulose-basierten Materialien als Ersatz für Kunststoffe zu ermöglichen, muss Cellulose auf molekularer oder kolloidaler Ebene leicht verarbeitbar sein. Im Gegensatz zu den meisten Kunststoffen lässt sich Cellulose nicht in herkömmlichen Lösungsmitteln auflösen, sondern erfordert den Einsatz schädlicher Chemikalien, um sie zu verarbeiten. Die Zellulosefaser besteht aus hoch geordneten (kristallinen) Bereichen, die sich mit kleineren ungeordneten Bereichen abwechseln. Durch chemische Spaltung der Faser in den ungeordneten Bereichen mit einer starken Säure können stäbchenförmige teilkristalline Partikel entstehen, die als Cellulose-Nanokristalle (CNC) bezeichnet werden. Dank ihrer geringen Größe im Nanometerbereich und ihrem hydrophilen Charakter sind diese Partikel in Wasser dispergier- und verarbeitbar.

Aufgrund ihres natürlichen Ursprungs und ihrer biologischen Abbaubarkeit sind CNCs eine vielversprechende nachhaltige Alternative zu fossilbasierten Verbindungen und Materialien. Starke Mineralsäuren wie Schwefelsäure, die üblicherweise für die Extraktion von CNCs verwendet werden, sind jedoch in großem Maßstab nicht sicher und erzeugen Partikel mit einer hohen negativen Oberflächenladung, die nicht immer wünschenswert ist. Ziel dieser Arbeit ist die Entwicklung einer nachhaltigeren Extraktionsmethode zur Isolierung von CNCs aus Zellulosequellen. Die Methode verwendet ein tief eutektisches Lösungsmittel aus Ammoniumformiat und natürlichen organischen Säuren als Extraktionsmedium, das auch eine reaktive Funktionalität aufweist. Es werden verschiedene Medien und Reaktionsbedingungen getestet und das neue Material charakterisiert, um den zugrundeliegenden Extraktionsmechanismus zu untersuchen. Es zeigt sich, dass durch die Behandlung kationische CNCs mit einem erhöhten Stickstoffgehalt entstehen, was auf eine zusätzliche Funktionalisierung mit Aminogruppen hindeutet, deren Vorhandensein durch eine Reihe von Experimenten belegt wird. Die CNCs weisen einen niedrigen Substitutionsgrad und damit eine niedrige positive Oberflächenladung auf, was ihre einfache Anwendung als Pickering-Stabilisator ermöglicht. Im Hinblick auf den Stand der Technik in der Literatur ist dies die erste einstufige CNC-Extraktion unter Einführung kationischer

Funktionalitäten und stellt somit eine wichtige Ergänzung des Baukastens für Biomaterialien dar und erweitert das Anwendungsspektrum von Nanocellulosen.

Ausgehend von den Eigenschaften der CNCs werden im zweiten Teil dieser Arbeit verschiedene Anwendungen untersucht, bei denen CNCs synthetische Polymere oder Chemikalien ersetzen können. Zunächst werden CNCs aufgrund ihrer hohen Kristallinität und ihrer Fähigkeit, selbststehende, dichte und porenfreie Filme zu bilden, für Membranen in Gastrennungsanwendungen in Betracht gezogen. Dazu werden CNCs mit ionischen Flüssigkeiten als funktionelle Additive kombiniert. Die resultierenden Filme weisen im Vergleich zu reinen CNC-Filmen eine höhere Flexibilität und Gasdurchlässigkeit auf. Obwohl keine wünschenswerten Gasselektivitäten beobachtet werden, zeigt sich eine regelbare Gasdurchlässigkeit in Abhängigkeit von der Cellulosequelle und den daraus resultierenden CNC-Eigenschaften. Zweitens werden die Gasbarriereeigenschaften von CNCs mit ihrer Fähigkeit, Pickering-Emulsionen zu stabilisieren, kombiniert, um eine CNC-reiche Emulsion von natürlichen Ölen und Wachsen herzustellen. Der Einschluss von Leinöl in CNC-Dispersionen führt zu einer hydrophoben Papierbeschichtung mit einer reduzierten Wasserdampfdurchlässigkeit. Schließlich werden die in einem umweltfreundlichen, einstufigen Verfahren unter Verwendung von tief eutektischen Lösungsmitteln hergestellen CNCs für eine emulsionsbasierte Tinte für den extrusionsbasierten 3D-Druck mit ausschließlich natürlichen Komponenten verwendet, um die Möglichkeit eines nachhaltigen dreidimensionalen Drucks unter ausschließlicher Verwendung von Produkten aus Holz, Sonnenblumen, Kartoffeln und Algen zu demonstrieren. Dazu werden konzentrierte CNC-stabilisierte Emulsionen mit α-Cyclodextrin co-stabilisiert. Hierbei führt die Synergie zwischen den Co-Stabilisatoren zu einer exzellenten Druckbarkeit und einer hohen Formtreue, was zu einer Plattformtinte führte, die über den Einschluss von diversen Komponenten sowohl in der Wasser- als auch in der Ölphase an verschiedene Ansprüche und Anwendungen angepasst werden kann. Dies wird durch die Zugabe von Alginat zur kontinuierlichen Phase demonstriert, die dem gedruckten Objekt mechanische Integrität verleiht.

Contents

Contents

List of Abbreviations

3D	three-dimensional
α-CD	α-cyclodextrin
DP	Degree of Polymerization
AF	Ammonium Formate
ATR-IR	Attenuated Total Reflection Infrared
BNC	Bacterial Nanocellulose
CLSM	Confocal Laser Scanning Microscopy
CNC	Cellulose Nanocrystal
CNF	Cellulose Nanofiber
CP-MAS	Cross-Polarization Magic Angle Spinning
dbi	1,3-dibutylimidazolium
DES	Deep Eutectic Solvent
DIW	Direct Ink Writing
DSC	Differential Scanning Calorimetry
dthfi	1,3-ditetrahydrofurfurylimidazolium
EDC	1-Ethyl-3-(3-dimethylaminopropyl)carbodiimide
fC	Pre-fibrillated pulp
GPC	Gel Permeation Chromatography
HBA	Hydrogen Bond Acceptor
HBD	Hydrogen Bond Donor
HIPPE	High Internal Phase Pickering Emulsion
HSQC	Heteronuclear Single Quantum Coherence

IL	Ionic Liquid
LVR	Linear Viscoelastic Range
MCC	Microcrystalline Cellulose
MS	Mass Spectrometry
NADES	Natural Deep Eutectic Solvent
NHS	N-hydroxysuccinimide
NMR	Nuclear Magnetic Resonance
o/w	Oil-in-Water
PEG	Polyethylene glycol
REM	Reactive Eutectic Medium
SFC	Short-fiber cellulose
SILM	Supported Ionic Liquid Membranes
SLS	Static Light Scattering
TEM	Transmission Electron Microscopy
TGA	Thermogravimetric Analysis
XPS	X-ray Photoelectron Spectroscopy
XRD	X-ray Powder Diffraction

CHAPTER 1

Introduction

Our modern way of living has brought us to a point at which by polluting our atmosphere, oceans, and soil, we are destroying not only habitats of innocent and powerless species, but our very own source of life and prosperity. Luckily, we are slowly coming to an understanding that humanity's future on planet Earth is only possible and sustainable in harmony with Nature. The appointment of the 17 United Nations Sustainable Development Goals in 2015 demonstrates that the message reached people in power and constitutes a call to action. Scientists all around the world are therefore turning to Mother Nature, who provides us with the most fascinating and efficient solutions to all kinds of research questions. One of our biggest problems nowadays is the pollution of even the most remote places on Earth with non-degradable plastic trash and microplastics. A solution to this problem is the use of natural biopolymers which are naturally degradable by microorganisms. The most abundant biopolymer on earth is cellulose, with an estimated annual bioproduction of $7.5 \cdot 10^{10}$ metric tons.[1] Together with lignin and hemicelluloses, cellulose is the main component of the plant cell wall and as such has been used since the beginnings of the history of humankind. The abundance of hydrogen bonds along with the linearity of the polymer chains give rise to a highly crystalline, fibrous structure. The resulting strength of the cellulose fiber has been valued in the use of wood as a construction material, in using papyrus as the predecessor of paper for writing, and in the use of cotton and flax for weaving fabrics or making rope – all of which were crucial to the development of modern societies. Cellulose continued to be an important resource in the development of new materials and technologies in the 19th and 20th century: Although the strong inter-fiber hydrogen bonds and its high crystallinity render cellulose difficult to dissolve in conventional solvents, alternative pathways were developed to process cellulose into some of the first semi-synthetic plastics. More recent material research has discovered cellulose as a source of a versatile bio-nanomaterial, sparking a vast amount of reviews on their fabrication, properties and applications.[2;3] Nanocelluloses combine remarkable properties with sustainable natural origin and biodegradability and are considered to be among the most

promising material building blocks of the future.[4] However, a truly sustainable material must also be sustainable in its production. Large parts of the production of materials and chemicals rely on the use of organic solvents derived from fossil resources which often pose risks to living organisms and environmental health. Conceptually new pathways for a more sustainable chemical and material production following the Principles of Green Chemistry defined by Anastas and Warner in 1998[5] are much sought-after. Among those principles is the development of safer solvents along with the use of a renewable feedstock. From the point of view of atom economy and environmental factor, the greenest solvent is no solvent. Therefore, research efforts went into solvent-free syntheses, attempting solid, gas, or mixed-phase syntheses.[6] However, the complete elimination of solvent is not feasible for every process. Neoteric solvents are crucial as alternative solvents for those cases. Among the promising candidates, deep eutectic solvents (DESs) emerge as a class of sustainable designer solvents.

This work presents the development of a new sustainable DES-based process for the isolation of cationic cellulose nanocrystals and explores possible applications which this new material might enable. Applications which are usually fulfilled by synthetic polymers or compounds harmful to the environment are the focus of this study, attempting to contribute to the development of more sustainable and less polluting materials. This thesis is structured as follows:

Chapter 2 covers fundamental knowledge applied in this thesis and reviews important aspects of the main topics, focusing on deep eutectic solvents, nanocelluloses, and their applications in specific fields of colloid and material science.

Chapter 3 describes the development of a new CNC extraction process using a new deep eutectic solvent based on ammonium formate and organic acids. The extraction mechanism is investigated and the novel material is characterized in order to rationally explore possible applications.

In **Chapter 4**, the CNCs are applied as a bulk material in the form of self-standing films and the feasibility of functional CNC-supported ionic liquid membranes for gas separation applications is investigated.

Chapter 5 reports on the application of CNCs as a nanomaterial to stabilize Pickering emulsions of natural oils and waxes for hydrophobic paper and wood coatings.

Chapter 6 extends the use of CNCs from two-dimensional (films) to three-dimensional objects by applying them in medium internal phase Pickering emulsions that are suitable for direct ink writing.

All experimental methods are summarized in Chapter 8.

CHAPTER 2

Fundamentals

2.1 Deep eutectic solvents as sustainable reaction media

Deep eutectic solvents are binary or ternary mixtures of Lewis or Brønsted acids and bases with a eutectic point at a specific molar ratio. The melting point of the mixture at the eutectic point is considerably lower than the melting temperature of the pure compounds. Since the first report on DESs in 2003 by Abbott et al.,[7] there has been ongoing controversy over a clear definition of deep eutectic solvents and their differentiation from other eutectics.[8] Most definitions of DESs include a melting point below or around room temperature at the eutectic composition as well as the presence of hydrogen bonding, the latter causing a delocalization of charge that is responsible for the deep depression of the melting point. However, this definition has been criticized as being too unspecific.[9] To give meaning to the qualifier "deep" and promote a less arbitrary use of it, Martins et al. suggest defining deep eutectics by a negative deviation of the real melting temperature T_m from the predicted ideal T_m of the mixture. The prediction of the ideal phase diagram, however, can be challenging if the necessary thermodynamic data such as enthalpy of fusion of the pure compounds are unavailable due to their decomposition before melting. The authors also underline that a DES, as opposed to an ionic liquid (IL), is neither a new compound nor a stoichiometrically defined complex. Instead of being the result of the formation of a fixed-composition complex with a low melting temperature, the formation of a eutectic is rather based on the thermodynamics of mixing. As a consequence, the composition of a DES is variable around the eutectic composition, as long as the mixture remains in the liquid state at the solvent's operating temperature (see Figure 2.1). This extra degree of freedom provides a broad variety and tunability of the physical properties of the DES, which can be adjusted according to process requirements.

As an emerging class of neoteric solvents, DESs are often considered green and sustainable alternatives to ILs. Due to the almost endless pool of available compounds and their
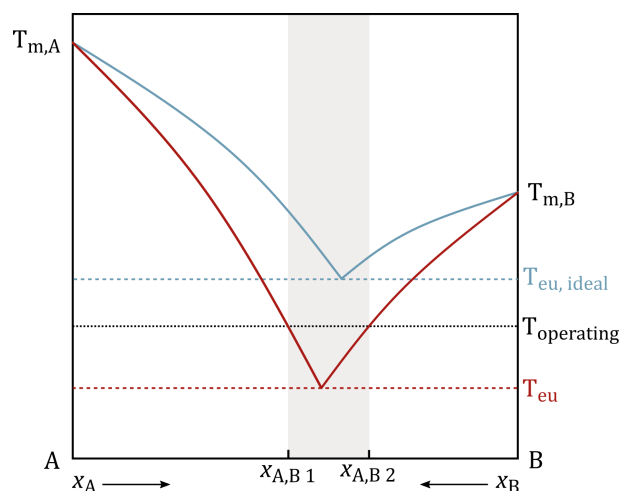
Figure 2.1: Schematic phase diagram of a mixture of two components A and B with a eutectic point.

flexible composition, DESs share the designer solvent status of ILs. The following four classes of DESs are commonly differentiated:

Type I:	quaternary ammonium salt + metal chloride
Type II:	quaternary ammonium salt + metal chloride hydrate
Type III:	quaternary ammonium salt + hydrogen bond donor
Type IV:	metal chloride hydrate + hydrogen bond donor

While Type I, II, and IV DESs are appealing for electrochemical or catalytic applications, only the metal-free DES Type III can be considered a sustainable alternative to organic solvents. Type III DESs can be prepared solely from natural compounds such as primary metabolites. These so-called natural deep eutectic solvents (NADES) have been hypothesized to occur naturally in living cells and organisms and to be a missing link that explains their survival at extreme environmental conditions.[10] For the sake of brevity, the term "DES" will be used to refer to Type III DESs in this work.

DESs are straightforward to prepare by simple mixing and can be composed of a large variety of harmless nontoxic components, which can be derived from renewable resources.[11;12] By thoughtful choice of the hydrogen bond acceptor (HBA, the quaternary ammonium salt) and the hydrogen bond donor (HBD), the DES's physicochemical properties can be tailored for specific applications to replace organic solvents which the chemical industry strongly relies on. In contrast to those volatile organic compounds, DESs have low volatility and are therefore non-flammable, which makes them very safe compounds to work with. The implication of this non-volatility, however, is one of the reasons why DESs cannot simply replace VOCs in the processes in which they are applied: Reaction workups such as separation of the product and recycling of the solvent often rely on the evaporation of the solvent. Another drawback that hampers the applicability of DESs is their high viscosity, which has a big impact on mass and heat transfer. The application of DESs therefore

requires entirely new process designs, and DESs should be considered as an enabling technique rather than a direct replacement of organic solvents.[13] Nevertheless, DESs have great potential in various fields. They have been shown to efficiently extract organic compounds such as polyphenols[14] and proteins,[15;16] although the efficiency and sustainability of such extractions are debatable due to tedious back-extraction steps. Thanks to their remarkably high solubility of metal oxides and salts, DESs were considered good alternatives for the leaching of ores and general metal winning[17] and were proven efficient in metal recycling of low-value metals[18] and batteries.[19] The multifunctionality of DESs is interesting for organic reactions[20] and polymer synthesis,[21] where the DES can be a solvent, reactant, and sometimes catalyst at the same time. Their inherent ionic conductivity makes DESs promising in electrochemical applications as well: They have already found their way into industrial electropolishing[22], electrodeposition,[23] and electrowinning of metals.[24] DESs have also proven efficient for the treatment of biomass, for instance for lignin extraction.[25] Many alternative processing methods for cellulose involve alternative solvents such as ionic liquids[26] and DESs due to their high polarity and their ability to form strong hydrogen bonds. Based on the favorable interactions with the abundant hydroxy groups, DESs were shown to provide good conditions for the processing of carbohydrates in a sustainable way, as reviewed by Zhang et al.[27] They have been successfully applied in wood treatment, lignocellulose delignification, and nanocellulose extraction and modification.[28;29;30] The treatment of cellulose in eutectic media can also facilitate the subsequent mechanical disintegration, as they cause swelling of the cellulose fibers and partially dissolve the hemicellulose fraction.[29;30]DESs can therefore be considered promising media for new pathways for the processing of cellulose in a sustainable way.

2.2 Cellulose

Cellulose is the most abundant natural polymer on Earth and is primarily known as the major component of the plant cell wall. Certain bacteria[31] and even animals of the tunicate species[32] also produce cellulose as an extracellular polymer for biological functions. It is synthesized enzymatically by cellulose synthase complexes in the organism's membrane from glucose units, which are linked through β-1,4-glycosidic bonds to form a linear, unbranched polymer, also called glucan chain. As every anhydro-D-glucose unit is corkscrewed 180° respective to its neighbors, the molecular structure of cellulose is often presented with cellobiose, the dimer of glucose, as a structural repeating unit, which reflects the chain conformation (see Figure 2.2). Hydrogen bonds between the units result in a coplanar orientation of the glucopyranose rings and a high rigidity of the chain. The hemiacetal at one end of the polymer chain, the so-called reducing end, is in equilibrium with its open-chain aldehyde form due to mutarotation, giving rise to site-specific chem-

ical modification possibilities, as reviewed by Heise et al.[33] Cellulose can reach a high degree of polymerization (DP) of up to 20 000, dependent on its source.[34]
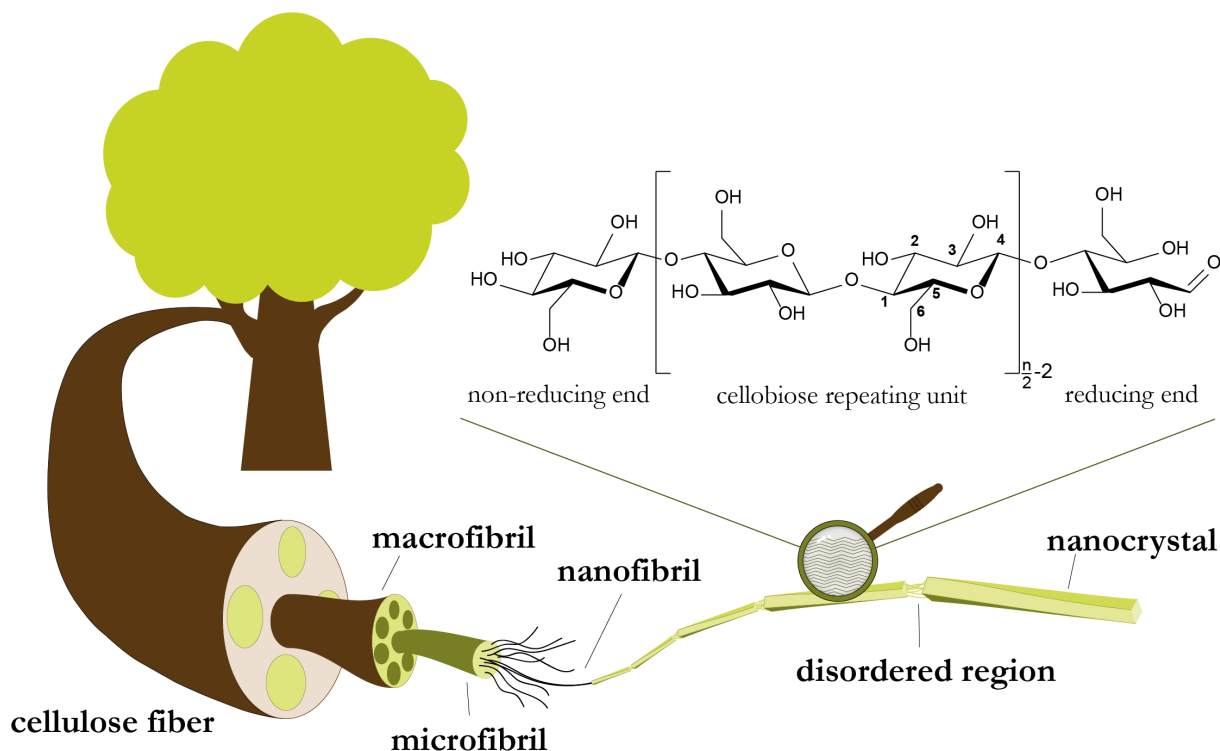

Figure 2.2: Macro to nano structure of cellulose fiber in the plant cell wall.

Upon biosynthesis, microfibrils are formed by association of 24-36 individual glucan chains.[35] Intermolecular hydrogen bonding as well as van der Waals attractions between the glucopyranose rings causes strong inter-chain interactions. The linearity and the rigid, flat structure of the glucan chain enable a highly crystalline microstructure that periodically alternates with smaller disordered, or amorphous, domains. In cotton, for example, the disordered regions were found to consist of only 4-5 residues for every 300 residues in crystalline domains.[36] Natural cellulose exists in the crystalline allomorphs I_α and I_β, in which the glucan chains are in a parallel arrangement.[37] In cellulose II, an unnatural crystalline state, the chains are arranged in an antiparallel way.[38] Despite the seemingly planar structure of the glucan chain, a helical twist was observed in the microfibrils' crystallites.[39;40] The cellulose microfibrils assemble into larger bundles, or macrofibers, with high tensile strength.[41] Those fibers are embedded in a matrix of hemicellulose, pectin, and proteins, to form the plant cell wall in which cellulose holds a structure-giving role. Upon woodification, or lignification, of plant tissue, the hydrophobic polyphenol lignin is deposited in the vacancies between the embedded cellulose fibers, rendering the cell wall hydrophobic and stronger with respect to resistance to pressure. This composite of cellulose, hemicellulose and lignin is commonly referred to as lignocellulosic biomass, or wood. Lignocellulosic biomass is the main source of circulating cellulose due to its vast availability. Separation of cellulose from the embedding polymers is nowadays mainly

achieved using the kraft pulping, or sulfate pulping, process. Here, wood chips are cooked in a mixture of sodium hydroxide, sodium sulfide, and sodium sulfate to cleave lignin end hemicelluloses into soluble compounds and remove them from the biomass.

The main purpose of cellulose in the plant cell wall is to permanently provide strength to the plant structure. The high mechanical strength and chemical stability of the cellulose fibril are enabled by the strong intermolecular interactions, hydrogen bonding, and van der Waals forces, between the chains. Those attractive interactions make cellulose challenging to process on a molecular level. Cellulose is not soluble in common solvents, but the vast amount of hydroxyl groups on the fiber invites a large possibility of surface modifications. Early attempts of processing cellulose therefore involved derivatization to transfer it into a soluble or processable form: Celluloid (nitrocellulose synthesized via nitration of cellulose with nitric acid and sulfuric acid), plasticized with camphor, was the first thermoplastic developed in the 1850s, which enabled developments in mass production of luxury articles and in the film industry. However, its high explosivity led to many fatal accidents. The viscose method employs harmful carbon disulfide to transfer cellulose into a soluble form that can be regenerated to the original cellulose structure after being spun into filaments or pressed into a film. Other derivatization methods transform the biopolymer into compounds such as cellulose acetate which are unknown to nature, thus decreasing the biodegradability of the material compared to pristine cellulose.[42] A promising alternative method is to process cellulose on the colloidal level, in the form of nanocelluloses.

2.2.1 Classification of Nanocelluloses

Nanocelluloses are defined as cellulosic particles with at least one dimension on the nanoscale, that is between 1 nm and 100 nm. Like synthetic nanomaterials, nanocelluloses can be produced via top-down or bottom-up approaches. Commonly, three classes of nanocellulose are described: Bacterial nanocellulose (BNC), cellulose nanofibers (CNF), and cellulose nanocrystals (CNC). BNC is produced by the bacterium *komagataeibacter xylinus* from glucose and constitutes the only bottom-up process for nanocellulose. It consists of fibers of varying lengths up to several micrometers with a diameter of 20 nm to 100 nm.[3] As it naturally occurs on the nano-scale, BNC was the first cellulose nanomaterial utilized by humans: Since the 18th century, Filipinos have been using it to produce jelly desserts from pineapple juice (*nata de piña*) or coconut water (*nata de coco*). Its biocompatibility along with high mechanical strength and gel-forming properties has sparked many research and business ideas, a big part of those in the field of biomedical materials such as dental implants, wound dressings, or tissue-regenerative implants. BNC can be produced on an industrial scale via fermentation at mild conditions, making it a promising sustainable material with a green synthesis. However, it was estimated by

Dourado et al. that despite the affordable resources, high capital costs would hamper the commercialization of BNC and restrict its use to high-value niche markets.[43]

CNFs are obtained via mechanical fibrillation (or delamination) methods from plant fibers. Due to the strong attractive inter-fibril hydrogen bonds arising from the abundance of hydroxyl groups, the disintegration of the cellulose fiber into single fibrils requires enormous amounts of energy and suitable devices to apply this energy. For this reason, the first method to obtain microfibrillated cellulose was reported only in 1983 by Turbak et al. who used a high-pressure homogenizer to produce cellulose fibers on the nano- to microscale from wood pulp. The product was a jelly 2 % suspension with thixotropic properties that was intended primarily as a food additive.[44] Later developments employed grinders or microfluidization, improving homogeneity and decreasing fiber diameter, but, all of them being based on shear, still required the same energy input for the separation of the fibrils. To facilitate disintegration, modern developments follow the approach of introducing charged functional groups to the fiber surface before the mechanical treatment: The inter-fibril electrostatic repulsion counteracts hydrogen bonding and can drastically decrease the energy needed to separate the individual fibrils. Approaches included phosphorylation,[45] sulfonation,[46] periodate chlorite oxidation,[47;48] cationization with 2,3-epoxypropyltrimethylammonium chloride,[49] and carboxymethyl grafting.[50] The most established method for this is the oxidation of the primary hydroxyl groups mediated by the (2,2,6,6-tetramethylpiperidin-1-yl)oxyl radical (TEMPO), first reported by Saito et al., which produces surface carboxylic groups.[51] Their anionic character in aqueous media reduces attractions between the fibrils to such an extent that simple blending induces their separation, yielding CNFs with a diameter of 3 nm to 5 nm. CNFs are appreciated for their high tensile strength of 1.6 GPa to 3 GPa[52] which is comparable to multiwalled carbon nanotubes and aramid fibers.[53] Their high aspect ratio causes a low percolation threshold that allows an efficient use as a rheology modifier, binder, or in fiber-reinforced materials. It also allows their processing into macrofibers, for instance via flow-focusing methods, which can be used for high-performance textiles. Possible applications were extensively reviewed by the Dufresne group.[54]

The smallest obtainable cellulosic particle is the CNC, which is the single isolated crystalline domain of the cellulose fiber. For the isolation of this colloidal type of nanocellulose, the low solubility and high chemical stability of cellulose are exploited: Amorphous regions of the fibril can be selectively cleaved by a strong acid, while the recalcitrant crystalline domains remain largely unaffected. The result is highly crystalline, rod-shaped particles, often also referred to as cellulose nanowhiskers, with dimensions between 3 nm to 30 nm in width and 50 nm to 3000 nm in length, depending on the cellulose source.[55] Dimensions found for the most common sources are summarized in Table 2.1. CNCs are inherently

chiral, expressed by torsion in the rod-shaped particle that arises from a spontaneous strain build-up within the crystal structure of the glucan chains.

Table 2.1: Dimensions of CNCs obtained from different cellulose sources. [55]

Cellulose source	width [nm]	length [nm]
Bleached wood pulp[56;57]	3–5	50–150
Cotton linters[58;59]	6–8	50–300
Tunicate[56]	10–20	500–3,000
Bacterial cellulose[60;61;62]	10–15	500–1,500

Most studies on CNCs use Whatman filter paper No.1, made from cotton linters, as a cellulose source, likely due to its purity, availability, and consistency of cellulose properties in between the different labs. However, while the production of paper or cotton yarn relies on intact, long fibers, CNCs, as the building blocks of the fiber, can be extracted from virtually any pristine cellulose-containing source. The use of valuable cotton linters for CNC production therefore only makes sense on the lab scale – a large-scale production of CNCs should use non-competitive product streams. In that spirit, there has been a continuing trend of reporting on the valorization of waste streams by extraction of CNCs from a plethora of cellulose-containing plant wastes, from sunflower stalks[63] to tomato peel.[64] Consequentially, CNC production can be introduced as a side chain of paper production facilities, valorizing recycled cellulose with a quality too low for paper products. Being the protagonist of this present work, isolation and functionalization methods, characteristics, as well as possible applications of CNCs are reviewed in detail in the following section.

2.2.2   Isolation of cellulose nanocrystals

After it was discovered that cellulose can be completely degraded to glucose by hydrolysis, early research on CNCs started with the intention of investigating the fine structure of the cellulose fiber. By studying weight loss and degree of polymerization (DP) upon degradation of cellulose with hydrochloric acid, researchers like Nickerson and Habrle, Battista, and Davidson, to name a few, discovered a change of hydrolysis rate with proceeding reaction time, which was attributed to the different cellulose morphologies present in the fiber. They demonstrated that after an initial rapid decrease in molecular weight, i.e. rapid hydrolysis, it tends to level off with proceeding hydrolysis time.[65] This was interpreted as an initial hydrolytic cleavage of the polymer in the highly accessible and swollen amorphous domains, followed by only slow degradation of the crystallized cellulose. The DP at which a plateau of slow hydrolysis rate is reached is known as the leveling-off degree of polymerization (LODP) and is considered to correspond to the aver-

age crystallite length.[66] By choosing mild conditions, Nickerson was the first to control hydrolysis conditions to only cleave glycosidic bonds in the amorphous domains, reporting the first hydrolytic extraction of CNCs.[67] Their value outside of analytical purposes, however, was not appreciated until the works of the group around Gray in 1992, who discovered the spontaneous formation of a chiral nematic phase in concentrated dispersions of CNCs isolated via hydrolysis in 65 % sulfuric acid.[68] Treatment of cellulose with H_2SO_4 not only hydrolyses amorphous domains but also causes functionalization of the isolated particles by esterification of the surface hydroxyl groups with sulfate, creating sulfate esters as anionic groups that aid colloidal stability. The high charge density of usually 0.1 mmol/g to 0.4 mmol/g[3] enables a close interaction of the nanorods while avoiding their aggregation, translating their inherent chirality into the liquid crystalline phase. Cholesteric phases with a pitch in the range of the wavelength of visible light can interfere with light to produce so-called structural color. This property has given rise to great research efforts into nature-inspired decorative colors or optical materials based on CNCs, as reviewed by Parker et al.[69] Sulfuric acid hydrolysis presents the most popular method for CNC extraction to this day, due to the high colloidal stability of the resulting particles. Although it is an inexpensive method, a lot of water is needed for quenching of the reaction, which furthermore impedes the recyclability of the used acids. The colloidal stability of sulfuric acid-hydrolyzed CNCs, moreover, comes at a cost: The sulfate half-ester groups aggravate the CNCs thermal stability, compared to pristine cellulose.[70] Hydrochloric acid hydrolyzed CNCs have higher thermal stability but are uncharged so they do not form a stable colloidal suspension and are difficult to disperse and handle.[71] Other mineral acids, such as hydrobromic acid (no charge)[72] and phosphoric acid[71;73], have also been successfully applied for CNC extraction. Phosphoric acid hydrolysis leads to thermally more stable CNCs, while phosphate esters provide a stabilizing surface charge.[71;74] Hydrolysis with dicarboxylic acids like oxalic and maleic acids was shown to yield highly stable CNCs functionalized with carboxylic acid groups via esterification of the other carboxyl group with cellulose hydroxyl groups. The product displayed similar charge density and colloidal stability as sulfate-CNCs, and even a higher thermal stability. Moreover, the authors claim that the solid acid can be fully recycled due to its low water solubility at lower temperatures, which is a promising step towards a more sustainable CNC production.[75] Besides the extraction of functionalized CNCs in the one-step processes presented above, a plethora of two-step approaches exists in which the CNC isolation via conventional hydrolysis is followed by a post-functionalization step. Those methods use either the classic and well-known chemistry of the pristine hydroxyl groups or modify the groups introduced during the acid hydrolysis to tailor the surface properties of the nanocrystals for specific applications.

2.3 Applications of CNCs

CNCs have gained attention as sustainable materials in various fields of material science from low-tech to high-tech, owing to its versatile properties. Their availability from abundant sustainable resources makes CNCs a promising nanomaterial even for large-scale industrial applications. Freed from the majority of the weak disordered regions of the CNF, the CNC has a remarkable tensile strength of 7.5 GPa and a Young's modulus of 100]GPa to 140 GPa, similar to Kevlar.[76] Combined with their low density, CNCs have proven efficient mechanical reinforcing agents in nanocomposites with synthetic polymers, such as PVA[77] or polyurethanes,[78] and natural polymers, such as natural rubber[79] or gluten[63], but also inorganic materials, such as cement.[80] Their high degree of crystallinity has a second effect of decreasing gas permeability,[81] which is desirable for instance for food packaging applications or gas separation membranes. Their ability to self-assemble into chiral nematic liquid crystal structures that produce tunable structural color offers possibilities not only as biodegradable pigments, but also in sensing and security paper applications.[82] Due to their anisotropic geometry, CNCs are also efficient rheology modifiers promoting shear thinning behavior[83] with the potential to replace petroleum-based additives for instance in paints and coatings or drilling fluids.[84] Moreover, the rod-shaped particles can be manipulated into anisotropic bulk materials by external forces, for instance through directional freeze-casting to form foams for insulating construction materials.[85] Amphiphilic particle properties also allows their use as Pickering stabilizers in sustainable and biocompatible food emulsions or emulsions for personal care.[86] Thanks to their tailorable surface chemistry, many more applications have been explored and reviewed in an abundance of articles. A large part of common-good applications for synthetic polymers are based on films, form-stable three-dimensional (3D) objects, or their diverse behavior as additives or interfacial agents. While CNCs can be applied as niche products, those large-scale applications would have the highest environmental impact due to their sheer mass. For this reason, applications attempted in this work focus on the applicability of CNCs for those purposes, which are covered in more detail in the following sections.

2.4 Self-standing films of cellulose nanocrystals

Many applications of synthetic fossil-based polymers which are in need of replacement with biopolymers, such as packaging, flexible devices, or membranes, require self-standing films of those polymers. While cellulose derivatives such as cellulose acetate or regenerated cellulose, i.e. cellophane, have been used as packaging films since the early 1900s,[87] the application of CNCs as freestanding films is limited. Their inherent brittleness makes pure CNC films difficult to manage or apply in mechanically demanding applications, so that

research on CNC films is rare and focused primarily on composites with other polymers. Composite materials exploiting CNCs as reinforcing agents in flexible polymer matrices have previously been studied extensively, as reviewed by Kargarzadeh et al. [54] and Calvino et al. [88] As a highly crystalline form of cellulose, largely cleared of amorphous, gas transport-enabling domains, CNCs are not only appreciated for their mechanical strength but were also discovered as excellent gas barrier materials. The addition of crystalline particles decreases the free transient volume and increases tortuosity, hampering the gas transport through the material. Both HCl- and H_2SO_4-hydrolyzed CNCs have been found to cause a decrease in gas permeability when blended with other polymers. For instance, Rafieian et al. described gluten/CNC composites that presented improved air barriers and decreased water vapor permeability, along with increased tensile strength compared to the pure gluten film, while exhibiting decreased elongation at break, demonstrating a higher brittleness in the blend. [89] Nuruddin et al. found high barrier properties in polyvinyl alcohol-CNC composites. [90] With CNCs themselves being born from the idea of sustainable materials and green chemistry, most research on CNC-reinforced polymer composites focuses on bio-based polymer matrices, such as polyesters such as poly lactic acid, [91] polysaccharides like starch and gum arabic, [92] or proteins such as gluten. [93] Due to the brittleness of the rigid cellulose whiskers, reports of freestanding CNC films without a polymer matrix are rare: Poor mechanical properties, despite their high individual strength, make application challenging and seemingly unpromising. Therefore, CNCs are underrepresented in advanced film applications compared to CNFs, which produce more flexible and mechanically stable films thanks to their entangling fibrils. Only in 2021, Fernandez-Santos et al. reported studies on CNC films which they plasticized with small natural molecules such as sugar alcohols and ethylene glycol, exhibiting good barrier properties. [94] Such plasticizers, rich in hydroxyl groups, interact with the surface hydroxyl groups of cellulose, thereby decreasing the inter-particle attraction that leads to the rigid 3D structure. This way, the film-forming properties and flexibility of the film were improved.

2.4.1 Gas permeation through non-porous polymer materials

Regardless of whether a film is used as a protective sealing coating or an active gas separation membrane, the permeation behavior of gases plays a crucial role. Due to the small size of the molecules and their un-condensed state, gases can easily pass through porous materials. Gas-tight or gas-separating materials should ideally exhibit very low porosity. In non-porous polymer materials, gas transport follows a solution-diffusion mechanism: Gas is dissolved in the material and is then transported through the material via diffusion. Diffusion is only possible in dynamic systems in which a transient free volume exists that allows Brownian motion of gases – that is, in amorphous materials. [95]

In polymer crystallites, chain movement is restricted such that no transient free volume is available. It was shown that the permeability of polymeric materials decreases with an increasing degree of crystallinity.[96] Mixtures of gases can be separated based on different individual gas permeabilities, due to differences in their diffusivity and their solubility in the membrane material. For an effective separation of gases, a high selectivity of one gas over the other, i.e. a big difference in their permeabilities, is necessary. At the same time, the permeability should be high enough to ensure an efficient permeation and separation. There is, unfortunately, a trade-off between permeability and selectivity, called the upper bound, as proposed by Robeson.[97;98] This means that an increase of permeability usually goes at the cost of selectivity. Membranes that overcome the Robeson upper bound via facilitated transport mechanisms are in high demand to improve efficiency of membrane processes. Facilitated transport membranes contain a carrier (facilitator) which selectively interacts or reacts with a solute, carrying it across the membrane, while the transport of other gases is inhibited due to a low overall gas permeability. This way, selectivity and permeability of the targeted solute are increased.

2.5 Pickering emulsions

Emulsions are mixtures of two immiscible liquids in which one of the liquids is dispersed as fine droplets in a continuous phase of the other liquid. This dispersion is in a thermodynamic non-equilibrium that tends toward phase separation, unless it is stabilized by interfacially active agents, usually by molecular surfactants. As independently discovered by W. Ramsden and S.U. Pickering in the 1900s, small solid particles can also adsorb at the oil-water interface and form highly stable emulsions, so-called Pickering emulsions, named after just one of their discoverers.[99;100] The stabilization mechanism is based on the adsorption of particles to the oil-water interface which minimizes the high interfacial tension between oil and water, the driving force for coalescence and phase separation. For a particle to adsorb at the interface, it needs a certain affinity for, or wettability in, both the aqueous and the oil phase. If the particle has too low an affinity for either of the phases, it will remain dispersed in this phase and not adsorb at the interface. The stability of a Pickering emulsion is thus dependent on the energy of adsorption of the particle at the interface ΔE, which is described in Equation 2.1 for a spherical particle:[101]

$$\Delta E = \pi r^2 \cdot \gamma_{\mathrm{ow}} \cdot (1 - |\theta_{\mathrm{ow}}|)^2 \tag{2.1}$$

with r: particle radius, γ_{OW}: interfacial tension between oil and water phase, and θ_{OW}: contact angle between the particle tangent and the o/w interface. For an ideal stabilization, the water contact angle θ_{w}, which is a measure of the hydrophilicity of a surface, should be close to 90°: Here, the particle has an equal affinity for both phases and will

adsorb at the interface under energy release. For particles with a preference for one phase, the phase with higher affinity to the particle will be the continuous phase and the other phase will be dispersed. A hydrophilic particle with $\theta_\text{w} < 90°$ will cause an oil-in-water (o/w) emulsion, while a hydrophobic particle with $\theta_\text{w} > 90°$ will produce an inverse, or water-in-oil (w/o) emulsion, as depicted in Figure 2.3.
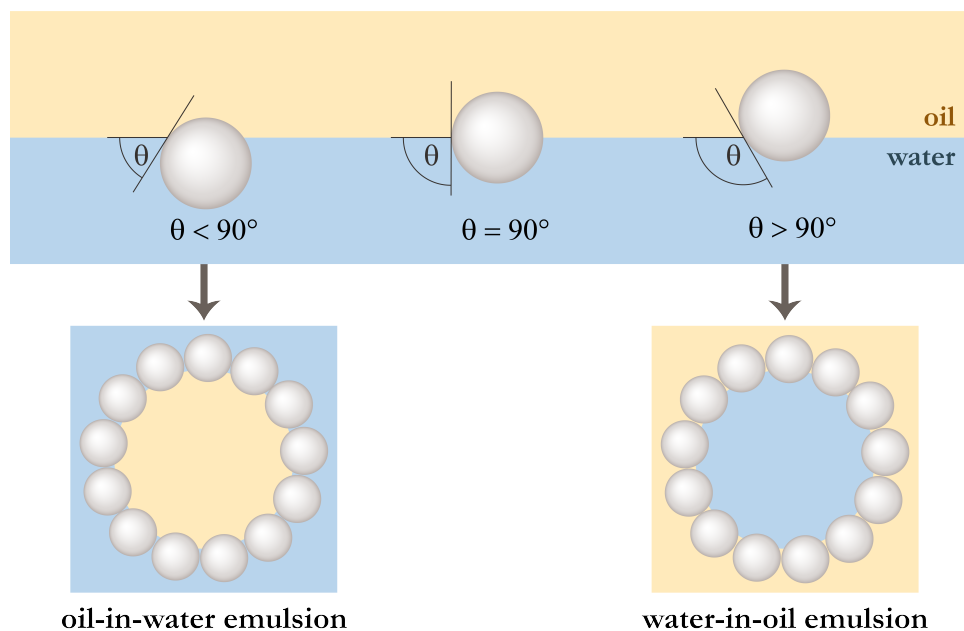

Figure 2.3: Schematic depiction of particles with a θ_OW smaller, equal to, and larger than 90° at the oil/water interface and the resulting Pickering emulsions.

For appropriate particles with θ_ow close to 90°, the adsorption energy is in the range of $10^4\ k_\text{B}T$, which is around a thousand times larger than for normal surfactants, explaining the superior stability of Pickering emulsions.[102] Pickering stabilizers are increasingly gaining attention as environmental and health concerns about molecular surfactants grow. They are already widely spread in foods, such as margarine, mayonnaise, or milk, and are considered sustainable and harmless alternatives to conventional surfactants.

2.5.1 Rheology of emulsions

Rheology, or the study of the flow of matter, describes how matter behaves under the influences of shear forces. The reaction of a substance to an external shear is determined by its inner friction, or resistance, against the shear. This is the viscosity of the substance, which is defined as the force that is necessary to move two plates sandwiching a fluid against each other. Newtonian fluids exhibit a linear dependence of shear stress τ versus shear rate $\dot{\gamma}$, the slope of which is the viscosity. Fluids that are not just a pure liquid but for instance a polymer solution, a suspension, or an emulsion, also described as structured fluids, tend to have a more complicated rheology: Here, the magnitude of η depends on the rate at which the fluid is sheared. A fluid whose viscosity increases with

increasing $\dot{\gamma}$ is called shear-thickening, while a decreasing η with increasing $\dot{\gamma}$ is called shear-thinning. This non-Newtonian behavior is due to intermolecular entanglements or elastic interactions between dissolved macromolecules or suspended particles or droplets.

Every matter, solid or soft, can be classified in terms of viscosity and elasticity, summarized in the dynamic modulus G^*. G^* is composed of the storage modulus G', its real portion, and the loss modulus G'', its imaginary portion. G' expresses the portion of the deformation energy which is stored in the matter, or a reversible deformation. G'' expresses the viscous portion of the matter, an irreversible deformation whose energy is dissipated as heat (Equation 2.2).

$$G^* = G' + iG'' \tag{2.2}$$

with i: imaginary unit. For ideal elastic solids, G'' converges to 0, while for ideal viscous matter, G' converges to 0. As viscous deformation is time-dependent, G^* can be measured in oscillation experiments as the ratio of stress to strain under vibration. Many substances show both an elastic and a viscous response on different time scales and can be described as viscoelastic matter. If the viscous behavior dominates ($G'' > G'$), the material is called viscoelastic liquid. If the elastic behavior dominates ($G' > G''$), it is called viscoelastic solid. Viscoelastic solids have a point of yield at which the stress (or modulus) becomes dependent on the strain, which is the stress at which the material changes its rheology from solid to fluid, called yield stress σ. It is the minimum shear stress required to break the internal structure of the material to make it flow. Small deformations (strains) do not change the viscoelastic properties of the material, causing a plateau called the linear viscoelastic region (LVR) in which the moduli are independent of strain. The yield stress can be defined either as the onset point at which G' deviates from the LVR or as the crossover point of G' and G'', at which the viscous behavior becomes dominant.

The viscosity of a suspension of spherical particles, as described in the Krieger-Dougherty equation (Equation 2.3), is dependent on the viscosity of the continuous phase η_c, the particle concentration Φ and the space filling, or close packing concentration, Φ_C.[103]

$$\eta = \eta_1 \left(1 - \frac{\Phi}{\Phi_C} \right)^{-2} \tag{2.3}$$

Stoke's law (2.4) describes the force experienced by a sphere falling through a viscous liquid by balancing the weight of the sphere and gravitational forces with the friction of the fluid and the buoyancy which counteracts the falling:

$$F = (\rho_\mathrm{s} - \rho_\mathrm{f} g \frac{4}{3} \pi R^3) \tag{2.4}$$

with ρ_s and ρ_f the mass densities of sphere and fluid, g the gravitational acceleration and R the radius of the sphere. It follows that in emulsions and suspensions, a high viscosity of the continuous phase aids dispersion stability by preventing gravitational separation of continuous and dispersed phase.

2.5.2 CNC-stabilized Pickering emulsions

Rod-shaped particles have the potential of stabilizing Pickering emulsions more efficiently compared to spherical particles due to their ability to form a percolating network. For rod-shaped particles like CNCs, Equation 2.1 is adapted to the surface of the rod defined by its length l and its width b:

$$\Delta E = l \cdot b \cdot \gamma_{ow} \cdot (1 - |\theta_{ow}|)^2 \tag{2.5}$$

 The group around Isabelle Capron proved in 2011 that unmodified CNCs obtained from BNC can adsorb at the oil-water interface and produced hexadecane-in-water Pickering emulsions that were stable for over a year.[104] Despite the abundantly present hydroxyl groups, CNCs evidently exhibited a certain affinity for the hydrophobic oil phase as well. This was explained by the chemical inequivalence of the different crystalline faces in the nanocrystal: The (200) plane is composed only of the methylene groups of the cellulose, which makes it hydrophobic. This face has a higher affinity towards oil and will seek contact to the oil phase, as depicted in Figure 2.4. The hydrophilic faces (110), (1-10), and (010) are rich in hydroxyl groups and will face the aqueous phase.[105] Those different polarities within the same particle give the CNC an amphiphilic character. The hydrophobic edge plane was proven by several groups through adsorption,[106] molecular modeling,[107;108] X-ray scattering,[109] and small-angle neutron scattering experiments.[110]
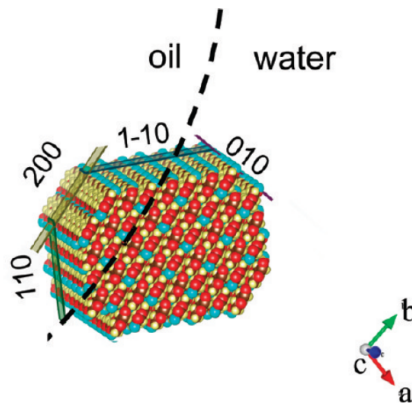

Figure 2.4: Schematic representation of the stabilization of the I_β cotton CNCs at the oil/water interface, exposing the hydrophobic edge (200) to the oil phase.[105]

As functionalization of the CNCs occurs at the hydroxyl groups on the hydrophilic faces, the hydrophobic edge plane is expected to be preserved in modified CNCs. However,

Capron's group found that sulfate-CNCs were not able to stabilize emulsions, which they attributed to the high negative surface charge that prevents the CNCs' assembly at the interface due to particle repulsion. Screening of the charge through addition of salt was found to sufficiently reduce repulsion and allow emulsification also for charged CNCs. [111] Due to their biocompatibility and biodegradability, CNC-stabilized emulsions are also considered promising for edible emulsions.

2.6 3D printing of nanocellulose

Additive manufacturing is becoming increasingly popular in every field of material science in which parts are not mass-produced, but rather created on-demand and customized. One of the most versatile ways for 3D printing is direct ink writing (DIW), a method in which the ink is simply extruded from a nozzle to build a layer-by-layer structure. DIW is possible with a broad range of materials, from metal to ceramics or polymers, as long as the ink meets the rheological requirements for successful printing. [112] Those requirements are summarized in the concept of a viscoelastic solid, which is solid at rest and liquid when sheared above the yield stress: Shear-thinning allows the extrusion of the ink through the printing nozzle under shear stress and its arrest when deposited. To retain the printed shape, a high storage modulus (higher than the loss modulus) that is restored quickly after printing is important. Moreover, inks need sufficiently high yield stress (which is the pressure required to make the ink flow) to support the weight of the printed structure without yielding.

Tissue engineering or the engineering of biomaterials benefits greatly from efficient DIW techniques, as the required parts are often highly personalized and complex. Using additive manufacturing techniques, the desired tissue, or organ, is first imaged by scanning methods like MRI or CT and segmented to build a 3D computer model, which is then printed using a suitable bio-ink. The printed object acts as an extracellular matrix in which the appropriate cells will be able to proliferate and grow into the shape of the provided matrix. Bioprinting inks evidently must be biocompatible and cannot release toxic degradation products. It is therefore advantageous to use inherently biocompatible natural compounds.

Biomaterials in general are largely based on synthetic polymers, which can be designed to match the required mechanical properties of natural tissue through tailoring chain lengths, branching, or adding other functionalities during their synthesis. One of the most commonly used polymers is polyethylene glycol (PEG). However, the biocompatibility of synthetic polymers is not as good as inherently biocompatible natural polymers such as collagen, fibrin, gelatin, or alginate. Those biopolymers are therefore promising alternatives for synthetic polymers, but their properties are determined by nature.

With their shear-thinning, gel-like properties, nanocellulose dispersions have a suitable rheology profile for DIW. However, the results are usually unsatisfactory due to low achievable solid contents especially in CNF dispersions due to entanglements: The evaporation of around 99 wt.% of water causes an extremely high shrinkage upon drying and with that a low shape fidelity.[113] Elaborate methods like wet densification[114] achieve a certain degree of control of the shrinkage by slow exchange of the solvent to a non-solvent that causes the nanocellulose to de-swell and densify. The object has to be printed several times larger than its desired dimensions. To reduce shrinkage and improve mechanical properties, printed structures can also be infiltrated with photo-polymerizable monomers, which eliminates the biodegradability of the ink.[114;115] A popular approach especially in tissue engineering is the combination of nanocellulose with the biopolymer alginate, which can cross-link in the presence of calcium ions to form a hydrogel.[116]

CHAPTER 3

Extraction of cellulose nanocrystals using a reactive eutectic medium

The most common methods to obtain electrostatically stabilized colloidal CNCs involve large amounts of highly corrosive concentrated inorganic acids such as H_2SO_4 or HCl, the latter one requiring a further reaction step in which hydroxyl groups are oxidized to carboxyl groups catalyzed by the TEMPO radical. Large-scale applications of concentrated strong acids entail a high risk for the worker as well as high demands on the materials in contact with the medium. Aggressive methods like these are not in agreement with the Green Chemistry Principles. Moreover, both methods produce anionic CNCs. Electrostatically stabilized particles as well as polyelectrolytes are highly sensitive to their environment. A broad applicability of CNCs requires their colloidal stability in a variety of media, and in contact with both cationic and anionic species. Cationic CNCs are therefore a necessary addition to the toolbox of bio-based, sustainable nanomaterials. They might open new doors for colloidal applications and formulations for, among others, pharmaceutics, cosmetics, personal care, and detergents, as well as composite materials. For instance, CNCs, or nanocelluloses in general, are regarded as promising sustainable systems for water remediation, as reviewed recently by Das et al.[117] Conventional anionic CNCs were found efficient as adsorbents in waste water treatment to remove cationic contaminants.[118] Cationic CNCs are an important counterpart to allow coagulation or flocculation of anionic pollutants, such as nitrates, fluorides, sulphates and phosphates[119]

To date, most pathways to cationic CNCs have followed a two-step process, in which the conventional acid hydrolysis is followed by a second functionalization step. Cationization agents used in this step are often toxic epoxy compounds: Hasani et al. used epoxypropyltrimethylammonium chloride to introduce a trimethylammonium functionality to the hydroxyl groups of CNCs obtained via hydrochloric and sulfuric acid hydrolysis.[120] Akhlagi et al. produced amine-functionalized CNCs by grafting epichlorhydrin,

aminated with ammonium hydroxide, onto pre-isolated CNCs.[121] Apart from using unsustainable and dangerous chemicals, those approaches also changed the native structure of cellulose, possibly impacting its biocompatibility and -degradability.

DESs have been applied to isolate or functionalize CNCs due to their highly polar nature that provides good interactions with the rich in hydroxy groups cellulose. Many methods use derivatizing media, in which the DES is not merely the reaction medium, but takes on a second role as a reagent. Those media are also called reactive eutectic media (REM), as they cause chemical modification of the carbohydrate. Most reported DES treatments introduce carboxyl groups to the CNC,[122;123;124;125;126] thereby giving it an anionic surface charge, just like conventional TEMPO or H_2SO_4 treatments. Few REM treatments are reported to introduce cationic groups, such as guanidine, and they usually require multiple processing steps.[119;127;128;129] The most-used DESs are based on the quarternary ammonium salt choline chloride, paired with a large variety of HBDs. A drawback of choline chloride-based DESs is their high viscosity due to strong intermolecular interactions, which makes them difficult to work with. It is therefore crucial for their large-scale application to find alternative systems with workable viscosities. One way to lower viscosity can be the exchange of choline chloride with a different ammonium salt. The use of low-molecular weight molecules in DESs might decrease their viscosity and aid their applicability. Previously to my work in this group, ammonium formate was used as a component in a reactive eutectic medium with different monosaccharides, in which it was found to take part in the reductive amination of those sugars.[130] Ammonium formate is the salt of ammonia with formic acid, two of the cheapest bulk chemicals, and as such highly available and more affordable than choline chloride (48 €/kg versus 110 €/kg[1]).

Its reactivity towards sugars makes ammonium formate interesting for the derivatizing treatment of carbohydrates, such as cellulose, as well. In this thesis, its application as an HBA in an REM aims at introducing amino groups to the cellulose, which carry a positive charge in neutral to acidic aqueous media. As HBD, a myriad of naturally occurring components is available. Here, organic acids are chosen as potential eutectic-forming partners for AF, to catalyze the cleavage of the disordered cellulose domains and isolate the crystalline domains, the CNCs. The presence of ammonium in the form of ammonium formate is expected to induce aminolytic instead of hydrolytic cleavage, which would cause additional amino-functionalization. Many organic acids occur naturally and hold the potential to be produced from biomass in a sustainable way, which makes them good candidates for a sustainable reaction medium. For instance, lactic acid is already primarily produced by the fermentation of sugars and starch.[131]

---

[1]Prices retrieved on 10/10/2022 from sigmaaldrich.com for similar grades and packaging size of 1 kg; large-scale costs will deviate.

This chapter reports on the development of a new method for isolating cationic CNCs in a one-step process using an REM, which aims at meeting Green Chemistry principles with minimal impact on the environment and worker safety. Only abundant and nontoxic chemicals are used. Parts of the presented analyses were conducted by collaborators: X-ray photoelectron spectroscopy (XPS) was performed by Dr. Oleksandr Selyshchev (TU Chemnitz, group of Prof. Dr. Dr. h.c. Zahn) and Dr. Sarah Vogl (TU Berlin, group of Prof. Dr. Arne Thomas). Cross-polarization magic angle spinning (CP-MAS) nuclear magnetic resonance (NMR) was performed by Dr. Michaela König (TU Berlin, group of Prof. Dr. Arne Thomas). Heteronuclear single quantum coherence (HSQC) NMR experiments were conducted by Lukas Fliri (Aalto University, group of Prof. Michael Hummel). Transmission electron microscopy (TEM) images were partially recorded by Dr. Yu Ogawa (CERMAV-CNRS). Parts of this section are published and patented. [132;133]

3.1 Results and Discussion

In the scope of this project, a variety of organic acids is first screened as potential HBD in ammonium formate-based eutectics. Their effectiveness regarding the treatment of cellulose and the extraction of CNCs is then tested and evaluated using simple small static autoclaves. The most promising system is further optimized and scaled up and the products are analyzed to verify the underlying mechanism and characterized to discover their potential for application.

3.1.1 Screening of organic acids as hydrogen bond donors in ammonium formate-based REM

The formation of a eutectic between ammonium formate as HBA and six organic acids as HBDs, glycolic, lactic, levulinic, propionic, oxalic, and succinic acid, was first tested. The eutectics, denoted REM1-6 in the following (see Table 3.1) were then applied as REM to extract CNCs from short-fiber cellulose as a model compound. The extracted cellulosic products will be denoted as NC1-6, the number corresponding to the respective REM denomination.

3.1.1.1 Investigation and properties of possible REM

Based on previous findings in our group, REM were prepared using ammonium formate (AF, T_m 120°C) as the hydrogen bond acceptor component and different natural organic acids as hydrogen bond donors in a molar ratio of 2:1 (AF:acid). Sample identifiers for the resulting REM and the phase transition temperatures for the used acids are given in Table 3.1. It must be noted that lactic acid was applied as 85-90 % solution, as due to its hygroscopic nature, it is significantly more expensive to obtain at higher purity.

Table 3.1: Melting points of the used organic acids and ammonium formate

	Organic acid	T_m [°C]	T_b [°C]
REM1	Glycolic acid	78-80	100 (decomposition)
REM2	Lactic acid	17	122 (20 hPa)
REM3	Levulinic acid	33	245
REM4	Propionic acid	-21	141
REM5	Oxalic acid	102	157 (decomposition)
REM6	Succinic acid	185-190	235

For a large-scale application of a reaction medium, economic factors are of high concern. However, the inclusion of water into the DES can be an attractive way of reducing its viscosity to improve its performance.[134] Moreover, for the application in biomass or pulp processing, it is advantageous that the reaction medium has a certain tolerance for water, as those raw materials often have residual wetness that is energy-expensive to remove.

Upon mixing of AF and acid, the mixture cools down and slowly transforms into a colorless transparent liquid, indicating the formation of a eutectic. To facilitate the endothermic mixing, the REM, apart from REM4, were kept in the oven at 60 °C until a single liquid phase was formed with occasional mixing. REM4 contains flammable propionic acid and was kept only in a 40 °C water bath for safety reasons. Figure 3.1 shows the REM after one hour at 80 °C and after 24 hours. REM1 and REM2 form a clear and colorless liquid within an hour even without mixing. REM3 turns yellow upon the influence of
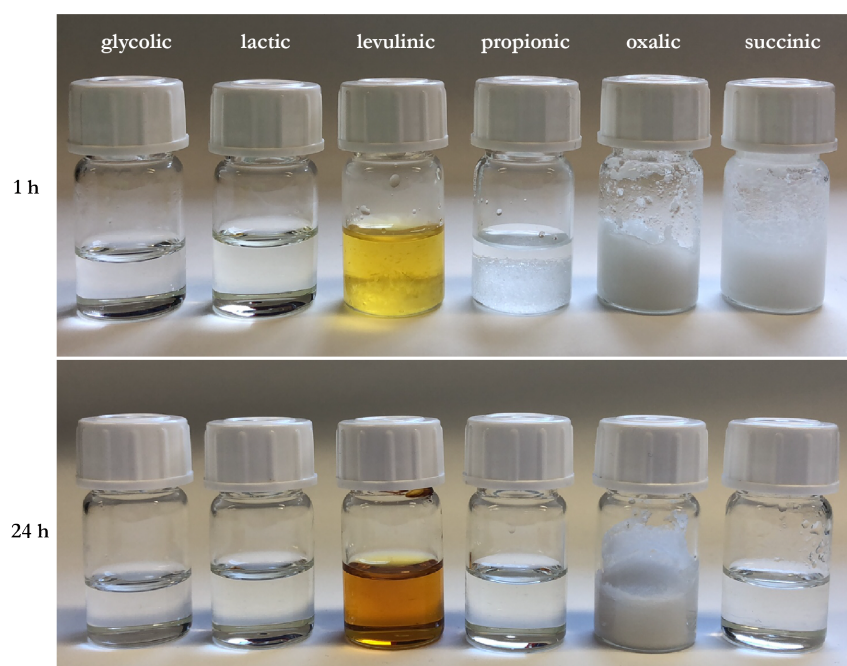

Figure 3.1: Photographs of REM1-REM6 (from left to right) composed of ammonium formate and the respective acid noted in the image, after 1 h and 24 h at 80 °C.

heat, indicating the formation of by-products, and takes 4 h to form a single liquid phase. REM4 and REM6 take significantly longer, while oxalic acid (REM5) does not form a eutectic with ammonium formate at the chosen molar ratio, even after heating to 100 °C, which is close to the melting temperature of the used oxalic acid dihydrate. REM3, 4 and 6 show a high tendency to recrystallize during storage. REM1 and REM2 remain liquid and are therefore the most reliable eutectics to work with.
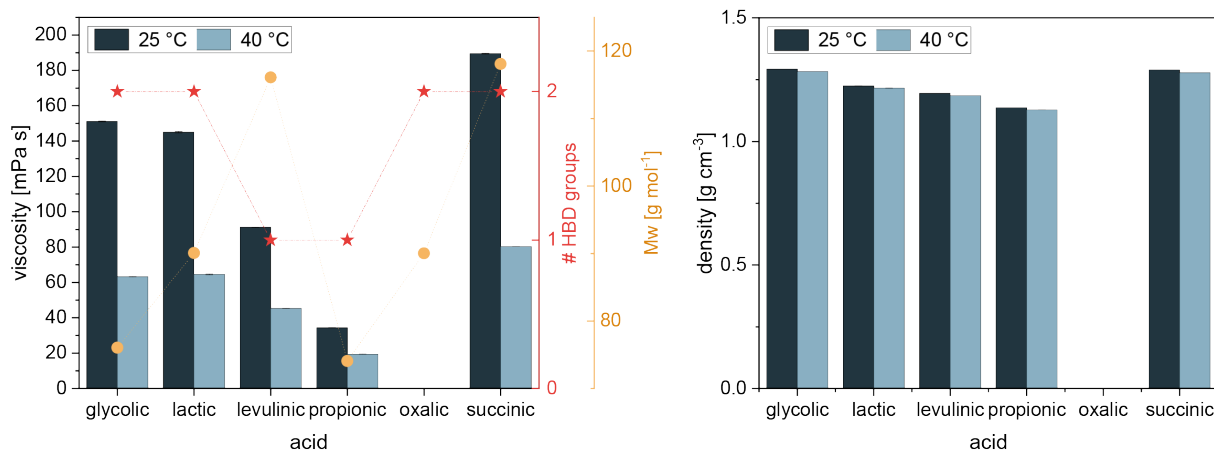

Figure 3.2: Viscosities and densities measured at 25 °C and 40 °C for REM 1-6. REM5 could not be measured as it did not form a eutectic at the measurement temperature.

Figure 3.2 shows the viscosities and densities of the REMs measured at 25 °C and 40 °C. Among the tested acids, the REM with propionic acid has the lowest viscosity of 34 mPas, while the use of succinic acid leads to the highest viscosity of 189 mPas. For comparison, the classic DES system choline chloride/urea has viscosities between 636 mPas (2.5:1) and 821 mPas (1.5:1).[135] ChCl:LA (2:1) prepared in the scope of this work exhibits a viscosity of 238 mPas at 40 °C, which is significantly higher than the viscosity of the AF:LA eutectic (64.6 mPas) at the same temperature. At 25 °C, ChCl:LA solidifies, proving that AF results in a lower melting point depression as well as eutectics with lower viscosities compared to ChCl, as it was intended. The density of the REMs follows the trend of their viscosities. Like low viscosity, low density is also advantageous for extraction and solubility purposes, as it allows better penetration into the material.

REM1-3 seem the most promising systems, as they show the fastest formation of the eutectic phase. Differential scanning calorimetry (DSC) was performed on those REMs to investigate their phase transitions (Figure 3.3). REM1 shows a glass transition at around -83 °C, a recrystallization at -38 °C and a melting point at -21 °C. REM2 shows very similar transformations with a glass transition temperature of -85 °C, a crystallization temperature T_c of -41 °C and a melting temperature T_m of -21 °C. Both curves are reproducible over multiple cycles. Remarkably, the water included in REM2 through the lactic acid does not cause a separate crystallization event, which implies that it is tightly incorporated into the eutectic structure. The determined T_m for both REM1 and REM2

proves the effective melting point depression respective to AF and both organic acids (compare Table 3.1). REM3 exhibits a weak glass transition at a temperature shifting between -89 °C and -76 °C. The curves are not reproducible, and the inclination at higher temperatures changes between cycles, suggesting ongoing chemical changes in the REM at elevated temperatures. This was also observed by change of color from transparent to yellow to orange. A melting point is not observed.
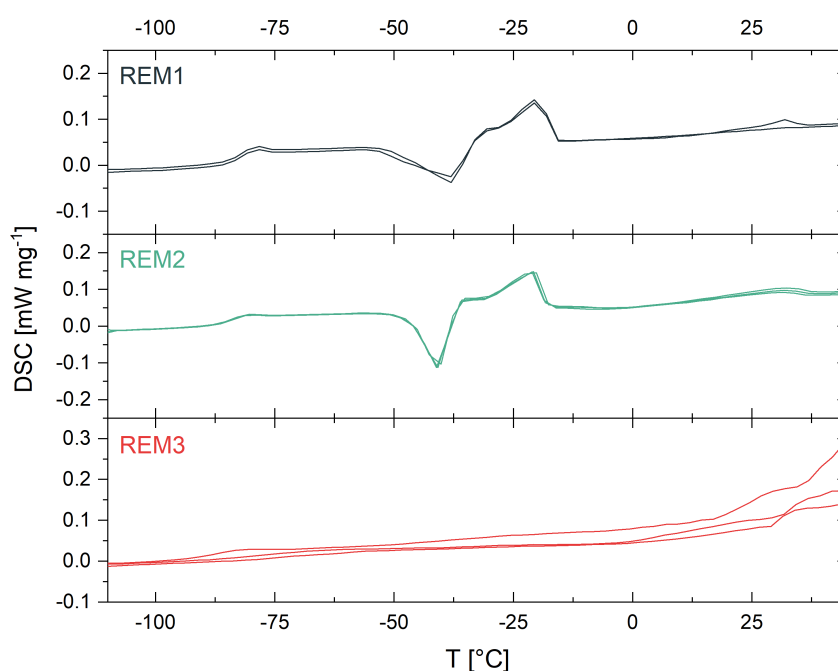

Figure 3.3: Differential scanning calorimetry (DSC) traces for the eutectic mixtures REM1, REM2 and REM3.

3.1.1.2 Application and evaluation of eutectics as REM

All REM were tested as extracting and functionalization media of CNCs. Although REM5 was not observed to form a eutectic, it is possible to test it as a reaction medium, since the reaction temperature lies above the melting points of ammonium formate and oxalic acid, so that the medium is liquid at operating temperature. According to the hypothesized reductive amination of reducing ends and aminolysis of the amorphous domains, cellulose particles with a positive charge due to the introduced amino groups, which are protonated in neutral to acidic media, would be expected. To test their activity, REM were mixed with a fibrous granulated cellulose in a mass ratio of 2:1, yielding a thick slurry. The mixture was reacted in small static autoclaves at 180 °C for 4 h. After this time, all of the reaction mixtures are browned and exude an aromatic smell, indicating the formation of Maillard products (see Figure 3.4). The Maillard reaction is a non-enzymatic browning reaction between amines and reducing sugars and it is responsible for the aromatic taste of browned food.
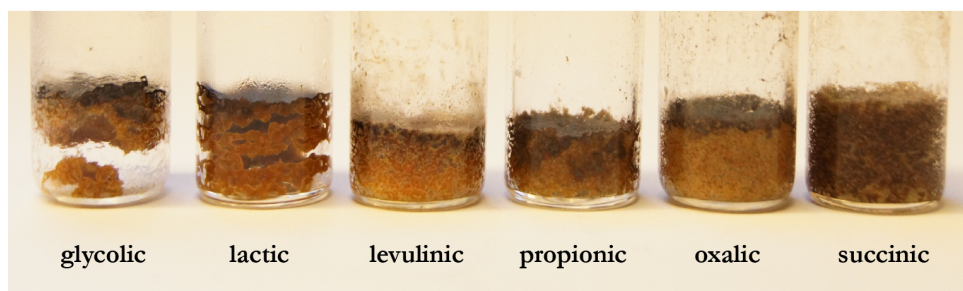
Figure 3.4: Products of extraction attempts with REM1-REM6.

The presence of Maillard products implies partial cleavage of the polysaccharides into oligo- or monosaccharides (glucose derivatives) via aminolysis, which can further react with ammonium or with each other, forming the brown by-products. There exists a large variety of different reaction pathways and possible Maillard products to occur, so that a specific by-product is difficult to identify. Exemplary ^{1}H NMR spectra of REM2 before and after the extraction are shown in Figure 3.5. The medium appears largely unchanged but indications for the contained by-products are found in the range of 3.3 ppm to 3.6 ppm. This range corresponds to protons in hydroxy or amino groups, but the overlapping signals do not allow identification of a specific compound.
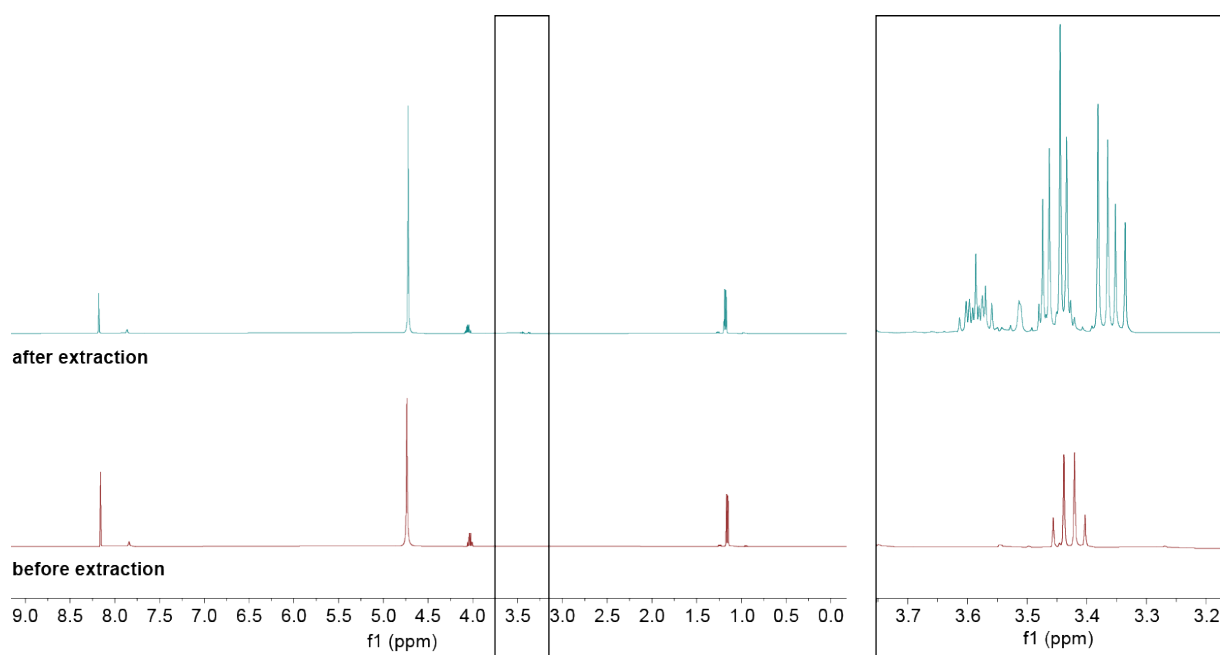

Figure 3.5: ^{1}H NMR spectra of REM2 before and after the extraction of cellulose.

To remove the REM and by-products, the slurries were washed with water and ethanol via centrifugation to obtain the cellulosic product as the solid sediment. In the samples treated with REM1, 2, 3, and 4, part of the solid remains in the supernatant after several washing cycles, indicated by a whitish turbidity. While a considerable part of the product still precipitates, the colloidal suspension of cellulosic particles remains stable for several months. This hints at particles on the nano-scale and possible electrostatic stabilization

of the particles. The products of REM5 and REM6 retain a darker brown shade and seem to contain mainly larger particles that sediment quickly. Preliminary observations with polarized optical microscopy show a significantly reduced fiber length and separation through the REM treatment (see Figure 3.6).
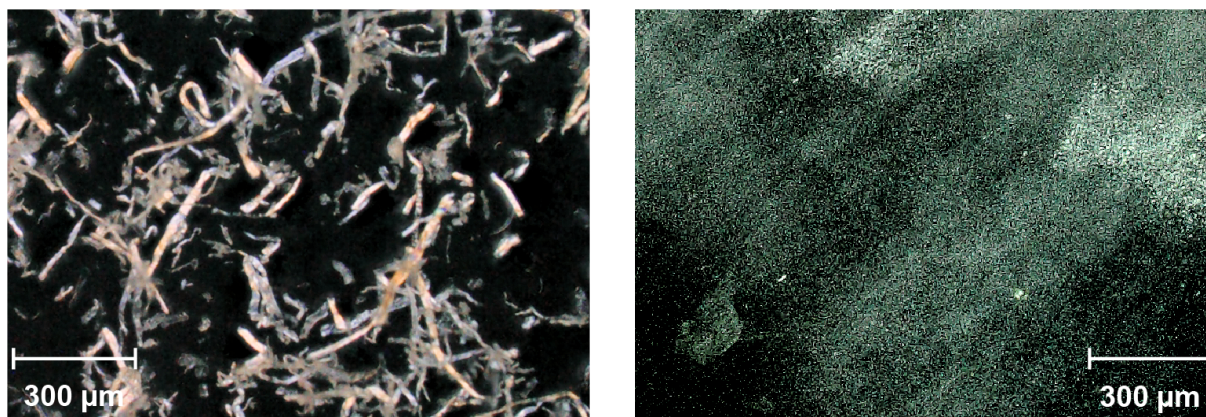

Figure 3.6: SFC starting material (left) and treated cellulose (right) observed with cross-polarized optical microscopy.

Verification of the presence of amino groups

Elemental analysis of the solid samples shows a significant increase of nitrogen content in the REM-treated samples compared to the starting material (0.06 % N). For most samples, the nitrogen content is around 0.4 %. For the sample treated with REM3, the nitrogen content is particularly high at 0.7 %. The specific values are given in Table 3.2. A ninhydrin probe, which is commonly used to verify the presence of amino groups, was performed on one of the samples (see Figure 3.7 A). The blue coloration confirms that the measured nitrogen is present in the form of amino groups introduced during the treatment.

Zeta potential (ZP) measurements (see Figure 3.7 B) reveal a positive surface charge on the particles NC1-5 in the range of +23 mV to +35 mV, while NC6 has acquired a low negative surface charge of around -12 mV. The positive charge implies the successful functionalization with amino groups.The highest charge is observed in the products extracted by REM1 and REM2, which reflects their colloidal stability observable by eye. The high N content of NC3 is not, as could be expected, reflected in a higher charge: Instead, NC3 has one of the lowest charges.

Although NC6 contains a nitrogen amount similar to the other samples, implying the presence of amino groups, the particles bear a negative charge. REM6, containing succinic acid, seems to induce another reaction. A possible explanation for this might be partial esterification of the cellulose's hydroxyl groups with the dicarboxylic acid, resulting in a carboxylate group on the surface. This might also explain the lower charge of NC5, since
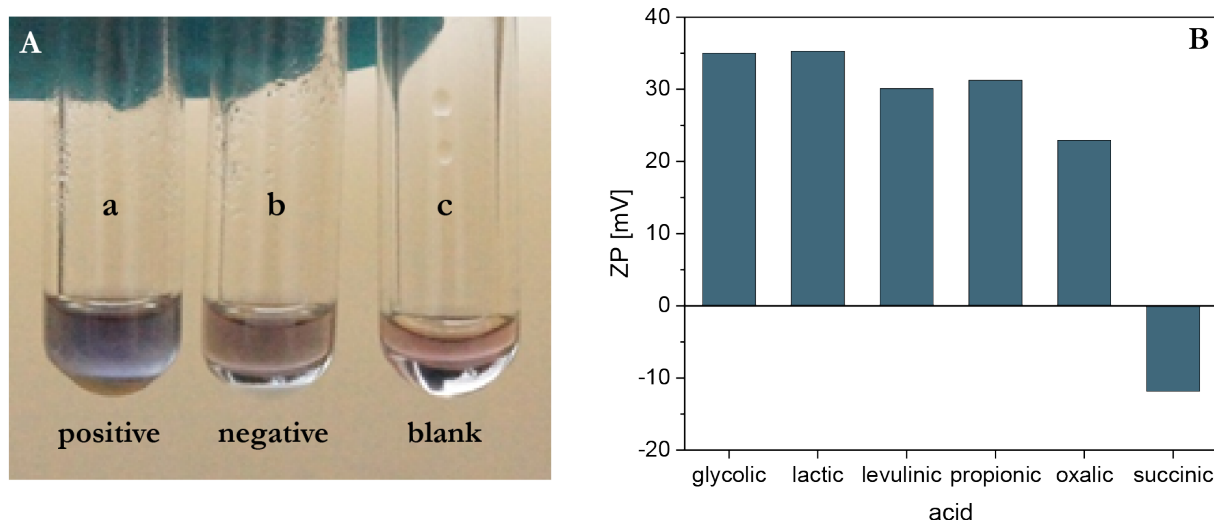
Figure 3.7: (A) Ninhydrin probe of (a) SFC sample treated in the REM1 at 140 °C for 4h, (b) untreated SFC and (c) blank probe without sample; (B) Zeta potential of the colloidal cellulose particles obtained through the extraction with REM1-REM6.

oxalic acid is also a dicarboxylic acid and might neutralize some of the positive charge of the amino groups by its binding to the cellulose surface.

Attenuated total reflection infrared (ATR-IR) spectra of the extracted material (Figure 3.8) show no substantial differences from the untreated cellulose. This proves that the natural cellulose structure is preserved and not severely modified. The generally agreed-upon assignment of all the vibration bands of pristine cellulose is as follows: 3334 cm^{-1} O-H stretch; 2900 cm^{-1} C-H stretching; 1645 cm^{-1} O-H from adsorbed water/conjugated C=O; 1430 cm^{-1} C-H deformation (asymmetric); 1370 cm^{-1} C-H deformation (symmetric); 1336 cm^{-1} O-H in-plane deformation; 1316 cm^{-1} CH2-wagging; 1203 cm^{-1} O-H deformation; 1160 cm^{-1} C-O-C asymmetric vibration; 1105 cm^{-1} glucose ring stretch (asymmetric); 1056-1031 cm^{-1} C-O stretch; 896 cm^{-1} glucose ring stretch.[136] Unfortunately, bands associated with the amino group around 3380 cm^{-1} and 3300 cm^{-1} overlap with those of the abundant hydroxy groups and cannot be observed. Nevertheless, the spectral range between 1580 cm^{-1} and 1750 cm^{-1} contains evidence for minor modifications: A weak band appears at 1588 cm^{-1}, which can be assigned to N-H bending in primary amines. Note that this band overlaps with the broad absorption band at 1640 cm^{-1} attributed to adsorbed O-H in pristine cellulose and is therefore difficult to detect. NC3 shows the most obvious absorption band at this wavenumber compared to the other samples. This is in accordance with the highest relative nitrogen content (0.72 %) in this sample. An additional band around 1700 cm^{-1} (C=O stretching), predominantly observed in NC6, implies the presence of carbonyl in carboxylic acid groups, supporting the hypothesis of the esterification of cellulose in REM6. Other primary amine-related bands would be expected around 3300 cm^{-1} (N-H stretch), 1060 cm^{-1} (C-N stretch), and

900-770 cm^{-1} (N-H wag),[137][138] but overlap with the cellulose bands and are impossible to see considering the low degree of substitution.
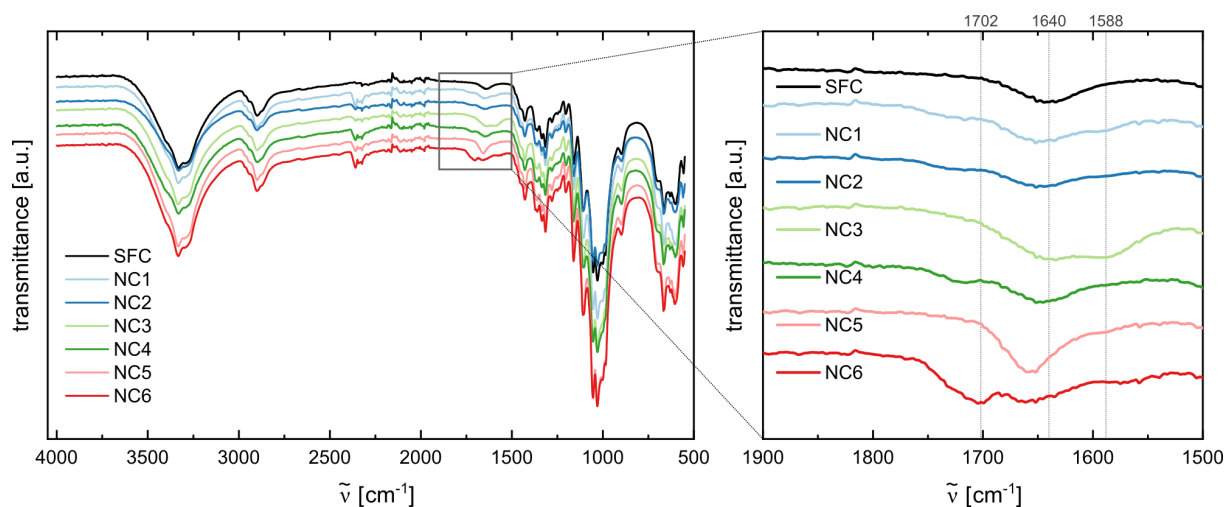

Figure 3.8: ATR-IR spectra of untreated starting material and cellulose products from the treatment of SFC with REM of ammonium formate and the respective acid in a ratio of 2:1. Adapted from[132].

Further evidence for the amino-functionalization was sought using solid-state NMR, or CP-MAS NMR. ^{13}C {^{1}H } CP-MAS NMR (Figure 8.2 in the Appendix) was performed on the starting material pulp and one exemplary REM-treated sample. Both samples produce the following signals in agreement with the literature[37][139]: δ 105 ppm: C1, 88 ppm: C4 (crystalline), 83: C4' (amorphous), 74-71 ppm: C2, C3 and C5, which are indistinguishable, 64 ppm: hydroxymethyl C6 (crystalline), 62 ppm C6' (amorphous). However, at the obtained resolution, additional signals in the treated sample attributable to N-bound carbons in ^{13}C CP-MAS NMR can not be distinguished. Taking chitosan data as a reference, C-N carbon should give a signal around 57 ppm[140][141] which overlaps with the tail of the rather broad C6' signal. A clear signal that proves the amino group cannot be expected, considering the low degree of substitution. The empty low-field and high-field regions in the ^{13}C spectrum confirm that no additional carbon-containing functional groups (carbonyl, aromatic, or aliphatic[142]) were introduced in significant amounts, for example through esterification: Carbonyl-carbons from carboxylic acids, for instance, would show up around 175 ppm, amide carbon at 170 ppm, as reported by Akhlagi et al.[139] and Azzam et al.[143]

X-ray photoelectron spectroscopy (XPS, Figure 3.9) of the REM-treated material detects nitrogen with a binding energy of 399.6 eV with a small intensity, reflecting the low degree of substitution. This signal could be attributed to amine or amide N 1s (compare chitosan[144]) and supports the supposed presence of nitrogen in the form of amino groups. However, the low signal-to-noise ratio impedes a reliable deconvolution of possibly underlying overlapping peaks that could indicate other functional groups, so that definite conclusions on the nature of the nitrogen bond are not possible.
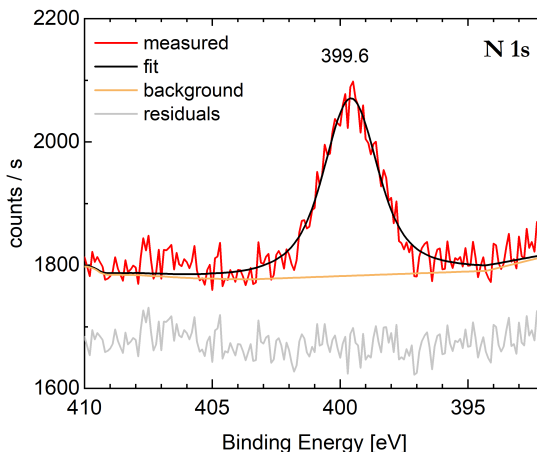
Figure 3.9: High-resolution XPS of the REM-treated CNC sample proves the presence of covalently bound nitrogen.

Verification of crystallinity and nanoscale

Due to undesirable side reactions, insufficient or opposite surface charge, and the lasting brown color of the products, REM5 and REM6 were excluded as candidates for an extraction medium of cationic CNCs and further studies were only conducted on REM1-4. To verify if amorphous domains on the cellulose fiber were cleaved and dissolved, X-ray powder diffraction (XRD) of the purified solid products NC1-4 was performed. In NC1-3, the crystallinity index (CrI) (see Table 3.2) increased by 4 % – 7 % compared to the starting material SFC, proving the dissolution of the more susceptible amorphous cellulose sections in all of the tested REMs, while crystalline regions remain intact. The highest crystallinity of approximately 85 % is achieved in the treatment with REM2. REM1 and REM3 achieve similarly high values of 84 % and 83 % respectively. In NC4, CrI is even 2.5 % lower than the untreated material, which makes REM4 unfavorable. The decreased CrI might indicate that the medium REM4 is partially dissolving crystalline regions, possibly due to its lower viscosity and density compared to the other media. Although

Table 3.2: Nitrogen (N) content and crystallinity index CrI of extraction products obtained with REM1-6.

treatment	acid	N content [%]	CrI
-		0.06 %	78.6
REM1	glycolic acid	0.37±0.04	83.8
REM2	lactic acid	0.36±0.00	85.2
REM3	levulinic acid	0.72±0.04	82.6
REM4	propionic acid	0.46±0.28	76.1
REM5	oxalic acid	0.37±0.03	-
REM6	succinic acid	0.43±0.01	-

REM4 has the lowest viscosity and yields particles with a high charge, its application is also riskier than the other REM due to the flammability of propionic acid. That, along with its unpleasant smell and irritation of the respiratory system, makes REM4 a non-preferred medium for larger-scale application.

Exemplary electron microscopy imaging (Figure 3.10) of NC1 confirms the presence of whisker-shaped cellulose particles about 100 – 300 nm in length and ca. 10 nm in width. This is in the common range for CNCs obtained from wood pulp.[34]
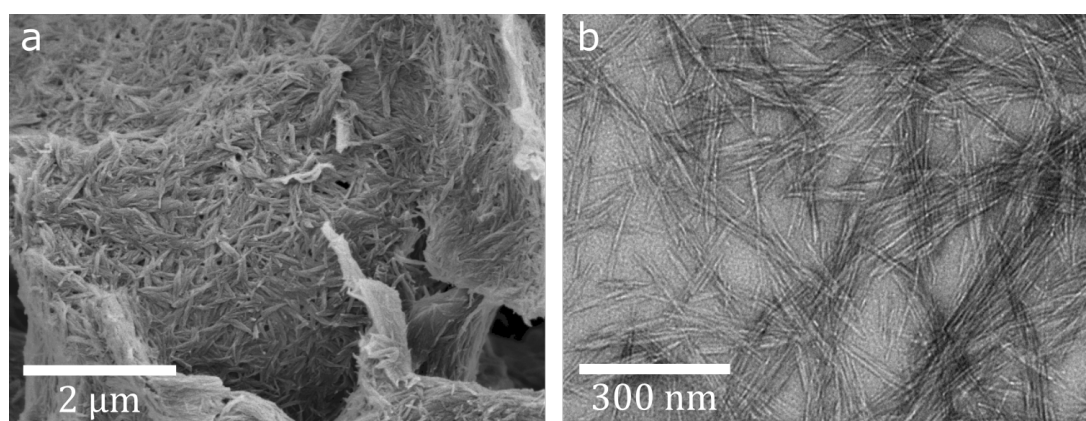

Figure 3.10: (a) SEM and (b) TEM image of CNC extracted from SFC with REM1.

3.1.2 Optimization and further investigation of the extraction using REM1

For further investigation and optimization of the extraction and influences of reaction conditions on the product characteristics, one REM was chosen to be studied more closely. REM1-3 led to similar products, so that a variation of type of acid between glycolic, lactic, and levulinic acid does not seem to have a big influence on the mechanism of the extraction. Besides the fact that the yellow discoloration in REM3 implies by-products even before the extraction, which might lead to more impurities in the extract, REM1 and REM2 also resulted in CNC with a higher surface charge than REM3. Between REM1 and REM2, REM1 was chosen as a model system in this first optimization attempt due to the presence of 10 % of water in the used lactic acid, which adds another variable to be investigated to the system. It should be noted here, however, that lactic acid (47 €/kg) is the economically preferable HBD compared to glycolic acid (350 €/kg[2]) and will be used more later on.

---

[2]Prices retrieved on 10/10/2022 from sigmaaldrich.com for similar grades and packaging size of 1 kg; large-scale costs will deviate.

3.1.2.1 Thermal behavior of REM1 revealed through TGA-MS

To reveal thermal decomposition processes in the REM and species that may be active at the elevated temperatures of 180 °C, thermogravimetric analysis (TGA)-mass spectrometry (MS) was performed on REM1. Through coupling of MS to the TGA, volatile species that are produced upon heating are revealed.

Glycolic acid analyzed individually shows one single sharp mass loss peak at 118.9 °C, corresponding to its complete decomposition to volatile products. The temperature is higher than the literature value for the degradation temperature of 100 °C[145], which might be due to a fast heating rate. Ammonium formate exhibits a main mass loss peak at 135.9 °C, which is its decomposition to volatile ammonia and formic acid. Those decomposition products can further react to formamide and water.[146] Formamide decomposes at 185 °C,[147] generating the higher temperature peak in mass loss.

The weight loss onset temperature T_o in REM1 at 82 °C is at a significantly lower temperature than for the single components glycolic acid (T_o 102 °C) and ammonium formate (T_o 109 °C). The shallow mass loss curve, starting to decrease already from 50 °C, could be evaporation of water, present due to the hygroscopic nature of the DES. Loss of water starting from 45 °C is confirmed in the constantly high water signals in the MS (Figure 3.11), detected in the fragments m/z : 18, 17, 16. The early onset implies the presence of residual water instead of its being a degradation product. The first mass loss peak in the REM at 103.7 °C corresponding to the decomposition of glycolic acid is lower than that of the pure component and more in agreement with literature. Instead of indicating a lower thermal stability of the REM, the lower T_{max} can also be explained by a better heat transfer in the liquid REM than in the solid acid. The second peak at 139.9 °C is in good agreement with the decomposition peak of ammonium formate. As pure ammonium formate is molten at that temperature, the heat transfer should be similar to the
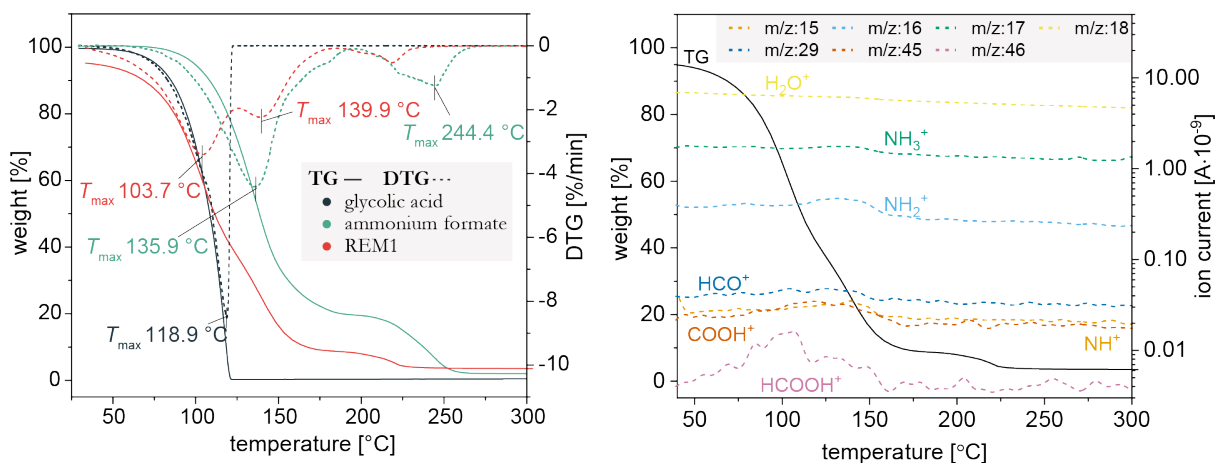

Figure 3.11: Left: TGA of REM1 composed of ammonium formate and glycolic acid in 2:1 molar ratio and of the individual components. Right: TGA-MS of REM1.

liquid DES, which explains the better agreement of mass loss peaks compared to glycolic acid. Ammonium formate is in Lewis acid-base dissociative equilibrium with ammonia and formic acid in the liquid DES. The presence of the additional acid would shift the equilibrium towards formic acid and ammonium. Formic acid is detected as in $m/z=46$ and its fragments ($m/z=45$: HCOO, $m/z=29$: HCO) around its boiling temperature of 100 °C. Thermal dissociation of ammonium formate is also detected in the MS by increased production of ammonia between 120 °C and 150 °C, represented in the fragments m/z: 17,16,15 (NH_3, NH_2, NH). This *in situ*-generated ammonia provides the reactivity of the REM towards the reductive amination reaction or Leuckart reaction.[148] A small peak at higher temperatures is also present in the REM, indicating formamide as an intermediate reaction product. The fragment with $m/z=45$ that corresponds to the molecule ion of formamide, however, is not detected at increased intensity at its boiling point (210 °C), so that a high concentration of formamide is difficult to confirm.

It should be noted that the conditions during the TGA measurement are not identical to the reaction conditions, as the extraction takes place in a pressure-sealed autoclave, which prevents the evaporation and escape of REM components or gaseous decomposition products. The thermodynamic equilibrium in the autoclave will shift to the liquid species upon the pressure build-up so that the REM is not completely dissociated or degraded even at the initially chosen temperature of 180 °C. Nevertheless, a reduction of the extraction temperature might reduce the formation of by-products and lowers the energy demands of the procedure.

3.1.2.2 Variation of reaction conditions and their influence on CNC product characteristics

TGA-MS of REM1 showed that the formation of ammonia, the active species in reductive amination and aminolysis, peaks in the temperature range of 120 °C to 150 °C. A reduction of reaction temperature from 180 °C used in the preliminary screening experiments down to this range seems therefore feasible. In an attempt to optimize extraction conditions, the temperature is therefore varied between 140 °C, 160 °C, and 180 °C with the reaction time varying between 1 h, 2 h, 4 h and 6 h. Moreover, a stirred reactor with a higher volume compared to the static autoclaves is introduced to promote homogeneous extraction conditions throughout the whole reaction volume. Next to short-fiber cellulose (SFC) similar to the one used previously, the REM-treatment is tested on bleached softwood pulp. This cellulose source contains longer fibers with a higher molecular weight (M_w(pulp))=900 kDa compared to SFC (M_w(SFC)=520 kDa). The swelling of those long fibers leads to a more viscous mixture with the REM than observed for SFC. Consequentially, a lower loading of 5 wt.% pulp in REM (instead of 25 wt.% SFC) has to be applied to obtain a mixture that can still be stirred. The products extracted in this series of

experiments are characterized and their properties such as nitrogen content, crystallinity index, degree of polymerization, and Zeta potential are compared to probe the limits of suitable reaction conditions. Due to exceedingly high work and material efforts, this is not a comprehensive optimization, but rather a rough screening of reaction conditions to identify general trends.

The extraction of SFC in the stirred reactor produces a brown, viscous liquid at every tested condition, from 1 h reaction time at 140 °C to 4 h at 180 °C. Under milder conditions, i.e. lower temperature or shorter reaction time, the amount of brown by-products is reduced, as indicated by the much lighter-colored reaction mixture. The same trend is observed for pulp. Here, however, a short reaction time of 1 h at 140 °C is not sufficient to yield CNCs: After 1 h, the mixture only has a pale brown hue and contains a lot of seemingly intact and unreacted fibers. A prolongation of reaction time to 4 h yields a more disintegrated product. This indicates that a temperature of 140 °C provides the required activation energy for the cleavage of the amorphous cellulose domains. While 1 h reaction time is enough to isolate CNCs from the small SFC particles, the cleavage of the pulp fibers into CNCs takes longer. This is due to hornification of cellulose fibers known to occur in dried pulp, which decreases its swelling capacity.[149]

Figure 3.12 shows the FTIR spectra for CNCs from SFC (left) and pulp (right) extracted at high- and low-temperature conditions. Interestingly, the extraction at the lowest temperature of 140 °C gives rise to a new band at 1716 cm^{-1} after a reaction time of 1 h. This range is indicative of carbonyl groups. The intensity of this band decreases at prolonged reaction times of 4 h. At 180 °C, it disappears almost completely and instead, the band attributed to $-NH_2$ at 1555 cm^{-1} becomes more pronounced. This evidence might point to an intermediate carbonyl functionality in a first phase of the extraction, which then undergoes reductive amination with proceeding reaction time.
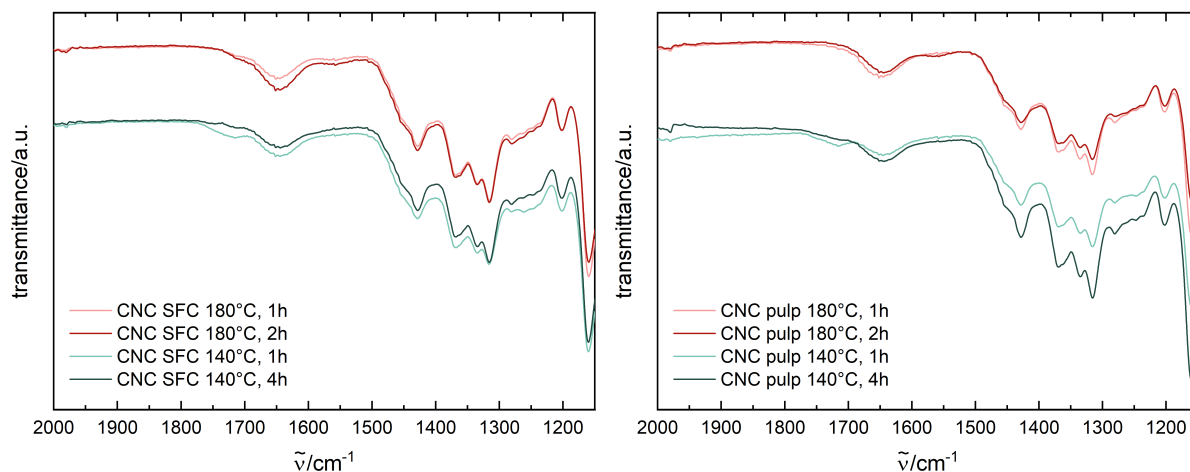

Figure 3.12: ATR-IR spectra of cellulose products from the treatment of SFC with REM of ammonium formate and glycolic acid in a ratio of 2:1 in different conditions.

The measured nitrogen (N) content, CrI, and ZP for all tested reaction conditions are summarized in Figure 3.13 and numeric values are given in Table 8.4. Although the data set is limited, some general trends emerge from the diagrams. Compared to the cellulose source, every tested reaction condition yields a product with increased N content in the range of 0.19 % to 0.43 % and increased CrI between 73 % and 85 %. Apart from the pulp extracted at 140 °C for 1 h, which did not yield measurable CNCs, every product mixture contains positively charged CNCs with ZP between 21 mV and 37 mV. The N content generally increases with time and reaction temperature in both SFC and pulp, demonstrating a proceeding functionalization reaction. Due to the higher crystallinity of the starting material pulp (CrI=75 %) compared to SFC (CrI=67 %), CNCs from pulp generally exhibit higher CrI values. CrI peaks for the products extracted at 160 °C from both SFC and pulp and declines at higher temperatures. Lower values for CrI at 180 °C could indicate the onset of the undesirable degradation through depolymerization of crystalline domains through aminolysis. CrI as well as ZP values generally vary strongly between extractions conducted at 180 °C for different times, showing no clear dependence on the reaction time. This low reproducibility supports the hypothesis of uncontrolled cleavage of the crystalline phase, which would generate a higher amount of by-products. The increased formation of by-products at higher temperatures is indicated by a darker brown color of the mixtures after the reaction.
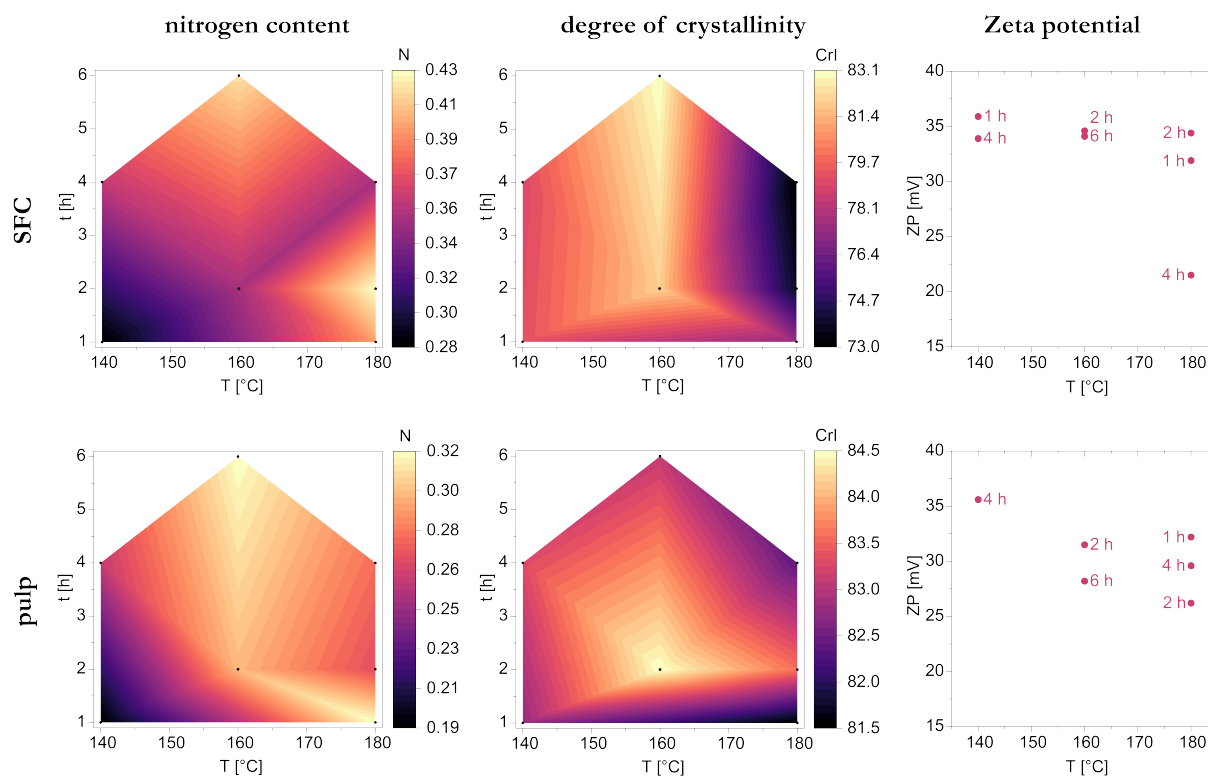

Figure 3.13: Nitrogen contents and CrI for CNC samples from SFC and pulp for different sets of reaction time and temperature. Black dots are the result of real experiments, the color map in between is interpolated to visualize possible trends.

Degree of polymerization at different reaction conditions

To further compare the effectiveness of the treatment, the degree of polymerization (D_P) of the cellulose in selected samples of the extracted material was determined using two methods: a standardized viscosimetric method and gel permeation chromatography (GPC). Using the viscosimetric method, the limiting viscosity of a solution of the cellulose sample in cupriethylene diamine is determined, according to the ISO 5351 standard. For GPC, the samples were first derivatized following the carbanilation method proposed by Evans et al.,[150] as cellulose is not soluble in common solvents, and then analyzed against a pullulan standard (see Chapter 8.3.4). Both methods are relative and rely on standards different from the specific samples regarded here, so that the values are not considered absolute, but rather comparative values between the cellulose sources and the extracted material. The values determined with both methods for selected samples, one lower and one higher temperature sample of SFC and pulp each, are given in Table 3.3.

Table 3.3: DP determined with the viscosimetric cuen method (DP_v) and with GPC (number average DP_n and weight average DP_w.) Note that DP_n and DP_w are given in pullulan equivalents.

sample	DP_v	DP_n	DP_w
SFC	2308	141	1003
SFC, 140 °C, 4 h	309	49	214
SFC, 160 °C, 2 h	325	46	215
pulp	-	160	1735
pulp, 140 °C, 4 h	318	72	1421
pulp, 180 °C, 4 h	327	29	1352

The viscometrically determined DP_v of the anhydroglucose chains decreases significantly from 2308 in the pristine SFC to around 300-330 in the extracted particles. CNCs extracted from pulp yield DP values in the same range, confirming the successful cleavage of cellulose chains. Since DP_v remains constant among the analyzed samples, this value appears to be the LODP. SFC and pulp both come from the same cellulose source, bleached softwood pulp, so that similar values for the LODP are expected. Considering the length of one anhydroglucose unit of 0.518 nm,[151] this DP corresponds to a chain length of 155 – 170 nm. This is in the expected range for crystalline domains in bleached wood pulp (140 – 200 nm[152]) and in good agreement with the particle length observed in TEM.

GPC of the carbanilated and dissolved CNCs gives insight into the molecular weight (M) distribution of the cellulose chains composing the extracted material. The distribution curves for the chosen samples are shown in Figure 3.14. The range corresponding to polymer chains with lengths in the expected nano range from 100 nm to 1000 nm is highlighted in the diagram. This length is equivalent to an approximate DP range of 190-1900. The DP was converted from the M in pullulan equivalents.
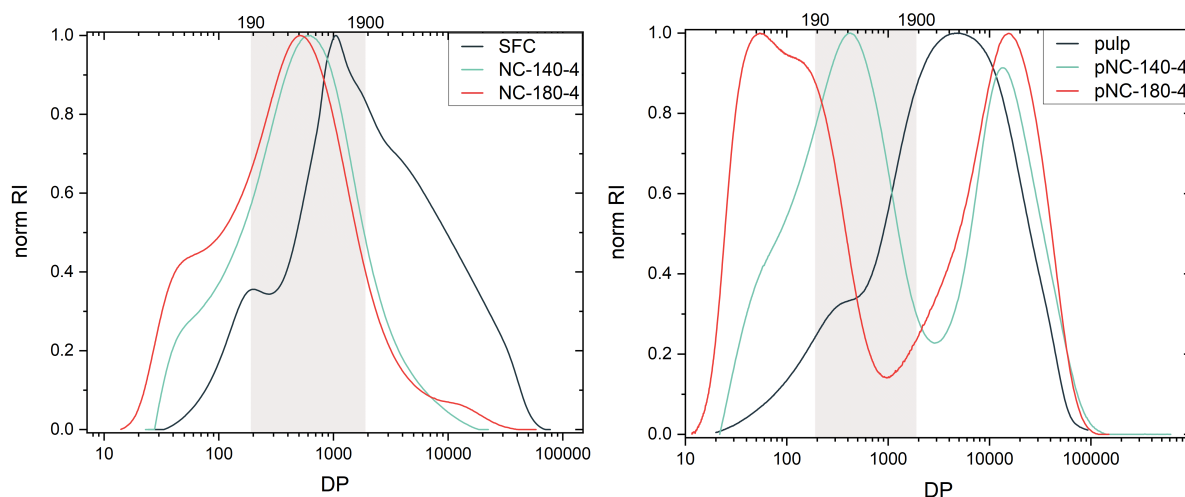
Figure 3.14: GPC analysis data for the CNC samples prepared under different conditions: the first number represents reaction temperature in °C; the second number represents the reaction time in h. The gray area highlights chains in the length range between 100-1000 nm, representing nanocellulose. The CNCs obtained from pulp exhibit a bimodal molar mass distribution, which arises from the presence of larger fibers in this starting material, compared to the short-fiber cellulose.

For products extracted from SFC, the GPC gives a monomodal distribution with the biggest fraction in the M range of 10 kDa to 1000 kDa, or DP of 100-3000, which is roughly in the calculated nano range. A small shoulder in the range of 1 kDa to 10 kDa corresponds to a DP of 10-60 and indicates the presence of oligosaccharides, or cellodextrins, possibly originating from the cleaved amorphous regions. Those oligosaccharides are presumably adsorbed at the CNC surface as they were not washed out during the extraction workup. The large number of oligosaccharides leads to a very small number average DP_n of 49 for the 140 °C/4 h sample and 46 for the 160 °C/2 h sample, which might not be representative of the CNC-composing chains. From both the number averages and the weight averages DP_w of 214 and 215 respectively, no significant differences between the samples are observed, which demonstrates that most chains are already cleaved after 4 h at 140 °C and the reaction does not proceed significantly at higher temperature for a longer time when extracting SFC.

Pulp extraction products exhibit a bimodal M distribution with the main peak in the nano range, but a considerable fraction of long chains in the M range of 1000 kDa-10 000 kDa, (DP around 3000-100 000). This confirms the presence of larger, uncleaved fibers among the CNCs due to the nature of the starting material: Fiber aggregates are not homogeneously distributed in the extraction medium and tend to remain clumped together due to their hornification. Complete cleavage might be achievable with longer reaction times or more efficient mixing, which would make every fiber more available from the beginning of the reaction time. Pre-fluffing with a blender could also help loosening up the fibers, increasing the surface and maximizing contact with the REM. The comparison

between the 140 °C-4 h and the 180 °C-4 h sample shows a shift toward lower DP for the sample reacted at higher temperature for a longer time especially in DP_n, which is also obvious in the distribution curve. In contrast to SFC, pulp is not fully cleaved after 4 h at 140 °C and instead requires a longer time or higher reaction temperature to yield smaller particles.

The screening of extraction conditions shows that the REM is active at a lower temperature of 140 °C, although the complete cleavage of pulp requires longer reaction times than tested here. The bimodal M distribution suggests the presence of unreacted material, which might be overcome with a reactor design more suitable for the highly viscous and inhomogeneous mix, such as an extrusion reactor. Cationic CNCs from SFC, on the other hand, can be extracted at very mild conditions of 140 °C and a reaction time of only 1 h with high CrI and the highest measured ZP.

3.1.2.3 Upscaling of REM treatment

The extraction process was upscaled to a stirred 1 L reactor in the course of this work to obtain more material to investigate possible applications of it. Without performing systematic studies, the process was found to work well at 160 °C for SFC, while 140 °C even at a prolonged time of 4 h did not yield CNCs. Using REM1 in this reactor, excessive foaming was observed which, at this scale, is less manageable than on the smaller scale. To limit the formation of gaseous degradation products, the medium was changed to REM2, which contains lactic acid instead of glycolic acid. While glycolic acid starts to decompose at 100 °C, contributing to high pressure and foaming, lactic acid does not decompose and only boils at low pressure (20 hPa) at 122 °C. Using REM2 as a reaction medium, the operating pressure decreases drastically from 85 bar to a maximum of 20 bar. Moreover, foaming is significantly reduced as the decomposition of the acid into gaseous compounds does not occur.

3.1.3 Variation of cellulose source

The efficiency of the REM treatment was tested also on other cellulose sources, namely cotton, cellulose from tunicate, microcrystalline cellulose (MCC), and pre-fibrillated pulp (fC), and compared to the previously used SFC. Cotton is a very pure form of cellulose, as it contains no lignin residues and only little hemicellulose (5-7 %[153]). Tunicate cellulose, the only cellulose produced by animals, contains no lignin or hemicelluloses due to its non-plant origin and is rather embedded in a matrix of other polysaccharides and proteins[154]. MCC is produced through acidic hydrolysis depolymerization of bleached wood pulp[155] and consists of considerably shorter particles than SFC. The pre-fibrillated pulp is a mechanically milled pulp consisting of fibrils with cross sections in the nm range. SEM images of all sources are shown in Figure 3.15.
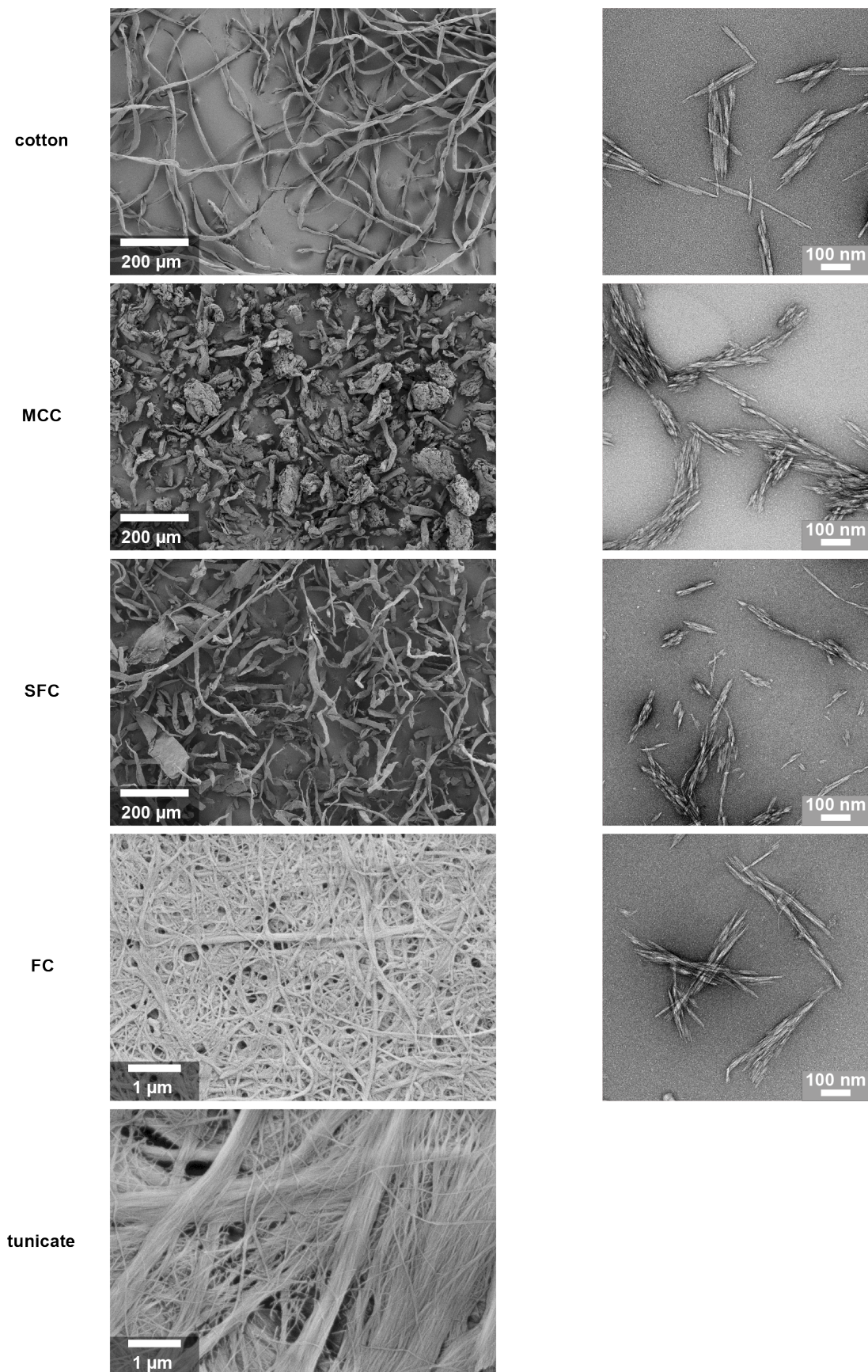
Figure 3.15: SEM images (left) of cellulose sources used in this chapter and TEM images (right) of the extracted CNCs.

The extractions were performed in a stirred 1 L reactor with a low solid loading due to limited amounts of material. MCC, cotton, and fC yield the same viscous and dark brown liquid mixtures as observed for SFC and pulp. Tunicate cellulose remains largely unchanged in appearance and consistency. After the reaction, the medium remains transparent without exhibiting the usual brown color, only a slight green-gray hue, indicating that no aminolysis took place. The products were purified as usual and analyzed via EA, Zetasizer, GPC, static light scattering (SLS), TEM, and XRD.

CNCs from cotton, MCC, and fC exhibit a nitrogen content significantly increased to 0.26-0.29 % compared to the source material and consequentially, they bear a positive surface charge in the range of 32-36 mV. Those values are comparable to CNCs from SFC. REM-treated tunicate only has an insignificantly increased nitrogen content, proving that aminolysis did not, or only to a small extent, take place. No CNCs with measurable surface charge could be isolated.
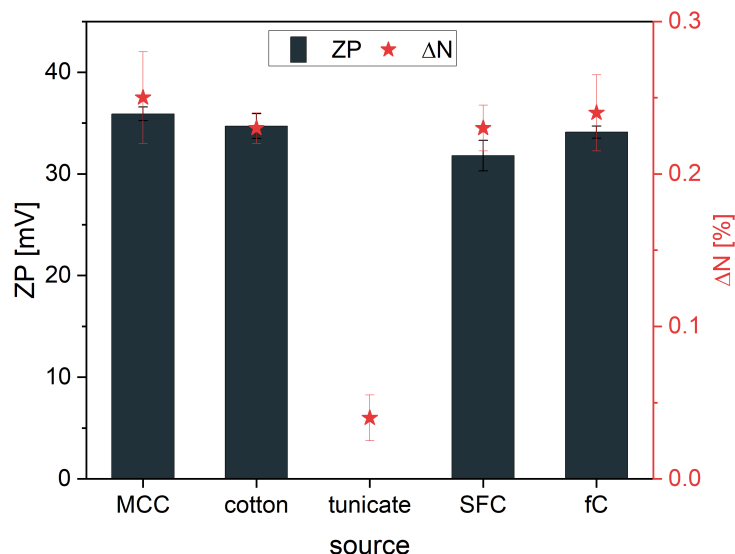

Figure 3.16: Zeta potential (ZP) and change of nitrogen content ΔN of CNCs extracted from the different sources MCC, cotton, tunicate cellulose, SFC and fC.

CNCs from MCC exhibit a CrI that is only insignificantly higher (82.6 %) than the untreated material (81.7 %). Cotton starts from an even higher crystallinity of 87.1 %, but the increase to 90.8 % is much stronger than in MCC. The cellulose source with the highest crystallinity before the treatment is tunicate cellulose with $CrI = 96.7$ %, indicating that it contains very small amounts of amorphous domains to be cleaved. In fact, the crystallinity is even decreased to 94.3 % after the treatment, hinting at the slight dissolution of crystalline regions. The strongest increases in CrI are measured for SFC and fC, the materials with the lowest CrI and therefore the highest amount of available amorphous domains. In both samples, the crystallinity increases by about 11 %. CNCs extracted from fC even exceed the level of crystallinity measured for MCC. Since MCC, SFC, and fC all originate from bleached kraft pulp, they should ultimately contain similar
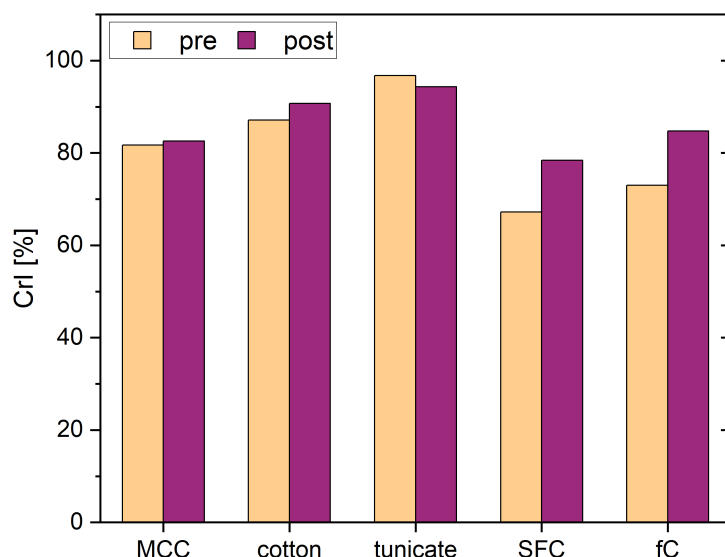
Figure 3.17: CrI values of sources and extracted cellulose determined via XRD measurements.

crystallites. Cotton and tunicate are different sources of cellulose and contain crystalline domains of different dimensions. The CrI reached in cotton CNCs may therefore not even be reachable by using pulp sources, as smaller crystalline regions entail a higher ratio of crystallite ends which always are a site of disorder.

GPC analysis of the derivatized samples before and after treatment proves a decrease of molecular weight in every sample, as shown in the obtained DP distributions in Figure 3.18. To illustrate the effect of the treatment on different fractions of the cellulose samples, Figure 3.19 shows M_n, M_w, and M_z before and after treatment as well as the ratio of the post-treatment to the pre-treatment molecular weight for the different averages. Due to the differently weighted averages, changes in M_n indicate changes in the low M fraction, while M_z reveals changes in the high M region. M_w considers the largest part of the sample. The ratio M_{post}/M_{pre} can be considered a measure of treatment efficiency: the lower this value, the higher the efficiency.

In the tunicate samples, derivatization and dissolution was not complete, as the solution still contained particles visible to the eye after the derivatization protocol. Those undissolved fibers were removed by filtration before GPC analysis. Since they probably contain the higher M chains or chains that were in more crystalline regions, which take longer to dissolve, the resulting GPC is not representative of the entire sample. Nevertheless, GPC shows a shift toward smaller M for the analyzed fraction. Compared to the other samples, treatment efficiency is very low, especially in the small M fraction. For tunicate cellulose, a DP of 700-3500 has been reported,[156] and the length of CNCs from tunicate is reported to be 500 nm to 1000 nm. This corresponds to a LODP of around 1000. Most of the cellulose is therefore already in small chains composing the crystallite and barely contains amorphous domains that can be cleaved, as was shown in the XRD analysis.
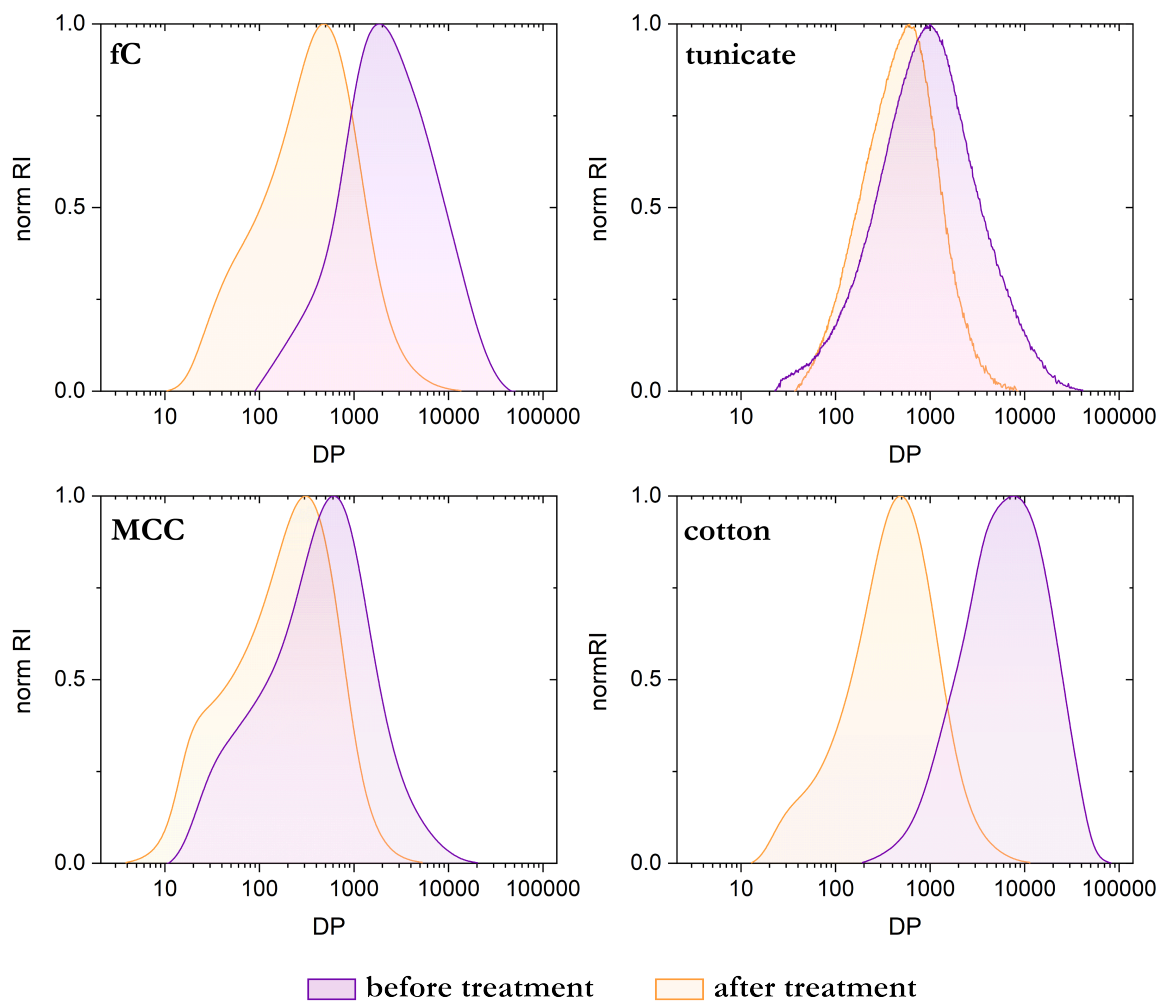
Figure 3.18: DP distribution in pullulan equivalents of the untreated and REM-treated materials fC, MCC, cotton and tunicate cellulose. Note that untreated as well as treated tunicate cellulose did not dissolve completely during the derivatization, so that possibly larger undissolved fiber were filtered out before GPC measurement and are not represented in the GPC.
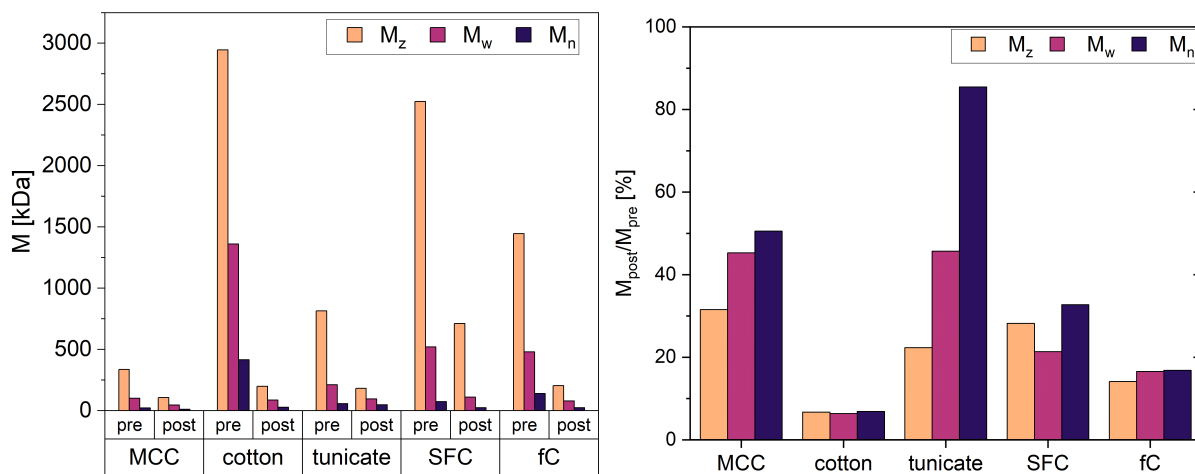

Figure 3.19: Molecular weight averages of cellulose samples pre and post treatment (left) and the ratio of molecular weight average after to before the treatment (right).

Low treatment efficiency is therefore to be expected. Cleaving occurs mostly in the higher M range. Similar behavior is observed in the MCC sample. MCC also starts at a very low DP due to the fact that they are obtained through acid hydrolysis of pulp, which means that they are already pre-cleaved. The cleaving efficiency of the REM treatment is therefore low. Nevertheless, CNCs from MCC have one of the highest nitrogen contents, which indicates that the hydrolyzed ends, equivalent to reducing ends, are aminated as well. The molecular weight averages in SFC and fC samples are more drastically reduced than in tunicate and MCC and show efficient cleavage in every fraction enabled by the relatively low CrI. For cotton, the treatment seems the most efficient: all M averages are reduced to around 7 % of the starting value.

The number density size distribution of the obtained CNC samples is shown in Figure 3.20. Although TEM shows distinct particles on the nanoscale for all cellulose sources except tunicate, SLS only does so for CNCs obtained from fC. Particles from other sources appear to be in the range of 1 µm to 10 µm. The larger apparent sizes indicate the formation of agglomerates of the colloidal particles, which is also observable by eye upon the dilution of the CNC suspensions concerned. The difference in agglomeration behavior and with that in the particle sizes obtained via SLS cannot be explained by a lower electrostatic stabilization, as CNCs from MCC and cotton exhibited slightly higher surface potentials than CNCs from fC (compare Figure 3.16). This phenomenon is the subject of future studies.
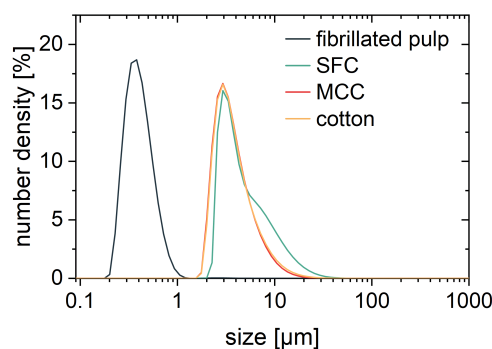

Figure 3.20: Sizes distributions of CNCs obtained from different sources, measured via SLS.

3.1.4   Discussion and verification of the extraction mechanism

The presumption of this work was that the REM treatment of cellulose has a twofold effect: 1) Reductive amination of carbonyl groups in the reducing ends through the Leuckart reagent ammonium formate (Scheme 3.1) and 2) acid-catalyzed aminolysis cleaves the amorphous domains while leaving the crystalline domains intact (Scheme 3.2). The resulting aldosylamine unit (**2**) is unstable and likely undergoes Amadori rearrangement to the aminodeoxyketose unit (**3**, Scheme 3.3).[157]
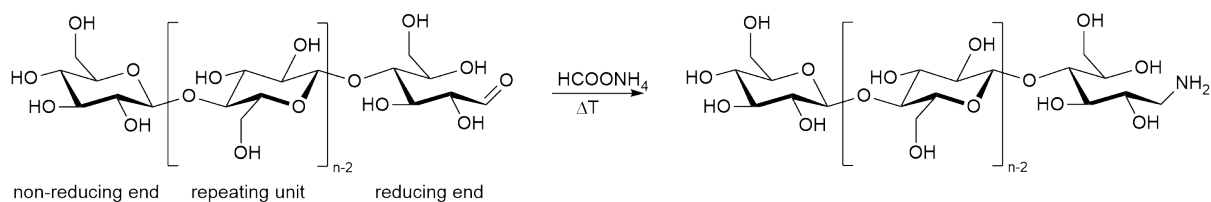
Scheme 3.1: Reductive amination (Leuckart-Wallach reaction) of the reducing end of a cellulose polymer chain with ammonium formate at elevated temperatures.
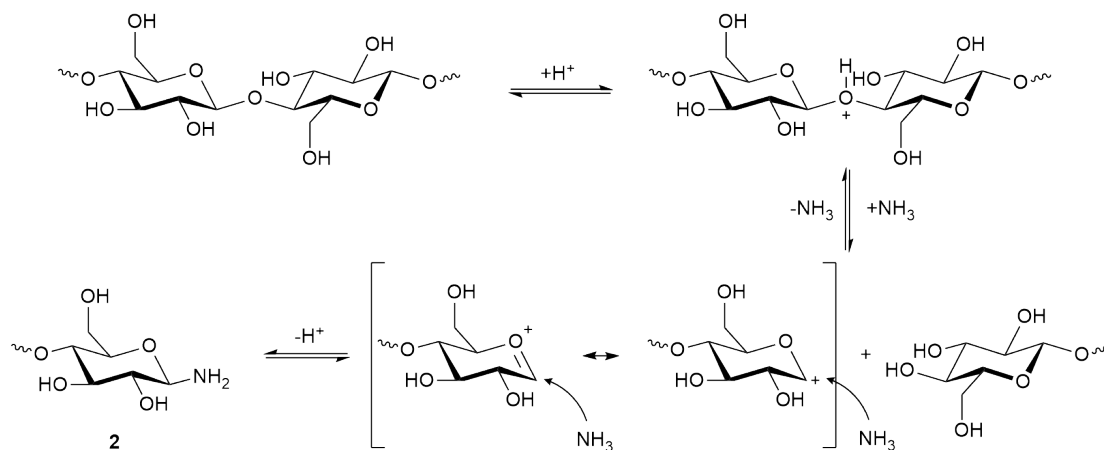
Scheme 3.2: Mechanism of aminolysis in the amorphous regions of the cellulose chain.
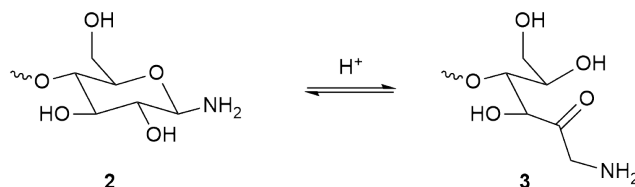
Scheme 3.3: Amadori rearrangement of the unstable aldosylamine unit **2** to an aminodeoxyketose unit **3**.

Both reductive amination and aminolysis would yield aminated, cationic cellulose nanocrystals. Proof for the presence of amino groups was presented in Chapter 3.1.1.2, but those groups have not been located yet to prove the mechanism of extraction. Both mechanisms 1) and 2) would introduce amino groups at the end of the CNC: Reducing aldehyde ends cause disordered sites and are unlikely to be present in the crystalline regions, and aminolysis occurs in the amorphous regions, placing the amino group at the end of the crystallized chains as well. Knowing the DP, the degree of substitution of the cellulose chains with amino groups can be compared to the number of end groups. Considering the DP_v of approximately 300 (since this DP is in best agreement with TEM observations), the reducing end group should make up 0.33 % of the polymer chain. According to EA, however, 4 – 5 % of the anhydroglucose units contain nitrogen (amino groups). This value exceeds the number of reducing end groups by one order of magnitude. The extra nitrogen might indicate the presence of more carbonyl sites along the chain that can be aminated in the process. In the cellulose sources, carbonyl bands were not visible

in the FTIR. Instead, the FTIR of SFC and pulp reacted for only a short time at mild temperatures showed some evidence of yet unreacted carbonyl groups, that disappeared at prolonged reaction time (compare Chapter 3.1.2.2). An alternative explanation for the excess of nitrogen could be adsorbed oligosaccharides, which were implied in the GPC data and which would contain a higher density of nitrogen-containing groups due to their shorter length.

3.1.4.1 Thermal stability and reducing ends in REM-treated cellulose compared to hydrolyzed cotton

Previous studies on CNCs obtained via acid hydrolysis report a decrease in thermal stability in the CNCs compared to the cellulose source. This observation was linked to the decreased DP, which results in a higher ratio of reducing ends generated upon acid hydrolysis. The carbonyl groups at the reducing ends are believed to be the initiating sites for cellulose degradation through dehydration and subsequent hydrolysis.[158][70] In the case of functionalized CNCs, the thermal instability of the functional group can add another degradation step, such as self-catalyzed desulfation in sulfate-CNCs obtained through sulfuric acid hydrolysis.[159] The REM treatment presented here is intended to aminate the reducing ends and cleave the amorphous chains via aminolysis instead of hydrolysis. As a consequence, no new reducing ends should be produced and the number of existing reducing ends should decrease. Therefore, the thermal stability should not suffer. Thermogravimetric analysis (TGA) is used to determine the degradation temperature of the starting material and the REM-treated cellulose. The degradation onset temperature T_o is determined at a weight loss of 5 % from the TG curve, corrected by the residual moisture (around 2 %) that evaporates in the beginning during heating to 100 °C. The maximum degradation temperature T_{max} is the minimum of the weight loss (DTG) curve. Values are given for a heating rate of 2.5 °C/min. As shown in Figure 3.21, T_{max} does not differ significantly between the untreated material SFC (331 °C) and the REM-treated SFC (334 °C). The onset of degradation, however, is significantly lower for the untreated material with T_o 269 °C than for the REM-treated SFC with a T_o of 300 °C, attesting an increase of thermal stability through the treatment.

Following the aforementioned hypothesis, the higher onset degradation temperature of the treated material implies that not only no reducing ends are introduced through the treatment, but also that naturally existing reducing ends are transformed during the treatment. The REM treatment yields a material with higher thermal stability than previously reported carboxylated,[160] carboxy-methylated,[161] or phosphorylated[45] CNCs. A high thermal stability is beneficial for instance in construction materials and when using CNCs as reinforcing additives to broaden the window of applicability.
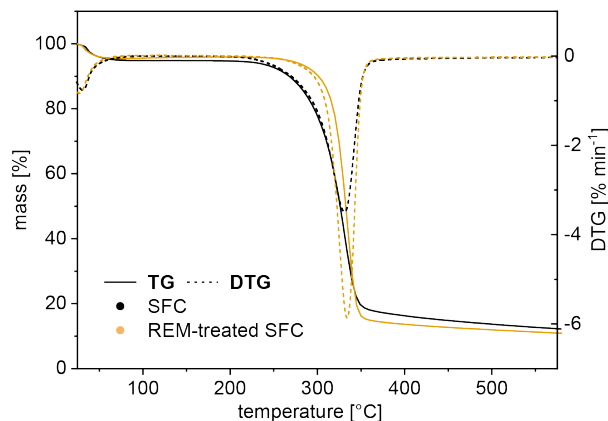
Figure 3.21: TGA of CNC extracted by treatment with REM composed of 2 parts ammonium formate and 1 part of the respective acid, compared with the starting material SFC.

To prove the functionalization of the existing reducing ends through the REM treatment, HCl-hydrolyzed cotton (hycot-CNCs) was investigated with TGA-MS as a model compound. HCl hydrolysis of cellulose, according to Battista et al.[152], only produces reducing ends through hydrolytic chain cleavage and no additional functional groups on the CNCs. The higher content of reducing ends compared to SFC should produce a more pronounced effect on thermal stability. Half of the hycot-CNCs was subjected to REM treatment and the other half was analyzed as-prepared. Similarly to what was observed for SFC, degradation of the hycot-CNCs starts at $T_{5\%} = 273$ °C, while for the REM-treated hycot-CNCs, $T_{5\%}$ is significantly higher at 301 °C (see Figure 3.22). As expected, owing to the larger amount of reducing ends, the higher thermal stability is more pronounced in $T_{\max}$, with 309 °C for the hydrolyzed cotton and 342 °C for REM-treated hydrolyzed cotton. This supports the hypothesis that reducing ends are modified during
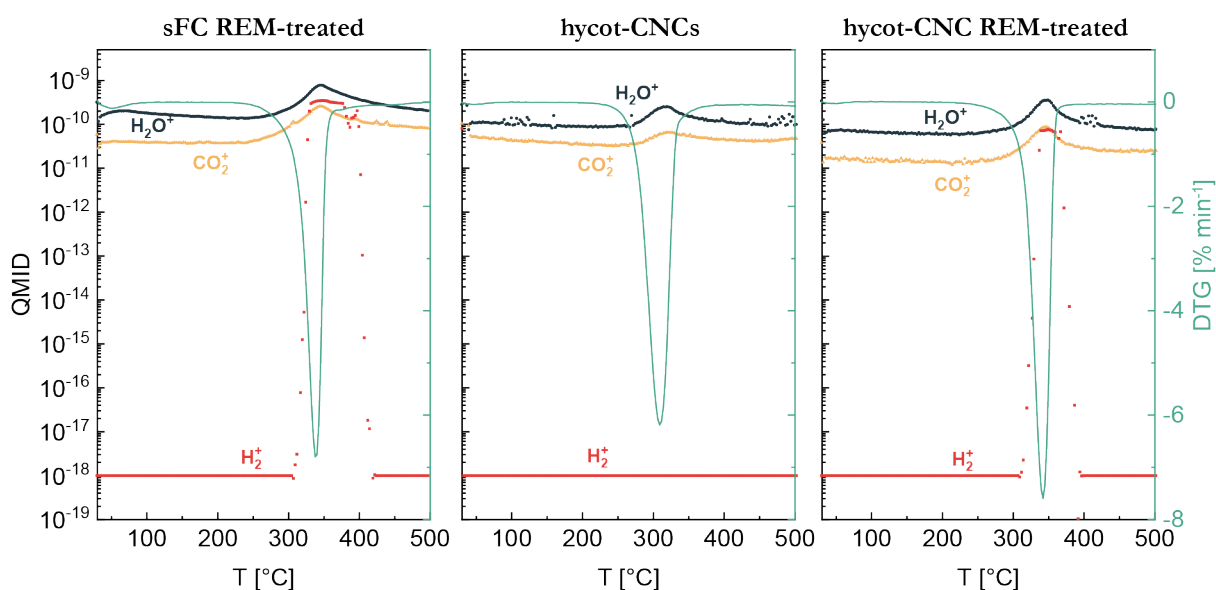

Figure 3.22: TGA and selected MS fragments dependent on the temperature measured for a sample of HCl-hydrolyzed cotton and a sample of post-REM-treated hydrolyzed cotton.

45

the REM treatment. MS, coupled with the TGA, analyses the degradation products dependent on the temperature. Interestingly, the REM-treated samples, hydrolyzed cotton as well as SFC, show a distinct peak of hydrogen at the decomposition temperature, while untreated hydrolyzed cotton does not show this signal. This indicates a different decomposition mechanism due to the absence of reducing ends. The analysis of this degradation mechanism, however, was beyond the scope of this thesis.

To ultimately prove the absence of reducing ends in the REM-treated cellulose, the samples are analyzed via liquid state NMR after dissolution in the ionic liquid tetrabutylphosphonium acetate, following the procedure developed by King et al.[162] The HSQC spectra of hycot-CNCs and REM-treated hycot-CNCs are compared in Figure 3.23. The attribution of the most distinguishable signals for reducing ends and non-reducing ends are shown in the image. The comparison shows the disappearance of signals attributable to reducing ends (RE) after the REM treatment (see marked signals in Figure 3.23), while signals for non-reducing ends (NRE) remain. This is another proof of the modification of the reducing ends during the REM treatment. New signals appearing in the range of 4 ppm to 5 ppm (^{1}H)/65 ppm to 85 ppm (^{13}C) have not been assigned yet and are the subject to future investigations in collaboration with Aalto University.

3.1.4.2 FITC-coupling to cationic CNCs probes presence of amino groups and Pickering-stabilizing abilities

Since the low amount of amino groups proved difficult to detect through conventional spectroscopic methods, indirect approaches to prove their presence were explored. Using amino-specific coupling reactions, amino sites can be marked by compounds that are easier to detect. Fluoresceine-5'-isothiocyanate (FITC), a fluorescent dye that is used for fluorescent labeling of peptides,[163] shows such a specific reactivity: The isothiocyanate group is reactive toward protein-born nucleophiles such as amine (or thiol) moieties, forming a thiourea. Exploiting this specific reaction, Xu et al. for instance used FITC to evaluate the accessibility of surface amino groups in modified mesoporous silicon.[164] Adapting their facile protocol for FITC coupling, CNCs are reacted with FITC to form a covalent bond between the supposed amino functionality of the CNC and the isothiocyanate group of the FITC according to Scheme 3.4.
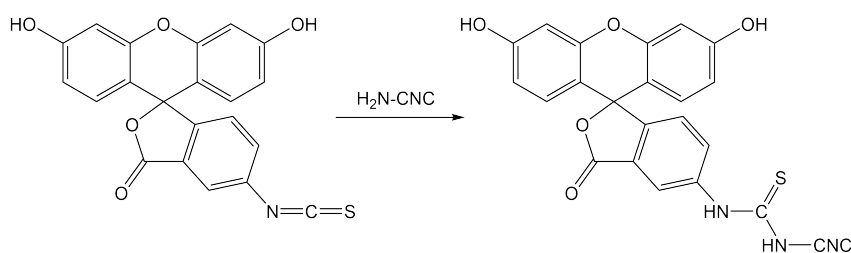
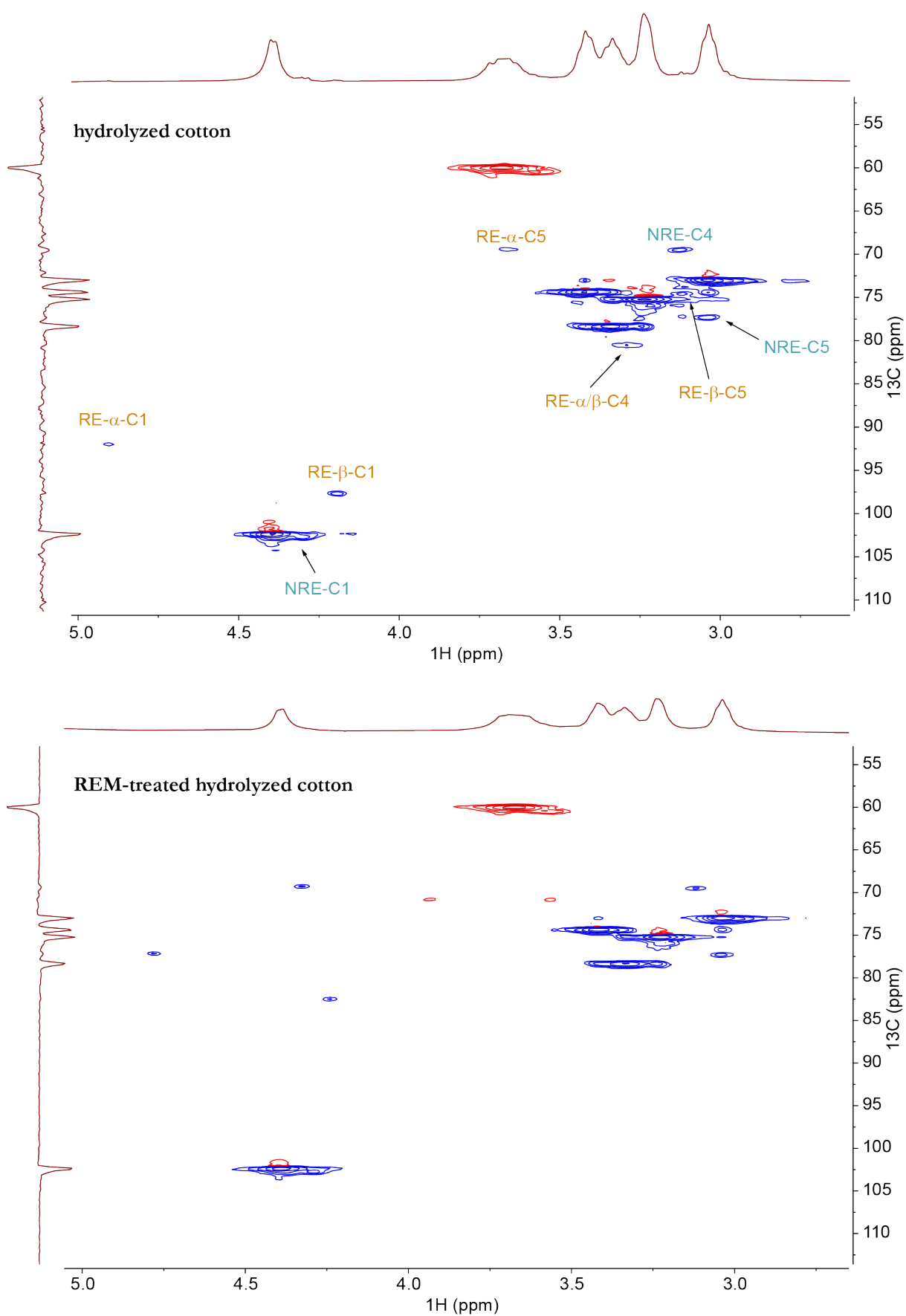**Scheme 3.4:** Reaction of FITC with amino-functionalized CNCs.

Figure 3.23: Liquid state NMR of hydrolyzed cotton as-prepared and treated with REM. RE: reducing ends, NRE: non-reducing ends.

To prove that FITC does not bind to the abundant and also nucleophilic hydroxyl groups in cellulose, or just adsorbs to the CNC surface, the same protocol is applied to CNCs obtained from HCl hydrolysis of cotton (hycot-CNCs), which contain only hydroxyl groups and no further functionality. The aqueous CNC dispersions are mixed with a solution of FITC (Acros Organics) in ethanol (concentration $1 \ \mathrm{mg \, mL^{-1}}$) and stirred for 16 h in the dark. The CNCs are recovered via centrifugation. The precipitated CNCs show a significant difference in color between the two types, as shown in Figure 3.24 A: While the precipitated REM-treated CNCs exhibit an intense yellow color, hycot-CNCs are precipitated as white sediment.
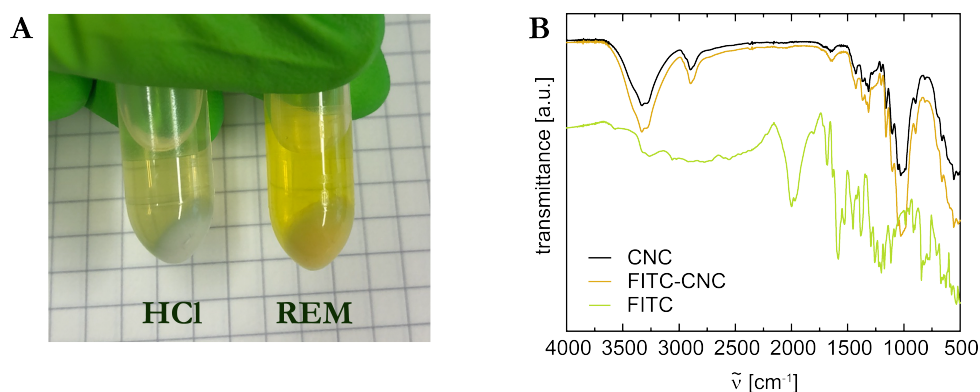

Figure 3.24: (A) Precipitated CNCs obtained from HCl hydrolysis (hycot-CNCs) and via REM treatment after reaction with FITC. (B) FTIR of washed FITC-CNC obtained with REM-treated cellulose compared to FITC and CNC

Free FITC (unbound or unadsorbed) is removed by the addition of an excess of ethanol and sonication in an ultrasound bath. The solvent is then exchanged for water. Re-dispersion of the cleaned REM-treated FITC-CNCs results in a turbid yellow dispersion. The dispersion of washed FITC-reacted hycot-CNCs does not exhibit a significant change of color after reaction with FITC. The FTIR of the washed FITC-CNC (Figure 3.24 B) does not show distinct changes or signals attributable to the FITC, likely due to the low degree of substitution.

To simultaneously probe successful dyeing of the CNC and their ability to stabilize Pickering emulsions, the two suspensions of FITC-CNCs are used to emulsify sunflower oil and the emulsions are observed using confocal laser scanning microscopy (CLSM). CNCs adsorb at the oil-water interface so that an increased fluorescence intensity around the droplet shows that the fluorescence of the dispersion originates from FITC coupled to CNCs and not from free FITC. Emulsions attempted with hycot-CNCs quickly phase-separate, indicating that hycot-CNCs are no suitable Pickering stabilizers. As shown in Figure 3.25 A, no fluorescent signal is detected in the emulsion, neither in the continuous phase nor at the oil-water interface. This observation indicates that no FITC is bound or adsorbed to the hycot-CNCs. REM-treated CNCs, on the other hand, produce a stable emulsion that is visualized in Figure 3.25 B. The CLSM images reveal an intense fluo-

rescence concentrated at the oil-water interface, proving the association of FITC to the CNCs.
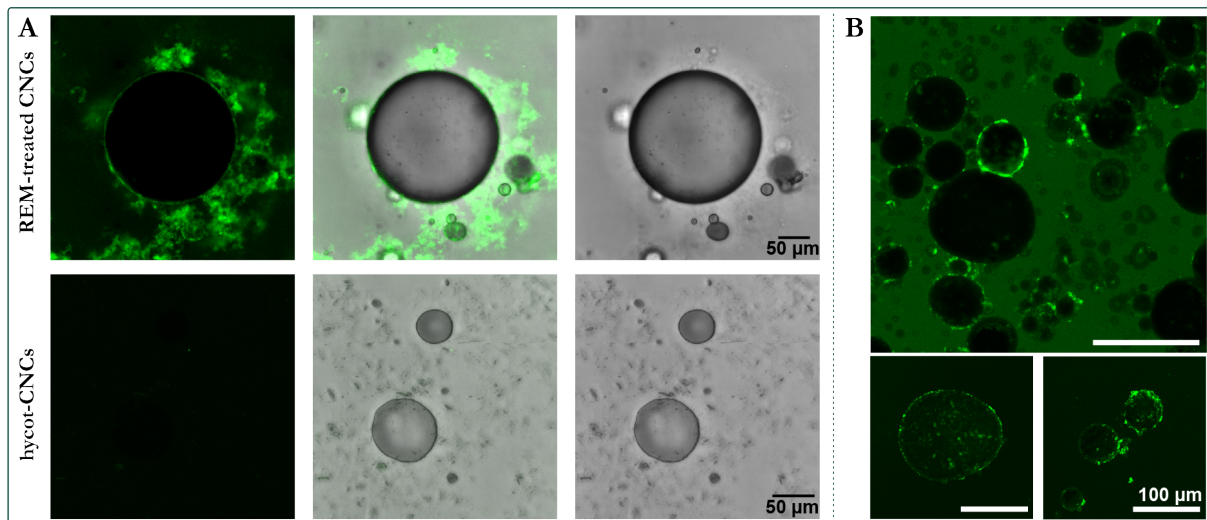

Figure 3.25: CLSM images of sunflower oil-in-water emulsions stabilized by REM-treated and hycot-CNCs reacted with FITC. (B) CLSM images of a sunflower oil-in-water emulsion obtained using REM-treated CNCs.

The presence of FITC on the CNCs does not prove a covalent bond between them. The dye could also merely be adsorbed on the CNC surface. XPS measurements can reveal the presence and nature of the bonds. The deconvoluted spectra of the dried product (Figure 3.26 C) show an N 1s peak at 400.1 eV with a shoulder at 401.6 eV. N 1s in a thiourea bond (N-C=S) was reported at 400.9 eV, which is in between the deconvoluted peaks. Similarly to the XPS spectrum of the CNCs shown above, this relatively low-intensity peak is also inconclusive. However, sulfur is detected with low intensity, which implies the presence of low amounts of FITC.
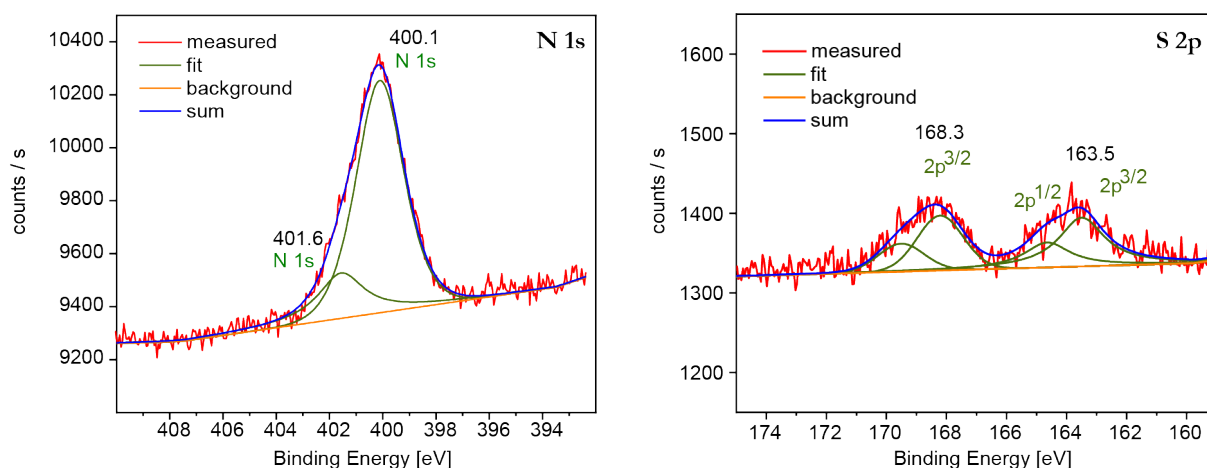

Figure 3.26: XPS spectra of product A show the presence of nitrogen and sulfur from the thiourea formed between CNC and FITC.

Fluorescent marker particles such as FITC-CNCs can also be interesting for bio-imaging applications and biodistribution (that is the distribution of compounds in organisms)

studies with nanoparticle-based medical methods.[165] Previous approaches to coupling FITC to CNCs required preliminary amination following a three-step procedure that involved the reaction with epichlorhydrin to introduce an epoxy functionality that is opened in a second step by a reaction with ammonium hydroxide. This step introduces the amino functionality, which is then reacted with FITC.[165] Having amine-functionalized CNCs after the extraction step allows direct coupling of FITC and eliminates the need for post-extraction functionalization.

3.1.4.3 Indirect gold labeling of amino groups via specific biotin-streptavidin binding

In an attempt to localize the amine functionality, a gold labeling experiment was conceived to target the amino groups on the CNCs (see Scheme 3.5). For that, the CNCs were first reacted with biotin in an amide coupling reaction using the activating agents 1-ethyl-3-(3-dimethylaminopropyl)carbodiimide (EDC)/N-hydroxysuccinimide (NHS). This reaction is commonly used for peptide production and is used here to couple the activated carboxylic group of the biotin to the aminated CNCs. In the second step, a streptavidin gold nanoparticle conjugate (10 nm diameter) is added to bind to the biotin sites thanks to their high specific affinity.[166] TEM is then used to localize the bound gold in relation to the CNC.
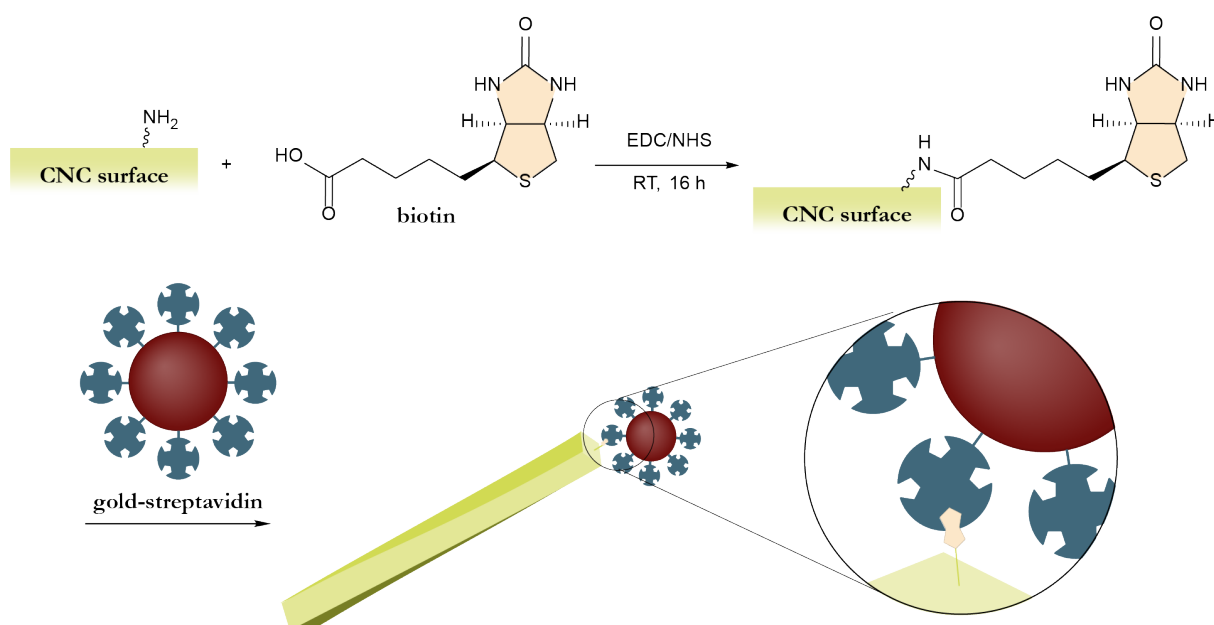
Scheme 3.5: Gold-labeling of cationic CNCs: Biotin is coupled via EDC/NHS to the supposed amino groups of CNCs. In a second step, a gold-streptavidin conjugate is added, which specifically binds to the coupled biotin.

The first step should eliminate the positive ZP of the CNCs due to the lowered basicity of the amide compared to the amine. ZP measurements before and after the coupling show a decrease to only two thirds of the charge after the reaction (from 35 mV to

26 mV), showing that some of the cationic groups reacted. An increase of reaction time or concentration of the coupling agents or biotin did not lower the ZP further and thus does not increase coupling yield. FTIR does not show a clear signal of coupled biotin, which might be due to the low degree of substitution (see Figure 8.6).

The CNC-Au conjugates obtained upon mixing the biotinilated CNCs with streptavidin-gold are visualized with TEM, shown in Figure 3.27. The agglomeration tendency of the CNCs makes a definite localization difficult, as individualized particles are rarely available. Moreover, the attachment of gold-streptavidin conjugates to the CNCs might also be due to unspecific inter-particle interactions, like hydrogen bonding or van der Waals forces. However, the gold nanoparticles seem to be predominately, but not exclusively, located at the extremities of the CNCs. This confirms functionalization at the reducing ends. Some gold nanoparticles are situated along the particle length, implying amino functionalities across the entire particle, as was estimated from the high nitrogen content.
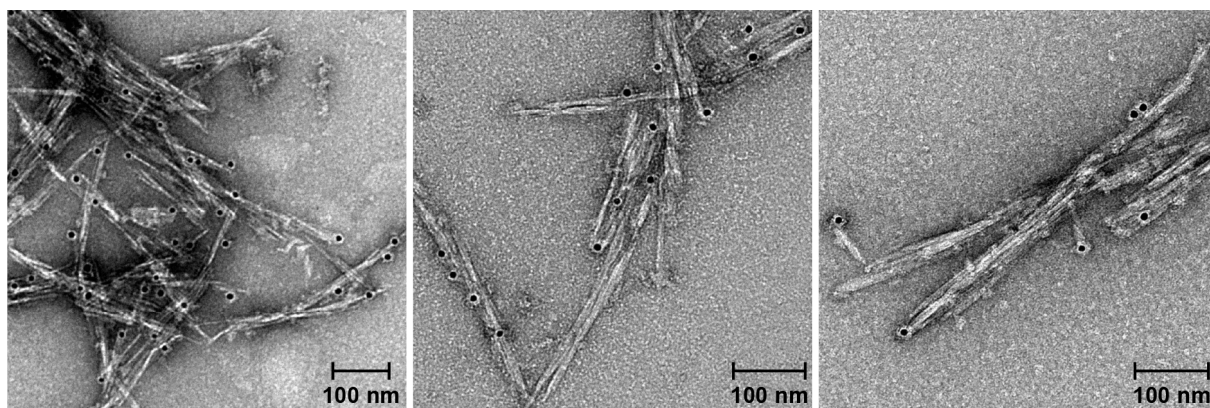
Figure 3.27: CNC-gold conjugates obtained via Scheme 3.5, visualized with TEM.

3.1.5 Homogenization of extracted CNCs

Next to colloidal CNCs, samples obtained from the REM-treatment usually also contain high amounts of bigger fibrils and particles on the micrometer scale that were not fully disintegrated during the extraction, especially when treating sources of such diverse nature as pulp with a wide fiber size distribution. Large scale material applications do not require the smallest of small particles. Instead of separating the small from the big particles via separation, samples can also be homogenized to break up agglomerates and unseparated particles and assimilate particle sizes (decreasing the polydispersity). High-pressure homogenization creates strong shearing forces in the dispersion and thus separates crystallites held together by hydrogen bonds. Some functionalizations of cellulose, such as TEMPO oxidation, aim at decreasing the attractive forces between the cellulose fibers by introducing electrostatically charged groups to induce repulsion between the fibers and thus decreasing the forces needed to break them apart in homogenization processes. Using a high-pressure homogenizer at a pressure of 1000 bar, the amount of passes required

to homogenize a sample of treated SFC was compared to the amount needed for the untreated sample. The untreated sample was passed through the homogenizer 90 times before starting to exhibit a notable increase of viscosity, indicating entangling chains on the nanoscale, and eventually turning milky-transparent. The treated sample, of low viscosity before, became jelly and more transparent after two passes through the homogenizer. This drastic decrease of mechanical energy necessary for disintegration of particles reflects the successful treatment and presence of smaller particles in the treated sample. The smaller the agglomerate, the smaller the energy needed to separate particles due to the lower amount of hydrogen bonds that need to be broken. The positive surface charge additionally decreases the necessary energy and stabilizes the particles after separation from re-agglomeration.

SLS measurements show a narrowing of the size distribution peak with increasing number of homogenization passes, shown in Figure 3.28 A for the example of CNCs extracted from FSC. The shoulder at larger sizes observed for the unhomogenized sample is flattened after two passes and disappears after six passes. Homogenization causes a slight shift of the peak to higher sizes, which could indicate a higher tendency for coagulation. The reversible formation of agglomerates in homogenized samples is visually observable upon dilution and is demonstrated in the measurement time-dependent SLS data for Figure 3.28 B: At the start of the measurement, particle sizes are largely around 50 μm (dark purple curves). The sample is then continuously sonicated and stirred in the device while the measurement proceeds, causing the agglomerates to break, which is demonstrated in the decrease of the number density of the large sizes and an emerging shoulder at smaller sizes. The small size shoulder gradually develops into a sharp peak with a maximum
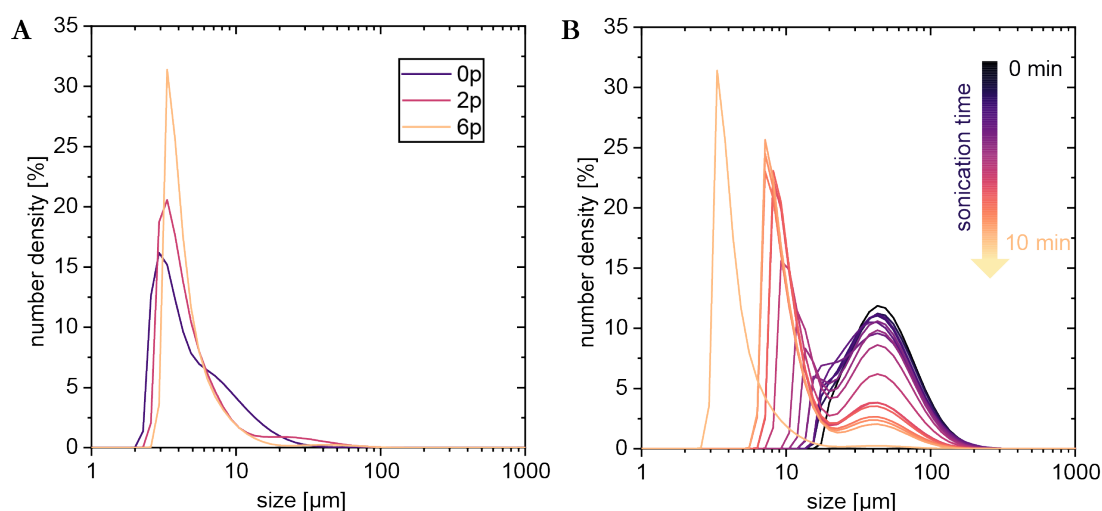

Figure 3.28: (A) SLS curve dependent on the number of passes (p) of sNC through the homogenizer. (B) SLS curve of sNC-6p dependent on the measurement time, equivalent to mixing and sonication time, demonstrates the presence of agglomerates that are broken up after 10 min of ultrasonication in the device.

around 4 µm (yellow curve), while the large size peak declines to a flat shoulder around 50 µm after a sonication time of ten minutes.

The increased tendency for coagulation is an indication for a functionalization or electrostatic stabilization predominantly at the surface of cellulose particles. As a consequence, cellulose might not have been disintegrated into the singular nanocrystals through the REM treatment, but into nanocrystal bundles which only bear the surface charge around the bundle surface. This is in agreement with the findings of, for instance, Elazzouzi-Hafraoui et al., who proved the presence of CNCs as lateral aggregates composed of two to four individual crystallites after acid hydrolysis of cellulose.[56] Upon homogenization, bundle particles with a high surface charge and colloidal stability are broken up into smaller particles with a lower surface charge, as the amount of charged groups that previously stabilized the single bundle is now divided between a larger number of CNCs, so that CNC faces on the inside of the bundle are left without any electrical charge. Thus, homogenized CNCs would have a lower average surface charge than the bundled CNC aggregates.
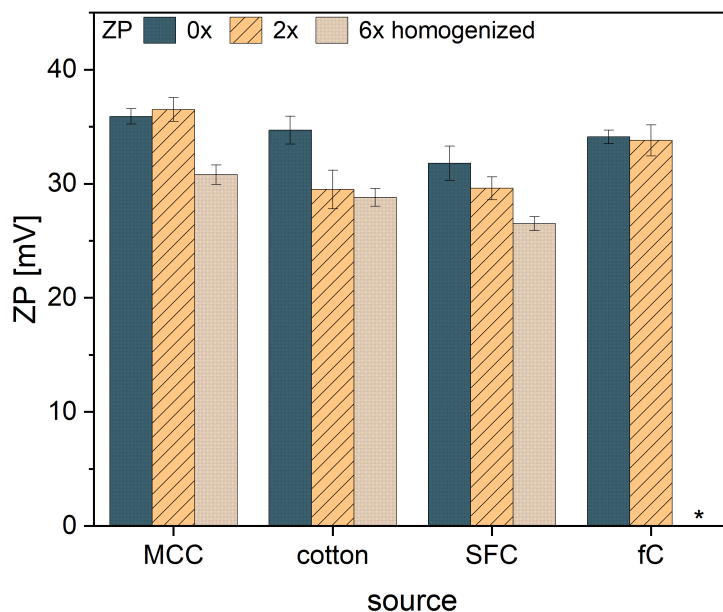
Figure 3.29: Comparison of the ZP measured for CNCs from different sources as-prepared and homogenized with two and six passes through the homogenizer at 1500 bar. *: CNCs from fC form a homogeneous transparent suspension already after 2 passes, after which homogenization was not continued.

This effect is observed via ZP measurements for the samples of CNCs from all different tested sources, as shown in Figure 3.29. Although homogenization leads to a decreased colloidal stability in some samples, it individualizes the CNCs, as visualized in the TEM images in Figure 3.30.

Homogenization of the entire cellulosic product enables the large scale production of materials with homogeneous properties, due to a narrow size distribution. Small sizes can be reached even when using the sedimenting cellulosic particles and not only the part
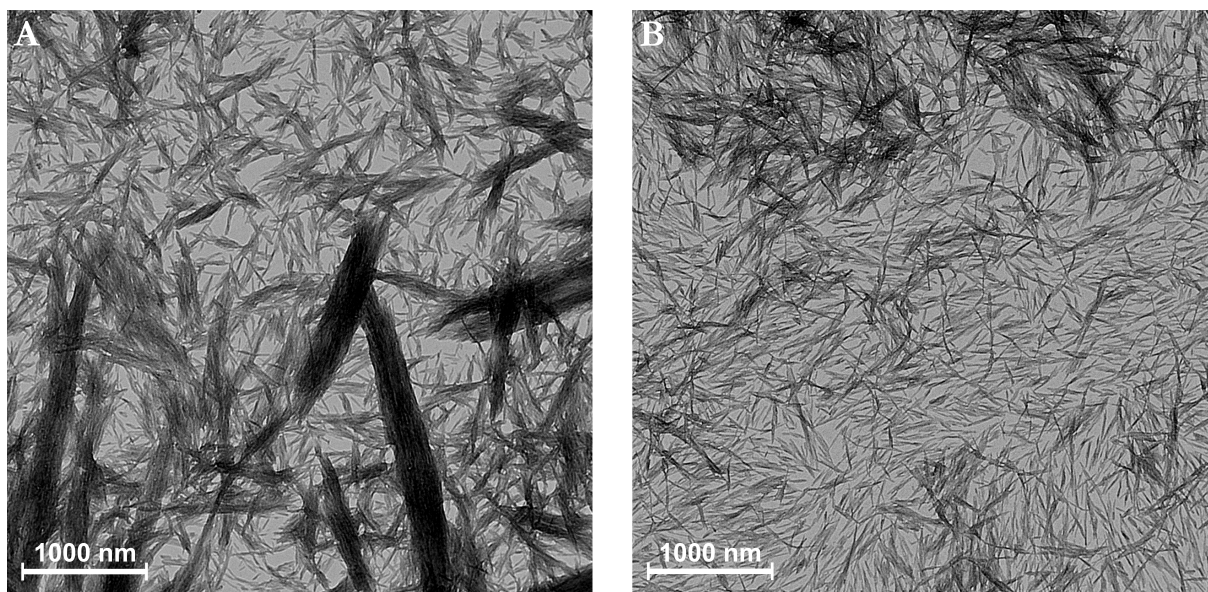
Figure 3.30: TEM of an as-prepared and a homogenized sample of fNCs.

that exhibits high colloidal stability even before homogenization. The yield of fNCs after homogenization is approximately 60 % to 65 %. CNCs obtained from the homogenized entire fraction of cellulosic product are small enough to produce thin films with high transparency (see Figure 3.33 C in the next section).

3.1.6   Colloidal characterization of fNC

To define the colloidal behavior of CNCs, a solution of fNC was analyzed via conducto-metric titration (pH titration) using HCl starting from pH 10. The titration curve, shown in Figure 3.31, shows an equivalence point at pH 7.43, corresponding to the pK_a value of the CNCs. This value is in the expected range for ammonium groups: The reported
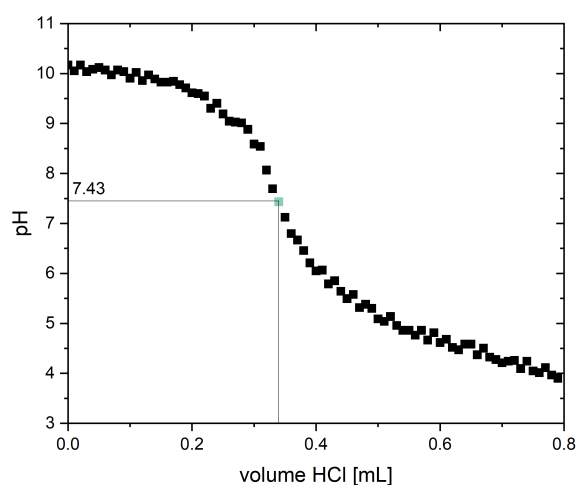
Figure 3.31: Titration curve for fNC. Equivalence point at pH 7.43 marked in turquoise.

pK_a for ammonium groups in chitosan (poly glucosamine, which can be considered a comparative system due to its chemical equivalency to aminated glucose) is around 7-8[167], dependent on the degree of deacetylation and dissociation. The density of amino groups in chitosan, however, is quite high so that a direct comparison is not accurate. Depending on the specific anomer, pK_a for glucosamine was determined to 7.38[168], 7.87 or 8.12,[169] which is also in good agreement with the pK_a determined for the CNCs, supporting the hypothesized presence of amino groups.

To optimize the dispersion medium, i.e. the electrolyte, for maximum colloidal stability, corresponding to a maximum charge, pH and ionic strength of the surrounding medium are varied to find a balance between protonation of the amino groups and ionic strength. An increasing ionic strength decreases the screening length of the colloids due to association of counter ions, leading to a lowered energy barrier for agglomeration and a destabilized colloid. Varying concentrations of the weak acetic acid and the strong hydrochloric acid were used, resulting in different pH at different ionic strengths of the medium, as acetic acid only partially dissociates. Starting from a ZP of around 17 mV at neutral pH in MilliQ water, the potential first increases with increasing concentration of acid, i.e. decreasing pH, as amino groups are protonated. A peak is reached after which the ZP decreases, as counter ions start shielding and the Debye screening length decreases at the critical coagulation concentration, so that CNCs undergo flocculation. Due to the higher disassociation constant of HCl, flocculation occurs at lower concentrations than for acetic acid, as the ionic strength increases more drastically, as seen in Figure 3.32 B. Therefore, variations of HCl concentration also have a higher impact on colloid stability than observed for acetic acid. This is seen in the more rapid decrease of ZP with c(HCl) than with c(AcOH) in Figure 3.32 A (note the logarithmic scale). A maximum charge of +41 mV is found in 50 mM acetic acid, corresponding to pH 3. For HCl, the maximum ZP of 35 mV is found at a higher pH of 3.4, or a concentration of 0.4 mM.
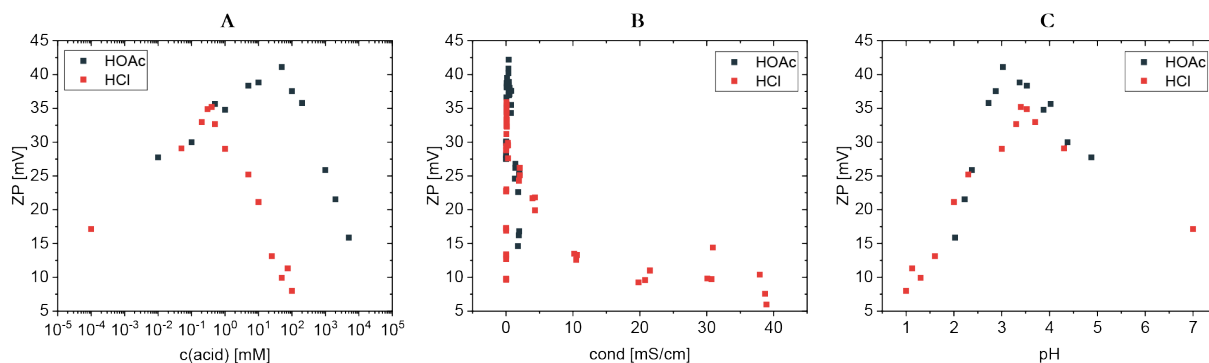

Figure 3.32: Correlations of Zeta potential of CNCs with concentration of a weak acid (acetic acid) and a strong acid (hydrochloric acid), shown as dependencies of ZP on concentration (c), conductivity, and pH of the dispersion.

3.1.6.1 Do REM-extracted cationic CNCs form a cholesteric phase?

Conventional CNCs obtained from sulfuric acid hydrolysis form a cholesteric, or chiral nematic, phase, that produces structural color. Cholesteric phases are usually observed in CNC dispersions concentrated to around 10 wt.%. At this point, the dispersion still has to be liquid so that CNCs have the rotational freedom to rotate in response to the chiral interaction and form the cholesteric phase. Gelation or kinetic arrest occurs upon evaporation of the solvent and freezes the structure so that it is retained in the dried film. In the course of this work, the formation of a cholesteric phase from REM-extracted CNCs was never observed. The cationic CNCs form dispersions that become jelly at concentrations around 1-2 wt.% already. Films obtained via dispersion casting do not show the typical regularly ordered, seemingly layered cholesteric pattern when observed in SEM, as shown in Figure 3.33.

Vacuum-assisted self-assembly was shown to produce cholesteric films of CNCs with tunable structural color by Chen et al. [170] The authors simply vacuum-filtrated a dispersion of CNCs obtained via sulfuric acid hydrolysis through a polytetrafluoroethylene membrane. When this method is applied to the REM-extracted cationic CNCs, colorful iridescent films are produced on the membrane (Figure 3.34 A). Thicker films, however, do not exhibit any color. The SEM image of the cross-section in Figure 3.34 B does not reveal
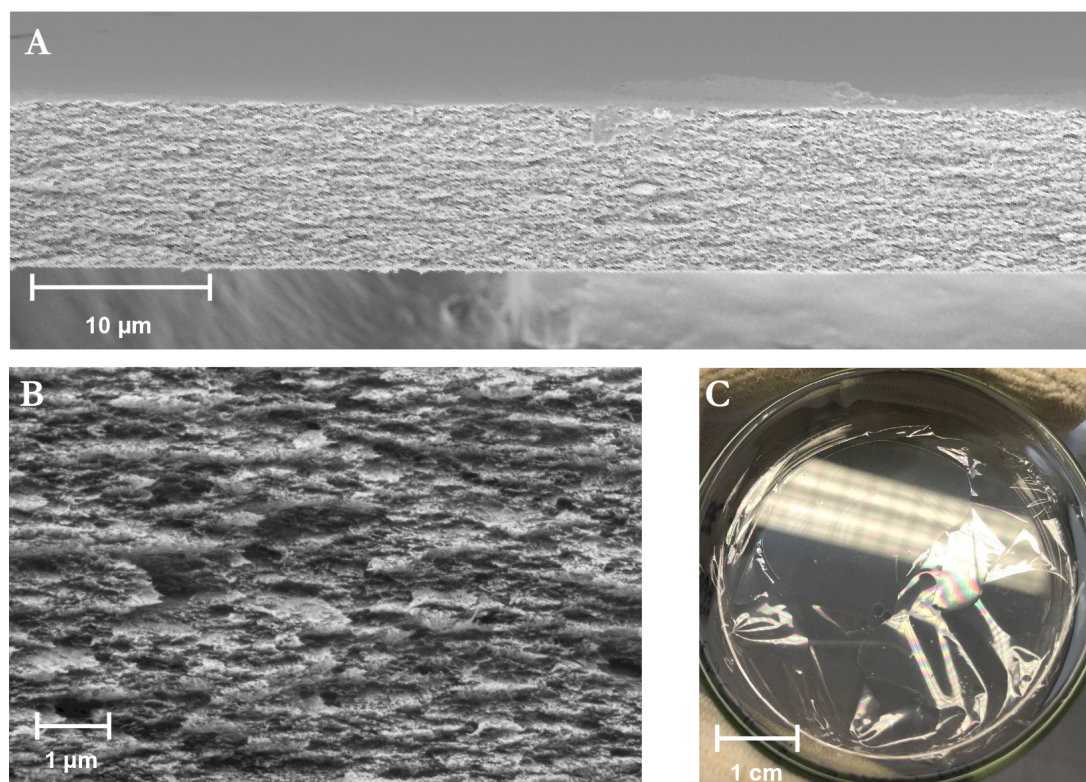

Figure 3.33: (A) and (B) SEM images of a film dried via slow evaporation do not show a self-assembled cholesteric phase. (C) Transparent fNC film dried via slow evaporation shows thin film interference, but no structural color.

a cholesteric structure. The shimmering color must therefore be attributed to thin film interference instead of structural color.

The formation of the cholesteric phase depends on the chiral interaction between the particles. To react to each other's chirality, particles have to be able to approach each other at close distance without agglomerating. According to DLVO theory, this is only possible if the repelling electrostatic forces are strong enough, that is stronger than the attractive hydrogen bonds. ZP values measured for a comparative sample of CNCs extracted via sulfuric acid hydrolysis exhibited a charge that was approximately twice as high as the cationic charge on the REM-extracted CNCs. The charge of our cationic CNCs seems to be too low to guarantee an appropriate distance. This is in rough agreement with Hasani et al., who also did not observe the formation of a chiral nematic phase on cationic CNCs with a ZP of 30 ± 5 mV.[120]

3.1.6.2 Cationic CNCs as Pickering stabilizers

The low positive charge of the CNCs developed and described in this work that is too low to lead to the formation of a cholesteric phase can be beneficial for other applications for which the high negative charge of sulfate CNCs is too high: The stabilization of Pickering emulsions. As shown above, our novel CNCs display the tendency to aggregate and form networks, which demonstrates a non-excessive inter-CNC repulsion. Moreover, their cationic charge should support their association at the negatively charged oil-water interface. To assess the possibility of using the novel cationic CNCs as Pickering stabilizers, a selection of oils of different origins are emulsified in a dispersion of CNCs in water. Those preliminary tests prove the stabilization of the triglycerides sunflower oil and linseed oil as well as the alkane hexane, as shown in the micrographs in Figure 3.35.

The photograph of the produced emulsions after 5 h shows that the emulsions are prone to creaming, especially the hexane emulsion that only exhibits a slight turbidity in the bulk with a creaming layer on top after this time. The triglyceride emulsions also exhibit
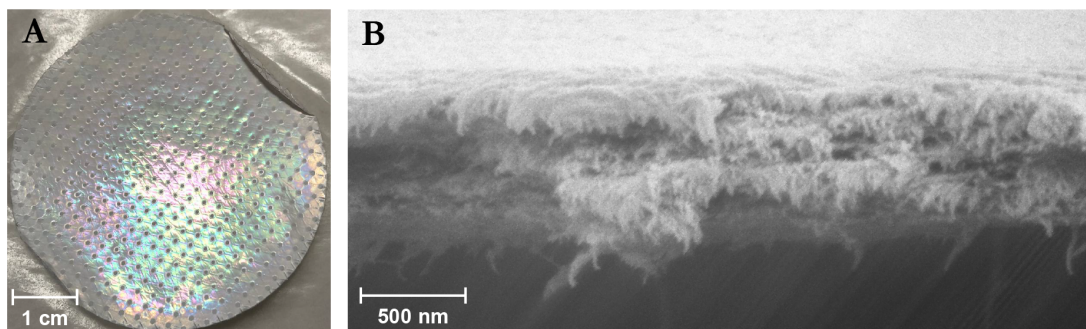

Figure 3.34: (A) Photograph of thin CNC film produced via vacuum-assisted self-assembly through filtration through a polytetrafluoroethylene membrane. (B) SEM image of the cross-section of the thin film.
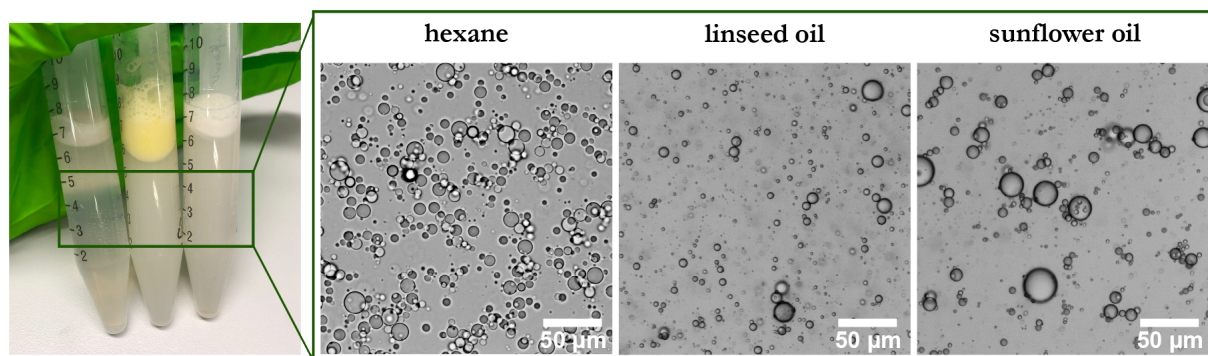
Figure 3.35: Photograph and optical micrographs of 5 % o/w emulsions with hexane, linseed oil and sunflower oil (from left to right) stabilized with 0.2 wt.% cationic CNCs (relative to emulsion mass).

a creaming layer, but considerably higher turbidity, indicating that more droplets are still dispersed in the continuous phase. Since creaming is the result of buoyancy of the lightweight oil droplets to the top of the emulsion, this difference can be explained by the significantly lower density of hexane (0.66 $\mathrm{g\,mL^{-1}}$) compared to vegetable oils (around 0.92 $\mathrm{g\,mL^{-1}}$).

3.1.7 Recyclability of REM

The recyclability of the reaction medium is crucial when considering large-scale application of a reaction. Their non-existent volatility complicates the recyclability of DESs in terms of their separation from by-products. The REM used for the presented CNC isolation method is considerably browned after the reaction and separation of the cellulosic product, proving the presence of by-products with good solubility in the eutectic. ^{1}H NMR spectra of the used medium compared to the medium before the extraction showed impurities with peaks in the chemical shift range of 3.3 ppm to 3.6 ppm, which can be attributed to protons in the vicinity of heteroatoms and indicates the presence of oxygen- and nitrogen-rich Maillard products. To investigate the recyclability of REM1, an extraction was attempted at the same conditions of the isolation of sNC1 but using the used REM as a solvent. The product is visibly browner than the sNC obtained with fresh REM. Other product properties do not show significant differences: Elemental analysis states a nitrogen content of $0.27\pm0.02\%$, which is close to the value obtained for sNC1 (0.29 ± 0.03). XRD analysis gives a CrI of 78.6 %, which is also close to the value obtained for sNC1 (78.4 %). FTIR (see Figure 3.36 A) does not show additional bands and SLS (see Figure 3.36 B) shows a similar maximum peak around 3 μm. However, the shoulder at larger sizes is more pronounced, indicating a marginally less effective cleavage. Overall, the evidence of these preliminary experiment suggests that the once used REM1 is still efficient in the isolation of CNCs and that recycling of the reaction medium is feasible. Future studies may investigate the limits of recyclability as well as ways to improve it. One goal here

should be to suppress the formation of Maillard products, for which the inclusion of more water in the REM might be beneficial and should be investigated.
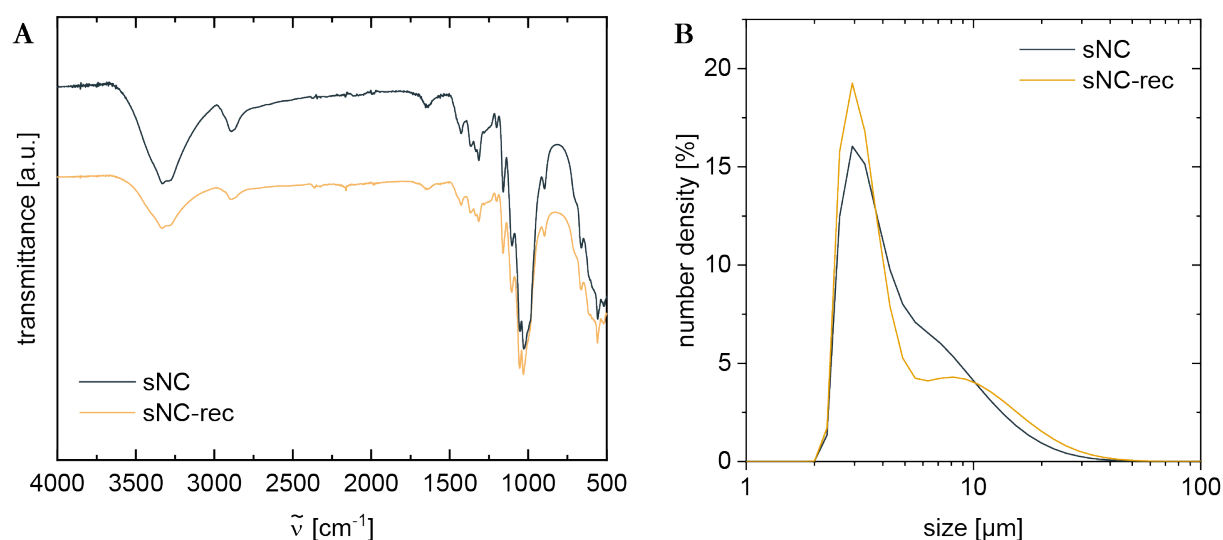
Figure 3.36: (A) FTIR spectra and (B) size distribution (determined via SLS) of sNC product obtained with fresh REM (sNC) and with the re-used REM (sNC-rec).

3.2 Conclusions

A new method was developed to isolate cellulose nanocrystals with a positive surface charge using a deep eutectic solvent, or reactive eutectic medium, based on ammonium formate as the hydrogen bond acceptor, paired with an organic acid as the hydrogen bond donor. Among the tested acids, lactic acid was found to both be the economically favorable and practically best applicable one, due to its liquid state and the reliable formation of a eutectic with ammonium formate. Its water content of 10 % does not affect product properties adversely compared to REM without water, such as glycolic acid/ammonium formate. This insensitivity to water is important for the treatment of often wet biomass. Future systematic studies on the effect of water in the eutectic can help to reduce chemical costs as well as the viscosity of the medium, which could enhance mass and heat transfer and make the REM treatment more efficient.

The treatment was found most effective and controllable in the temperature range of 140 °C and 160 °C. In this range, amorphous cellulose domains are cleaved, while the native crystalline structure is preserved and nitrogen-containing groups are introduced. Colloidal cellulosic particles are evolved which carry a positive surface charge indicated by a Zeta potential of 30 mV to 40 mV at neutral to acidic pH. The comparison of different cellulose sources showed that hornification, as found in dried pulp, and high crystallinity, as found in tunicate cellulose, impede the treatment due to limited wetting of the material with the REM. Those materials require prolonged reaction times. Never-dried pre-fibrillated pulp and cotton, which are not expected to exhibit hornification,

yielded the best results, expressed in high reduction of molecular weight and high Zeta potentials. The use of never-dried cellulose sources is therefore preferable and possible due to the demonstrated water-insensitivity of the treatment.

Based on the evidence, it is presumed that the treatment of cellulose in the reported REM has a twofold effect: Firstly, the eutectic dissolves amorphous cellulose domains by aminolysis, induced by ammonium and organic acid. Secondly, the Leuckart reagent ammonium formate causes derivatization by introducing cationic nitrogen-containing groups into the crystalline cellulose, thus evolving electrostatically stabilized, nanocrystalline particles. The evidence suggests the nitrogen-containing groups to be amino groups, however, the low degree of substitution makes a definite conclusion difficult. Future experiments will include the synthesis and NMR analysis of model compounds to verify the reaction mechanism.

Optimizations on an engineering level can include a more proficient mixing that breaks up cellulose aggregates already during the extraction process and makes it more available for chain cleavage and amination. The high viscosity of the mixture pre-extraction would make it suitable for an extrusion-type reactor.

Cationic CNCs in self-standing films for gas barriers and gas separation

The novel cationic CNCs developed in the first part of this work form smooth, transparent and free-standing films from the cast dispersion. Those films exhibit a limited degree of flexibility due to the rigid nature of the short nanocrystals. Even though CNC films might not compete with all the mechanical properties of polymer films used for packaging, they are still worth investigating. Not every application of films is mechanically demanding: Functional films used, for instance, as membranes or separators in electronic devices usually do not undergo great mechanical stress and they are often embedded between supports. Functionality can be introduced through an additive, which, besides a passive role as a plasticizer, can also take on an active role to give the film a certain property. This can be, for instance, conductivity, or, in the case of gas separation membranes, a specific solubility for specific gases. Imidazolium-based ionic liquids show high solubilities for CO_2,[171] the most emitted climate-impacting greenhouse gas. The separation of CO_2 from gas mixtures, for instance, from exhaust gases, is of great importance in the pursuit of an emission-reduced industry. The liquid state of ILs, however, impedes their straightforward application in gas separation processes. The solution is to immobilize the IL on a solid substrate: So-called supported ionic liquid membranes (SILM) are designed to take advantage of the functionality of an IL while being easy to manage and implement into existing processes. SILMs for carbon capture often use porous PVDF as support, which is a so-called forever chemical and should be avoided when possible.[172;173] In a more sustainable approach, Lam et al. reported increased selectivity of CO_2 over CH_4 and N_2 when doping cellulose triacetate membranes with different imidazolium-based ionic liquids.[174] Despite its natural origin, the chemical modification of cellulose acetate renders its biodegradability problematic.[175] The use of colloidal, chemically pristine cellulose, realized in CNCs, is preferable. The solubility of cellulose in some imidazolium-based ILs[176;177] indicates good interactions between the two, which makes the application of such ILs as additives

and possibly plasticizers worth investigating. The potential of nanocellulose-IL blends in gas separation applications was demonstrated by Janakiram et al. in 2020, who reported good selectivities along with high permeabilities in a blend of CNF with the ionic liquid 1-ethyl-3-methylimidazolium acetate.[178] Danyliv et al. proved the feasibility of an SILM even with the more rigid CNCs in a 2021 study in which they used the membrane as a polymer electrolyte for a fuel cell.[179] To date, CNC-based SILMs have, to the best of my knowledge, not been investigated for their gas transport behavior.

This chapter is an investigation into the feasibility of the application of CNCs in free-standing barrier films and gas separation membranes. As the new type of cationic CNCs, introduced in the first part of this work, are a new material in itself, barrier properties in a glucose-CNC film are tested. Glucose was chosen as an additive based on its similarity to cellulose, allowing excellent interaction between additive (or plasticizer) and matrix. The amino groups hypothesized on the CNC surface are not only intrinsic to the biopolymer chitosan, making the CNCs readily biodegradable compared to standard sulfate group-bearing CNCs – amino groups have also been exploited for their carbon dioxide adsorbing capabilities.[180;181] I was therefore curious to see if there is a selective effect attributable to the aminated CNCs. To increase gas permeability and introduce functionality into the films, two ILs, 1,3-dibutylimidazolium acetate (dbi acetate) and 1,3-ditetrahydrofurfurylimidazolium acetate (dthfi acetate), are applied. Matrix and additive contributions to gas permeation are analyzed by comparing the CNC-based films to membranes with chitosan as matrix material with the same additives. For that, gas solubilities and diffusivities were considered separately. Chitosan, or polyglucosamin, was chosen as a reference due to its chemical similarity to the amino-functionalized CNCs. Chitosan is also considered a gas barrier material.[182]

This study was a collaboration with Dr. Steven Kluge and Dr. Steffen Tröger-Müller from the Fraunhofer Institute for Applied Polymer Research, Potsdam, Germany, who performed the gas permeability tests and prepared the chitosan reference membranes. The results presented in this chapter were previously published in *ACS Sustainable Chemistry & Engineering*.[183]

4.1 Results

This chapter describes the attempt to produce SILMs with the two ILs dbi acetate and dthfi acetate supported by biodegradable cationic CNCs. The preparation of self-standing films from two types of CNCs and chitosan as a reference, both combined with the ILs, is first described. The resulting membranes are then characterized physically and with regard to their gas permeation properties.

4.1.1 Preparation of CNC films

In Chapter 3, we saw that REM-extracted CNCs have different properties depending on the cellulose source used, providing us with options to choose from tailored to the application that we aim for. Here, the goal is to produce self-standing films that can be handled without breaking or cracking and therefore need a certain degree of flexibility. To support flexibility, CNCs with the lowest CrI were first chosen for film preparation. These were CNCs extracted from SFC, with $CrI = 79\,\%$. CNCs made from this material, henceforth called sNC, are disperse in size and contain longer nanofibers next to actual CNCs, as observed via TEM (Figure 4.1). Later, the more homogeneous CNCs extracted from the pre-fibrillated pulp (fNC) were also applied. The specific properties determined for the CNCs used in this study, such as dimensions, DP, and ZP, are listed in Table 4.1.

Table 4.1: Properties of used CNCs. Average dimensions as determined through TEM, degree of polymerization (DP) refers to the molecular weight of the cellulose chains of dissolved CNCs, determined by GPC.

	length [nm]	width [nm]	aspect ratio	Zeta potential [mV]	DP
sNC	125 ± 16	6 ± 1	21	35 ± 3	215-396
fNC	81 ± 14	9 ± 1	9	41 ± 3	153-283
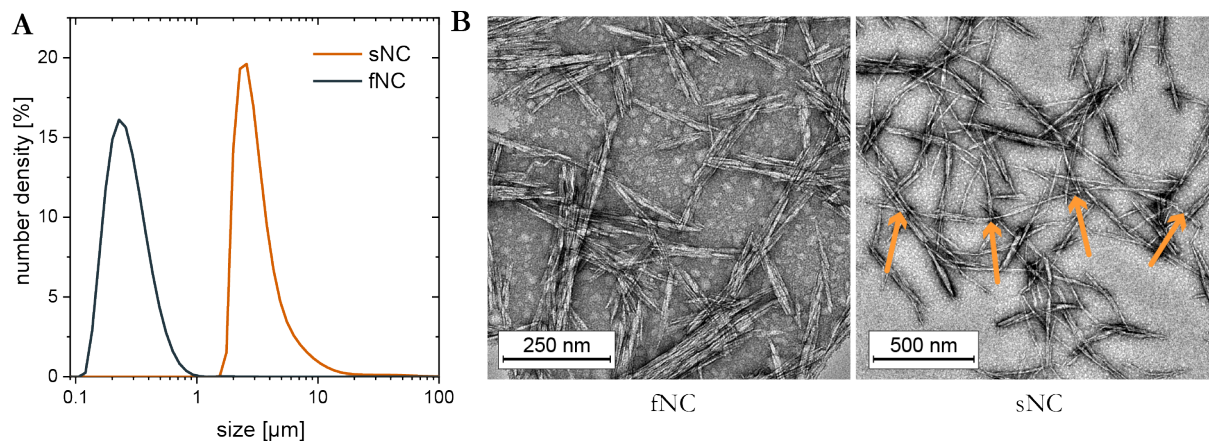
Figure 4.1: (A) Size distribution as measured with SLS and (B) TEM micrographs of CNCs obtained from pre-fibrillated cellulose (fNC) and short-fiber cellulose (sNC). Orange arrows indicate a fibril observed only in the sNC samples, explaining the larger size observed via SLS.

sNCs were mixed with the additive, i.e. glucose (glu), dbi acetate (bi) or dthfi acetate (thfi) in a constant weight ratio of 4:1 (CNC:additive). The corresponding films are denoted with sNC:(additive abbreviation). sNC:glu is semi-transparent and more flexible than a comparable pure sNC film, as judged by bending by hand. Flexibility of all produced films is demonstrated in Figure 4.3 and ensures that they can be handled and applied for membrane-purposes without too much care. SEM images of the cross section show a layered structure (see Figure 4.2 A) which has built up through the horizontally

63

settling particles. The film exhibits some inhomogeneities and a rough surface caused by the polydispersity of the CNCs. Those aspects might hamper the reproducibility of the film's properties.

Upon mixing of CNC dispersion and IL, the formation of small, jelly domains is observed when the dispersion is cast, indicating local agglomeration of the colloidal particles. This is due to the increase of ionic strength of the solvent through the addition of the ionic liquid, in combination with the electrostatic stabilization mechanism of the CNCs. The increase of ionic strength decreases the screening length of the electric charge on the CNC particles and facilitates their approaching to lengths at which inter-particle attractions dominate and the particles agglomerate (reversibly). Uncontrolled particle agglomeration like this might partially prevent particles from a gravity-driven horizontal settling onto the surface, causing inhomogeneities, which are observed in the SEM images. Although sNC:IL films both still exhibit a layered structure, (see Figure 4.2 A), evidence of agglomerates are visible: In contrast to sNC:glu, some areas exhibit local curvature around what appears to be conglomerates, giving the whole cross section a heterogeneous appearance. Heterogeneities might lead to irreproducible material properties.
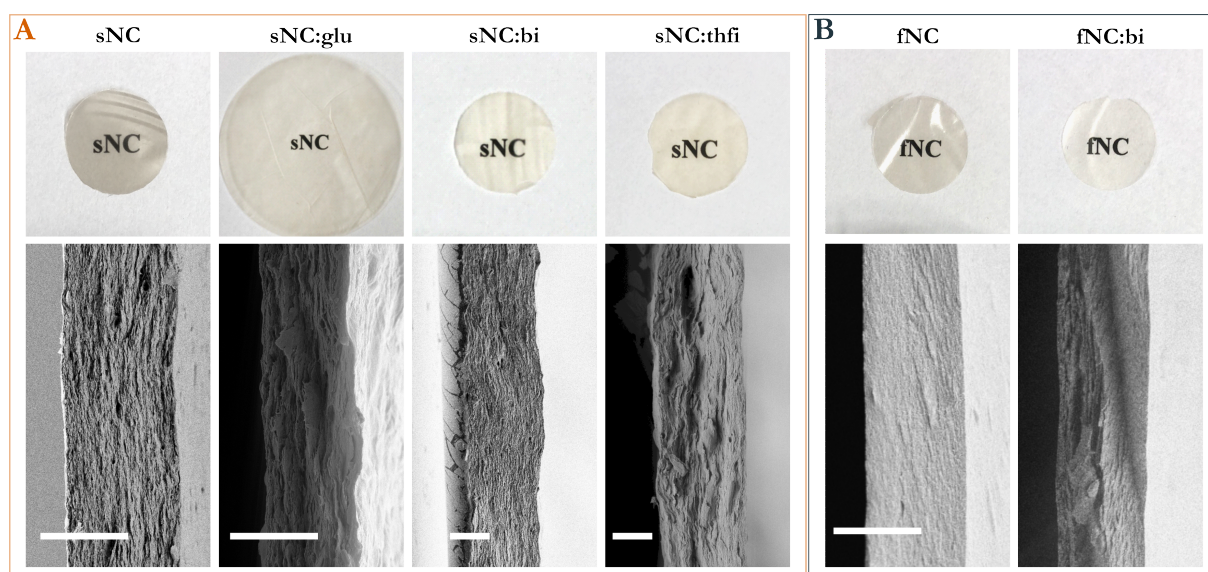
Figure 4.2: Photographs (top row) and SEM cross section micrographs (bottom row) of (A) the sNC-based and (B) fNC-based films. Scale bar = 10 µm. Adapted from[183].

To improve the homogeneity of the CNC film, fNCs were applied next. fNCs, extracted from mechanically pre-fibrillated never-dried pulp, gave a more narrow size distribution and smaller average sizes ($D_x(50)$=246 nm vs. 2.85 µm) in SLS (see Figure 4.1 A), note the logarithmic scale). Their average aspect ratio of 9, determined by TEM image evaluation, is significantly lower than for sNC (21), and no residual fibers were observed in TEM images, reflected in their higher CrI (85 % vs. 79 %, determined by XRD). Moreover, the increased surface charge of fNC (+41 mV) compared to sNC (+35 mV) was hoped to decrease the particles' sensitivity to a change in the ionic strength of the

solvent and minimize the observed uncontrolled agglomeration. These aspects should contribute to a higher brittleness but also a more homogeneous film. The film cast from a pure fNC dispersion appears more homogeneous in the cross section and has a much smoother surface than the sNC film (Figure 4.2 B, left), as reflected in its shininess. The higher transparency demonstrates smaller particle sizes compared to sNC. As expected, the short crystals and absence of entangling fibers result in increased brittleness and proneness to cracking. Agglomeration, however, is not fully prevented in the fNC:IL casting mixture by the increased particle charge: Slight gelling is still observed. A self-standing fNC:thfi film correspondent to sNC:thfi could not be obtained: the cast mixture remained wet and sticky after solvent evaporation. This might be due to the lower content of amorphous cellulose which makes up the part of the cellulose that is easily swollen or locally dissolved by IL. This leaves the IL freely surrounding the CNCs instead of being incorporated into the amorphous cellulose domains. The addition of dbi acetate, on the other hand, produces a film that is self-standing and has an increased flexibility, which makes the film easily manageable without breaking it (compare Figure 4.3). The cross section of fNC:bi (Figure 4.2 B, right) appears more homogeneous than the corresponding sNC:bi film, showing no wavy structures or agglomerates. Although agglomeration was observed upon mixing IL and fNC dispersion, the agglomeration of the smaller particles
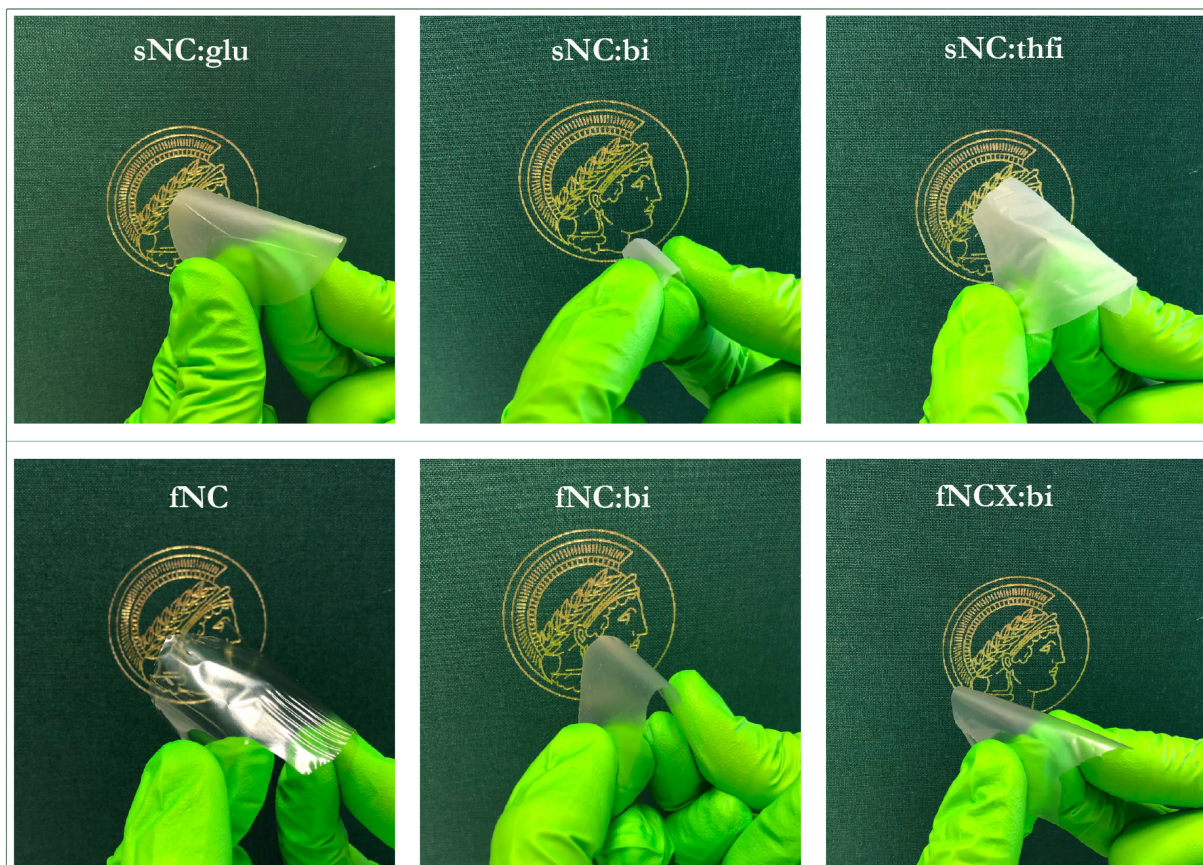

Figure 4.3: Produced CNC-based films can be bent, indicating their flexibility. Adapted from [183].

does not seem to increase disorder as much as the agglomeration of the bigger fibers from sNC, so that the overall film structure is barely disturbed. The film is therefore more densely packed, indicated by a significantly lower film thickness of approximately 10 µm compared to sNC:bi with a thickness of about 20 µm at the same mass-per-area density.

Films cast from fNC dispersions tend to crack during drying. Tensions arise in the drying film due to shrinking and cannot be dispersed in the rigid, highly crystalline material. The applied amount of IL visibly reduces the cracking tendency but does not eliminate it completely. The ratio of IL:CNC to obtain a self-standing film is limited, owing to the liquid state of the additive at RT: At higher ratios, the mixture will rather become a gel upon solvent evaporation, as observed for fNC:thfi, so that more IL cannot be applied to further reduce cracking tendency. In a different attempt to inhibit cracking, the amorphous polymer xylan, the main component of hemicellulose, was added to the casting mixture. Its natural function is to embed cellulose fibrils in the plant cell wall, which is why good interactions between CNC and xylan are naturally given. The amorphous xylan was hoped to not only disperse tensions but also act as an anti-agglomeration agent through sterical stabilization of the CNCs. The addition of 20 wt.% xylan (relative to CNC content) to the fNC:bi mixture notably decreases agglomeration visible to the eye and, as shown in Figure 4.4, effectively prevents cracking of the film.
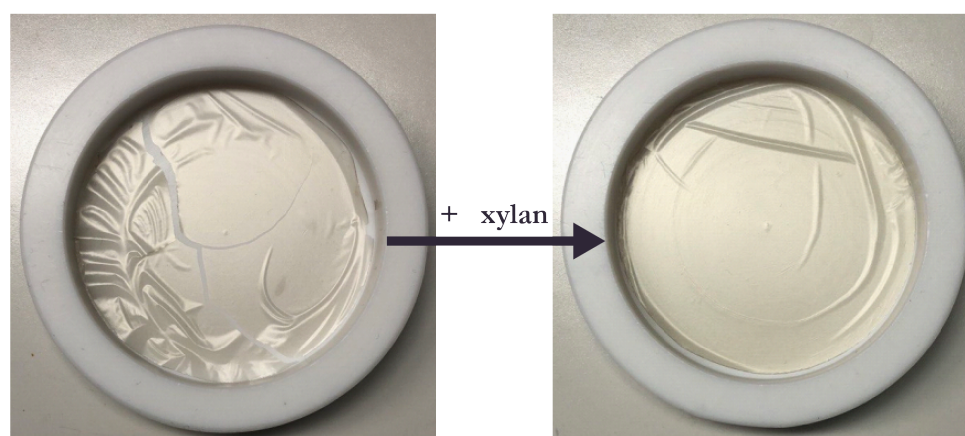
Figure 4.4: Comparison between fNC:bi membrane without (left) and with (right) addition of xylan. Adapted from [183].

4.1.2   Preparation of chitosan films

Chitosan, being a soluble polymer, forms smooth and flexible films even without additives. Entangled amorphous polymer chains ensure mechanical integrity. The cross sections of the films CS, CS:glu, CS:bi, and CS:thfi, shown in Figure 4.5, reveal a morphology dependent on the used additives. While the pure CS film exhibits a compact structure with some irregular voids (perhaps air inclusions), the addition of glucose leads to a spongy structure, possibly caused by local de-mixing due to incompatibility of additive

and matrix. IL-containing membranes exhibit a compact and homogeneous structure comparable to the pure chitosan film, indicating good compatibility between the ILs and chitosan. The films do not appear to have percolating pores so that they are applicable in gas permeation experiments.
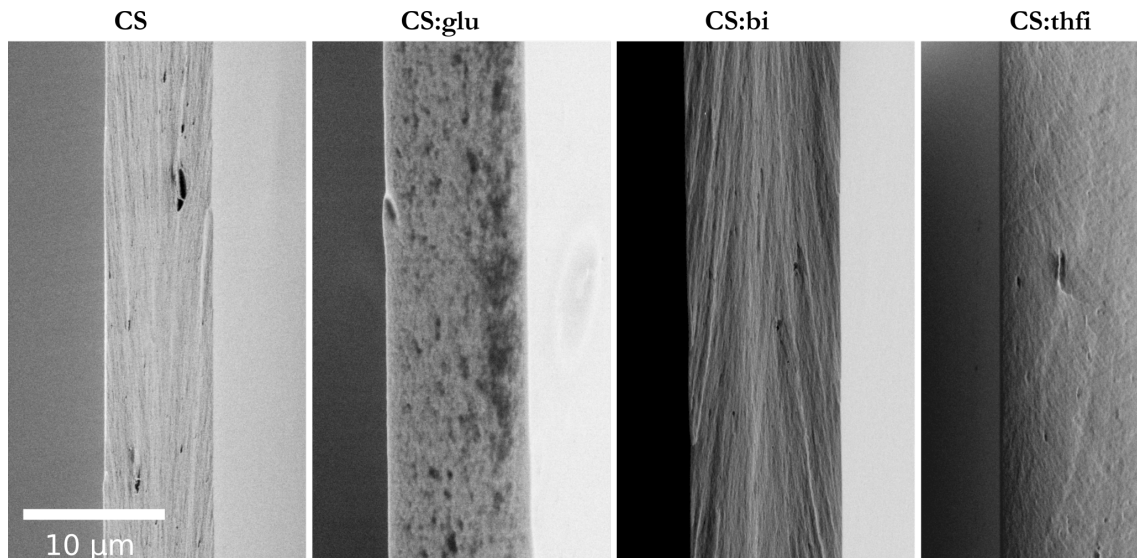
Figure 4.5: SEM micrographs of the chitosan based membranes: pure chitosan (CS), chitosan with added glucose (CS:glu), dibutylimidazolium acetate (CS:bi) and ditetrahydrofurfuryl-imidazolium acetate (CS:thfi). Adapted from [183].

4.1.3   Membrane Characterization

All successfully produced films were subjected to permeation measurements of the gases He, H_2, O_2, N_2, CO_2 and CH_4 in a time lag apparatus. Gas transport through nonporous membranes follows the solution-diffusion model. [184] According to this mechanism, gases are separated due to their different affinities to, or solubilities in, the membrane material, and molecular properties that influence their diffusivity. Table 4.2 lists gas properties relevant for gas permeation, namely molecular weight M, kinetic diameter, and critical temperature T_c, of the investigated gases.

Table 4.2: Molecular weight M, kinetic diameter d and critical temperature T_c of the tested gases.

gas	He	H_2	O_2	N_2	CH_4	CO_2
M [u]	4	2	32	28	16	44
d [Å] [95]	2.60	2.89	3.46	3.64	3.80	3.30
T_c [K] [185]	5.2	32.9	154.4	126.1	190.6 [186]	304.2

The following sections describe the gas permeation behavior by referring to permeabilities P, diffusion coefficients D and solution coefficients S of gases in the given membranes. Note that the used time lag apparatus determines only P and D, while S is calculated

from the two values as described in Chapter 8.4.4. Therefore, S does not represent an independent value and is just presented for visualization of the relations. The selectivity $\alpha_{A/B}$ of gas A over gas B is given here as a theoretical value calculated by relating the permeabilities of the pure gases (see Chapter 8.4.4), not from actual mixtures.

4.1.3.1 CNC-based membranes

Films with the matrix material sNC were produced using the three additives glucose, dbi acetate, and dthfi acetate. Gas permeabilities of the resulting membranes are shown in Figure 4.6 A. Numerical values for all permeabilities depicted in this chapter are given in Table 8.6.
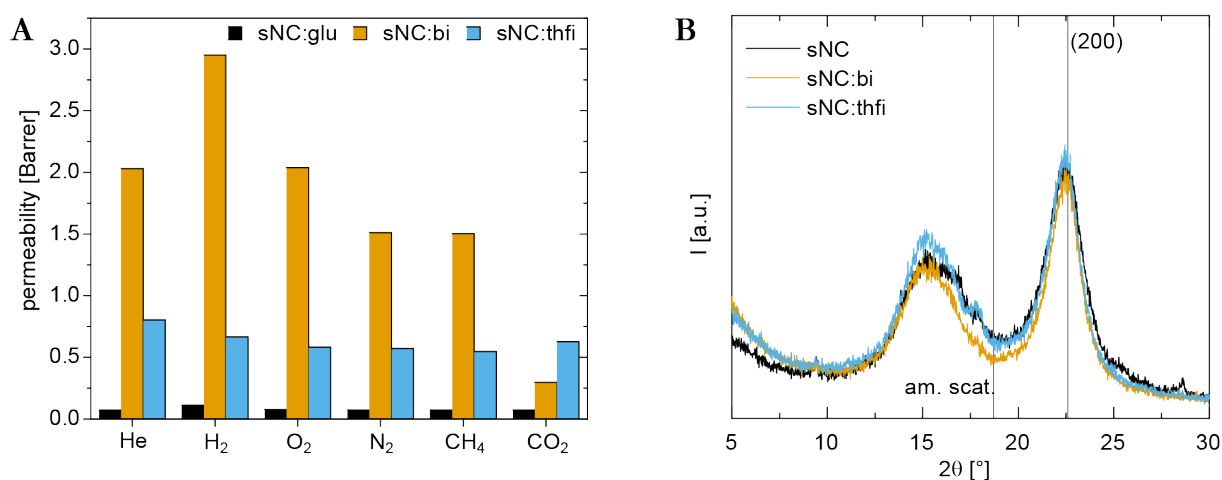
Figure 4.6: (A) Permeabilities of the sNC-based membranes with the additives glucose (glu), dbi acetate (bi) and dthfi acetate (thfi) (c.f. Table S1 for numerical permeabilities). (B) Diffractograms of sNC-based films. Positions of the (200) plane and the amorphous scattering reference point that can be used to calculated the crystallinity index are indicated. Adapted from [183].

sNC:glu exhibits a low permeability of 0.1 Barrer without any observable selectivity towards the tested gases. This value is several times lower than the values achieved with the most common biodegradable plastics polylactide (0.26 Barrer) or poly(γ-butyrolactone) (0.77 Barrer) and it is comparable to the permeability of PET (0.09 Barrer), which is a common commercial packaging material.[187] It attests to good barrier properties of the new type of cationic CNC, as expected due to their high crystallinity and little free transient volume in the film, restricting gas mobility.[188][96] The low permeability is in line with values reported by Chowdhury et al. for disordered pure CNC films, who measured permeabilities around 0.2 Barrer for O_2 and 0.1 Barrer for CO_2.[189] Glucose does not increase the permeability of the CNC film compared to the literature values, which is in agreement with the observations of Fernandez-Santos et al. for sugar alcohols in CNC films.[94]

To test the CNCs potential as matrix material in an SILM, membranes sNC:bi and sNC:thfi were investigated. The possible effects of the IL additives are twofold: ILs

were shown to plasticize synthetic polymers[190] as well as natural polysaccharides[191] by reducing their crystallinity, thereby increasing the permeability of the host material. Moreover, they can provide gas-specific interaction sites. Such sites can be amines or carbenes, which are present in imidazolium-based ionic liquids.[192] Specific interaction sites increase the affinity of the material towards target gases and can thereby introduce gas selectivity into the composite by increasing gas solubility. Facilitated transport can even break the Robeson upper bound,[98] increasing both permeability and selectivity.

The use of both ILs as membrane additives increases the permeability of the films by one order of magnitude compared to sNC:glu (Figure 4.6 A). Although significant, this increase is not as high as expected. A possible reason for this is revealed in a comparative EDX analysis of the film surface and the cross section: The nitrogen content on the surface is almost three times as low (3.95 wt.%) as the one measured in the cross section (10.95 wt.%), indicating a retraction of the IL into the bulk. This might be caused by drying in air, which is non-polar and renders the interface unattractive for the highly polar IL, causing its depletion. As a consequence, the surface permeability is lower than the bulk permeability, resulting in overall lower values. Different drying conditions, for instance a higher humiditiy, might help overcome this issue but have not been tested in the scope of this thesis.

Table 4.3: Weight percentage of carbon (C), nitrogen (N) and oxygen (O) measured on the surface and the cross section of the membranes fNC:bi and sNC:bi, determined with EDX.

		C [wt.%]	N [wt.%]	O [wt.%]
sNC:bi	surface	72.41	3.92	23.67
	cross section	50.15	10.95	38.9
fNC:bi	surface	51.25	2.91	45.84
	cross section	84.58	5.74	9.68

In contrast to sNC:glu that showed almost no differences in the permeabilities of the individual gases, i.e. no particular selectivity, IL addition creates a more diverse behavior. Permeabilities of individual gases increase to different extents: H_2 shows the highest, CO_2 the lowest permeability. The differences in permeability imply that selectivities in specific gas pairs increase. Ideal selectivities (calculated from the permeabilities of the individual gases, not measured for the real gas mixture) of relevant gas pairs are shown in Table 4.4. The chosen gas pairs reflect industry-relevant gas separation applications.

The permeability increase in sNC:thfi is less pronounced than in sNC:bi, implying a weaker plasticizing effect of dthfi acetate compared to dbi acetate. The reason might lie in the lower viscosity of dbi acetate: The cellulose-solubilizing capabilities of ILs were found to

Table 4.4: Comparison of the selectivities α of sNC:glu membrane with the sNC-based membranes containing ILs for different gas pairs.

gas pair	sNC:glu	sNC:thfi	sNC:bi
CO_2 /CH_4	0.9	1.0	0.2
He/N_2	1.0	1.3	1.3
H_2/CH_4	1.1	1.6	2.0
O_2/N_2	1.0	1.1	1.4

increase with decreasing viscosities. [193] Another reason might simply be generally higher gas mobility or solubility in dbi acetate.

To investigate the plasticization mechanism of the ILs in the CNC matrix, the films were analyzed with XRD. The diffractograms, shown in Figure 4.6 B, show no significant change of crystallinity in the IL-doped films compared to the pure film. This proves that no crystalline domains of the CNCs are dissolved so that the used ILs can be considered nonsolvent or secondary plasticizers for cellulose. As such, they only plasticize or interact with amorphous regions already present in the material and lower the glass transition temperature. Due to the low amorphous ratio, no glass transition was observed in the CNC samples in DSC experiments so that this is not proven, but only hypothesized here.

CO_2 displays a rather peculiar behavior in the IL-containing films. Due to its high critical temperature of 304.2 K, the highest among the measured gases, its solubility in polymeric materials is generally high: The solubility of a gas in a medium correlates with its critical temperature. [194] The inclusion of imidazolium-based IL was expected to have an additional positive influence on CO_2 solubility, which was expected to result in a high permeability. However, the measured CO_2 permeability in sNC:thfi is in the low range of O_2 and N_2 or, in the case of sNC:bi, even significantly lower (see Figure 4.6 A). To analyze the origin of this permeation behavior, the separate contributions of diffusion and solubility coefficient are considered. Figure 4.7 shows those values for the tested gases in both membranes. Despite its higher molecular weight, the diffusion coefficient of CO_2 is significantly higher in sNC:bi than those of the other gases. According to Graham's law, the diffusion rate of a gas is inversely proportional to the square root of the gas's molecular weight. [95] This implies facilitated transport of CO_2 caused by strong attractive interactions or even reactions between membrane and gas. In contrast, a low solubility for CO_2 is calculated. Apparently, the gas can pass the membrane at a high rate but quickly saturates the membrane. In sNC:thfi, this behavior is not observed.

As described above, the use of the lower aspect ratio fNCs yielded more ordered and densely packed films. A dense packing as well as the lower amorphous content should be reflected in lower gas permeabilities. Indeed, fNC:bi exhibits lower permeabilities than
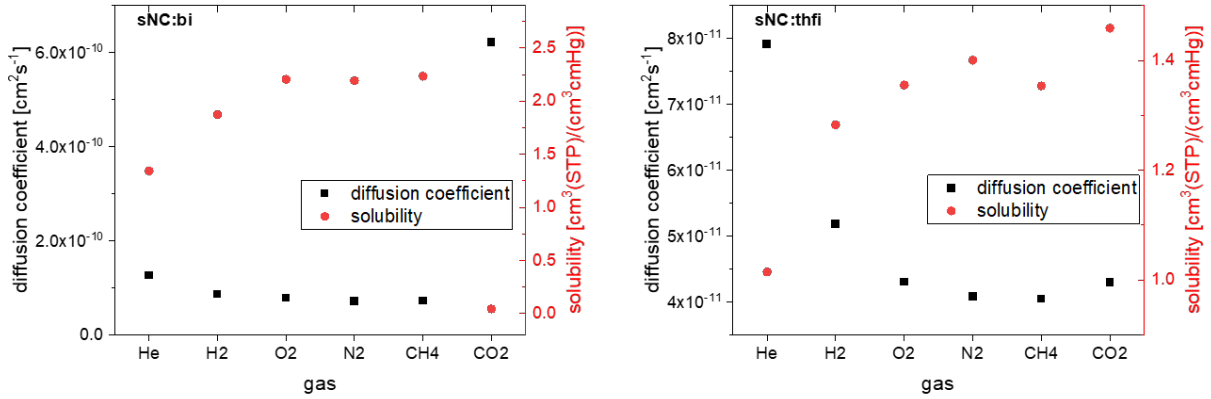
Figure 4.7: Diffusion coefficients and solubilities of selected gases in membranes sNC:bi and sNC:thfi. Adapted from [183].

the corresponding sNC:bi. Addition of xylan (fNC:X:bi) has no drastic effect on the permeabilities. Increases in the permeability towards oxygen and nitrogen are observed, changing the selectivities in their favor. The low CO_2 permeability seen in sNC:bi is not observed for either fNC:bi or fNC:X:bi, contradicting the attribution of the described effect to dbi acetate. Clarification of this phenomenon requires more experiments, which were beyond the scope of this work, owing to the long measurement time.

Another peculiarity is observed when comparing the fNC:bi membranes to sNC:bi: the selectivity towards the gas pair O_2/N_2. Following the solution-diffusion mechanism, the properties of molecular oxygen and nitrogen should allow O_2 a faster permeation through polymeric membranes than N_2 due to the higher critical temperature and smaller kinetic diameter of O_2 [195] (compare Table 4.2). fNC:bi, however, has an O_2/N_2 selectivity of around 0.9, whereas it was 1.4 in sNC:bi. This selectivity was reproducible over three measured membranes, as shown in Table 4.5, and can therefore not be considered a measurement error or deviation. The trend also remains consistent in the xylan-containing films fNC:X:bi. This inversed behavior in the fNC membranes compared to sNC membranes implies a different interaction mechanism.

An O_2/N_2 selectivity below 1 usually indicates a pore flow-dominated gas transport, or more specifically Knudsen diffusion. This is because the Knudsen diffusion coefficient

Table 4.5: Ideal selectivities α for selected gas pairs in the fNC:bi-type membranes compared to sNC:glu. The number represents different samples of the same composition.

gas pair	sNC:glu	fNC:bi 1	fNC:bi 2	fNC:bi 3	fNC:X:bi 1	fNC:X:bi 2
CO_2/CH_4	0.9	0.7	0.5	0.4	1.0	1.1
He/N_2	1.0	1.7	2.1	1.3	1.0	1.0
H_2/CH_4	1.1	1.9	2.3	1.0	1.1	0.8
O_2/N_2	1.0	0.9	0.9	0.9	0.9	0.8

correlates with the gas molecule's mean free path length and is proportional to $M_w^{-1/2}$: The smaller M_w of N_2 compared to O_2 therefore causes a slightly higher permeability, when gas is transported through pores. Ismail et al., for instance, calculated α_{O_2/N_2} of 0.93 for porous membranes[95], Pinnau et al. 0.91 for defective membranes.[196] Pore flow, however, requires the presence of percolating pores, which were not visible in the SEM images. Moreover, pores would also lead to higher permeabilities for the lower M_w gases, such as He, H_2, and CH_4, compared to the heavier gases. However, the permeability of the significantly lighter H_2 only lies in the same range as nitrogen. In the membrane fNC:X:bi, which shows the same inversed O_2/N_2 selectivity, H_2 even has the lowest permeability, which strongly contradicts the hypothesized pore flow.
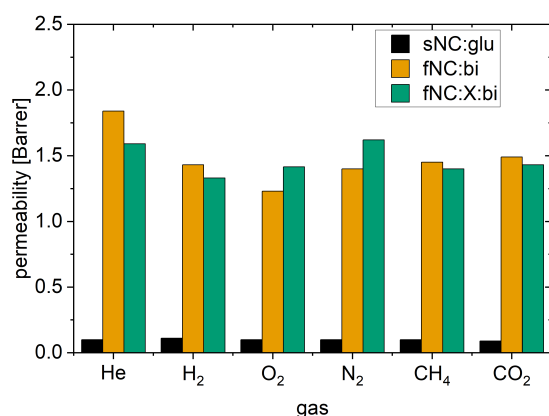
Figure 4.8: Permeabilities of the fNC-based membranes with the additives dbi acetate (bi) and xylan (X) compared to the sNC:glu membrane (c.f. Table 6 for numerical permeabilities). Adapted from[183].

Figure 4.9 displays diffusion and solubility coefficients separately, exemplary for fNC:bi-3 and for fNC:X:bi-1. In fNC:bi, the diffusivity of O_2 is slightly higher than that of N_2. The higher permeability, which is the product of diffusion coefficient and solubility, according to Equation 8.8 (see Chapter 8.4.4), must therefore arise from a higher solubility, as reflected in the Figure 4.9. Membrane fNC:X:bi, exhibits both a higher diffusion coefficient and a higher solubility for N_2.

Figure 4.9: Diffusion coefficients and solubilities of selected gases in membranes fNC:bi and fNC:X:bi. Adapted from[183].

4.1.3.2 Chitosan-based membranes

The influence of IL addition on the gas transport behavior was observed in chitosan membranes, to understand the origin of the peculiar gas permeation behavior observed in CNC-based membranes. As demonstrated by XRD spectra of the dried CS films, chitosan forms highly amorphous membranes: Only broad amorphous scattering without sharp diffraction peaks (020) plane at 10° and the (110) plane at 20° was recorded for all films.
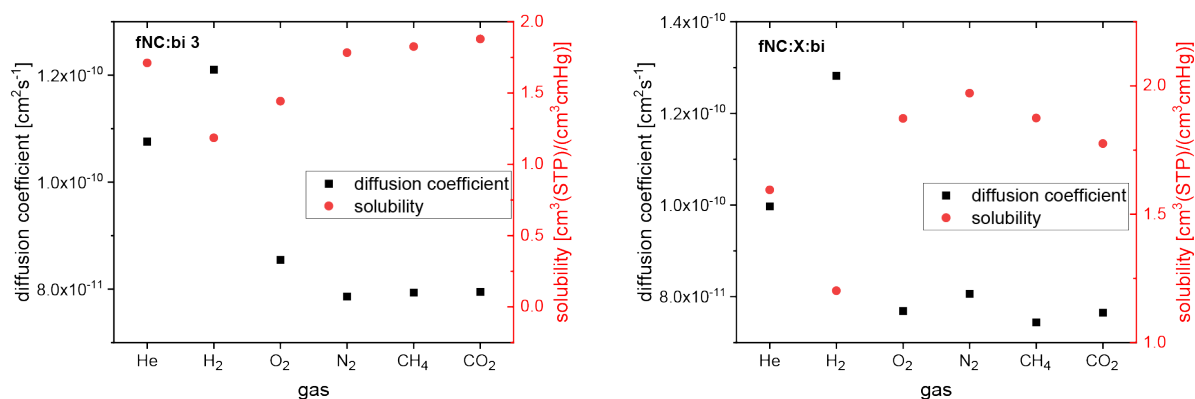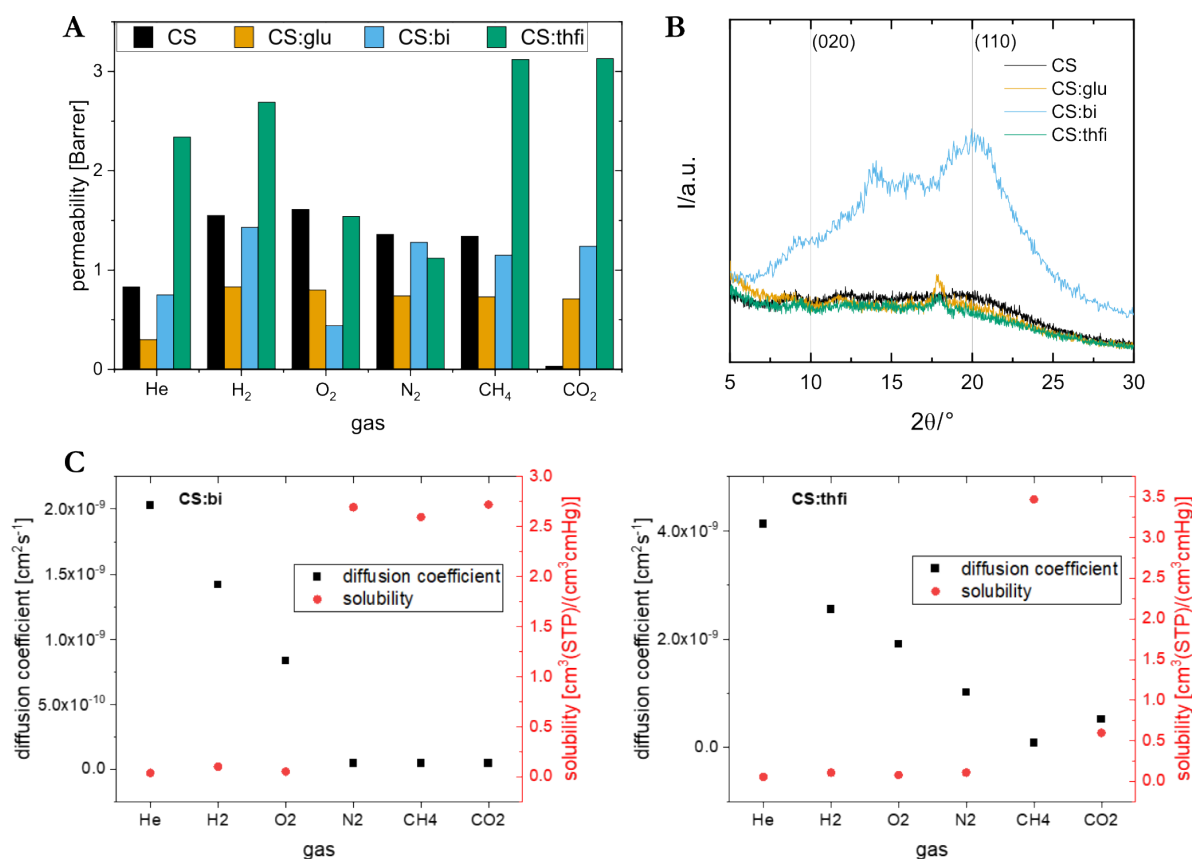

Figure 4.10: (A) Permeabilities of the chitosan based membranes CS, CS:bi and CS:thfi. (B) Diffractograms of the chitosan-based membranes show mostly amorphous scattering, indicating a low degree of crystallinity. (C) Diffusion coefficients and solubilities of selected gases in membranes CS:bi and sNC:thfi

The measured permeabilities are given in Figure 4.10 A. The values are expectedly low, as pure chitosan is known to have a low gas permeability.[182] The used additives do not generally increase permeability in CS membranes: In fact, glucose and dbi acetate decrease the permeability for most gases and cannot be considered efficient plasticizers for chitosan. An exception is CO_2, which has an extremely low permeability in pure CS, possibly due to its carbamate formation with amino groups that leads to saturation of the polymer.[197] Every additive increases the permeability of CO_2, which might be due to the inhibition of carbamate formation through interactions between the additive and the amino groups in the chitosan. With the exception of O_2 and N_2, dthfi acetate efficiently increases the gas permeability. As opposed to cellulose, chitosan is more efficiently plasticized by dthfi

acetate than by dbi acetate. Table 4.6 lists the calculated ideal selectivities of selected gas pairs for comparison.

Table 4.6: Comparison of the selectivities of CS:pure with the CS-based membranes containing ILs.

gas pair	CS	CS:bi	CS:thfi
CO_2 /CH_4	0.02	1.1	1.0
He/N_2	0.6	0.6	2.1
H_2/CH_4	1.2	1.2	0.9
O_2/N_2	1.2	0.3	1.4

CS:bi exhibits the same trend of inversed O_2/N_2 selectivity as in the fNC analogue. With a α_{O_2/N_2} of 0.3, the higher solubility for N_2 compared to O_2 (see Figure 4.10 C) is even more pronounced than in fNC:bi (α_{O_2/N_2}=0.9) and is not observed in CS:thfi or pure CS, supporting the attribution of this effect to dbi acetate. CS:thfi exhibits a selectively and significantly increased solubility of methane while other gases show very low solubilities. Instead, gas transport is accelerated mainly through higher diffusion rates in comparison to the other chitosan membranes, which proves the plasticizing effect of the IL.

4.2 Discussion

An unexpected gas permeation behavior of the gas pair N_2/O_2 was observed in the dbi acetate-containing membranes. For a closer investigation of the contributions of IL and matrix material to this behavior, the diffusion coefficient D and solubility S are depicted in relation to the molecular properties that normally determine their value in nonporous polymeric membranes: kinetic diameter d and critical temperature T_c. The data for the tested gases and membranes is plotted in Figure 4.11. D normally decreases with increasing d, while S increases with increasing T_c.

D and S in sNC-based membranes predominantly follow the expected relations to d and T_c, respectively. Gas transport in sNC membranes seems dominated by the normal transport behavior of the polymer matrix. IL addition leads to increased S for all gases except CO_2, while D is not increased.

CO_2 has a drastically decreased S and an increased D in sNC:bi. This specific behavior is not observed in the other dbi acetate-containing membranes and therefore, it does not seem to be an effect traceable to the IL. One other membrane, however, does exhibit a very low CO_2 permeability: The additive-free chitosan membrane (CS). While D_{CO_2} is in the lower range of the other gases with a higher d, S_{CO_2} is significantly lowered, as observed in sNC:bi. I attributed the low permeability to the amino groups in chitosan, which can immobilize CO_2 via carbamate formation and saturate the membrane. The gas
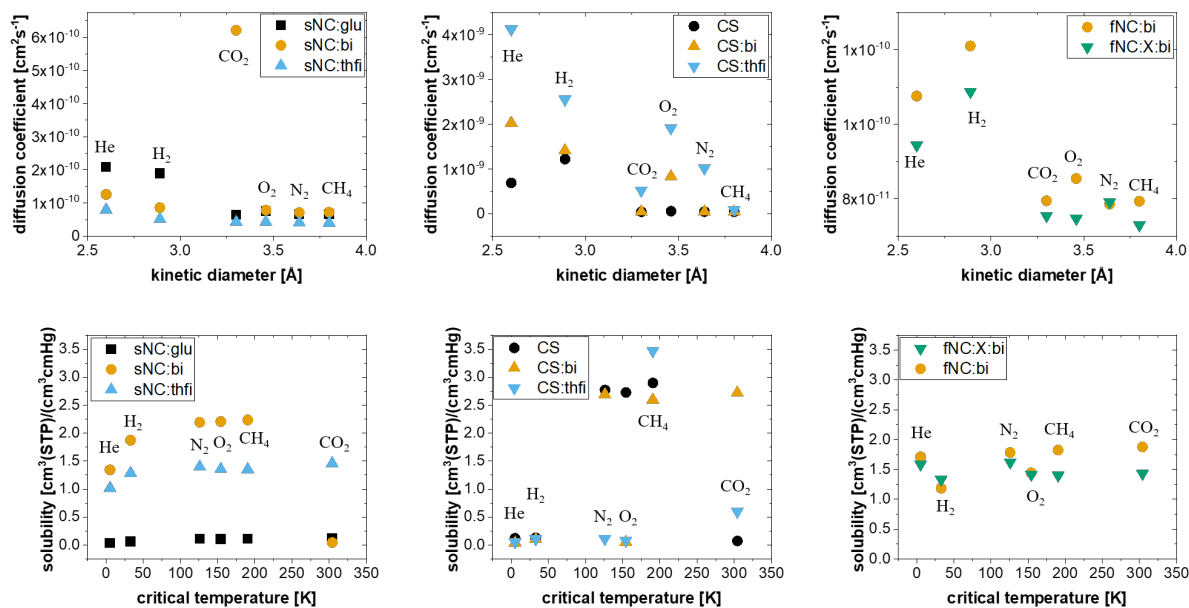
Figure 4.11: Diffusion coefficients in relation to the kinetic diameter and solubilities in relation to critical temperature of selected gases in membranes CS:bi and sNC:thfi. [183]

desorption step could be impeded by a high desorption energy barrier, leading to a low CO_2 permeability. The presence of amino groups in sNC could hypothetically have the same effect, but to a much lower extent due to the low degree of substitution of around 4 % so that such a drastic as observed here seems unlikely and could be a measurement error. The availability of only one data set does not allow definite conclusions. To exclude the possibility of a measurement error, a repetition of the experiment would be necessary to verify the reproducibility of the effect. Due to the long duration of one measurement, owing to the overall low permeabilities, this measurement could not be conducted in the scope of this thesis.

The unusual O_2/N_2 selectivity smaller than 1 was observed for dbi acetate-containing membranes only. Membranes CS:bi, fNC:bi and fNC:X:bi all exhibit an uncharacteristically high solubility for nitrogen. Other membranes exhibit $\alpha_{O_2/N_2} > 1$, as expected for nonporous polymer membranes. This gives rise to the assumption that the low O_2/N_2 selectivity is a trait of the IL rather than the polymer matrix. Interestingly, there is one exception in sNC:bi, which shows no particularly high N_2 solubility. This supports the aforementioned hypothesis that in sNC membranes, the influence of the matrix, sNC, on gas transport is bigger than that of the IL. The reason might be the higher amorphous ratio in sNC that causes a difference in the type of free transient volume available for gas transport compared to fNC membranes. With more amorphous and swellable cellulose present, more IL will be incorporated into the polymer as a plasticizer. An indication for this was observed in the preparation of the membranes, when fNC would not form a self-standing film with the same ratios of CNC:dthfi acetate as used for sNC:thfi. Hence, the plasticized amorphous cellulose domains dominate gas transport behavior, while IL is

mostly consumed for plasticization and is not available for active gas solubilization. The smaller amorphous ratio in fNC provides less plasticizable cellulose for IL and little free transient volume so that gas transport predominantly occurs through the free IL and not through amorphous cellulose. Another indication for this hypothesis can be seen in the different permeation behavior of CH_4 in the dthfi acetate-containing membranes. CS:thfi shows a significantly increased solubility for CH_4 compared to the other gases and membranes, which implies a good solubility of CH_4 in dthfi acetate. This is not reflected in sNC:thfi, where S_{CH_4} is in the same range as the other gases' solubilities.

4.3 Conclusions

The possibility to produce flexible self-standing films from the new type of cationic amine-functionalized CNCs extracted from two different sources in combination with different additives was demonstrated. For CNC-glucose membranes, excellent barrier properties were found, in accordance with previous studies on other types of small molecule-plasticized CNC films, owing to a high CrI. Along with their low degree of substitution and consequentially excellent biodegradability and -compatibility, this behavior makes the CNCs interesting for food-related packaging applications. Hydrophilicity and poor mechanical properties of films of this kind, however, make their application in packaging difficult. A possible solution to this problem is presented in Chapter 5. A particular gas selectivity due to amino groups on the CNCs could not be concluded, which affirms the novel CNCs as neutral support for additives such as selectivity-inducing ILs. CNC-IL composites display increased gas permeability with low selectivities. The effects of the applied ILs were studied by separate consideration of diffusion coefficient and solubility of the tested gases in the series of membranes based on sNC, fNC and chitosan.

Even though sNC and fNC consist of the same polymer, cellulose, a reproducible difference in their gas permeation behavior was observed: fNC:bi exhibited an unusual selectivity of the gas pair O_2/N_2 smaller than 1, which was not reflected in the sNC:bi analogue. The comparison to the chitosan-based membrane with equivalent composition allowed tracing of this behavior to the ionic liquid dbi acetate, which appears to have a high N_2 solubility. Whether the IL or the polymer matrix dominates gas transport seems to change depending on the used polymer, with the role of the IL switching from nonsolvent/secondary plasticizer in sNC to active gas transport agent in fNC membranes. It appears that in a matrix with a CrI as high as the CNC films, the gas permeation mechanism of the fabricated CNC-SILMs can be considered a function of the crystallinity of the applied CNCs. Even though no high permeabilities or selectivities were achieved at this first attempt at CNC-based gas separation SILMs, the results highlight the diversity and tunability of bio-derived functional materials. Moreover, the finding of a reversed O_2/N_2 selectivity

might open interesting possibilities in the application of dbi acetate in gas separation applications when used more efficiently.

The investigated SILMs are complex systems and definite conclusions are difficult to draw due to the limited amount of data. A deeper understanding of those systems requires further experiments to investigate gas solubility in the ILs as well as IL-CNC interactions. However, considering the low selectivities even at low permeabilities, the fabricated membranes are not very promising for application in gas separation so that further research effort might be better invested in developing systems with better performance, for instance, by increasing permeability. This could be done by increasing the ratio of amorphous polymer or the amount of IL. As IL content reached its limit already in the attempt to produce fNC:thfi, the former solution is more promising. To that end, the ratio of xylan could be increased or another soluble polymer can be tested.

CNCs as Pickering emulsifiers utilized for protective coatings

The previous chapter confirmed excellent barrier properties of cationic CNCs in line with several other literature reports. Barrier properties are interesting for food packaging applications, which require low permeabilities for gases, particularly oxygen. Packaging, however, requires not only gas tightness, but also resistance against water and humidity. As a stand-alone material, CNC films suffer from hydrophilicity so that they cannot be straightforwardly applied for packaging.

It was demonstrated in Chapter 3 that the REM-extracted cationic CNCs stabilize oil droplets in water. Their low charge is convenient for the application as Pickering stabilizer, as it prevents strong repulsion between the particles that would hinder their assembly at the interface. Another factor that presumably facilitates the adsorption of cationic CNCs is the negative net charge of oil droplets[198] which causes electrostatic attraction between interface and CNCs: The interface of triglycerides (natural vegetable oils) and water is known to bear a negative charge due to fatty acid impurities[198] or rearrangements of polar groups to the interface.[199] While unmodified CNCs obtained via HCl hydrolysis are also able to stabilize Pickering emulsions, they tend to agglomerate and do not form stable colloids. The necessity of individualizing them beforehand complicates their use. CNCs obtained from H_2SO_4 hydrolysis, on the other hand, can only be used for Pickering emulsions when their high charge is screened by salt.[111] Cationic CNCs developed in the present work are easily dispersible in water, and their charge is low enough that no screening of charge is necessary, ensuring a straightforward and more versatile application. As bio-based and biodegradable Pickering emulsifiers, they can therefore help the processibility of oils and waxes surfactant-free and sustainably. Natural oils and waxes can be and have been used for the hydrophobization of surfaces and pose sustainable alternatives to methods like silanizations or coatings with fluorinated synthetic polymers like

polyvinylidenefluoride. Especially drying oils like tung oil and linseed oil are convenient for hydrophobic coatings, as they are applicable as a liquid and harden upon spontaneous oxidative crosslinking of their high amount of polyunsaturated fatty acids. For instance, submicron coatings of linseed oil on alginate-based films, achieved by partially washing away the macroscopic coating with hexane, exhibited a 25 % lower water permeability than pure alginate films.[200]

In combination with the CNCs' excellent barrier properties, CNC-stabilized oil or wax emulsions could be a promising dual system to achieve gas tightness and hydrophobicity as a two-in-one coating. The coating can then be applied on paper, which is already established as a biodegradable and -compatible packaging material. To fulfill demands for food packaging, it is often necessary to coat it with a polymer that provides resistance towards water and grease and makes it impermeable for oxygen and water vapor. A competitive coating that is compatible with existing polymer coating procedures requires an all-in-one, easily applicable coating.

This chapter explores the possibility to apply cationic CNCs in a dual role as pore sealing agent and as Pickering stabilizer to stabilize linseed oil-in-water emulsions. The extension of the concept to wax particle dispersions is also demonstrated as an outlook for future opportunities. The results presented here are published in *RSC Advances*.[201]

5.1   Results and Discussion

CNC-rich and -stabilized emulsions of linseed oil are first produced at varying ratio of CNCs to oil and varying dry contents. The emulsions are then applied and dried on paper. The resulting coating is finally tested in terms of hydrophobicity and water vapor transmission.

5.1.1   CNC-stabilized linseed oil-in-water emulsions

CNC-stabilized emulsions of linseed oil in water are fabricated by mixing with a high-speed lab homogenizer. Successful emulsification is proven with optical microscopy. Droplets with diameters between 1 µm and 20 µm are observed. The emulsions are stable for at least 12 weeks. As Figure 5.1 shows, neither phase separation nor change of droplet size, indicating Ostwald ripening or coalescence, were observed within this period.

Linseed oil in water emulsions were produced with an oil content of 2 %. Two different CNC concentrations, $4 \mathrm{\ mg\ mL^{-1}}$ and $12 \mathrm{\ mg\ mL^{-1}}$ were tested, resulting in different CNC:oil mass ratios of 1:4.5, denoted CL1, and 1:1.5, denoted CL2. Compositions of all samples are listed in Table 5.1.
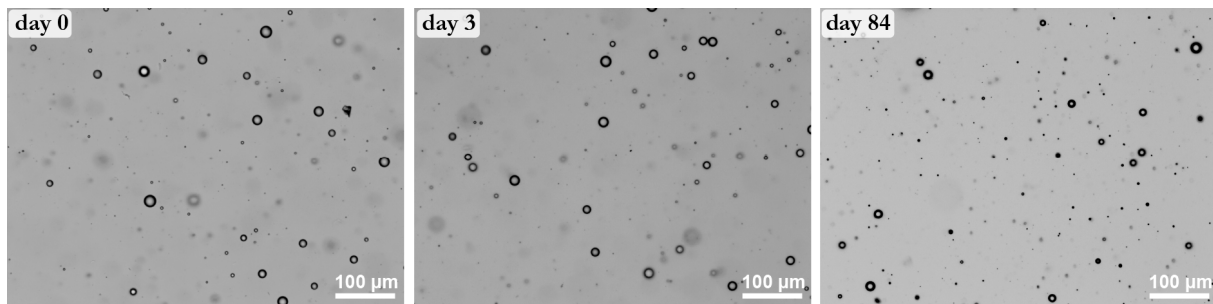
Figure 5.1: Optical micrographs of CLl-1 taken on day 0 (immediately after preparation), day 3, and day 84 (12 weeks)

Table 5.1: Compositions of the emulsion coatings fabricated.

	ρ(CNC) mg/mL	vol.% oil in emulsion [%]	dry mass CNC [%]	dry mass oil [%]
CL1	4	2	18	82
CL2	12	2	40	60
CL3	2.4	0.5	60	40
CL4	5	0.6	90	10

Both mixtures yield stable emulsions. Upon homogenization of CL2, however, air bubbles are included due to the high viscosity of the emulsion, which requires a degassing step or a homogenization method that introduces less air. CL2 is therefore degassed through a 15 min treatment with ultrasound.

Both coatings were tested on a filter paper (no. 619) by spreading 1 mL of it with a pipette (ca. 53 µL cm^{-2} or a solid mass of approximately 1.3 mg cm^{-2} (CL1) or 1.6 mg cm^{-2} (CL2, solid includes linseed oil). The coated paper was dried in the oven at 80 °C. A second sample was pressed in the hot press at 150 °C for 2 h to potentially facilitate cross-linking of the linseed oil and produce a flat surface. The linseed oil cross-links spontaneously within 1-2 weeks, which can be followed in FTIR by observing bands attributable to the double bond vibrations. Two bands indicative of the curing of linseed oil can be identified, marked with lines in the diagram: the *cis* ν(C-H) in C=C-H band at 3010 cm^{-1} and the -CH=CH- (possibly only *cis*) vibration at 1652 cm^{-1}. Their decrease marks the disappearance of double bonds through their oxidation or an isomerization from *cis* to *trans*. As the isomerization proceeds via the formation of a radical, followed by addition and elimination of hydrogen, it can be interrupted by the reaction with oxygen so that isomerization activity can be regarded as a measure of cross-linking activity.[202] The decrease of those bands indicates that linseed oil curing takes place as commonly known and expected. The comparison between FTIR spectra of the as-prepared and the hot-pressed sample shows that the applied heat in the hot press facilitates cross-linking, as the bands attributable to *cis* C=C double bonds become smaller. However, the high

temperature led to a discoloration that was not observed during room-temperature curing. Therefore, a lower temperature and shorter time (15 min at 60 °C) was chosen to produce a flat surface. Irradiation of the coatings with UV light does not affect cross-linking.
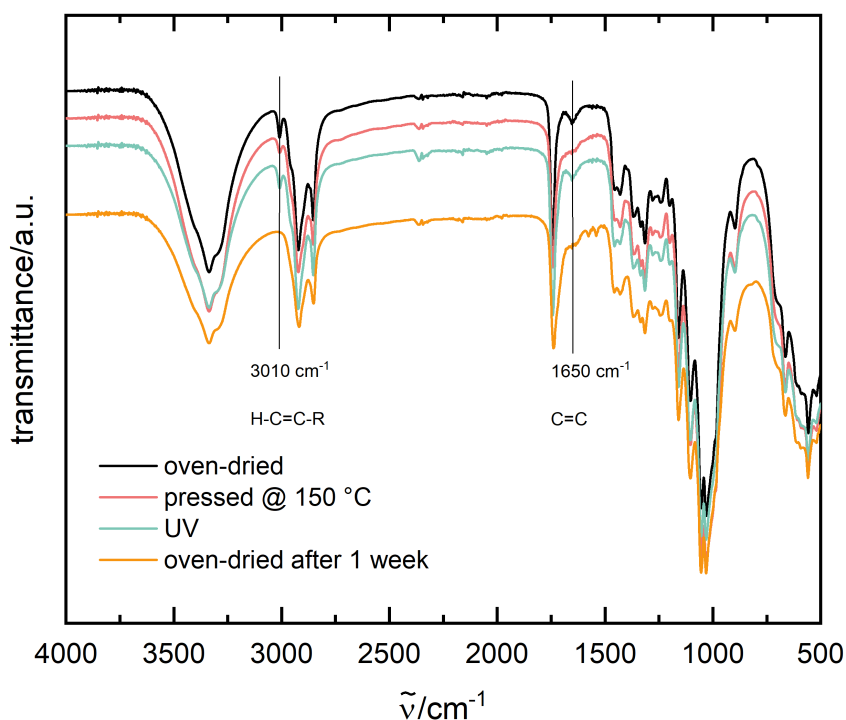

Figure 5.2: FTIR spectra of CL2 recorded immediately and after 1 weeks of curing time in air after drying in the oven, hot-pressing at 150 °C for 2 h and after keeping it under UV light for 6 h.

As visible in the SEM micrographs, both coatings result in good coverage of the paper without visible pores (see Figure 5.3). When pressed, an even and smooth surface is obtained (compare Figure 5.4 (A) and (B)). The resulting coatings are approximately 10 µm thick, as estimated from SEM images of the cross-sections.

For a simple preliminary water penetration test, a water droplet is placed on the coated paper. The droplet remains on the surface until it evaporates and is not absorbed by the paper, indicating successful hydrophobization and sealing of the pores. As a reference for the absorption behavior of normal paper and paper paint-coated with linseed oil, Figure 5.5 shows the quick absorption of a water droplet within less than a second in uncoated paper, which is only increased to an absorption time of 14 s in a paper coated with linseed oil, despite the high hydrophobicity of linseed oil. This demonstrates the importance of both sealing the pores and hydrophobization.

Hydrophobicity was quantified by measuring the water contact angle (θ_w) in a sessile drop experiment. θ_w of the paper coated with CL1 increases significantly to 99° compared to a paper coated with the same amount of only CNCs, which gives a θ_w of 60°. Hot pressing of CL1 results in a slightly lower θ_w of 94°. Perhaps, roughness that contributes to a high contact angle due to entrapping of air is smoothed by pressing.

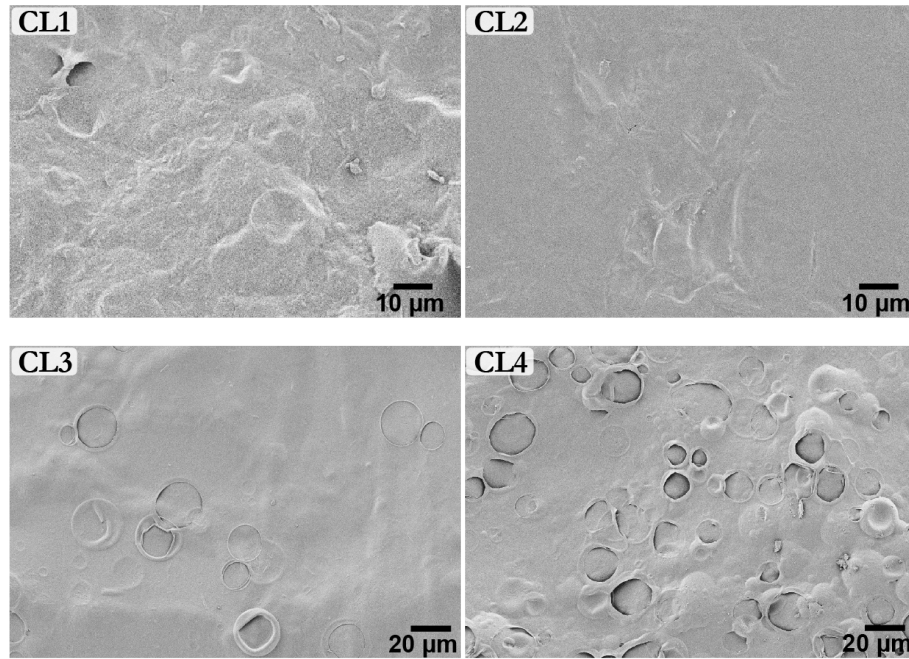**Figure 5.3:** SEM of the surfaces of paper coated with CL1-4.
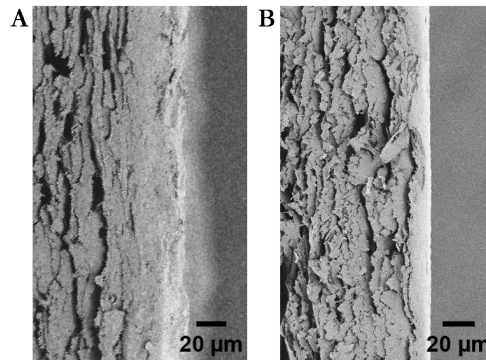

Figure 5.4: Cross-section of paper coated with CL1 as-prepared and after hot-pressing at 150 °C for 2 h.
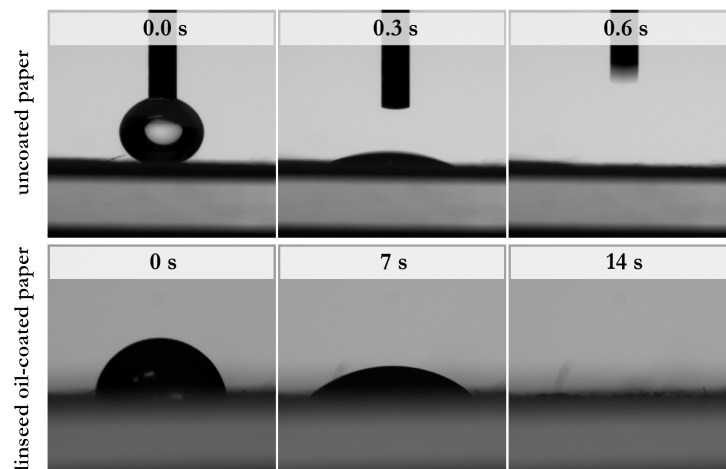

Figure 5.5: Uncoated filter paper absorbs the water droplet in less than a second; paper painted with linseed oil is more hydrophobic, but absorbs the droplet within 14 s as well, due to the presence of unsealed pores.

Table 5.2: Water contact angles θ_w for a pure CNC coating, CL1, and CL1 pressed at 150 °C with a pressure of 2 metric tons.

coating	water contact angle [°]	
CNC	60.71 ± 0.11	
CL1	99.30 ± 2.58	
CL1, hot-pressed	94.33 ± 0.57	

As the inclusion of oil in the coating might negatively affect gas barrier properties, the effect of CNC/oil ratio and the necessary mass coverage (solid mass/area) were further investigated in formulations containing a lower amount of oil, namely 40 % (CL3) and 10 % (CL4) of the dry mass. To have precise control over the final coating mass, the coatings were not filtrated through the paper, as this method entails an undefined loss of mass through the porous paper. Instead, a defined amount of the emulsion was cast on the paper and allowed to dry at room temperature. Coatings are cast onto a pre-wetted filter paper placed into a Petri dish of the same size. Pre-wetting ensures contact with the glass and a smooth surface, thereby improving the homogeneity of the coating. Due to low aspired mass coverages of $0.8~\mathrm{mg\,cm^{-2}}$, $1.6~\mathrm{mg\,cm^{-2}}$ and $2.4~\mathrm{mg\,cm^{-2}}$, more diluted emulsions (approximately 0.5 % oil in water) were required to homogeneously spread the coating over the entire surface of the paper. In realistic applications, a higher concentrated emulsion could be blade-cast or also spray-coated with professional coating equipment.

Table 5.3: Compositions of CL3 and CL4.

	contact angle	composition	area density
CL3	94 ± 2	60 % CNC, 40 % oil	$0.8~\mathrm{mg\,cm^{-2}}$
CL3	87 ± 2		$2.4~\mathrm{mg\,cm^{-2}}$
CL4	77 ± 4	90 % CNC, 10 % oil	$0.8~\mathrm{mg\,cm^{-2}}$
CL4	84 ± 12		$2.4~\mathrm{mg\,cm^{-2}}$

The wettability of the resulting coating was evaluated on the pressed papers by means of θ_w again. Compared to CL1, CL3 and CL-4 yield significantly lower contact angles. CL4, with the lowest dry mass ratio of oil of only 10 %, yields θ_w between 76° and 84°. This is still significantly increased compared to the pure CNC coating, but it does not classify CL4 as a hydrophobic coating. Moreover, the large deviation in θ_w between measurements indicates an inhomogeneous distribution of the oil. The higher content of 40 % oil in the dry coating, CL3, results in a hydrophobic θ_w up to 94°.

SEM images of CL3 and CL4 show bubbles on the surface of the coating much more distinctly than in the more concentrated coatings CL1 and CL2. CL2, with the highest solid content, did not show any such bubbles. Interestingly, the amount of open bubbles is drastically decreased for higher coverages (mass/area). The reason for the arising of open bubbles might lay in the thickness of the coating itself: The lowest coverage density of 0.8 mg cm^{-2} corresponds to film thicknesses of 5.1 µm for CL4 and 6.9 µm for CL3. This is lower than the diameter of the bigger droplets, which is up to 20 µm. Upon drying from the cast solution, the droplet, even if located close to the paper surface, will become exposed to the surface. As shown in Figure 5.6 A, this appears to cause the migration of interfacial agent CNC to the drying edge, due to the low interfacial tension between oil and air.
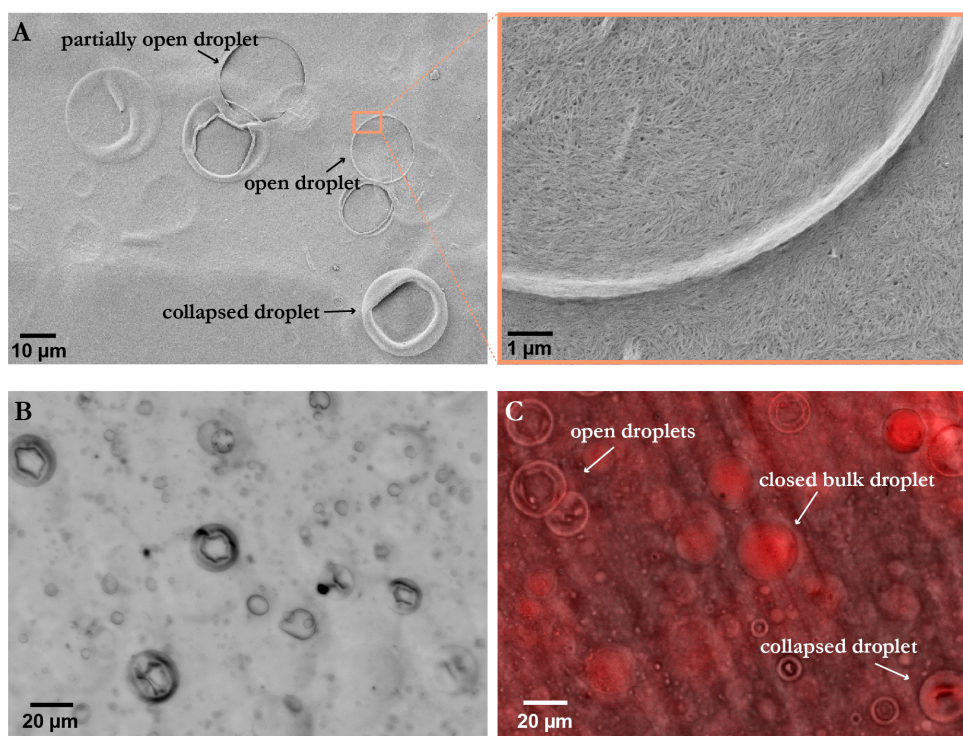
Figure 5.6: (A) SEM migrograph of the surface of a CL4-coated paper. (B) Optical micrograph of a freestanding film of CL3. (C) Confocal microscopy image of a freestanding film of CL3, fabricated with Nile red-stained linseed oil.

To investigate the distribution of the oil in the coating, a transparent self-standing film was dried from the emulsion on a Teflon tray at 80 °C. The optical microscopy image taken immediately after drying, shown in Figure 5.6 B, confirms the presence of collapsed surface droplets, indicating a quick depletion of oil unrelated to its curing, which only occurs later. To probe the location of the oil, the oil phase is stained with Nile red before emulsification so that it can be traced using confocal laser scanning microscopy (CLSM). Nile red is a lipophilic fluorescent dye with a fluorescence maximum around 585 nm in triglycerides. The CLSM image, Figure 5.6 C, shows fluorescence over the entire volume of the film. Oil droplets enclosed in the bulk exhibit increased fluorescence intensity,

indicating the enrichment of oil in an intact droplet. Open droplets are depleted of oil, showing no higher fluorescence intensity than the environment. Judging from the presence of fluorescence across the entire surface and volume of the film, surface droplets release their oil upon drying, which then spreads across the surface, resulting in the observed hydrophobicity. Lower oil contents, as in CL4, might not provide enough surface droplets for a full surface coverage to cause hydrophobicity, explaining the large deviations in θ_w for the thick coating.

SEM cross-sections, shown in Figure 5.7, reveal the presence of hollow, lentil-shaped pores arising from the oil droplets. These pores confirm the observation in the CLSM image that, as opposed to surface droplets, the droplets in the bulk remain intact during the drying process. The images also demonstrate that the coating forms a distinct film on top of the paper, instead of penetrating it and filling the pores formed by the randomly assembled cellulose fibers. Although this creates a smoother coating than one that would adapt to the surface morphology of the paper, thereby decreasing wettability and contact angle, it also entails low flexibility, leading to the ruptures visualized in Figure 5.7 B. Figure 5.7 C shows a paper coated with CL3 via vacuum filtration: Here, the coating is sucked more into the paper so that it adapts to the shape of the surface fibers and fills surface pores instead of covering them.
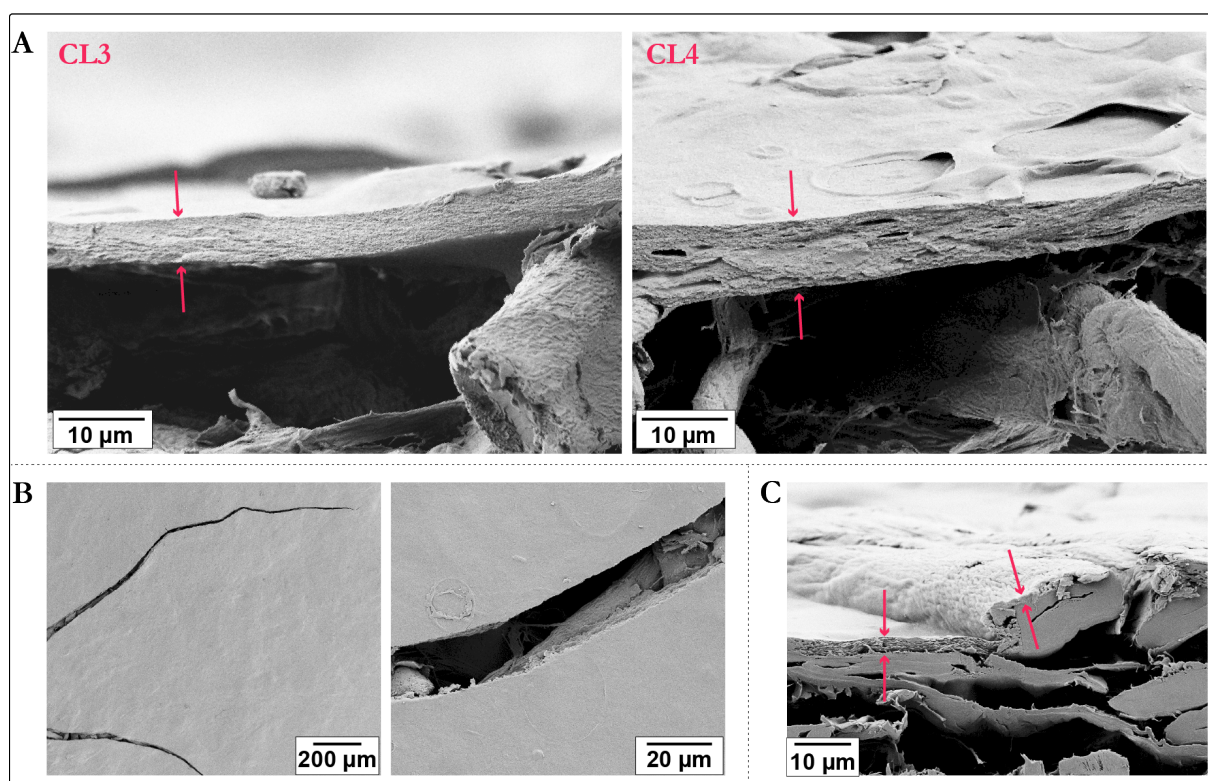

Figure 5.7: (A) Cross-sections of paper coated with CL3 and CL4, (B) cracks in coating with CL3 and (C) paper coated with CL3 via vacuum filtration. Surface coverage is $0.8\,\mathrm{mg\,cm^{-2}}$.

5.1.1.1 Water vapor transmission rate testing

The water vapor transmission rate (WVTR) is tested in WVTR cups in 85 % relative humidity at 20 °C. The water gain in a little chamber filled with desiccant through the coated paper is recorded gravimetrically over one week. The WVTR is determined as the slope of the water gain-time curve, once a linear gain is reached. CL3 and CL4 with different area densities are compared with a pure CNC coating with an areal mass of $0.8~\mathrm{mg\,cm^{-2}}$.

Figure 5.8 (left) shows the mass gains in the desiccant for the different coatings. The highest water uptakes of the desiccant are recorded for the pure CNC coating (0 % oil). As the amount of emulsified oil and the area density increase, the total water uptake decreases.

However, it becomes apparent that for low coating densities of $0.8~\mathrm{mg\,cm^{-2}}$, the cause for the decreased water uptake is not a slower WVTR, but a decreased initial uptake, before the system reaches the linear region. In fact, the WVTR of the 10 % (CL4) and 40 % oil (CL3) coatings with a density of $0.8~\mathrm{mg\,cm^{-2}}$ are higher than the pure CNC film, as visualized in Figure 5.8 (right). Only for higher coating thicknesses, the oil has a significant effect on the WVTR, which can be seen in the comparison between 10 % and 40 % oil at a higher area densitiy of $1.6~\mathrm{mg\,cm^{-2}}$. Here, the WVTR decreases from 121 g/m²/d to 89 g/m²/d. The trend persists for the thickest coating with a WVTR for CL3 of 106 g/m²/d versus 80 g/m²/d in CL4. This proves the reduction of WVTR of CNC films through the incorporation of linseed oil.
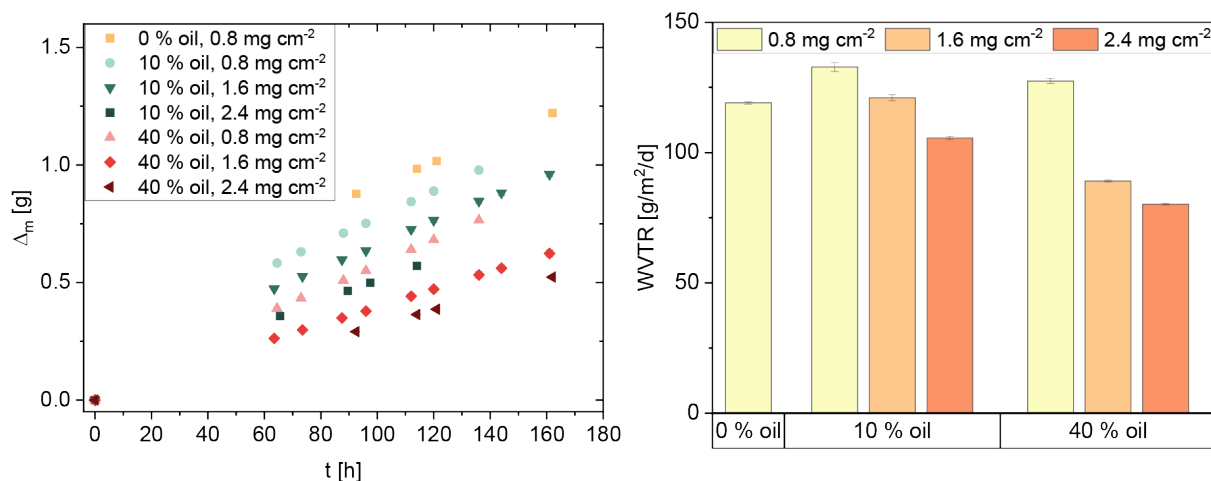
Figure 5.8: Water gain curves and water vapor transmission rates (WVTR) through a filter paper coated with CNC-based coatings with different oil contents and different area densities.

As expected, the lowest water uptake and WVTR are measured for the highest area density and oil content. This value, however, is still significantly higher than the values measured for instance for the common packaging material polypropylene, which has a WVTR of 2.5 g/m²/d.[90] It should be stressed that the paper used in this section is a filter

paper, which is not particularly dense to begin with. The use of smoothed and less porous packaging paper might improve WVTR values to get closer to values for commercial packaging products. Moreover, the inclusion of more oil could further improve water barrier properties. The coating could also easily be tuned by dissolving less hydrophilic compounds in the aqueous phase. To that end, other biopolymers, such as proteins, might also increase flexibility of the coating. Future experiments will evaluate the coatings in terms of their grease resistance and their gas permeability, since the included oil might change the oxygen barrier properties of the CNC film.

5.1.1.2   Rheology of the coatings

In actual application, emulsions can be more concentrated and applied using blade casting to yield a more homogeneous coating that does not require enormous amounts of water to be evaporated. Blade coating of films requires high viscosity between 1000-10000 mPa $\cdot$ s for a reliable film production[203] and benefits from shear-thinning properties, as the coating can be easily spread on the surface upon shearing but does not flow when deposited. The flow curves for the diluted and a more concentrated version of CL4 Figure 5.9 shows shear-thinning properties for both owing to the presence of CNCs in the continuous phase. While the diluted emulsion (5.2 $\mathrm{mg\,mL^{-1}}$ CNC, 0.6 $\mathrm{mg\,mL^{-1}}$ oil) has a low viscosity over the entire shear rate range, the concentrated sample (12.6 $\mathrm{mg\,mL^{-1}}$ CNC, 1.4 $\mathrm{mg\,mL^{-1}}$ oil) reaches a viscosity of 1000 Pa s at low shear rates to 1 Pa s at high shear rates, which is in the required range for blade coating, according to literature.
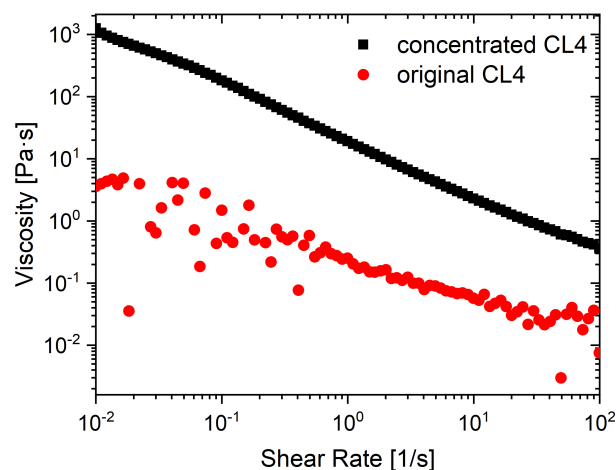
Figure 5.9: Flow curves of CL4 as used for the presented paper coating and as a concentrated version with the same ratio of CNC/oil.

5.1.2   CNC-stabilized wax particle dispersed in water

The feasibility of wax particle dispersion stabilized by cationic CNCs was tested for sunflower wax, beeswax (composed mostly of tricontanyl palmitate and cerotic acid), and paraffin (composed of C_{20}-C_{40} alkanes). Molten waxes are emulsified in a hot dispersion

of CNC (0.5 wt.% with respect to the emulsion) to yield a 20 wt.% wax-in-water emulsion when cooled down. The emulsions are white and opaque and have a low viscosity (not measured) so that they can be handled easily. Particles of beeswax and sunflower wax are between 1 µm and 40 µm in diameter. The size dispersity using paraffin wax is a little smaller with diameters between 1 µm and 30 µm. The particles are well dispersible at room temperature. Microscopic images recorded in normal brightfield mode and between cross-polarizers reveal that even upon increasing the temperature above the melting temperature of the wax, the droplets are stable against coalescence, as shown in Figure 5.10.
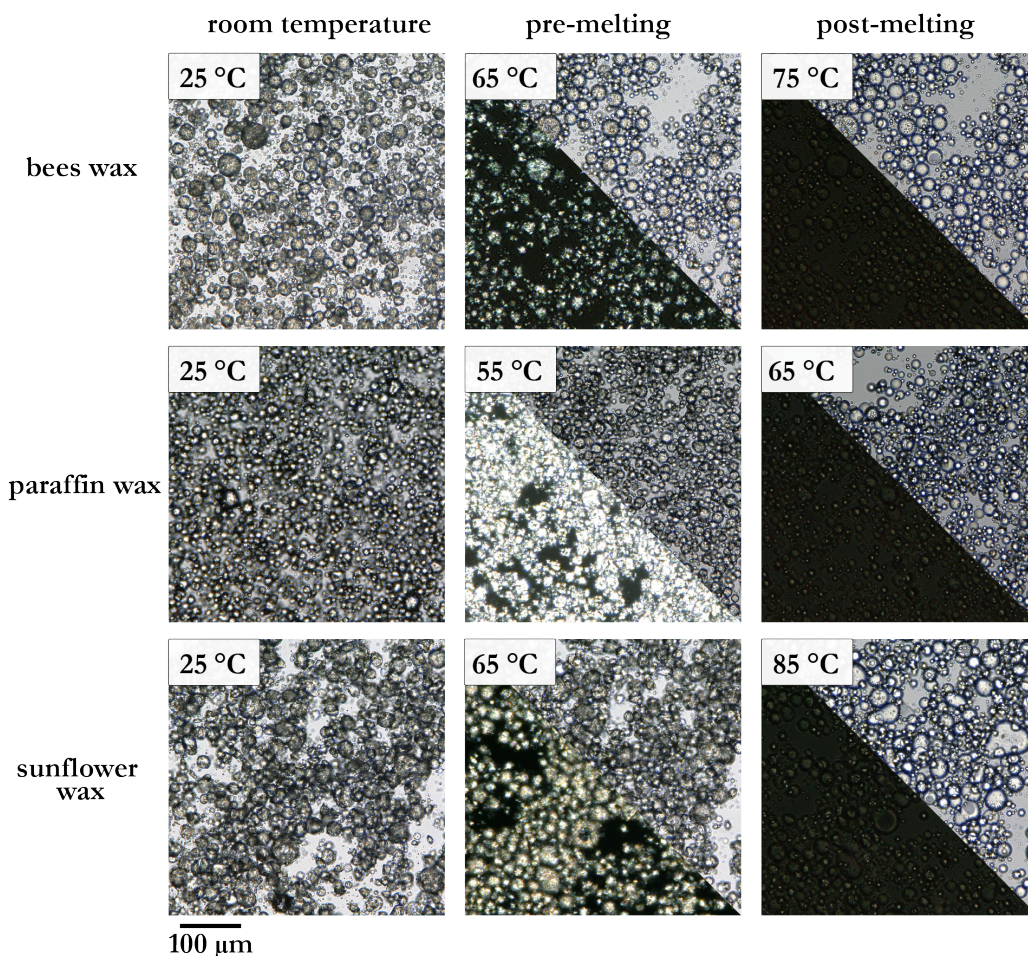
Figure 5.10: Wax particles Pickering-stabilized by cationic CNCs.

Such wax-in-water dispersions can be useful as easily applicable and versatile sustainable additives for formulations in decorative, protective, or functional coatings. Cationic CNC-stabilized wax dispersions might be particularly interesting for the application of a hydrophobic wood coating: Wood was found to have a negative surface charge as well, attributable to acidic groups in pectin low amounts of which are present in wood. [204] Electrostatic attraction between cationic CNC-stabilized droplets and anionic wood surface aids the coating's adhesion to the surface. Wood construction is experiencing its renaissance as the environmental implications of excessively using fossil-based plastics, concrete,

glass and steel are coming to light. The major drawback of wood, its hydrophilicity and dimensional instability upon water contact, is often overcome by using unsustainable and environmentally unfriendly polymer coatings, such as acrylate polymers. Despite their destroying the renewable aspect of wood, they completely seal the wood surface, impeding the positive moisture-buffering effect that was shown to aid passive air conditioning.[205] The same drawback is observed for continuous wax coatings, although natural waxes are promising hydrophobizing agents. The deposition of wax particles instead of continuous wax films on wood surfaces was shown by Lozhechnikova et al. to introduce water repellency while retaining the moisture buffering capacity of wood.[205] The availability of an easily dispersible and thermally stable wax particle dispersion aids the applicability of wax dispersions in straightforward coating applications, for instance spray-coating, and their implementation into other formulations.

5.2 Conclusions

In this chapter, the excellent barrier properties of CNC films were combined with their ability to stabilize Pickering emulsions to produce hydrophobic protective coatings. CNC-stabilized emulsions of natural oils and waxes in water were successfully fabricated. Using linseed oil, which spontaneously cures in air, emulsion-based paper coatings were produced and preliminary tests for their application were conducted. Applied as a coating for a common filter paper, a CNC-stabilized linseed oil emulsion with a dry mass oil content of 82 % produced a dense layer of CNCs that sealed the paper pores and produced a hydrophobic surface with a water contact angle of almost 100 °. θ_w decreases with decreasing oil content so that 10 % of oil in the dry mass yielded a hydrophilic contact angle with large deviations, indicating an inhomogeneous coating. A decrease to 40 % oil content in the dry mass, however, still yielded a hydrophobic surface. Water vapor transmission rates showed a decreasing trend with increasing oil content at area densities higher than 0.8 mg cm^{-2}. The highest tested area density and oil content produced the lowest rates of 80 g/m^2/d. The emulsions are highly stable over several months, owing to the increased viscosity of the continuous phase through the presence of CNCs, which prevents phase separation through creaming. The shear-thinning properties of the CNC-rich emulsion coatings enable a facile application for instance in larger scale blade coating. To be considered for food packaging applications, future tests will include grease barrier and oil permeability tests. Moreover, the effect of both linseed oil and wax emulsion coating on wood will be promising to investigate. Overall, this chapter demonstrates the potential of bio-based and bio-degradable materials to produce hydrophobic coatings in a straightforward way.

All-natural Pickering emulsions co-stabilized by cationic CNCs and α-cyclodextrin for high-fidelity direct ink-writing

The previous chapters demonstrated the use of CNCs in two-dimensional materials. If we truly want to replace synthetic polymers, however, we must also be able to fabricate three-dimensional structures. One quickly evolving way of processing polymers is 3D printing, for which CNC dispersions are attractive due to their gel-like rheology. As described in Chapter 2, however, the direct ink writing of pure CNC dispersions produces unsatisfactory results due to low solid contents in the ink. Meanwhile, high internal phase Pickering emulsions (HIPPEs) recently arose as candidates for DIW inks due to their suitable rheology. Sommer *et al.*, for instance, used concentrated Pickering emulsions stabilized by chitosan-functionalized silica nanoparticles as a biocompatible ink.[206] The novel cationic CNCs developed in this work stabilize Pickering emulsions, allowing to take a detour to print CNCs by applying them as Pickering stabilizers in concentrated o/w emulsions. Previously in our group, Pang et al. found that the aqueous continuous phase of the CNC-stabilized oil-in-water emulsion can be reinforced by adding a hydrogel to the aqueous continuous phase.[207] This hydrogel was composed of α-cyclodextrin (α-CD) and PEG, which are known to form host-guest supramolecular inclusion complexes. This composite of emulsion and gel was termed „emulgel“. Those emulgel inks were shown to perform excellently in direct ink writing tests and exhibited remarkably low shrinkage and high shape fidelity. However, even though PEG is considered biodegradable through decomposition, degradation is not immediate, especially for high M_w PEGs: In seawater, degradation of PEG with an M_w >10 300 was as low as 40 %.[208] It was shown that microplastics even from biodegradable plastics, such as polylactic acid, can alter the health of sea life such as blue mussels,[209] and not every impact on such sensitive ecosystems can be predicted. Moreover, as the scientific community was reminded during the first

rollout of the COVID-19 vaccines, PEGs can cause severe allergic reactions.[210;211] It is therefore desirable to eliminate the PEG from the formulation, which means finding another reinforcing system that yields a printable ink.

Cyclodextrins form a class of cyclical starches that is synthesized by enzymatic cleavage of natural potato or corn starch. They are considered biocompatible and biodegradable. The α-1,4-glycosidic linkage of glucose molecules gives rise to a toroid structure with a hydrophobic cavity and a hydrophilic outside surface. α-cyclodextrin, consisting of six glucose subunits, is known for its ability to form supramolecular hydrogels with small-cross section linear polymers, such as Pluronics[212] or PEGs[213], based on the formation of thread-needle-like host-guest inclusion complexes. It has also been shown that cyclodextrins can act as Pickering emulsifiers in o/w emulsions for a variety of oils such as tetradecane and silicone oils[214] but also glycerides[215] through such complexation.

This chapter describes the pursuit of eliminating PEG from the ink formulation to create an all-natural, bio-based, and truly biodegradable DIW ink. For this, the role of α-CD in the formulation is reconsidered and the reinforcement mechanism is investigated. This study is a collaboration with Prof. Orlando Rojas at Aalto University in Finland. Dr. Rubina Ajdary performed DIW and imaging of the printed structures. Development, characterization, and imaging of the inks, as well as interpretation of the results are my own work.

6.1   Results and Discussion

The sunflower oil-in-water emulsions used for this study were fabricated through stepwise emulsification of the oil phase in CNC dispersions and/or α-CD solutions at varying concentrations, as described in 8.6.2. Based on previous research in our group by Bo Pang,[207] a medium-high oil ratio of 60 % to 67 % oil was chosen for the emulsion formulations. The emulsions were first characterized rheologically to test their suitability as inks. As the basis for the suitability analysis of the fabricated inks, I define some rheological threshold values that the ink should exceed to print test structures that will be described later on. A minimum yield stress $\sigma_{\text{y,min}}$ required to support the self-weight of the printed structure without yielding to flow can be calculated using Equation 6.1 (neglecting capillary forces), as expressed by M'Barki et al.:

$$\sigma_{\text{y,min}} \geq \rho g h \qquad (6.1)$$

The product $\rho g h$ accounts for the mass that has to be supported by the lowest layer (ρ: ink density, $g = 9.81 \ \text{m} \cdot \text{s}^{-2}$: gravity of the earth, and h: height of the printed structure). For a 67 vol.% sunflower oil-in-water emulsion, ρ is about 946 $\text{kg} \cdot \text{m}^{-3}$ (951 $\text{kg} \cdot \text{m}^{-3}$ for

60 vol.% oil). Assuming a minimum reasonable aspired structure height of 1 cm, $\sigma_{\mathrm{y,min}}$ amounts to approximately 93 Pa for both oil ratios. To prevent sag of spanning ink filaments, a minimum storage modulus is required that can be estimated using elastic beam theory according to Smay et al.[216]:

$$G' \geq 1.4\gamma \left(\frac{l_{\mathrm{span}}}{d_{\mathrm{filament}}} \right)^4 \cdot D \tag{6.2}$$

with γ: specific weight of the ink (67 % oil: 9276 $\mathrm{kg\,m^{-2}\,s^{-2}}$; 60 % oil: 9332 $\mathrm{kg\,m^{-2}\,s^{-2}}$, l_{span}: length of the spanning filament, d_{filament}: diameter of the spanning filament). L is determined through the chosen printed structure and nozzle diameter, which, ideally, corresponds to D: The test structure to be printed is an upright square lattice with an infill fraction Γ_{p} of 25 %. For the given Γ_{p} and the chosen nozzle diameters d_{nozzle} of 250 µm and 410 µm (corresponding to the ideal d_{filament}), the spanning lengths are calculated according to Equation 6.3 to be 1000 µm and 1640 µm, respectively.

$$\Gamma_{\mathrm{p}} = \frac{D}{L} \tag{6.3}$$

This results in a calculated minimum required storage modulus G'_{min} in the range of 1 kPa. The exact values for G'_{min} and $\sigma_{\mathrm{y,min}}$ for both oil ratios and nozzle diameters are summarized in Table 6.1.

Table 6.1: Minimum yield stress $\sigma_{\mathrm{y,min}}$ and storage modulus G'_{min} required from inks with oil fractions of 60 % and 67 %.

		60 % oil	67 % oil
$\sigma_{\mathrm{y,min}}$ [Pa]		93.3	92.8
G'_{min} [kPa]	D: 0.25 mm, L: 1 mm	0.84	0.83
	D: 0.41 mm, L: 1.64 mm	1.37	1.36

6.1.1 Individually and co-stabilized oil in water emulsions using α-CD and cationic CNCs

To evaluate the roles of α-CD and CNCs in the emulsions, emulsions were fabricated with either stabilizer individually. 0.2 wt.% of CNC (respective to entire emulsion weight) were used to emulsify 67 vol.% sunflower oil in water. The photograph in Figure 6.1 A shows the resulting thick and opaque emulsion. The emulsion was studied using confocal laser scanning microscopy (CLSM), for which the oil phase was stained with Nile red prior to imaging. CLSM micrographs, Figure 6.1 B, show droplets with a broad size distribution in the range of 1 µm to 30 µm. This inhomogeneity of droplet size is due to the simple method of fabrication with a high-speed lab homogenizer, which cannot

guarantee every volume increment of the sample to experience the same shear forces. The use of a microfluidics device, in which the entire volume of the sample passes through the same gap, would allow precise control over the droplet size, if necessary, but would be entail a higher technological effort, making the technology less accessible and scalable.
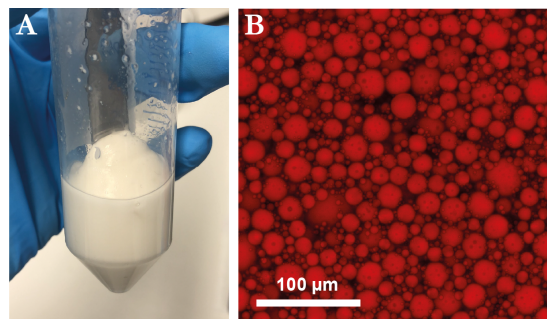

Figure 6.1: (A) Photograph and (B) CLSM image of Pickering emulsion of sunflower oil in water stabilized by 0.2 wt.% cationic CNCs.

Viscometry reveals that the CNC-stabilized sunflower oil-in-water emulsion exhibits the gel-like behavior (Figure 6.2 A) and shear-thinning (Figure 6.2 B) required for extrusion-based printing. The storage modulus, obtained from the oscillatory rheology experiment, in the LVR is 1 kPa, which should be just enough for a spanning length of 1 mm and a nozzle diameter of 250 µm, but too low for the larger diameter. However, the yield stress of 36 Pa, determined as the lowest point in the stress-shear rate diagram, is much lower than the required value of 93 Pa, rendering the emulsion unsuitable for application in DIW.
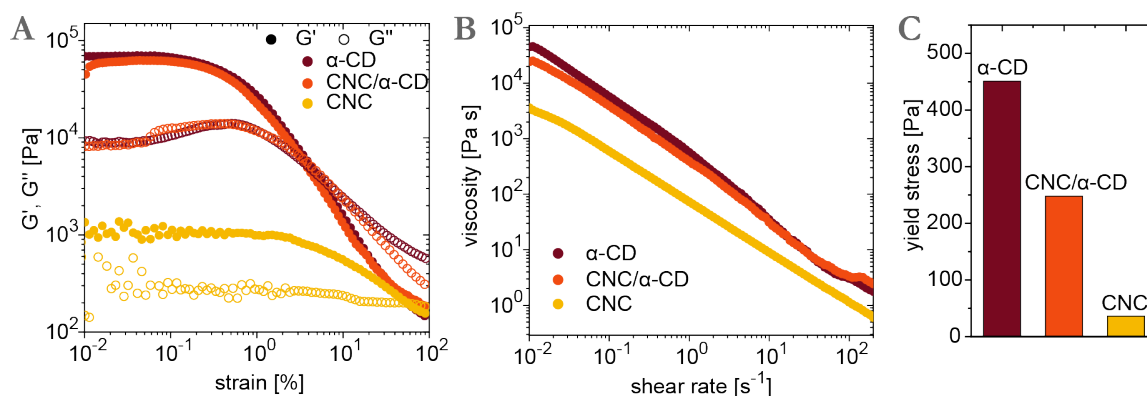
Figure 6.2: (A) Oscillatory rheology, (B) flow curves, and (C) yield stress of α-CD-stabilized, CNC-stabilized, and co-stabilized emulsions.

To prove the interfacial activity of α-CD, an emulsion with α-CD alone (3.6 wt.% adapted from Pang et al. [207]) was fabricated. The lasting opacity of the homogenized mixture (see Figure 6.3 A) as well as stable distinct oil domains in the micrometer range observed in CLSM micrographs (see Figure 6.3 B) indicate successful emulsification of the sunflower oil. However, as opposed to the emulsion stabilized with the CNCs, oil domains have irregular shapes, hinting at uncontrolled clustering of the supramolecular α-CD-oil complexes.

Figure 6.3: (A) Photograph and (B) CLSM image of Pickering emulsion stabilized by 3.6 wt.% α-cyclodextrin.

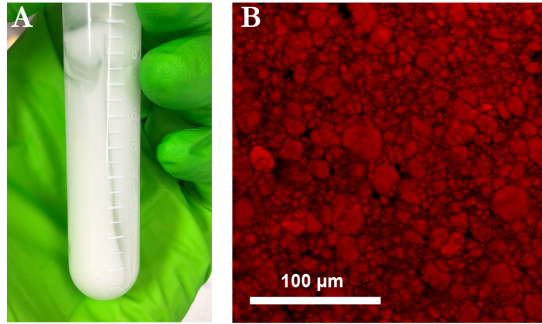In addition to that, the oil droplets are not easily separated upon dilution, which indicates that they stick together due to attractive hydrogen bonds between the cyclodextrins. As shown in Figure 6.2 A, those attractive forces between the oil domains contribute to a high elasticity represented by G', which is beneficial for the dimensional stability of the printed object. The yield stress of 451 Pa is considerably higher than the stated requirements and would ensure high strength and the ability to support high prints. This contrasts with the emulsion stabilized by cationic CNCs, which cause electrostatic repulsion between the droplets, resulting in much lower G', σ and a low viscosity.

The combination of the two stabilizers gives a more homogeneous emulsion with smaller droplets (Figure 6.4). It can therefore be concluded that α-CD and CNC act synergistically as co-stabilizers. The flow curve of the mixed-stabilizer emulsion lies in between the ones of the single-stabilized emulsions for low shear rates and follows the one of α-CD at high shear rates. The elastic modulus is slightly lower for the co-stabilized emulsion than for the α-CD-stabilized emulsion. This indicates a balancing between the attractive interactions between the α-CD molecules and the electrostatic repulsion of the positively surface-charged droplets. Despite the excess of α-CD compared to CNCs (20-fold mass-wise), the counter-balancing effect of the CNCs is considerably high: At 248 Pa, the yield stress of the co-stabilized emulsion is almost exactly the average of the values for the two single-stabilizer emulsions and significantly exceeds the calculated minimum value of

Table 6.2: Formulations and relevant rheological properties (yield stress σ and storage modulus G') for alginate-filled E inks.

identifier	m(CNC) [mg]	m(α-CD) [mg]	m(alginate) [mg]	V(oil) [mL]	V(H$_2$O) [mL]	σ [Pa]	G' [kPa]
E1	40	800	-	16	8	331	69 $\pm$ 1
E2	40	800	-	12	8	248	61 $\pm$ 1
E3	80	800	-	12	8	90	36 $\pm$ 1
E4	80	400	-	16	8	25	14 $\pm$ 0
E5	80	400	-	12	8	43	13 $\pm$ 1

93 Pa. Stable co-stabilized emulsions were fabricated on a range of oil-to-water ratios and stabilizer contents, which each have their individual influence on the emulsion and its rheological properties. The exact compositions are given in Table 6.2. CLSM images of all mixed-stabilizer emulsions in Figure 6.4 show emulsion droplets with sizes between 1 µm and 20 µm with rather irregular shapes, reflecting the attraction between the α-CD-decorated interfaces. Expectably, droplet shape becomes rounder for increased CNC to α-CD ratio (from E1 to E4). A higher oil/water ratio generally increases viscosity and complex modulus, demonstrated in Figure 6.5, according to the Krieger-Dougherty equation, due to a higher number of droplets and a consequentially higher space filling. A higher α-CD content significantly increases viscosity and G' and G''. A higher CNC content, on the other hand, decreases those values, likely due to increased electrostatic repulsion between the droplets. The values for G' in the LVR and σ are listed in Table 6.2. The emulsions exhibiting theoretically suitable rheology, E1, E2, and E3, were submitted to DIW tests.
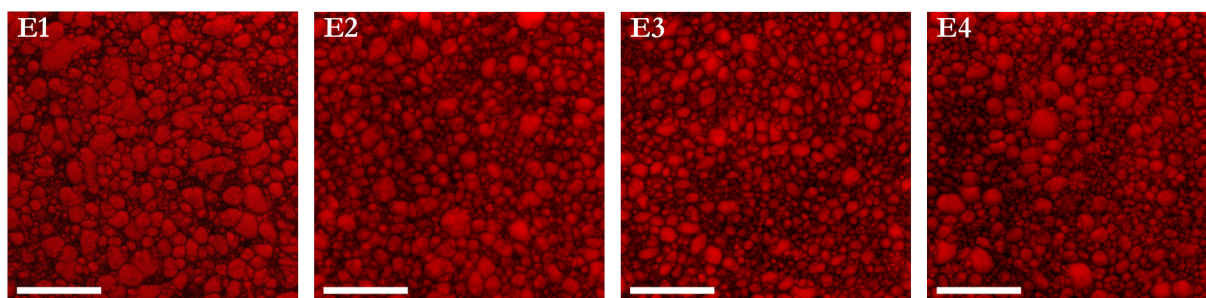

Figure 6.4: CLSM images of emulsions E1-4. Scale bar: 50 µm.

6.1.2   Reinforcement of the continuous phase using alginate

With the rheological ink requirements fulfilled, the α-CD/CNC-co-stabilized emulsion can serve as a two-phase platform, or a basis, for a DIW ink formulation. Both oil and water phase can be filled with other functional compounds that can be mechanically reinforcing or active agents. To produce objects with higher mechanical integrity and stability, the aqueous continuous phase, making up 33 %-40 % of the formulation, can be used. For instance, it can be filled with a water-soluble polymer, which will then form a network throughout the emulsion and ensure mechanical stability of the printed structure. Retaining the bio-basis and biodegradability of the ink, I chose sodium alginate as a filler to prove the concept. Inks EA1-3 were prepared with a constant 0.6 wt.% alginate respective to the aqueous phase, varying the amount of CNC content and oil ratio. The specific compositions are given in Table 6.3. The addition of a polymer to the continuous phase drastically increases the viscosity of the emulsion through an increase of the viscosity of the continuous phase (see Krieger-Dougherty equation 2.3). Figure 6.6 A shows a shift of the flow curve towards higher viscosities and an increase of viscosity of
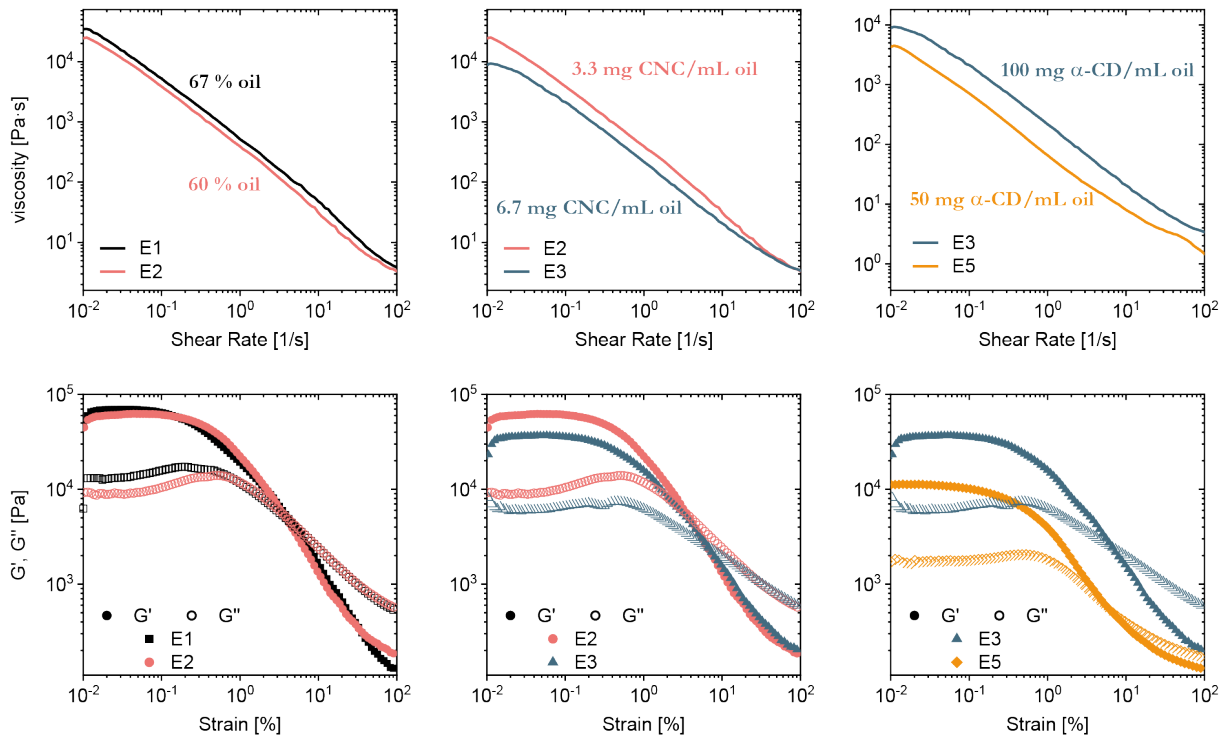
Figure 6.5: Flow curves (top) and oscillatory rheology curves (bottom) depict the influences of different parameters on emulsion rheology.

more than one order of magnitude at low shear rates in a formulation with alginate (EA3), compared to the same formulation without alginate (E4). Storage and loss moduli, shown in Figure Figure 6.6 B, also show a significant increase: For instance, at a strain of 0.03 %, G' increases by around 344 %, while G'' increases by 316 %. The stronger increase of G', representing the elastic part of the deformation, relative to G'', representing the viscous portion, should play in favor of the shape fidelity of the printed structure. Due to the strong increase in viscosity and storage modulus, EA inks were formulated using the lower α-CD concentration of 50 mg mL^{-1} in the aqueous phase, to obtain inks with rheological
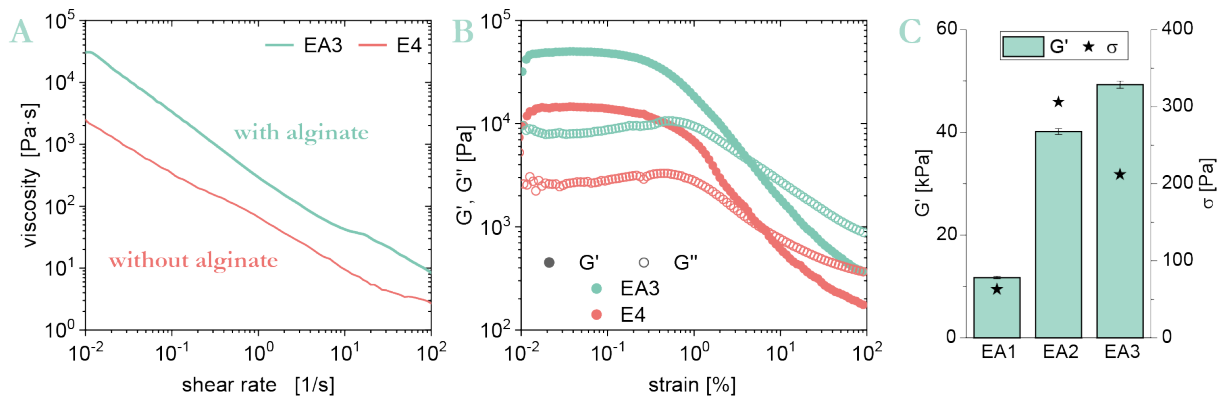

Figure 6.6: (A) Comparison of dynamic viscosity (flow curves) and (B) storage and loss moduli of emulsions of the basic formulation, E4, and with added alginate, EA3. (C) Storage modulus G' and yield stress σ of EA1-3.

properties comparable to the suitable E inks. Emulsions containing a higher amount of α-CD did not maintain the creamy texture observed in the E-series and instead were brittle and crumbly upon preliminary extrusion tests with a syringe. CLSM shows similar droplet sizes for the alginate-containing emulsions as for the emulsions without alginate. The droplets tend to be rounder with less irregularities, owing to the decreased amount of α-CD at the interface, compared to the E-series. The micrograph of EA1, which has the lowest CNC/oil ratio ($1.7 \mathrm{~mg\,mL^{-1}}$), reveals some larger, elongated droplets. Those might have formed from multiple smaller droplets by Ostwald ripening and have not yet relaxed into a spherical structure due to spatial constraints imposed by the high packing density. As such droplets are not observed in the samples with higher CNC/oil ratios, EA2 and EA3, this indicates a lower emulsion stability boundary at the CNC concentration of $1.7 \mathrm{~mg\,mL^{-1}}$ at a given α-CD concentration of $50 \mathrm{~mg\,mL^{-1}}$.
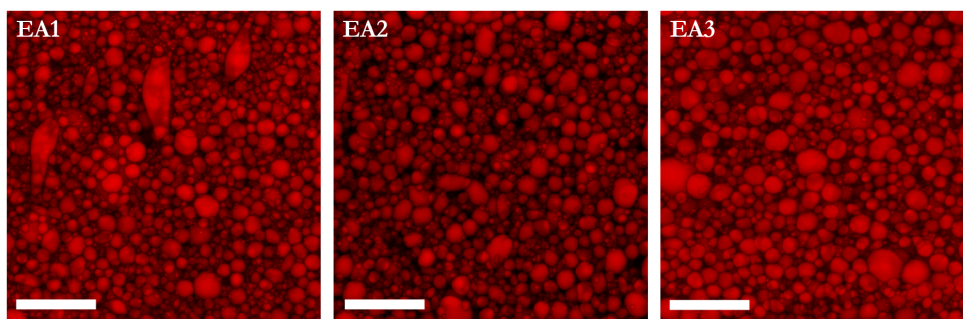

Figure 6.7: (A) CLSM images of alginate-filled inks EA1-3. Scale bar: 50 µm.

Table 6.3: Formulations and relevant rheological properties (yield stress σ and storage modulus G') for alginate-filled EA inks.

identifier	m(CNC) [mg]	m(α-CD) [mg]	m(alginate) [mg]	V(oil) [mL]	V(H$_2$O) [mL]	σ [Pa]	G' [kPa]
EA1	20	400	50	12	8	63	12 ± 0
EA2	40	400	50	12	8	306	40 ± 1
EA3	80	400	50	16	8	212	49 ± 1

6.1.3 Performance of emulsion inks in direct ink writing tests

Emulsions E1-3 and alginate-filled emulsions EA1-3 exhibited shear-thinning and gel-like behavior in oscillation rheology experiments as well as yield stress in the necessary range (or close to, in case of EA1) and were therefore submitted to DIW tests to my collaborator Dr. Rubina Ajdary. The formation of a filament upon extrusion is first verified for all the emulsions using a 410 µm nozzle. The photographic documentation is shown in Figure 6.8. All emulsions succeeded to form a filament. Squared lattice structures are printed with nozzle diameters of 250 µm and 410 µm. The printed structures are also shown in Figure 6.8.

	filament shape extrusion test	printed lattice and observation of printability			
		410 µm nozzle diameter		250 µm nozzle diameter	
E1			partial clogging		adhesion problems
E2			excellent		excellent
E3			excellent		adhesion problems
EA1			die swell		partial die swell
EA2			excellent		excellent
EA3			excellent		excellent for wide range of pressure
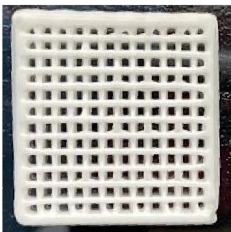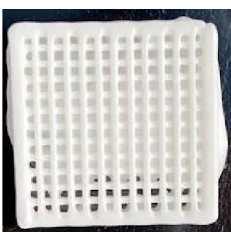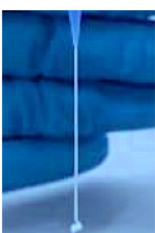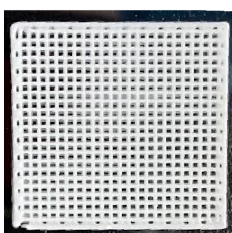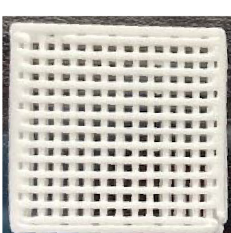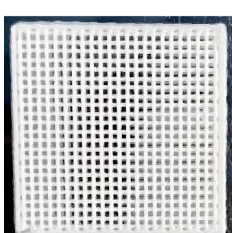
Figure 6.8: Photographs and evaluation of filament shape extrusion tests and the test printing of an upright square lattice (25 % fill) with nozzle diameters of 410 µm and 250 µm of the inks EG-1-3 and EGA-1-3. Photo credit: Rubina Ajdary.

Among the formulations without alginate, E2 performs the best, exhibiting excellent printability. E1 causes partial clogging using the smaller 250 µm needle and shows insufficient inter-filament adhesion, as shown in Figure 6.9. While E3 is well-printable, it exhibits some adhesion issues. Those problems are not present in the formulations containing alginate: EA2 and EA3 display excellent printability and good adhesion between the filaments. The polymer in the continuous phase appears to promote adhesion due to inter-filament hydrogen bonds and possibly entanglements.
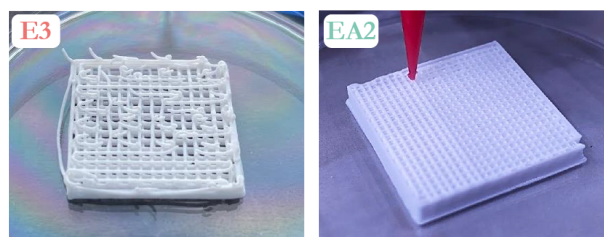
Figure 6.9: Emulsions E1 and E3 exhibit adhesion problems, as illustrated in the left image, which are not observed for alginate containing inks EA1-3, as shown on the right.

In accordance with the suitable rheology profile, EA2 and EA3 yield structures with a high shape fidelity and no visible yield in the lower layers. EA1, however, is not suitable for DIW, as predictable by the undercutting of σ: the lower layers of the test print started to flow under the pressure of the top layers and do not show distinguishable features anymore. Moreover, EA1 exhibits die swell, so that the extruded filament is larger than the diameter of the nozzle, which makes it unsuitable for DIW. Die swell is an entropic phenomenon originating from the relaxation of the polymer conformation, which is disentangled by extrusion through an orifice with a small diameter. When extruded from the die, the polymer will relax into the spherical, entangled conformation. Compared to EA2, which showed excellent printing results, EA1 contains half as much CNC and was shown to be prone to Ostwald ripening in the CLSM micrographs (see above). The die swell might therefore originate from local de-mixing of the emulsion, leading to a higher free aqueous volume for the alginate to relax, while in the other, more stable emulsions, it is trapped in the small space of aqueous phase between the emulsion droplets. This behavior is reflected in the overall low storage modulus (12 kPa) and yield stress (63 Pa) of EA1.

Figure 6.10: Optical micrographs of the lattice structures printed with E2 subjected to room temperature (RT) and freeze-drying.

The prints were both freeze-dried and dried at room temperature for 48 h. Freeze-drying causes a higher loss of shape fidelity compared to RT drying, observable with the optical microscope (see Figure 6.10). This may be due to formation of ice crystals despite the rapid freezing in liquid nitrogen, which can disrupt the droplet morph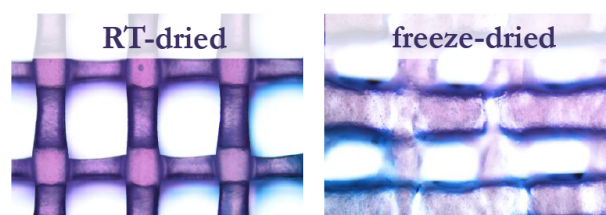ology and break the assembly upon their growth. Usually, the opposite is the case and RT drying causes a drastically higher shrinkage and lower shape fidelity than freeze-drying.[217]

To improve mechanical properties, alginate can be cross-linked by calcium ions, yielding a three-dimensional hydrogel network. The prints were therefore infused in a 1 M $CaCl_2$ solution. While E1-3 completely disintegrate, the alginate-containing inks retain their shape, as shown in Figure 6.11.

Figure 6.11: Emulsion inks based only on CNC/α-CD (E1-E3) disintegrate in a calcium bath, while alginate-filled emulsions EA1-EA3 cross-link and retain their shape.

The best-performing ink EA2 was further characterized with SEM to observe shrinkage and shape fidelity. The shrinkage is calculated from the ratio of the width of the dried filament, as marked in Figure 6.12 (left), to the nozzle diameter (here 250 µm). The obtained value of 4-5 % is very low compared to natural hydrogel-based DIW inks, which can exhibit shrinkage up to around 90 % when dried at room temperature (or 12-46 % when freeze-dried), for instance in the case of a CNF-reinforced aloe vera gel.[217] The cross-section of the square lattice structure printed with the 250 µm nozzle (Figure 6.12) shows no sagging of the spanning filaments across the spanning length of 1 mm. This demonstrates very high shape fidelity as well as high mechanical integrity and stability in the printed objects, which is a great improvement to the poor shape fidelity of (even CNF-reinforced) alginate-based inks.[218]
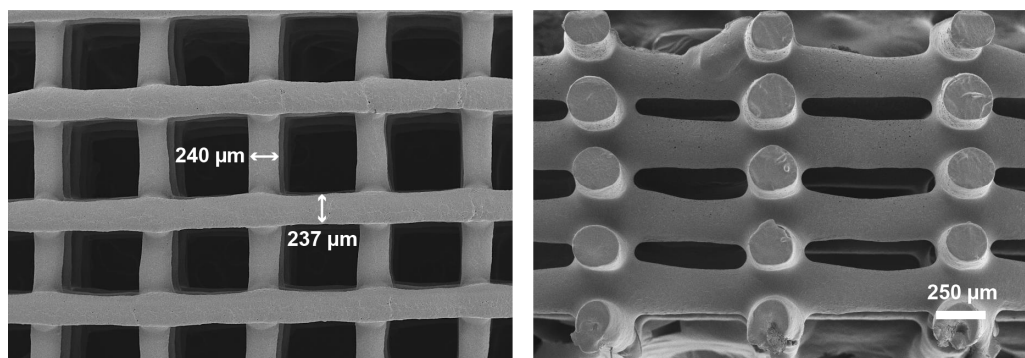
Figure 6.12: SEM micrograph of upright square lattice printed with EA-2 top view (left) and cross-section (right).

Using EA2, more complex objects were printed: a flower with rotating layers, introducing a declining angle, and a model of a human ear. Structures with a declining angle are challenging to print because the printed layer is only partially supported by the underlying layer. In many cases, such structures require a support structure to prevent the collapse or sagging of the top layers. Both ear and flower were printed successfully without signs of sagging. The printed objects were observed and photographically documented, immediately, 48 h, and 60 d after print (see Figure 6.13). While the structures are still partially opaque after 48 h, indicating incomplete drying, they appear translucent after a drying period of 60 d. By eye, no shrinkage or changes in the shape of the structure can be observed.
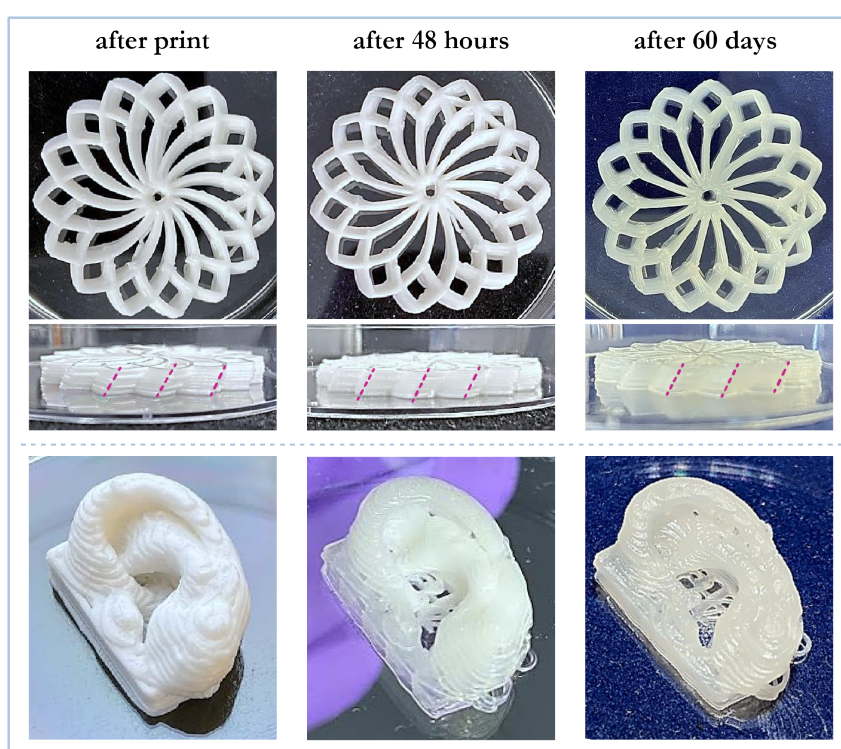
Figure 6.13: Rotating flower and model of human ear printed with EA2. Nozzle diameter: 410 µm.

Based on those good printing properties, higher structures with a declining angle were printed using the best-performing ink EA2. To test the mechanical limits of EA2, a support-free rotating square object was printed with a 410 µm nozzle. 55 layers of ink were printed before the feed syringe was exhausted. The structure, approximately 2 cm high, showed no signs of collapse (Figure 6.14). According to 6.1 and considering the σ_y measured for EA2 of 306 Pa, a maximum height of approximately 3 cm should be achievable before yielding. However, this could not be proven here due to early exhaustion of the ink.
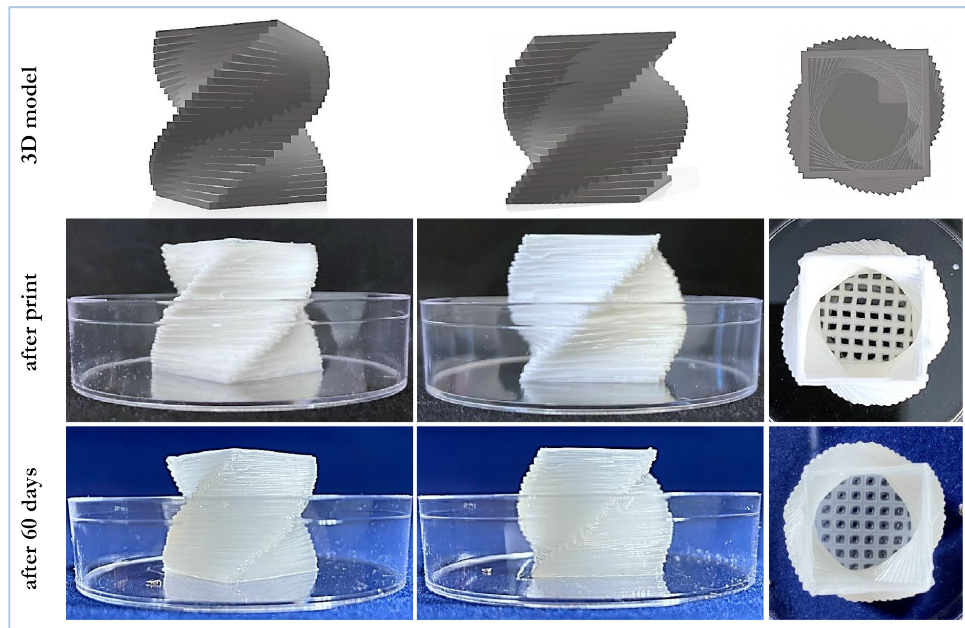
Figure 6.14: 3D model and print of 55 layers of a rotating square object. Nozzle diameter: 410 µm. Photographs taken right after, and 60 days after printing.

6.2 Conclusions

I developed a printable medium-internal phase Pickering emulsion formulation based entirely on components of natural origin. The revealed synergistic stabilization through CNCs and α-CD causes excellent rheological properties suitable, namely yield stress and storage modulus, for DIW. The resulting emulsion was shown to serve as a platform adaptable in rheology and composition through tuning of stabilizer amount, oil ratio, and filler in the continuous phase. As a proof-of-concept, it was shown that the aqueous continuous phase can be filled with alginate to provide structural integrity of the printed object. With that, complex structures could be printed that did not require a support structure. High shape fidelity as well as low shrinkage allow straightforward and efficient printing. Since all used components are biocompatible, the ink has the potential for biomedical applications. It is a promising platform as an extracellular matrix, i.e. a host medium for cells to proliferate in. The relatively low yield stress in particular is favorable for the printing of cells, as it was shown that a high extrusion pressure negatively affects the viability of cells when extruded through the nozzle.[219] The suitability of these inks for tissue engineering will be tested in the near future. With the presence of both oil and water phase, the hosting of hydrophilic and hydrophobic substances and compounds is possible. Instead of relying on the synthetic polymer PEG, the ink can be filled with other polymers to be adjusted to the desired properties and tailored to different applications. The inclusion of the other wood polymers, hemicellulose and lignin, might eventually enable the 3D printing of a sort of artificial wood.

CHAPTER 7

Summary

In the scope of this thesis, a new method to extract cationic cellulose nanocrystals in a one-step procedure was developed. The method uses a deep eutectic solvent, or reactive eutectic medium, based on ammonium formate as a hydrogen bond acceptor, in combination with an organic acid as a hydrogen bond donor. A variety of acids were explored and glycolic and lactic acid were found to produce the CNCs with the highest charge and crystallinities. Lactic acid was finally chosen as a preferred system for its higher thermal stability, its sustainable production, and its lower price. The REM treatment appears to have a two-fold effect of 1) aminolytic cleavage of the amorphous cellulose domains and 2) reductive amination of carbonyl groups, for instance at the reducing ends of the cellulose chain. Colloidal CNCs with a stabilizing positive surface charge in the range of 30 mV to 40 mV were isolated from different cellulose sources such as short-fiber cellulose powder, pulp, and cotton. The novel type of CNC was extensively characterized physically and chemically. The cationic charge appears to originate from surface amino groups. The elimination of reducing ends during the treatment causes high thermal stability of the CNCs, superior to the most commonly used sulfate-CNCs. The absence of non-natural functional groups promises good biocompatibility and biodegradability, making the cationic CNCs an environmentally friendly nanomaterial. In preliminary experiments, it was shown that CNCs form dense films, but do not produce structural color. Thanks to their low cationic charge, they can also absorb to oil-water interfaces, which usually bear a negative charge, thus enabling their use as Pickering stabilizers.

To explore the potential of this novel material, the CNCs were then tested in applications commonly fulfilled by synthetic petroleum-based polymers or additives. First, their application in supported ionic liquid membranes (SILMs) was tested by simply mixing and casting of the CNC dispersion with the imidazolium based ionic liquids 1,3-dibutylimidazolium acetate and 1,3-ditetrahydrofurfurylimidazolium acetate. Those ILs greatly enhanced the flexibility of the CNC films, but could not eliminate their tendency

to crack upon drying. This was solved by the addition of the water-soluble hemicellulose xylan to the mixture. Membranes were compared with CNC-glucose membranes, which proved to be excellent gas barriers and did not show any particular gas selectivity themselves, confirming the CNCs' suitability as a neutral support material for active gas transport additives such as ILs. The attempted CNC-SILMs exhibited increased gas permeabilities with only low selectivities. A comparison of CNCs from different cellulose sources showed an effect of the degree of crystallinity on the gas permeation behavior: While highly crystalline particles reflected the permeation behavior of the IL, CNCs with a higher ratio of amorphous domains appeared to consume the IL as a secondary plasticizer, making it unavailable for active gas transport. This demonstrated the tunability of gas permeation even when using natural polymers.

Combining the CNCs' excellent barrier properties with their ability to stabilize Pickering emulsions, a hydrophobic coating based on a CNC-stabilized linseed oil-in-water emulsion was developed. The coating can be applied on paper to simultaneously seal the pores and introduce hydrophobicity through the spontaneously curing linseed oil. Hydrophobic properties as well as decreased water vapor transmission rates of the emulsion coating were demonstrated. The feasibility of stable dispersions of wax particles in water was also demonstrated. The biocompatibility and -degradability makes such coatings promising for paper-based food packaging materials that allow easy recycling, as opposed to polymer-coated paper packaging. Wood coatings are another promising application.

Lastly, the CNCs were used to co-stabilize an all-natural Pickering emulsion direct ink writing ink together with α-CD. Both components were found to individually stabilize sunflower oil-in-water emulsions, but only in synergy, they produce a medium-internal phase Pickering emulsion that has rheological properties which make it suitable for extrusion-based 3D printing. An excellent printability along with a remarkably high shape fidelity and low shrinkage was observed for emulsions with different compositions. The presence of both hydrophilic and hydrophobic phase allow endless tailoring possibilities by the inclusion of polar and non-polar compounds. For instance, it was demonstrated that the aqueous phase can be filled with the water-soluble polymer sodium alginate, providing mechanical integrity to the printed object. This allowed for the printing of complex structures with declining angles, which often require a support structure. Since all components are biocompatible and natural, such an ink seems promising for bioprinting applications, which will be tested in future cell proliferation tests.

All in all, this thesis demonstrated the versatility of a new kind of CNC with the potential to replace fossil-based synthetic polymers in films, barriers, and surfactant-free emulsions. The addition of a sustainably produced cationic CNC to the bio-colloids toolbox opens new possibilities beyond the scope demonstrated in this thesis, such as water-remediation, reinforced fibers, construction materials, and more.

CHAPTER 8

Materials and methods

This chapter specifies the materials used and the analysis methods applied throughout this work. General characterization methods used in multiple chapters of this thesis are presented first. Further chapter-specific preparation procedures and analyses are described in the subsequent sections.

8.1   Imaging

Optical microscopy   was conducted on an Olympus BX41 (Shinjuku, Tokyoo, Japan). Images of cellulosic products were taken between cross-polarizers.

Transmission electron microscopy   (TEM) imaging was conducted on a JEM-F200, JEOL Ltd. (Akishima, Japan) using an accelerating voltage of 80 kV. Samples were stained using an aqueous uranyl acetate solution.

Scanning electron microscopy   (SEM) images were recorded on a Gemini 1550, Zeiss AG (Oberkochen, Germany) at an accelerating voltage of 3.00 kV. Cross-sections of films were prepared by breaking the films after freezing in liquid nitrogen.

Energy dispersive X-ray spectroscopy   (EDX) spectra were obtained on the same instrument, using a voltage of 5.00 kV.

Confocal laser scanning microscopy   (CLSM) was used for imaging of emulsions. For this, the used oil was stained with nile red (abcr GmbH, Karlsruhe, Germany) at a concentration of approximately 25 $\mu g\,mL^{-1}$ before the emulsions were fabricated. CLSM images of the as-prepared emulsions were recorded on a Leica TCS SP8 X (Leica Microsystems, Wetzlar, Germany) using an excitation wavelength of 514 nm for Nile red and an emission detection range of 550-600 nm.

8.2 Physicochemical analyses

Attenuated total reflection infrared (ATR-IR) spectra were recorded on a Nicolet iS5 with an iD5 ATR crystal, Thermo Fisher Scientific Inc. (Waltham, Massachusetts, USA), at a resolution of 0.5 cm^{-1}.

Zeta potential and electrophoretic light scattering (ELS) measurements were carried out on a Zetasizer Nano ZS, Malvern Instruments (Malvern Panalytical, United Kingdom). The measured electrophoretic mobility was converted to Zeta potential using Smoluchowski's approximation.

X-Ray diffractometry (XRD) was used to determine the crystallinity of the cellulose. The XRD diffractograms were recorded using a Bruker D8 X-Ray diffractometer (Bruker Cooperation, Billerica, Massachusetts, US). For the determination of the cristallinity index CrI, the obtained curves were smoothed using the Savitzky-Golay method with 20 points of the window and polynomial order of 2. Scattering intensities were determined from the smoothed curves at $2\Theta{=}22.6$ for I(200) and $2\Theta{=}18.7$ for I_{am}, the intensity of the amorphous scattering. CrI was determined using Equation 8.1:

$$CrI = \frac{I_{200} - I_{am}}{I_{200}} \tag{8.1}$$

Static light scattering (SLS) measurements were performed on a Mastersizer3000 with a HYDRO EV dispersion unit (Malvern Pananalytical, Malvern, UK). Samples were measured under constant stirring in an aqueous 50 mM acetic acid solution, as the colloidal stability was found to be the highest at this pH and ionic strength. The measurement was repeated until a reproducible size distribution curve was obtained for at least three consecutive measurements.

Thermogravimetric analysis (TGA) was conducted on a thermo microbalance TG 209 F1 Libra (Netzsch, Selb, Germany) in nitrogen and air atmospheres, both with a constant flow of 100 mL min^{-1}. The freeze-dried sample (10 ± 1 mg) was heated in an aluminum crucible from 25 to 600 °C at a heating rate of 10 °C min^{-1}. TGA was coupled with a mass spectrometer (MS) (Thermostar, Pfeiffer Vacuum, Asslar, Germany) with an ionization energy of 75 eV to detect the volatile decomposition products. These TGA-MS measurements were carried out on $10{\pm}1$ mg of the sample in a helium flow of 10 mL min^{-1} and a heating rate of 2 °C min^{-1}.

Differential scanning calorimetry (DSC) was performed in an aluminum crucible with a pierced lid at a heating rate of 5 °C min^{-1} using a DSC 204 F1 Phoenix (Netzsch, Selb,

Germany). Thermal analysis data were recorded and analyzed using the Proteus (6.1.0) and Quadstar (7.03, MID modus) software packages.

Rheological measurements were conducted on a Physica MCR-301 rheometer (Anton Paar GmbH, Graz, Austria) using a parallel plate setup (12 mm diameter). Gap spacing was 0.5 mm for all measurements. Flow curves were recorded at a shear rate from 0.01 s^{-1} to 100 s^{-1}. Oscillation experiments to measure the complex modulus were conducted at a constant frequency of 10 Hz while the shear amplitude varied between 0.01 % and 100 % strain. The storage modulus was determined by averaging over 20 points in the linear viscoelastic region. The yield stress was determined in two ways: 1) From the oscillatory rheology experiment and defined as the shear stress at which the loss modulus exceeds the storage modulus. 2) the limit of shear stress for shear rate $\dot{\gamma} \to 0$.

8.3 Extraction

8.3.1 Materials

Cellulose sources for the extraction were fibrous cellulose powder (Sigma Aldrich), commercial short-fiber cellulose (Opitec Handel GmbH, Giebelstadt, Germany, cellulose content unknown), and bleached softwood Kraft pulp (MERCER Stendal GmbH, Arneburg, Sachsen-Anhalt, cellulose content > 80 %). Fibrous cellulose and short-fiber cellulose powder were used without any pre-treatments. Softwood pulp was disintegrated through stirring in deionized water overnight at room temperature. Disintegrated pulp was filtered and washed with ethanol on a glass filter to prevent formation of a solid cake, and subsequently dried for 24 h at 60 °C. Ammonium formate (97 %, Alfa Aesar) was dried overnight in the vacuum oven at room temperature prior to use. Glycolic acid (98 %) was obtained from Alfa Aeser; levulinic acid (> 98 %), L(+)-lactic acid (90 % solution in water) and copper-ethylene diamine (CED)-solution (1 M in water) from Acros Organics. FITC was obtained from Acros Organics. Biotin and streptavidin gold from *streptomyces avidinii* (10 nm nominal diameter, buffered aqueous glycerol solution) were obtained from Sigma Aldrich and used as received.

8.3.2 Preparation of the reactive eutectic medium (REM)

The eutectic medium was prepared by mixing preliminarily dried ammonium formate and the respective organic acid in a molar ratio of 2:1. The mixture was ground thoroughly in an agar mortar and then kept at 80 °C in an oven to facilitate the formation of the eutectic under occasional stirring for at least two hours or until the disappearance of the crystalline phases.

8.3.3 Nanocellulose extraction in REM

8.3.3.1 Small static autoclave

SFC was applied as cellulose source and reacted with REM1-6 with the same amount of ammonium formate (1.26 g, 20 mmol) and half the molar equivalent of the organic acid counterpart (10 mmol). The amount of cellulose for the extraction was calculated to obtain 25 wt.% of SFC in the REM. The mixture was transferred into the glass inlet of an autoclave, which was then kept in an oven at 180°C for 4 h. After the reaction time, the autoclave was cooled to RT using an ice bath. The darkest brown upper layer of the product was removed. The residue was diluted with a few milliliters of distilled water and ultra-sonicated for 30 minutes to aid the removal of brown by-products. Subsequent centrifugation at 10000 g for 5 min separated the colloidal particles from the browned REM. The light brown precipitate was washed and worked-up using the following sequence: re-dispersion in water, vortexing for 30 s, ultra-sonication for 30 min, centrifugation at 12000 g (50000 g for last three runs) for 5 min, and decanting of the supernatant washing solution. The sequence was repeated with water and ethanol until the washing solution remained clear.

8.3.3.2 Small stirred reactor

Pulp or SFC were applied as cellulose source. 80 g of REM1 was applied as the extraction medium and mixed the cellulose to yield 5 wt.% pulp or 25 wt.% SFC in REM1. The mixture was filled into a PTFE inlet and reacted in a stirred autoclave at different temperatures (140 °C, 160 °C, and 180 °C) for a series of extraction times (1 h, 2 h, 4 h, and 6 h). After quenching the reactor in an ice bath and letting it cool down to room temperature, the mixture was diluted with 5 % acetic acid to facilitate the removal of the dark brown reaction by-products. The cellulosic product was separated from the REM by centrifugation at 10000 g for 15 min. The supernatant was removed and the sediment was washed using the same procedure as described above.

8.3.3.3 Big stirred reactor

The extraction was scaled up to a 1 L stirred reactor using 300 g of REM1 or REM2 at 160 °C and a reaction time of 4 h.

8.3.4 Further product characterization

The ninhydrin assay   was used to verify the presence of primary amino groups in the cellulose samples after the REM-treatment. The test was performed following the procedure described by Wellings et al.[220] Three test solutions were prepared according to the

following protocol: For reagent A, 16.5 mg of KCN were dissolved in 25 mL of distilled water. 1.0 mL of this solution were diluted with 49 mL of pyridine, which was freshly distilled from ninhydrin. For reagent B, 1.0 g of ninhydrin were dissolved in 20 mL of n-butanol. For reagent C, 40 g of phenol were dissolved in 20 mL of n-butanol.

To perform the test, 2-3 mg respectively of the dried REM-treated sample and the untreated material (SFC) were mixed with 1 mL of ethanol each in a dry glass test tube. A third tube was left empty for the reference experiment. 2 to 3 drops of reach Reagent A, B and C were added in this order. The tubes were heated to 110°C for 5 minutes, after which the colors developed were compared. A positive probe develops a blue hue, while a negative probe retains a pink coloration.

Viscosimetric determination of the average DP was performed according to the ISO 5351 standard from the limiting viscosity of a solution of cellulose in cupriethylene diamine (CED) solution. Samples were freeze-dried prior to their dissolution in 1 M CED solution in water. The limiting viscosity was determined using a falling ball viscometer. The evaluation follows the Mark-Houwink-Sakurada correlation of molecular weight and limiting viscosity (Staudinger index) applying experimentally derived parameters by da Silva Perez[221] according to Equation 8.2:

$$DP = \left(\frac{1.65[\eta] - 116H}{C} \right)^{1.111} \tag{8.2}$$

, with $[\eta]$: the Staudinger index, C: mass fraction of cellulose, and H: mass fraction of hemicellulose. The correction of $116H$ accounts for the contribution of residual hemicellulose with an average DP of 140 to the solution's viscosity. In pure cellulose samples (H=0), Equation 8.2 thus simplifies to

$$D_P = (1.65[\eta])^{1.111} \tag{8.3}$$

. Due to the broad variety and empirical nature of parameters and standards for similar systems, the DP is only considered a comparative value for starting material and REM-treated material, not as an absolute value.

Gel permeation chromatography (GPC) was performed in NMP/LiBr (0.05

M_n is directly related to the number average degree of polymerization DP_n through Equation 8.4 with M_0: molecular weight of the repeating unit. For the conversion, the molecular weight of the monomer of pullulan (anhydroglucose, $162 \, \mathrm{g \, mol^{-1}}$) is used, so that the DP is given in pullulan equivalents.

$$DP_n = \frac{M_n}{M_0} \tag{8.4}$$

Elemental analysis   Elemental analysis was performed on a vario MICRO cube CHNOS Elemental Analyzer (Elementar Analysensysteme GmbH, Langenselbold). The elements C, H and N are detected with a thermal conductivity detector and S is detected with an infrared detector.

Solid state NMR spectroscopy of pulp starting material and CNC product   was performed by Dr. Michaela König (TU Berlin). ^{13}C {^{1}H } CP/MAS and ^{1}H MAS using a Bruker range Advance 400 MHz Solid State spectrometer with a Bruker 4 mm double resonance probe-head operated at a spinning rate of 6500 Hz. 13C1H CP/MAS and 1H MAS measurements were carried out using a Bruker range Avance 400 MHz Solid State spectrometer and a Bruker 4 mm double resonance probe-head operating at a spinning rate of 6500 Hz. Acquisition time was 0.082 s for ^{1}H and 0.041 s for ^{13}C, and sweep-width was 50 kHz. The number of scans was 30 065 to 46 584 with a relaxation time of 1.0 s for ^{13}C NMR.

8.4   Membranes

CNCs were extracted from commercially available short-fibered cellulose powder (Opitec Handel GmbH, Giebelstadt, Germany) and pre-fibrillated, never-dried bleached kraft pulp (64 wt.% water) provided by MERCER Stendal GmbH, Arneburg, Germany. The used chitosan was obtained from Sigma-Aldrich and has a deacetylation degree of 75 – 85 % and a molecular weight of 50 -190 kDa (based on viscosity of 1 wt.% solution in acetic acid). Ammonium formate (97 %) and glycolic acid (98 %), obtained from Alfa Aeser, were used without further purification. D-(+)-glucose was obtained from Carl Roth GmbH, Karlsruhe, Germany. The IL additives 1,3-dibutylimidazolium acetate (dbi acetate) and 1,3-ditetrahydrofurfurylimidazolium acetate (dthfi acetate) were obtained from collaborators who synthesized them as described by Tröger-Müller et al. [222]

8.4.1   Preparation and characterization of CNC dispersion

Cationic amine-functionalized CNCs were extracted according to the method presented in this work using 10 wt.% of the cellulose source in REM1. The mixture was reacted in the small stirred autoclave at a temperature of 140 °C for 1 h. The product workup followed the optimized procedure described previously using washing and precipitation cycles with 5 % acetic acid and ethanol. Finally, the solvent was exchanged to water and the dispersion was homogenized using two passes at a pressure of 1500 bar in a SPCH-EP pressure cell homogenizer (Homogenising Systems Ltd, Stansted, UK). The CNC dispersion was diluted to 5 mg/mL before use.

Dimensions of the extracted and used CNCs, fNC and sNC, were determined from TEM images evaluating 13 distinguishable CNCs. Size distribution curves, Zeta potential of the particles and DP of the carbanilated and dissolved cellulose chains were determined as described in Chapter 8.3.4. The determined values are summarized in Table 4.1.

8.4.2 Fabrication of CNC-based films

The CNC dispersion was blended with the additives glucose ($100 \, \mathrm{mg \, mL^{-1}}$ solution), 1,3-dibutylimidazolium acetate (dbi acetate) or 1,3-ditetrahydrofurfurylimidazolium acetate (dthfi acetate), and xylan (100 mg/mL solution) in the desired mass ratio. To facilitate spreading and avoid rapid shrinkage of the drying films, 5 vol.% of butanol were added, decreasing the surface tension of the mixture. The mixture was stirred using a magnetic stirring bar until combined. To remove air bubbles, ultrasonication was applied in a cold bath for 15 minutes. It was then cast into a PTFE tray and dried at ambient temperature and humidity in the fume hood for around 3 days. The masses were chosen to produce films with a weight per area of $2 \, \mathrm{mg \, cm^{-2}}$, corresponding to film thicknesses of around 10-20 µm. Exact compositions along with descriptions used in this work are listed in Table 8.1.

Table 8.1: Overview of the masses of CNC and additives used to prepare the CNC-based membranes.

Code	CNC mass [mg]	additive	additive mass [mg]	self-standing
sNC	-	-	-	yes
sNC:glu	100	glucose	20	yes
sNC:bi	100	dbi acetate	20	yes
sNC:thfi	100	dthfi acetate	20	yes
fNC	-	-	-	yes
fNC:bi	100	dbi acetate	20	yes
fNC:thfi	100	dthfi acetate	20	no
fNC:X:bi	100	xylan/dbi acetate	20/20	yes

8.4.3 Fabrication of chitosan-based films

Chitosan films were prepared by Dr. Steffen Tröger-Müller in three steps. The casting solution was prepared by dissolving chitosan and the additive in a 1 wt.% acetic acid solution by adding the solvent in four portions and stirring the solutions using a roller mixer for 3-4 days at 20 rpm. The clear and highly viscous solutions were degassed in an ultrasonic bath for up to 2 h to remove air bubbles incorporated during mixing. The casting solution was cast onto float glass plates using an automated doctor blade with a blade height of 300 µm at a casting speed of $17 \, \mathrm{mm \, s^{-1}}$. The films were dried at room

temperature in ambient atmosphere for 6 days. The specific amounts of additives and polymer used for the described membranes are listed in Table 8.2.

Table 8.2: Overview of the masses and volumes used to prepare the chitosan-based membranes

Code	chitosan mass [g]	additive	additive mass [g]	added solvent [mL]
CS	3.500	-	-	4 × 25
CS:glu	3.504	glucose	0.700	4 × 25
CS:bi	3.504	dbi acetate	0.700	4 × 25
CS:thfi	3.510	dthfi acetate	0.707	4 × 25

8.4.4   Gas permeation tests

Gas permeation experiments were executed on an EESR time lag apparatus. The schematic representation of the setup is shown in Figure 8.1. The measurements were conducted at a constant temperature of 30 °C and a feed pressure of 1000 mbar. Permeate pressure at the beginning of the measurement was adjusted to 1×10^{-4} mbar. The samples were evacuated for 4.5 h after exchange and for a duration of 12 time lags Θ in between permeate switching (minimum 3 min, maximum 6 h).
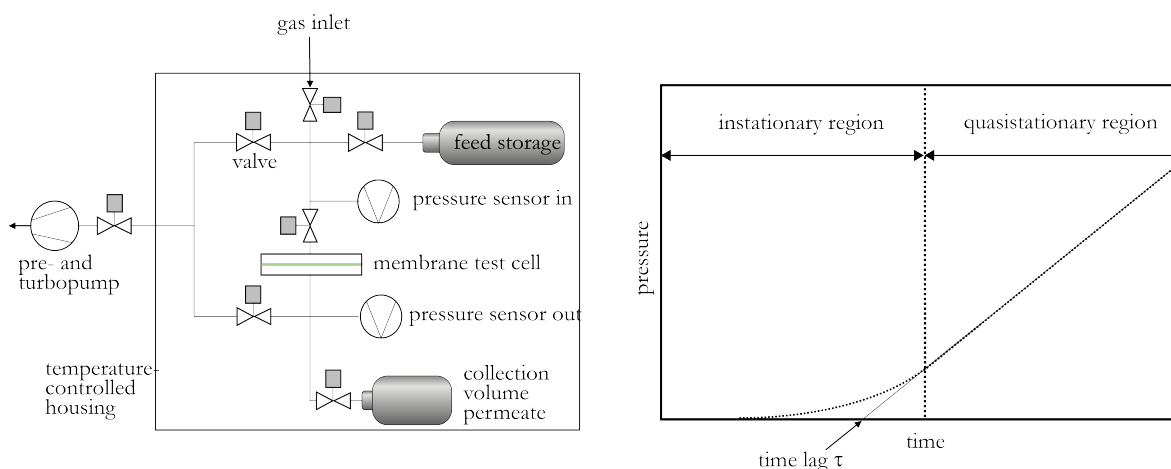
Figure 8.1: Setup of the EESR time lag apparatus used for gas permeation measurements and exemplary depiction of a time-pressure curve obtained from the measurement.

The time lag apparatus measures the pressure increase of the permeate dependent on the time, giving a time-pressure curve for every tested gas. A schematic representation of a time-pressure curve is shown in Figure 8.1 on the right. Two properties can be derived from the curve: The permeability P_i and the diffusion coefficient D_i of gas i. P_i is calculated according to 8.5:

$$P = \frac{l \cdot V(\text{STP})}{A \cdot t \cdot (\Delta p_F - \Delta p_p)} \tag{8.5}$$

with l: membrane thickness [cm]; $V(\text{STP})$: volume of the permeate [cm^3]; A: effective membrane area [cm^2]; t: passed time within the quasi-stationary range [s]; Δp_{F}: difference of the feed pressure within the quasi-stationary range [cmHg]; Δp_{P}: difference of the permeate pressure within the quasi-stationary range [cmHg]. Permeabilities are given in the unit Barrer with

$$1 \text{ Barrer} = 10^{-10} \cdot \frac{\text{cm}^3 \text{ (STP) cm}}{\text{cm}^2 \text{ s cmHg}} \tag{8.6}$$

D_{i} is calculated from the time lag Θ according to Equation 8.7.

$$D = \frac{l^2}{6\,\Theta} \tag{8.7}$$

Θ is determined by extrapolating the stationary curve to the time axis in the time-pressure plot (see Figure 8.1).

The solubility S of a gas can be calculated as the ratio of its permeability and diffusivity according to Equation 8.8.

$$S = \frac{P}{D} \tag{8.8}$$

Since it is only calculated from the measured values here, it has no independent significance and is only shown demonstratively.

The individually tested permeates were He, H$_2$, O$_2$, N$_2$, CH$_4$ and CO$_2$. By relating the individually measured permeabilities of gases A and B, an ideal selectivity $\alpha_{\text{A/B}}$ of gas A over gas B can be determined according to Equation 8.9.

$$\alpha_{\text{A/B}} = \frac{P_{\text{A}}}{P_{\text{B}}} \tag{8.9}$$

8.5 Coatings

8.5.1 CNC-stabilized linseed oil in water emulsions

Cold-pressed linseed oil (NaturPura, from the supermarket) was emulsified in an aqueous CNC dispersion using an IKA T18 digital ULTRA-TURRAX® high-speed lab disperser (IKA-Werke GmbH & CO. KG, Staufen, Germany) at 15000 rpm for one minute. Paper was coated by casting different volumes of the emulsion on a filter paper (Hahnemühle, thin, medium fast, type 595, 110 mm) placed in a glass petri dish of the same size so that no material was lost during the casting. The paper was dried at room temperature for 2 days. The coated paper was hot-pressed at 60 °C and a pressure of 3 bar between two sheets of packing paper after 7 days to allow the linseed oil to cure and avoid its absorption into the packing paper.

8.5.2   CNC-stabilized wax particle dispersions

Waxes were molten and the CNC dispersion was heated to approximately 90 °C. The melt and dispersion were combined in the desired ratio and emulsified with a pre-heated IKA high-speed lab homogenizer at 15000 rpm for one minute.

8.5.3   Water contact angle measurements

The water contact angle θ_{w} was measured using a Krüss contact angle measuring system G 10 (A. Krüss Optronic GmbH, Hamburg, Germany). The coated paper was fixated on a microscopic glass side with double-sided adhesive tape to ensure an flat horizontal surface. Droplets with a volume of 1 µL were placed on the surface and θ_{w} was evaluated by the software. Each measurement was repeated at least three times.

8.5.4   Water vapor transmission rate tests

Water vapor transmission rates (WVTR) were determined following the German industry norm DIN 53122-1 using TQC sheen permeability cups with a sample surface of 10 cm^2 (Industrial Physics, New Castle, Delaware, US). Silica gel (230-400 mesh particle size, Sigma-Aldrich) was dried for 24 h at 80 °C before placing 5.0 g of it into the cup's reservoir. The coated paper was placed coated-side-up on the cup and sealed with the screw lid. The assembly was weighed and placed into a desiccator containing a saturated solution of KCl. The resulting climate was a relative humidity of 85 % at approximately 20 °C. After an equilibration time of 3 days, the cups were taken out of the weighed at intervals of 8 h to 24 h to determine the mass change Δ_{m}. The results were plotted on a Δ_{m}-time curve and the weighing was repeated until at least three consecutive values were on a straight line with a deviation of less than 5 %.

8.6   Direct Ink Writing

Emulsion inks were made using CNCs extracted from pre-fibrillated pulp extracted at 160 °C for 4 h in the biggest reactor. The resulting aqueous CNC dispersion, approximately 10 mg mL^{-1}, was diluted to 5 mg mL^{-1} before use.

8.6.1   Fabrication of emulsions

Medium high-internal phase Pickering sunflower oil in water emulsions were fabricated using an IKA T25 basic ULTRA-TURRAX® (IKA-Werke GmbH & CO. KG, Staufen, Germany) in a two-step process: First, the desired volume of sunflower oil from a local supermarket was emulsified in the CNC dispersion for one minute at a speed of 24000 rpm.

Then, the α-CD solution (200 $mg\,mL^{-1}$) was added and the mixture was homogenized for another minute.

8.6.2 Direct ink writing

Direct ink writing was performed by Dr. Rubina Ajdary at the University of Aalto, Finland using a BIOX Bioprinter (CELLINK, Sweden) with a pneumatic printhead. The inks were transferred to a 20 mL clear syringe and were printed by extrusion through high-precision conical bioprinting nozzles 20-25 G with the diameters 250 µm and 410 µm. A plastic Petri dish served as solid support for the 3D-printed structures. The utilized 3D models were designed using the Autodesk Tinkercad software and the CELLINK 3D model archive. Printability was tested by printing an upright square lattice with 25 % infill density and the quality of the printing behavior was judged in terms of 1) formation of stable filament, 2) clogging, 3) occurrence of die swell, and 4) adhesion of printed layer to underlying layer. Two different nozzle diameters, 250 µm and 410 µm, were tested at a printing speed of 14 $mm\,s^{-1}$. Nozzle pressure varied between 19 kPa and 50 kPa. Specific values for all tested samples are given in Table 8.3. Printability was judged in terms of 1) formation of stable filament, 2) clogging, 3) occurrence of die swell, and 4) adhesion of printed layer to underlying layer.

Table 8.3: Printing pressures used for DIW of the tested emulsion inks.

	extrusion pressure [kPa]	
	nozzle size 250 µm	nozzle size 410 µm
EG-1	50	40
EG-2	38	33
EG-3	47	32
EGA-1	21-26	19-23
EGA-2	47	35
EGA-3	34	22-24

Bibliography

[1] J. I. Kroschwitz, M. Howe-Grant, R. E. Kirk, and D. F. Othmer, *Encyclopedia of chemical technology*. John Wiley & Sons, 1996.

[2] D. Klemm, F. Kramer, S. Moritz, T. Lindström, M. Ankerfors, D. Gray, and A. Dorris, "Nanocelluloses: A new family of nature-based materials," *Angewandte Chemie International Edition*, vol. 50, no. 24, pp. 5438–5466, 2011.

[3] D. Klemm, E. D. Cranston, D. Fischer, M. Gama, S. A. Kedzior, D. Kralisch, F. Kramer, T. Kondo, T. Lindström, S. Nietzsche, K. Petzold-Welcke, and F. Rauchfuß, "Nanocellulose as a natural source for groundbreaking applications in materials science: Today's state," *Materials Today*, vol. 21, no. 7, pp. 720–748, 2018.

[4] M. Antonietti, "Sustainable bulk structural material engineered from cellulose nanofibers," *Matter*, vol. 3, no. 2, pp. 339–340, 2020.

[5] P. T. Anastas and J. C. Warner, *Green chemistry: Theory and Practice*. Oxford England; New York: Oxford University Press, 1998.

[6] K. Tanaka and F. Toda, "Solvent-free organic synthesis," *Chemical Reviews*, vol. 100, no. 3, pp. 1025–1074, 2000.

[7] A. P. Abbott, G. Capper, D. L. Davies, R. K. Rasheed, and V. Tambyrajah, "Novel solvent properties of choline chloride/urea mixtures," *Chemical Communications*, no. 1, pp. 70–71, 2003.

[8] T. El Achkar, H. Greige-Gerges, and S. Fourmentin, "Basics and properties of deep eutectic solvents: a review," *Environmental Chemistry Letters*, 2021.

[9] J. A. Coutinho and S. P. Pinho, "Special issue on deep eutectic solvents: A foreword," *Fluid Phase Equilibria*, vol. 448, p. 1, 2017.

[10] Y. H. Choi, J. van Spronsen, Y. Dai, M. Verberne, F. Hollmann, I. W. Arends, G.-J. Witkamp, and R. Verpoorte, "Are natural deep eutectic solvents the missing link in understanding cellular metabolism and physiology?," *Plant Physiology*, vol. 156, no. 4, pp. 1701–1705, 2011.

[11] K. d. O. Vigier, G. Châtel, and F. Jérôme, "Contribution of deep eutectic solvents for biomass processing: Opportunities, challenges, and limitations," *ChemCatChem*, vol. 7, 2015.

[12] A. Satlewal, R. Agrawal, S. Bhagia, J. Sangoro, and A. Ragauskas, "Natural deep eutectic solvents for lignocellulosic biomass pretreatment: Recent developments, challenges and novel opportunities," *Biotechnology Advances*, vol. 36, 2018.

[13] E. Jaekel, K. S. Marcus, and S. Filonenko, "Chapter 4 - critical analysis of green solvent credentials of eutectic solvents," in *Current Developments in Biotechnology and Bioengi-*

neering (A. Pandey, B. Tiwari, A. Pandey, and S. Yusup, eds.), pp. 77–104, Elsevier, 2022.

[14] S. Bajkacz, J. Adamek, and A. Sobska, "Application of deep eutectic solvents and ionic liquids in the extraction of catechins from tea," *Molecules*, vol. 25, no. 14, 2020.

[15] N. Li, Y. Wang, K. Xu, Y. Huang, Q. Wen, and X. Ding, "Development of green betaine-based deep eutectic solvent aqueous two-phase system for the extraction of protein," *Talanta*, vol. 152, pp. 23–32, 2016.

[16] K. Xu, Y. Wang, Y. Huang, N. Li, and Q. Wen, "A green deep eutectic solvent-based aqueous two-phase system for protein extracting," *Analytica Chimica Acta*, vol. 864, pp. 9–20, 2015.

[17] A. P. Abbott, G. Capper, D. L. Davies, K. J. McKenzie, and S. U. Obi, "Solubility of metal oxides in deep eutectic solvents based on choline chloride," *Journal of Chemical & Engineering Data*, vol. 51, no. 4, pp. 1280–1282, 2006.

[18] A. P. Abbott, J. Collins, I. Dalrymple, R. C. Harris, R. Mistry, F. Qiu, J. Scheirer, and W. R. Wise, "Processing of electric arc furnace dust using deep eutectic solvents," *Australian Journal of Chemistry*, vol. 62, no. 4, pp. 341–347, 2009.

[19] M. K. Tran, M.-T. F. Rodrigues, K. Kato, G. Babu, and P. M. Ajayan, "Deep eutectic solvents for cathode recycling of li-ion batteries," *Nature Energy*, vol. 4, no. 4, pp. 339–345, 2019.

[20] S. Gore, S. Baskaran, and B. Koenig, "Efficient synthesis of 3,4-dihydropyrimidin-2-ones in low melting tartaric acid–urea mixtures," *Green Chemistry*, vol. 13, no. 4, pp. 1009–1013, 2011.

[21] F. del Monte, D. Carriazo, M. C. Serrano, M. C. Gutierrez, and M. L. Ferrer, "Deep eutectic solvents in polymerizations: a greener alternative to conventional syntheses," *ChemSusChem*, vol. 7, no. 4, pp. 999–1009, 2014.

[22] A. P. Abbott, K. J. McKenzie, and K. S. Ryder, *Electropolishing and Electroplating of Metals Using Ionic Liquids Based on Choline Chloride*, vol. 975 of *ACS Symposium Series*, book section 13, pp. 186–197. American Chemical Society, 2007.

[23] A. P. Abbott and K. J. McKenzie, "Application of ionic liquids to the electrodeposition of metals," *Physical Chemistry Chemical Physics*, vol. 8, no. 37, pp. 4265–4279, 2006.

[24] Y. Wang, K. H. Kim, K. Jeong, N.-K. Kim, and C. G. Yoo, "Sustainable biorefinery processes using renewable deep eutectic solvents," *Current Opinion in Green and Sustainable Chemistry*, vol. 27, p. 100396, 2021.

[25] M. Jablonsky, A. Haz, and V. Majova, "Assessing the opportunities for applying deep eutectic solvents for fractionation of beech wood and wheat straw," *Cellulose*, vol. 26, no. 13, pp. 7675–7684, 2019.

[26] T. Heinze, K. Schwikal, and S. Barthel, "Ionic liquids as reaction medium in cellulose functionalization," *Macromolecular Bioscience*, vol. 5, no. 6, pp. 520–525, 2005.

[27] Q. Zhang, K. De Oliveira Vigier, S. Royer, and F. Jérôme, "Deep eutectic solvents: syntheses, properties and applications," *Chemical Society Reviews*, vol. 41, no. 21, pp. 7108–7146, 2012.

[28] O. Laitinen, T. Suopajärvi, M. Österberg, and H. Liimatainen, "Hydrophobic, superabsorbing aerogels from choline chloride-based deep eutectic solvent pretreated and silylated

cellulose nanofibrils for selective oil removal," *ACS Applied Materials & Interfaces*, vol. 9, no. 29, pp. 25029–25037, 2017.

[29] P. Li, J. A. Sirviö, A. Haapala, and H. Liimatainen, "Cellulose nanofibrils from non-derivatizing urea-based deep eutectic solvent pretreatments," *ACS Applied Materials & Interfaces*, vol. 9, no. 3, pp. 2846–2855, 2017.

[30] T. Suopajärvi, J. A. Sirviö, and H. Liimatainen, "Nanofibrillation of deep eutectic solvent-treated paper and board cellulose pulps," *Carbohydrate Polymers*, vol. 169, pp. 167–175, 2017.

[31] U. Römling, "Molecular biology of cellulose production in bacteria," *Research in Microbiology*, vol. 153, no. 4, pp. 205–212, 2002.

[32] S. Kimura, C. Ohshima, E. Hirose, J. Nishikawa, and T. Itoh, "Cellulose in the house of the appendicularianoikopleura rufescens," *Protoplasma*, vol. 216, no. 1, p. 71, 2001.

[33] K. Heise, G. Delepierre, A. W. T. King, M. A. Kostiainen, J. Zoppe, C. Weder, and E. Kontturi, "Chemical modification of reducing end-groups in cellulose nanocrystals," *Angewandte Chemie International Edition*, vol. 60, 2020.

[34] Y. Habibi, L. A. Lucia, and O. J. Rojas, "Cellulose nanocrystals: Chemistry, self-assembly, and applications," *Chemical Reviews*, vol. 110, no. 6, pp. 3479–3500, 2010.

[35] A. N. Fernandes, L. H. Thomas, C. M. Altaner, P. Callow, V. T. Forsyth, D. C. Apperley, C. J. Kennedy, and M. C. Jarvis, "Nanostructure of cellulose microfibrils in spruce wood," *Proceedings of the National Academy of Sciences*, vol. 108, no. 47, pp. E1195–E1203, 2011.

[36] Y. Nishiyama, U.-J. Kim, D.-Y. Kim, K. S. Katsumata, R. P. May, and P. Langan, "Periodic disorder along ramie cellulose microfibrils," *Biomacromolecules*, vol. 4, no. 4, pp. 1013–1017, 2003.

[37] R. H. Atalla and D. L. VanderHart, "Native cellulose: A composite of two distinct crystalline forms," *Science*, vol. 223, no. 4633, pp. 283–285, 1984.

[38] C. M. Lee, A. Mittal, A. L. Barnette, K. Kafle, Y. B. Park, H. Shin, D. K. Johnson, S. Park, and S. H. Kim, "Cellulose polymorphism study with sum-frequency-generation (sfg) vibration spectroscopy: identification of exocyclic ch2oh conformation and chain orientation," *Cellulose*, vol. 20, no. 3, pp. 991–1000, 2013.

[39] K. Conley, L. Godbout, M. T. Whitehead, and T. G. van de Ven, "Origin of the twist of cellulosic materials," *Carbohydrate Polymers*, vol. 135, pp. 285–299, 2016.

[40] Z. Zhao, O. E. Shklyaev, A. Nili, M. N. A. Mohamed, J. D. Kubicki, V. H. Crespi, and L. Zhong, "Cellulose microfibril twist, mechanics, and implication for cellulose biosynthesis," *The Journal of Physical Chemistry A*, vol. 117, no. 12, pp. 2580–2589, 2013.

[41] D. P. Delmer and Y. Amor, "Cellulose biosynthesis," *Plant Cell*, vol. 7, no. 7, pp. 987–1000, 1995.

[42] J. Puls, S. A. Wilson, and D. Hölter, "Degradation of cellulose acetate-based materials: A review," *Journal of Polymers and the Environment*, vol. 19, no. 1, pp. 152–165, 2011.

[43] F. Dourado, A. Fontão, M. Leal, A. Cristina Rodrigues, and M. Gama, "Chapter 12 - process modeling and techno-economic evaluation of an industrial bacterial nanocellulose fermentation process," in *Bacterial Nanocellulose* (M. Gama, F. Dourado, and S. Bielecki, eds.), pp. 199–214, Amsterdam: Elsevier, 2016.

[44] A. Turbak, F. Snyder, and K. Sandberg, *Microfibrillated cellulose, a new cellulose product: properties, uses, and commercial potential.* Journal Name: J. Appl. Polym. Sci.: Appl. Polym. Symp.; (United States); Journal Volume: 37; Conference: 9. cellulose conference, Syracuse, NY, USA, 24 May 1982, ; ITT Rayonier Inc., Shelton, WA, 1983.

[45] M. Ghanadpour, F. Carosio, P. T. Larsson, and L. Wågberg, "Phosphorylated cellulose nanofibrils: A renewable nanomaterial for the preparation of intrinsically flame-retardant materials," *Biomacromolecules*, vol. 16, no. 10, pp. 3399–3410, 2015.

[46] H. Liimatainen, M. Visanko, J. Sirviö, O. Hormi, and J. Niinimäki, "Sulfonated cellulose nanofibrils obtained from wood pulp through regioselective oxidative bisulfite pretreatment," *Cellulose*, vol. 20, no. 2, pp. 741–749, 2013.

[47] H. Liimatainen, M. Visanko, J. A. Sirviö, O. E. O. Hormi, and J. Niinimaki, "Enhancement of the nanofibrillation of wood cellulose through sequential periodate–chlorite oxidation," *Biomacromolecules*, vol. 13, no. 5, pp. 1592–1597, 2012.

[48] A. Tejado, M. N. Alam, M. Antal, H. Yang, and T. G. M. van de Ven, "Energy requirements for the disintegration of cellulose fibers into cellulose nanofibers," *Cellulose*, vol. 19, no. 3, pp. 831–842, 2012.

[49] A. Olszewska, P. Eronen, L.-S. Johansson, J.-M. Malho, M. Ankerfors, T. Lindström, J. Ruokolainen, J. Laine, and M. Österberg, "The behaviour of cationic nanofibrillar cellulose in aqueous media," *Cellulose*, vol. 18, no. 5, p. 1213, 2011.

[50] A. Naderi, T. Lindström, J. Sundström, G. Flodberg, and J. Erlandsson, "A comparative study of the properties of three nanofibrillated cellulose systems that have been produced at about the same energy consumption levels in the mechanical delamination step," *Nordic Pulp & Paper Research Journal*, vol. 31, no. 3, p. 364, 2016.

[51] T. Saito, Y. Nishiyama, J.-L. Putaux, M. Vignon, and A. Isogai, "Homogeneous suspensions of individualized microfibrils from tempo-catalyzed oxidation of native cellulose," *Biomacromolecules*, vol. 7, no. 6, pp. 1687–1691, 2006.

[52] T. Saito, R. Kuramae, J. Wohlert, L. A. Berglund, and A. Isogai, "An ultrastrong nanofibrillar biomaterial: The strength of single cellulose nanofibrils revealed via sonication-induced fragmentation," *Biomacromolecules*, vol. 14, no. 1, pp. 248–253, 2013.

[53] J. Chen, Y. Zhu, Q. Ni, Y. Fu, and X. Fu, "Surface modification and characterization of aramid fibers with hybrid coating," *Applied Surface Science*, vol. 321, pp. 103–108, 2014.

[54] H. Kargarzadeh, M. Mariano, J. Huang, N. Lin, I. Ahmad, A. Dufresne, and S. Thomas, "Recent developments on nanocellulose reinforced polymer nanocomposites: A review," *Polymer*, vol. 132, pp. 368–393, 2017.

[55] E. Kontturi, *Preparation of cellulose nanocrystals: Background, conventions and new developments*, book section 3, pp. 27–44. CRC Press, 2018.

[56] S. Elazzouzi-Hafraoui, Y. Nishiyama, J.-L. Putaux, L. Heux, F. Dubreuil, and C. Rochas, "The shape and size distribution of crystalline nanoparticles prepared by acid hydrolysis of native cellulose," *Biomacromolecules*, vol. 9, no. 1, pp. 57–65, 2008.

[57] E. Kontturi and T. Vuorinen, "Indirect evidence of supramolecular changes within cellulose microfibrils of chemical pulp fibers upon drying," *Cellulose*, vol. 16, no. 1, pp. 65–74, 2009.

[58] X. M. Dong, J.-F. Revol, and D. G. Gray, "Effect of microcrystallite preparation conditions on the formation of colloid crystals of cellulose," *Cellulose*, vol. 5, no. 1, pp. 19–32, 1998.

[59] E. Niinivaara, M. Faustini, T. Tammelin, and E. Kontturi, "Mimicking the humidity response of the plant cell wall by using two-dimensional systems: The critical role of amorphous and crystalline polysaccharides," *Langmuir*, vol. 32, no. 8, pp. 2032–2040, 2016.

[60] A. Hirai, O. Inui, F. Horii, and M. Tsuji, "Phase separation behavior in aqueous suspensions of bacterial cellulose nanocrystals prepared by sulfuric acid treatment," *Langmuir*, vol. 25, no. 1, pp. 497–502, 2009.

[61] N. F. Vasconcelos, J. P. A. Feitosa, F. M. P. da Gama, J. P. S. Morais, F. K. Andrade, M. de Sá Moreira de Souza Filho, and M. de Freitas Rosa, "Bacterial cellulose nanocrystals produced under different hydrolysis conditions: Properties and morphological features," *Carbohydrate Polymers*, vol. 155, pp. 425–431, 2017.

[62] I. A. Sacui, R. C. Nieuwendaal, D. J. Burnett, S. J. Stranick, M. Jorfi, C. Weder, E. J. Foster, R. T. Olsson, and J. W. Gilman, "Comparison of the properties of cellulose nanocrystals and cellulose nanofibrils isolated from bacteria, tunicate, and wood processed using acid, enzymatic, mechanical, and oxidative methods," *ACS Applied Materials & Interfaces*, vol. 6, no. 9, pp. 6127–6138, 2014.

[63] E. Fortunati, F. Luzi, A. Jiménez, D. Gopakumar, D. Puglia, S. Thomas, J. Kenny, A. Chiralt, and L. Torre, "Revalorization of sunflower stalks as novel sources of cellulose nanofibrils and nanocrystals and their effect on wheat gluten bionanocomposite properties," *Carbohydrate Polymers*, vol. 149, pp. 357–368, 2016.

[64] F. Jiang and Y.-L. Hsieh, "Cellulose nanocrystal isolation from tomato peels and assembled nanofibers," *Carbohydrate Polymers*, vol. 122, pp. 60–68, 2015.

[65] O. A. Battista, "Hydrolysis and crystallization of cellulose," *Industrial & Engineering Chemistry*, vol. 42, no. 3, pp. 502–507, 1950.

[66] M. L. Nelson and V. W. Tripp, "Determination of the leveling-off degree of polymerization of cottonand rayon," *Journal of Polymer Science*, vol. 10, no. 6, pp. 577–586, 1953.

[67] R. F. Nickerson and J. A. Habrle, "Cellulose intercrystalline structure," *Industrial & Engineering Chemistry*, vol. 39, no. 11, pp. 1507–1512, 1947.

[68] J. F. Revol, H. Bradford, J. Giasson, R. H. Marchessault, and D. G. Gray, "Helicoidal self-ordering of cellulose microfibrils in aqueous suspension," *International Journal of Biological Macromolecules*, vol. 14, no. 3, pp. 170–172, 1992.

[69] R. M. Parker, G. Guidetti, C. A. Williams, T. Zhao, A. Narkevicius, S. Vignolini, and B. Frka-Petesic, "The self-assembly of cellulose nanocrystals: Hierarchical design of visual appearance," *Advanced Materials*, vol. 30, no. 19, p. 1704477, 2018.

[70] O. M. Vanderfleet, M. S. Reid, J. Bras, L. Heux, J. Godoy-Vargas, M. K. R. Panga, and E. D. Cranston, "Insight into thermal stability of cellulose nanocrystals from new hydrolysis methods with acid blends," *Cellulose*, vol. 26, no. 1, pp. 507–528, 2019.

[71] S. Camarero Espinosa, T. Kuhnt, E. J. Foster, and C. Weder, "Isolation of thermally stable cellulose nanocrystals by phosphoric acid hydrolysis," *Biomacromolecules*, vol. 14, no. 4, pp. 1223–1230, 2013.

[72] H. Sadeghifar, I. Filpponen, S. P. Clarke, D. F. Brougham, and D. S. Argyropoulos, "Production of cellulose nanocrystals using hydrobromic acid and click reactions on their surface," *Journal of Materials Science*, vol. 46, no. 22, pp. 7344–7355, 2011.

[73] T. Okano, S. Kuga, M. Wada, J. Araki, and J. Ikuina, "Nisshin oil mills ltd," *Patent JP*, vol. 98, p. 151052, 1999.

[74] O. M. Vanderfleet, D. A. Osorio, and E. D. Cranston, "Optimization of cellulose nanocrystal length and surface charge density through phosphoric acid hydrolysis," *Philosophical Transactions of the Royal Society A: Mathematical, Physical and Engineering Sciences*, vol. 376, no. 2112, p. 20170041, 2018.

[75] L. Chen, J. Y. Zhu, C. Baez, P. Kitin, and T. Elder, "Highly thermal-stable and functional cellulose nanocrystals and nanofibrils produced using fully recyclable organic acids," *Green Chem.*, vol. 18, pp. 3835–3843, 2016.

[76] S. J. Eichhorn, "Cellulose nanowhiskers: promising materials for advanced applications," *Soft Matter*, vol. 7, pp. 303–315, 2011.

[77] M. S. Peresin, Y. Habibi, J. O. Zoppe, J. J. Pawlak, and O. J. Rojas, "Nanofiber composites of polyvinyl alcohol and cellulose nanocrystals: Manufacture and characterization," *Biomacromolecules*, vol. 11, no. 3, pp. 674–681, 2010.

[78] X. Cao, H. Dong, and C. M. Li, "New nanocomposite materials reinforced with flax cellulose nanocrystals in waterborne polyurethane," *Biomacromolecules*, vol. 8, no. 3, pp. 899–904, 2007.

[79] G. Siqueira, H. Abdillahi, J. Bras, and A. Dufresne, "High reinforcing capability cellulose nanocrystals extracted from syngonanthus nitens (capim dourado)," *Cellulose*, vol. 17, no. 2, pp. 289–298, 2010.

[80] M. R. Dousti, Y. Boluk, and V. Bindiganavile, "The effect of cellulose nanocrystal (cnc) particles on the porosity and strength development in oil well cement paste," *Construction and Building Materials*, vol. 205, pp. 456–462, 2019.

[81] P. Dhar, U. Bhardwaj, A. Kumar, and V. Katiyar, "Poly (3-hydroxybutyrate)/cellulose nanocrystal films for food packaging applications: Barrier and migration studies," *Polymer Engineering & Science*, vol. 55, no. 10, pp. 2388–2395, 2015.

[82] J. P. F. Lagerwall, C. Schütz, M. Salajkova, J. Noh, J. Hyun Park, G. Scalia, and L. Bergström, "Cellulose nanocrystal-based materials: from liquid crystal self-assembly and glass formation to multifunctional thin films," *NPG Asia Materials*, vol. 6, no. 1, pp. e80–e80, 2014.

[83] D. Bagheriasl, P. J. Carreau, B. Riedl, C. Dubois, and W. Y. Hamad, "Shear rheology of polylactide (pla)–cellulose nanocrystal (cnc) nanocomposites," *Cellulose*, vol. 23, no. 3, pp. 1885–1897, 2016.

[84] M.-C. Li, Q. Wu, K. Song, C. F. De Hoop, S. Lee, Y. Qing, and Y. Wu, "Cellulose nanocrystals and polyanionic cellulose as additives in bentonite water-based drilling fluids: Rheological modeling and filtration mechanisms," *Industrial & Engineering Chemistry Research*, vol. 55, no. 1, pp. 133–143, 2016.

[85] B. Wicklein, A. Kocjan, G. Salazar-Alvarez, F. Carosio, G. Camino, M. Antonietti, and L. Bergström, "Thermally insulating and fire-retardant lightweight anisotropic foams based on nanocellulose and graphene oxide," *Nature Nanotechnology*, vol. 10, no. 3, pp. 277–283, 2015.

[86] H. Dai, J. Wu, H. Zhang, Y. Chen, L. Ma, H. Huang, Y. Huang, and Y. Zhang, "Recent advances on cellulose nanocrystals for pickering emulsions: Development and challenge," *Trends in Food Science & Technology*, vol. 102, pp. 16–29, 2020.

[87] G. C. Inskeep and P. V. Horn, "Cellophane," *Industrial & Engineering Chemistry*, vol. 44, no. 11, pp. 2511–2524, 1952.

[88] C. Calvino, N. Macke, R. Kato, and S. J. Rowan, "Development, processing and applications of bio-sourced cellulose nanocrystal composites," *Progress in Polymer Science*, vol. 103, p. 101221, 2020.

[89] F. Rafieian, M. Shahedi, J. Keramat, and J. Simonsen, "Mechanical, thermal and barrier properties of nano-biocomposite based on gluten and carboxylated cellulose nanocrystals," *Industrial Crops and Products*, vol. 53, pp. 282–288, 2014.

[90] M. Nuruddin, R. A. Chowdhury, R. Szeto, J. A. Howarter, K. A. Erk, C. R. Szczepanski, and J. P. Youngblood, "Structure–property relationship of cellulose nanocrystal–polyvinyl alcohol thin films for high barrier coating applications," *ACS Applied Materials & Interfaces*, vol. 13, no. 10, pp. 12472–12482, 2021.

[91] A. Nazrin, S. M. Sapuan, M. Y. M. Zuhri, R. A. Ilyas, R. Syafiq, and S. F. K. Sherwani, "Nanocellulose reinforced thermoplastic starch (tps), polylactic acid (pla), and polybutylene succinate (pbs) for food packaging applications," *Frontiers in chemistry*, vol. 8, pp. 213–213, 2020.

[92] N. Vigneshwaran, L. Ammayappan, and Q. Huang, "Effect of gum arabic on distribution behavior of nanocellulose fillers in starch film," *Applied Nanoscience*, vol. 1, no. 3, pp. 137–142, 2011.

[93] N. A. El-Wakil, E. A. Hassan, R. E. Abou-Zeid, and A. Dufresne, "Development of wheat gluten/nanocellulose/titanium dioxide nanocomposites for active food packaging," *Carbohydrate Polymers*, vol. 124, pp. 337–346, 2015.

[94] J. Fernández-Santos, C. Valls, O. Cusola, and M. B. Roncero, "Improving filmogenic and barrier properties of nanocellulose films by addition of biodegradable plasticizers," *ACS Sustainable Chemistry & Engineering*, vol. 9, no. 29, pp. 9647–9660, 2021.

[95] A. F. Ismail, K. C. Khulbe, and T. Matsuura, *Fundamentals of Gas Permeation Through Membranes*, pp. 11–35. Cham: Springer International Publishing, 2015.

[96] J. G. A. Bitter, "Effect of crystallinity and swelling on the permeability and selectivity of polymer membranes," *Desalination*, vol. 51, no. 1, pp. 19–35, 1984.

[97] L. M. Robeson, "Correlation of separation factor versus permeability for polymeric membranes," *Journal of Membrane Science*, vol. 62, pp. 165–185, 1991.

[98] L. M. Robeson, "The upper bound revisited," *Journal of Membrane Science*, vol. 320, no. 1, pp. 390–400, 2008.

[99] W. Ramsden and F. Gotch, "Separation of solids in the surface-layers of solutions and 'suspensions' (observations on surface-membranes, bubbles, emulsions, and mechanical coagulation).—preliminary account," *Proceedings of the Royal Society of London*, vol. 72, no. 477-486, pp. 156–164, 1904.

[100] S. U. Pickering, "Cxcvi.—emulsions," *J. Chem. Soc., Trans.*, vol. 91, pp. 2001–2021, 1907.

[101] B. Binks, "Macroporous silica from solid-stabilized emulsion templates," *Advanced Materials*, vol. 14, no. 24, pp. 1824–1827, 2002.

[102] K. Lee, ed., *Nanocellulose and Sustainability: Production, Properties, Applications, and Case Studies.* CRC Press, 2018.

[103] H. A. Barnes, "Rheology of emulsions — a review," *Colloids and Surfaces A: Physico-chemical and Engineering Aspects*, vol. 91, pp. 89–95, 1994.

[104] I. Kalashnikova, H. Bizot, B. Cathala, and I. Capron, "New pickering emulsions stabilized by bacterial cellulose nanocrystals," *Langmuir*, vol. 27, no. 12, pp. 7471–7479, 2011.

[105] I. Kalashnikova, H. Bizot, B. Cathala, and I. Capron, "Modulation of cellulose nanocrystals amphiphilic properties to stabilize oil/water interface," *Biomacromolecules*, vol. 13, no. 1, pp. 267–275, 2012.

[106] M. K. Inglesby and S. H. Zeronian, "Direct dyes as molecular sensors to characterize cellulose substrates," *Cellulose*, vol. 9, no. 1, pp. 19–29, 2002.

[107] K. Mazeau and A. Rivet, "Wetting the (110) and (100) surfaces of iβ cellulose studied by molecular dynamics," *Biomacromolecules*, vol. 9, no. 4, pp. 1352–1354, 2008.

[108] K. Mazeau, "On the external morphology of native cellulose microfibrils," *Carbohydrate Polymers*, vol. 84, no. 1, pp. 524–532, 2011.

[109] H. P. Fink, D. Hofmann, and B. Philipp, "Some aspects of lateral chain order in cellulosics from x-ray scattering," *Cellulose*, vol. 2, pp. 51–70, 1995.

[110] F. Cherhal, F. Cousin, and I. Capron, "Influence of charge density and ionic strength on the aggregation process of cellulose nanocrystals in aqueous suspension, as revealed by small-angle neutron scattering," *Langmuir*, vol. 31, no. 20, pp. 5596–5602, 2015.

[111] I. Kalashnikova, H. Bizot, P. Bertoncini, B. Cathala, and I. Capron, "Cellulosic nanorods of various aspect ratios for oil in water pickering emulsions," *Soft Matter*, vol. 9, pp. 952–959, 2013.

[112] M. A. S. R. Saadi, A. Maguire, N. T. Pottackal, M. S. H. Thakur, M. M. Ikram, A. J. Hart, P. M. Ajayan, and M. M. Rahman, "Direct ink writing: A 3d printing technology for diverse materials," *Advanced Materials*, vol. 34, no. 28, p. 2108855, 2022.

[113] R. Ajdary, S. Huan, N. Zanjanizadeh Ezazi, W. Xiang, R. Grande, H. A. Santos, and O. J. Rojas, "Acetylated nanocellulose for single-component bioinks and cell proliferation on 3d-printed scaffolds," *Biomacromolecules*, vol. 20, no. 7, pp. 2770–2778, 2019.

[114] M. K. Hausmann, G. Siqueira, R. Libanori, D. Kokkinis, A. Neels, T. Zimmermann, and A. R. Studart, "Complex-shaped cellulose composites made by wet densification of 3d printed scaffolds," *Advanced Functional Materials*, vol. 30, no. 4, p. 1904127, 2020.

[115] L. A. E. Müller, T. Zimmermann, G. Nyström, I. Burgert, and G. Siqueira, "Mechanical properties tailoring of 3d printed photoresponsive nanocellulose composites," *Advanced Functional Materials*, vol. 30, no. 35, p. 2002914, 2020.

[116] K. Markstedt, A. Mantas, I. Tournier, H. Martínez Ávila, D. Hägg, and P. Gatenholm, "3d bioprinting human chondrocytes with nanocellulose–alginate bioink for cartilage tissue engineering applications," *Biomacromolecules*, vol. 16, no. 5, pp. 1489–1496, 2015.

[117] R. Das, T. Lindström, P. R. Sharma, K. Chi, and B. S. Hsiao, "Nanocellulose for sustainable water purification," *Chemical Reviews*, vol. 122, no. 9, pp. 8936–9031, 2022.

[118] X.-M. Fan, H.-Y. Yu, D.-C. Wang, Z.-H. Mao, J. Yao, and K. C. Tam, "Facile and green synthesis of carboxylated cellulose nanocrystals as efficient adsorbents in wastewater treatments," *ACS Sustainable Chemistry & Engineering*, vol. 7, no. 21, pp. 18067–18075, 2019.

[119] H. Sehaqui, A. Mautner, U. Perez de Larraya, N. Pfenninger, P. Tingaut, and T. Zimmermann, "Cationic cellulose nanofibers from waste pulp residues and their nitrate, fluoride,

sulphate and phosphate adsorption properties," *Carbohydrate Polymers*, vol. 135, pp. 334–340, 2016.

[120] M. Hasani, E. D. Cranston, G. Westman, and D. G. Gray, "Cationic surface functionalization of cellulose nanocrystals," *Soft Matter*, vol. 4, pp. 2238–2244, 2008.

[121] S. P. Akhlaghi, M. Zaman, N. Mohammed, C. Brinatti, R. Batmaz, R. Berry, W. Loh, and K. C. Tam, "Synthesis of amine functionalized cellulose nanocrystals: optimization and characterization," *Carbohydrate Research*, vol. 409, pp. 48–55, 2015.

[122] T. Selkälä, J. A. Sirviö, G. S. Lorite, and H. Liimatainen, "Anionically stabilized cellulose nanofibrils through succinylation pretreatment in urea–lithium chloride deep eutectic solvent," *ChemSusChem*, vol. 9, no. 21, pp. 3074–3083, 2016.

[123] J. A. Sirviö, M. Visanko, and H. Liimatainen, "Acidic deep eutectic solvents as hydrolytic media for cellulose nanocrystal production," *Biomacromolecules*, vol. 17, no. 9, pp. 3025–3032, 2016.

[124] O. Laitinen, J. Ojala, J. A. Sirviö, and H. Liimatainen, "Sustainable stabilization of oil in water emulsions by cellulose nanocrystals synthesized from deep eutectic solvents," *Cellulose*, vol. 24, no. 4, pp. 1679–1689, 2017.

[125] J. A. Sirviö and M. Visanko, "Anionic wood nanofibers produced from unbleached mechanical pulp by highly efficient chemical modification," *Journal of Materials Chemistry A*, vol. 5, no. 41, pp. 21828–21835, 2017.

[126] J. A. Sirviö, J. Ukkola, and H. Liimatainen, "Direct sulfation of cellulose fibers using a reactive deep eutectic solvent to produce highly charged cellulose nanofibers," *Cellulose*, vol. 26, no. 4, pp. 2303–2316, 2019.

[127] H. Liimatainen, T. Suopajärvi, J. Sirviö, O. Hormi, and J. Niinimäki, "Fabrication of cationic cellulosic nanofibrils through aqueous quaternization pretreatment and their use in colloid aggregation," *Carbohydrate polymers*, vol. 103, pp. 187–192, 2014.

[128] P. Li, J. A. Sirviö, B. Asante, and H. Liimatainen, "Recyclable deep eutectic solvent for the production of cationic nanocelluloses," *Carbohydrate Polymers*, vol. 199, pp. 219–227, 2018.

[129] J. A. Sirviö, "Cationization of lignocellulosic fibers with betaine in deep eutectic solvent: Facile route to charge stabilized cellulose and wood nanofibers," *Carbohydrate Polymers*, vol. 198, pp. 34–40, 2018.

[130] S. Filonenko, A. Voelkel, and M. Antonietti, "Valorization of monosaccharides towards fructopyrazines in a new sustainable and efficient eutectic medium," *Green Chemistry*, vol. 21, no. 19, pp. 5256–5266, 2019.

[131] H.-J. Endres and A. Siebert-Raths, *Technische Biopolymere*. Hanser Verlag, 2009.

[132] E. E. Jaekel, J. A. Sirviö, M. Antonietti, and S. Filonenko, "One-step method for the preparation of cationic nanocellulose in reactive eutectic media," *Green Chemistry*, vol. 23, no. 6, pp. 2317–2323, 2021.

[133] M. Antonietti, S. Filonenko, and E. Jaekel, "An efficient green process for the preparation of nanocelluloses, novel modified nanocelluloses and their application.," Mar. 2022. WO2022042842.

[134] N. López-Salas, J. M. Vicent-Luna, S. Imberti, E. Posada, M. J. Roldán, J. A. Anta, S. R. G. Balestra, R. M. Madero Castro, S. Calero, R. J. Jiménez-Riobóo, M. C. Gutiérrez,

M. L. Ferrer, and F. del Monte, "Looking at the "water-in-deep-eutectic-solvent" system: A dilution range for high performance eutectics," *ACS Sustainable Chemistry & Engineering*, vol. 7, no. 21, pp. 17565–17573, 2019.

[135] F. S. Mjalli and J. Naser, "Viscosity model for choline chloride-based deep eutectic solvents," *Asia-Pacific Journal of Chemical Engineering*, vol. 10, no. 2, pp. 273–281, 2015.

[136] K. K. Pandey, "A study of chemical structure of soft and hardwood and wood polymers by ftir spectroscopy," *Journal of Applied Polymer Science*, vol. 71, no. 12, pp. 1969–1975, 1999.

[137] G. Socrates, "Infrared and raman characteristic group frequencies. tables and charts george socrates john wiley and sons, ltd, chichester, third edition, 2001.," *Journal of Raman Spectroscopy*, vol. 35, no. 10, pp. 905–905, 2004.

[138] P. J. Larkin, *General Outline for IR and Raman Spectral Interpretation*, book section 7, pp. 135–151. Elsevier, 2018.

[139] S. P. Akhlaghi, R. C. Berry, and K. C. Tam, "Surface modification of cellulose nanocrystal with chitosan oligosaccharide for drug delivery applications," *Cellulose*, vol. 20, no. 4, pp. 1747–1764, 2013.

[140] A. Domard, C. Gey, M. Rinaudo, and C. Terrassin, "13c and 1h n.m.r. spectroscopy of chitosan and n-trimethyl chloride derivatives," *International Journal of Biological Macromolecules*, vol. 9, no. 4, pp. 233–237, 1987.

[141] W. M. Facchinatto, D. M. d. Santos, A. Fiamingo, R. Bernardes-Filho, S. P. Campana-Filho, E. R. d. Azevedo, and L. A. Colnago, "Evaluation of chitosan crystallinity: A high-resolution solid-state nmr spectroscopy approach," *Carbohydrate Polymers*, vol. 250, p. 116891, 2020.

[142] P. B. Groszewicz, P. Mendes, B. Kumari, J. Lins, M. Biesalski, T. Gutmann, and G. Buntkowsky, "N-hydroxysuccinimide-activated esters as a functionalization agent for amino cellulose: synthesis and solid-state nmr characterization," *Cellulose*, vol. 27, no. 3, pp. 1239–1254, 2020.

[143] F. Azzam, L. Heux, J.-L. Putaux, and B. Jean, "Preparation by grafting onto, characterization, and properties of thermally responsive polymer-decorated cellulose nanocrystals," *Biomacromolecules*, vol. 11, no. 12, pp. 3652–3659, 2010.

[144] G. Lawrie, I. Keen, B. Drew, A. Chandler-Temple, L. Rintoul, P. Fredericks, and L. Grøndahl, "Interactions between alginate and chitosan biopolymers characterized using ftir and xps," *Biomacromolecules*, vol. 8, no. 8, pp. 2533–2541, 2007.

[145] R. A. L. Michael D. Larrañaga, Richard J. Lewis Sr., *Hawley's Condensed Chemical Dictionary*, ch. 7, p. 670. John Wiley & Sons, Ltd, 16 ed., 2016.

[146] O. Kröcher, M. Elsener, and E. Jacob, "A model gas study of ammonium formate, methanamide and guanidinium formate as alternative ammonia precursor compounds for the selective catalytic reduction of nitrogen oxides in diesel exhaust gas," *Applied Catalysis B: Environmental*, vol. 88, no. 1, pp. 66–82, 2009.

[147] F. Cataldo, G. Patanè, and G. Compagnini, "Synthesis of hcn polymer from thermal decomposition of formamide," *Journal of Macromolecular Science, Part A*, vol. 46, no. 11, pp. 1039–1048, 2009.

[148] C. B. Pollard and D. C. Young, "The mechanism of the leuckart reaction," *The Journal of Organic Chemistry*, vol. 16, no. 5, pp. 661–672, 1951.

[149] E.-L. Hult, P. Larsson, and T. Iversen, "Cellulose fibril aggregation — an inherent property of kraft pulps," *Polymer*, vol. 42, no. 8, pp. 3309–3314, 2001.

[150] R. Evans and A. F. A. Wallis, "Cellulose molecular weights determined by viscometry," *Journal of Applied Polymer Science*, vol. 37, no. 8, pp. 2331–2340, 1989.

[151] A. Thygesen, J. Oddershede, H. Lilholt, A. Bjerre, and K. Ståhl, "On the determination of crystallinity and cellulose content in plant fibres," *Cellulose*, vol. 12, pp. 563–576, 2005.

[152] O. A. Battista, S. Coppick, J. A. Howsmon, F. F. Morehead, and W. A. Sisson, "Level-off degree of polymerization," *Industrial & Engineering Chemistry*, vol. 48, no. 2, pp. 333–335, 1956.

[153] A. K. Mohanty, M. Misra, and G. Hinrichsen, "Biofibres, biodegradable polymers and biocomposites: An overview," *Macromolecular Materials and Engineering*, vol. 276-277, no. 1, pp. 1–24, 2000.

[154] Y. Zhao and J. Li, "Excellent chemical and material cellulose from tunicates: diversity in cellulose production yield and chemical and morphological structures from different tunicate species," *Cellulose*, vol. 21, no. 5, pp. 3427–3441, 2014.

[155] J. Bouchard, M. Méthot, C. Fraschini, and S. Beck, "Effect of oligosaccharide deposition on the surface of cellulose nanocrystals as a function of acid hydrolysis temperature," *Cellulose*, vol. 23, no. 6, pp. 3555–3567, 2016.

[156] V. H. Krässig, "Untersuchungen zur konstitution des tunicins. 408. mitteilung über makromolekulare verbindungen," *Die Makromolekulare Chemie*, vol. 13, no. 1, pp. 21–29, 1954.

[157] O. Theander and D. A. Nelson, "Aqueous, high-temperature transformation of carbohydrates relative to utilization of biomass," vol. 46 of *Advances in Carbohydrate Chemistry and Biochemistry*, pp. 273–326, Academic Press, 1988.

[158] S. Matsuoka, H. Kawamoto, and S. Saka, "What is active cellulose in pyrolysis? an approach based on reactivity of cellulose reducing end," *Journal of Analytical and Applied Pyrolysis*, vol. 106, pp. 138–146, 2014.

[159] H. Kargarzadeh, I. Ahmad, I. Abdullah, A. Dufresne, S. Y. Zainudin, and R. M. Sheltami, "Effects of hydrolysis conditions on the morphology, crystallinity, and thermal stability of cellulose nanocrystals extracted from kenaf bast fibers," *Cellulose*, vol. 19, no. 3, pp. 855–866, 2012.

[160] H. Fukuzumi, T. Saito, Y. Okita, and A. Isogai, "Thermal stabilization of tempo-oxidized cellulose," *Polymer Degradation and Stability*, vol. 95, no. 9, pp. 1502–1508, 2010.

[161] D. de Britto and O. B. G. Assis, "Thermal degradation of carboxymethylcellulose in different salty forms," *Thermochimica Acta*, vol. 494, no. 1, pp. 115–122, 2009.

[162] A. W. T. King, V. Mäkelä, S. A. Kedzior, T. Laaksonen, G. J. Partl, S. Heikkinen, H. Koskela, H. A. Heikkinen, A. J. Holding, E. D. Cranston, and I. Kilpeläinen, "Liquid-state nmr analysis of nanocelluloses," *Biomacromolecules*, vol. 19, no. 7, pp. 2708–2720, 2018.

[163] M. Jullian, A. Hernandez, A. Maurras, K. Puget, M. Amblard, J. Martinez, and G. Subra, "N-terminus fitc labeling of peptides on solid support: the truth behind the spacer," *Tetrahedron Letters*, vol. 50, no. 3, pp. 260–263, 2009.

[164] W. Xu, J. Riikonen, T. Nissinen, M. Suvanto, K. Rilla, B. Li, Q. Wang, F. Deng, and V.-P. Lehto, "Amine surface modifications and fluorescent labeling of thermally stabilized

mesoporous silicon nanoparticles," *The Journal of Physical Chemistry C*, vol. 116, no. 42, pp. 22307–22314, 2012.

[165] S. Dong and M. Roman, "Fluorescently labeled cellulose nanocrystals for bioimaging applications," *Journal of the American Chemical Society*, vol. 129, no. 45, pp. 13810–13811, 2007.

[166] P. C. Weber, D. H. Ohlendorf, J. J. Wendoloski, and F. R. Salemme, "Structural origins of high-affinity biotin binding to streptavidin," *Science*, vol. 243, no. 4887, pp. 85–88, 1989.

[167] P. Sorlier, A. Denuzière, C. Viton, and A. Domard, "Relation between the degree of acetylation and the electrostatic properties of chitin and chitosan," *Biomacromolecules*, vol. 2, no. 3, pp. 765–772, 2001.

[168] T. Nakamura, S. Nishihama, and K. Yoshizuka, "A novel extractant based on d-glucosamine for the extraction of molybdenum and tungsten," *Solvent Extraction Research and Development*, vol. 16, 01 2009.

[169] A. Blaskó, C. A. Bunton, S. Bunel, C. Ibarra, and E. Moraga, "Determination of acid dissociation constants of anomers of amino sugars by 1h nmr spectroscopy," *Carbohydrate Research*, vol. 298, no. 3, pp. 163–172, 1997.

[170] Q. Chen, P. Liu, F. Nan, L. Zhou, and J. Zhang, "Tuning the iridescence of chiral nematic cellulose nanocrystal films with a vacuum-assisted self-assembly technique," *Biomacromolecules*, vol. 15, no. 11, pp. 4343–4350, 2014.

[171] S. Wang and X. Wang, "Imidazolium ionic liquids, imidazolylidene heterocyclic carbenes, and zeolitic imidazolate frameworks for co2 capture and photochemical reduction," *Angewandte Chemie International Edition*, vol. 55, no. 7, pp. 2308–2320, 2016.

[172] E. Santos, J. Albo, and A. Irabien, "Acetate based supported ionic liquid membranes (silms) for co2 separation: Influence of the temperature," *Journal of Membrane Science*, vol. 452, pp. 277–283, 2014.

[173] M. Younas, T. Tahir, C. Wu, S. Farrukh, Q. Sohaib, A. Muhammad, M. Rezakazemi, and J. Li, "Post-combustion co2 capture with sweep gas in thin film composite (tfc) hollow fiber membrane (hfm) contactor," *Journal of CO2 Utilization*, vol. 40, p. 101266, 2020.

[174] B. Lam, M. Wei, L. Zhu, S. Luo, R. Guo, A. Morisato, P. Alexandridis, and H. Lin, "Cellulose triacetate doped with ionic liquids for membrane gas separation," *Polymer*, vol. 89, pp. 1–11, 2016.

[175] N. Yadav and M. Hakkarainen, "Degradable or not? cellulose acetate as a model for complicated interplay between structure, environment and degradation," *Chemosphere*, vol. 265, p. 128731, 2021.

[176] R. P. Swatloski, S. K. Spear, J. D. Holbrey, and R. D. Rogers, "Dissolution of cellose with ionic liquids," *Journal of the American Chemical Society*, vol. 124, no. 18, pp. 4974–4975, 2002.

[177] Y. Fukaya, K. Hayashi, M. Wada, and H. Ohno, "Cellulose dissolution with polar ionic liquids under mild conditions: required factors for anions," *Green Chemistry*, vol. 10, no. 1, pp. 44–46, 2008.

[178] S. Janakiram, L. Ansaloni, S.-A. Jin, X. Yu, Z. Dai, R. J. Spontak, and L. Deng, "Humidity-responsive molecular gate-opening mechanism for gas separation in ultraselective nanocellulose/il hybrid membranes," *Green Chemistry*, vol. 22, no. 11, pp. 3546–3557, 2020.

[179] O. Danyliv, M. Strach, O. Nechyporchuk, T. Nypelö, and A. Martinelli, "Self-standing, robust membranes made of cellulose nanocrystals (cncs) and a protic ionic liquid: Toward sustainable electrolytes for fuel cells," *ACS Applied Energy Materials*, vol. 4, no. 7, pp. 6474–6485, 2021.

[180] E. Vilarrasa-García, J. A. Cecilia, P. A. S. Moura, D. C. S. Azevedo, and E. Rodríguez-Castellón, "Assessing co(2) adsorption on amino-functionalized mesocellular foams synthesized at different aging temperatures," *Front Chem*, vol. 8, p. 591766, 2020.

[181] Z. Qian, L. Wei, W. Mingyue, and Q. Guansheng, "Application of amine-modified porous materials for co2 adsorption in mine confined spaces," *Colloids and Surfaces A: Physicochemical and Engineering Aspects*, vol. 629, p. 127483, 2021.

[182] M. Kurek, M. Ščetar, A. Voilley, K. Galić, and F. Debeaufort, "Barrier properties of chitosan coated polyethylene," *Journal of Membrane Science*, vol. 403-404, pp. 162–168, 2012.

[183] E. E. Jaekel, S. Kluge, S. Tröger-Müller, M. Tutuş, and S. Filonenko, "Tunable gas permeation behavior in self-standing cellulose nanocrystal-based membranes," *ACS Sustainable Chemistry & Engineering*, vol. 10, no. 38, pp. 12895–12905, 2022.

[184] A. Javaid, "Membranes for solubility-based gas separation applications," *Chemical Engineering Journal*, vol. 112, no. 1, pp. 219–226, 2005.

[185] D. R. Haynes, William M. Lide, *CRC handbook of chemistry and physics*. internet version 2020, 101st print edition ed., 2020.

[186] D. Ambrose and C. Tsonopoulos, "Vapor-liquid critical properties of elements and compounds. 2. normal alkanes," *Journal of Chemical & Engineering Data*, vol. 40, no. 3, pp. 531–546, 1995.

[187] A. Sangroniz, J.-B. Zhu, X. Tang, A. Etxeberria, E. Y. X. Chen, and H. Sardon, "Packaging materials with desired mechanical and barrier properties and full chemical recyclability," *Nature Communications*, vol. 10, no. 1, p. 3559, 2019.

[188] H. Horacek, "Diffusion, löslichkeit und permeation niedrigmolekularer verbindungen in polymeren," *Berichte der Bunsengesellschaft für physikalische Chemie*, vol. 83, no. 4, pp. 352–360, 1979.

[189] R. A. Chowdhury, M. Nuruddin, C. Clarkson, F. Montes, J. Howarter, and J. P. Youngblood, "Cellulose nanocrystal (cnc) coatings with controlled anisotropy as high-performance gas barrier films," *ACS Applied Materials & Interfaces*, vol. 11, no. 1, pp. 1376–1383, 2019.

[190] M. Rahman and C. S. Brazel, "Ionic liquids: New generation stable plasticizers for poly(vinyl chloride)," *Polymer Degradation and Stability*, vol. 91, no. 12, pp. 3371–3382, 2006.

[191] A. Sankri, A. Arhaliass, I. Dez, A. C. Gaumont, Y. Grohens, D. Lourdin, I. Pillin, A. Rolland-Sabaté, and E. Leroy, "Thermoplastic starch plasticized by an ionic liquid," *Carbohydrate Polymers*, vol. 82, no. 2, pp. 256–263, 2010.

[192] O. Hollóczki, D. S. Firaha, J. Friedrich, M. Brehm, R. Cybik, M. Wild, A. Stark, and B. Kirchner, "Carbene formation in ionic liquids: Spontaneous, induced, or prohibited?," *The Journal of Physical Chemistry B*, vol. 117, no. 19, pp. 5898–5907, 2013.

[193] A. Pinkert, K. N. Marsh, S. Pang, and M. P. Staiger, "Ionic liquids and their interaction with cellulose," *Chemical Reviews*, vol. 109, no. 12, pp. 6712–6728, 2009. PMID: 19757807.

[194] M. G. De Angelis, G. C. Sarti, and F. Doghieri, "Nelf model prediction of the infinite dilution gas solubility in glassy polymers," *Journal of Membrane Science*, vol. 289, no. 1, pp. 106–122, 2007.

[195] S. Kluge and M. Weiß, "Herstellung und charakterisierung von polysulfon-membranen für die gastrennung," *Chemie Ingenieur Technik*, vol. n/a, no. n/a, 2021.

[196] I. Pinnau and W. J. Koros, "Structures and gas separation properties of asymmetric polysulfone membranes made by dry, wet, and dry/wet phase inversion," *Journal of Applied Polymer Science*, vol. 43, no. 8, pp. 1491–1502, 1991.

[197] A. K. Qaroush, K. I. Assaf, S. K. Bardaweel, A. Al-Khateeb, F. Alsoubani, E. Al-Ramahi, M. Masri, T. Brück, C. Troll, B. Rieger, and A. F. Eftaiha, "Chemisorption of co2 by chitosan oligosaccharide/dmso: organic carbamato–carbonato bond formation," *Green Chemistry*, vol. 19, no. 18, pp. 4305–4314, 2017.

[198] K. Roger and B. Cabane, "Why are hydrophobic/water interfaces negatively charged?," *Angewandte Chemie International Edition*, vol. 51, no. 23, pp. 5625–5628, 2012.

[199] A. Lozhechnikova, H. Bellanger, B. Michen, I. Burgert, and M. Österberg, "Surfactant-free carnauba wax dispersion and its use for layer-by-layer assembled protective surface coatings on wood," *Applied Surface Science*, vol. 396, pp. 1273–1281, 2017.

[200] N. Nehchiri, S. Amiri, and M. Radi, "Improving the water barrier properties of alginate packaging films by submicron coating with drying linseed oil," *Packaging Technology and Science*, vol. 34, no. 5, pp. 283–295, 2021.

[201] E. E. Jaekel and S. Filonenko, "Cationic cnc-stabilized pickering emulsions of linseed oil for hydrophobic coatings," *RSC Adv.*, vol. 13, pp. 16860–16866, 2023.

[202] L. de Viguerie, P. A. Payard, E. Portero, P. Walter, and M. Cotte, "The drying of linseed oil investigated by fourier transform infrared spectroscopy: Historical recipes and influence of lead compounds," *Progress in Organic Coatings*, vol. 93, pp. 46–60, 2016.

[203] R. Cherrington and J. Liang, "2 - materials and deposition processes for multifunctionality," in *Design and Manufacture of Plastic Components for Multifunctionality* (V. Goodship, B. Middleton, and R. Cherrington, eds.), pp. 19–51, Oxford: William Andrew Publishing, 2016.

[204] S. Renneckar and Y. Zhou, "Nanoscale coatings on wood: Polyelectrolyte adsorption and layer-by-layer assembled film formation," *ACS Applied Materials & Interfaces*, vol. 1, no. 3, pp. 559–566, 2009.

[205] A. Lozhechnikova, K. Vahtikari, M. Hughes, and M. Österberg, "Toward energy efficiency through an optimized use of wood: The development of natural hydrophobic coatings that retain moisture-buffering ability," *Energy and Buildings*, vol. 105, pp. 37–42, 2015.

[206] M. R. Sommer, L. Alison, C. Minas, E. Tervoort, P. A. Rühs, and A. R. Studart, "3d printing of concentrated emulsions into multiphase biocompatible soft materials," *Soft Matter*, vol. 13, no. 9, pp. 1794–1803, 2017.

[207] B. Pang, R. Ajdary, M. Antonietti, O. Rojas, and S. Filonenko, "Pickering emulgels reinforced with host–guest supramolecular inclusion complexes for high fidelity direct ink writing," *Materials Horizons*, vol. 9, no. 2, pp. 835–840, 2022.

[208] J. P. Eubeler, M. Bernhard, and T. P. Knepper, "Environmental biodegradation of synthetic polymers ii. biodegradation of different polymer groups," *TrAC Trends in Analytical Chemistry*, vol. 29, no. 1, pp. 84–100, 2010.

[209] D. S. Green, T. J. Colgan, R. C. Thompson, and J. C. Carolan, "Exposure to microplastics reduces attachment strength and alters the haemolymph proteome of blue mussels (mytilus edulis)," *Environmental Pollution*, vol. 246, pp. 423–434, 2019.

[210] K. Wylon, S. Dölle, and M. Worm, "Polyethylene glycol as a cause of anaphylaxis," *Allergy, Asthma & Clinical Immunology*, vol. 12, no. 1, p. 67, 2016.

[211] P. Sellaturay, S. Nasser, and P. Ewan, "Polyethylene glycol–induced systemic allergic reactions (anaphylaxis)," *The Journal of Allergy and Clinical Immunology: In Practice*, vol. 9, no. 2, pp. 670–675, 2021.

[212] A. A. Klyamkin, I. N. Topchieva, and V. P. Zubov, "Monomolecular films of pluronic-cyclodextrin inclusion complexes at the water-gas interface," *Colloid and Polymer Science*, vol. 273, no. 6, pp. 520–523, 1995.

[213] A. Harada, J. Li, and M. Kamachi, "Preparation and properties of inclusion complexes of polyethylene glycol with. alpha.-cyclodextrin," *Macromolecules*, vol. 26, no. 21, pp. 5698–5703, 1993.

[214] B. G. Mathapa and V. N. Paunov, "Cyclodextrin stabilised emulsions and cyclodextrinosomes," *Physical Chemistry Chemical Physics*, vol. 15, no. 41, pp. 17903–17914, 2013.

[215] D. Duchêne, A. Bochot, S.-C. Yu, C. Pépin, and M. Seiller, "Cyclodextrins and emulsions," *International Journal of Pharmaceutics*, vol. 266, no. 1, pp. 85–90, 2003.

[216] J. E. Smay, J. Cesarano, and J. A. Lewis, "Colloidal inks for directed assembly of 3-d periodic structures," *Langmuir*, vol. 18, no. 14, pp. 5429–5437, 2002.

[217] H. Baniasadi, R. Ajdary, J. Trifol, O. J. Rojas, and J. Seppälä, "Direct ink writing of aloe vera/cellulose nanofibrils bio-hydrogels," *Carbohydrate Polymers*, vol. 266, p. 118114, 2021.

[218] E. B. Heggset, B. L. Strand, K. W. Sundby, S. Simon, G. Chinga-Carrasco, and K. Syverud, "Viscoelastic properties of nanocellulose based inks for 3d printing and mechanical properties of cnf/alginate biocomposite gels," *Cellulose*, vol. 26, no. 1, pp. 581–595, 2019.

[219] A. Blaeser, D. F. Duarte Campos, U. Puster, W. Richtering, M. M. Stevens, and H. Fischer, "Controlling shear stress in 3d bioprinting is a key factor to balance printing resolution and stem cell integrity," *Advanced Healthcare Materials*, vol. 5, no. 3, pp. 326–333, 2016.

[220] D. A. Wellings and E. Atherton, *Standard Fmoc protocols*, vol. 289, pp. 44–67. Academic Press, 1997.

[221] D. da Silva Perez and A. Van Heiningen, "Determination of cellulose degree of polymerization in chemical pulps by viscosimetry," in *Seventh European workshop on lignocellulosics and pulp, Turku*, pp. 393–396, 2002.

[222] S. Tröger-Müller, J. Brandt, M. Antonietti, and C. Liedel, "Green imidazolium ionics-from truly sustainable reagents to highly functional ionic liquids," *Chemistry*, vol. 23 49, pp. 11810–11817, 2017.

Appendix

Chapter 2

Table 8.4: Numerical values for ZP, nitrogen content and CrI depicted in Figure 3.13.

source	medium, reactor	T [°C]	t [h]	ZP [mV]	N [%]	CrI [%]
SFC	REM1, stirred	180	4	21.5	0.35	73
SFC	REM1, stirred	180	2	34.4	0.43	73.8
SFC	REM1, stirred	180	1	31.9	0.40	77.3
SFC	REM1, stirred	160	6	34.1	0.42	83.1
SFC	REM1, stirred	160	2	34.6	0.35	82
SFC	REM1, stirred	140	4	33.9	0.36	79
SFC	REM1, stirred	140	1	35.9	0.28	79.2
pulp	REM1, stirred	180	4	29.6	0.28	82.4
pulp	REM1, stirred	180	2	26.2	0.27	83.6
pulp	REM1, stirred	180	1	32.2	0.32	81.5
pulp	REM1, stirred	160	6	28.2	0.32	83.1
pulp	REM1, stirred	160	2	31.5	0.3	84.5
pulp	REM1, stirred	140	4	35.6	0.26	83.3

Table 8.5: Viscosities and calculated DP for the cuen method.

sample	c mg/mL	$[\eta]$ mL/g	DP
Short-fiber cellulose	2.55	645.3012	2308
Short-fiber cellulose, 140 °C, 4 h	2.62	105.4777	309
Short-fiber cellulose, 160 °C, 2 h	2.50	110.4000	325
Softwood pulp, 140 °C, 4 h	2.55	108.2353	318
Softwood pulp, 180 °C, 4 h	2.48	111.1409	327

Chapter 3
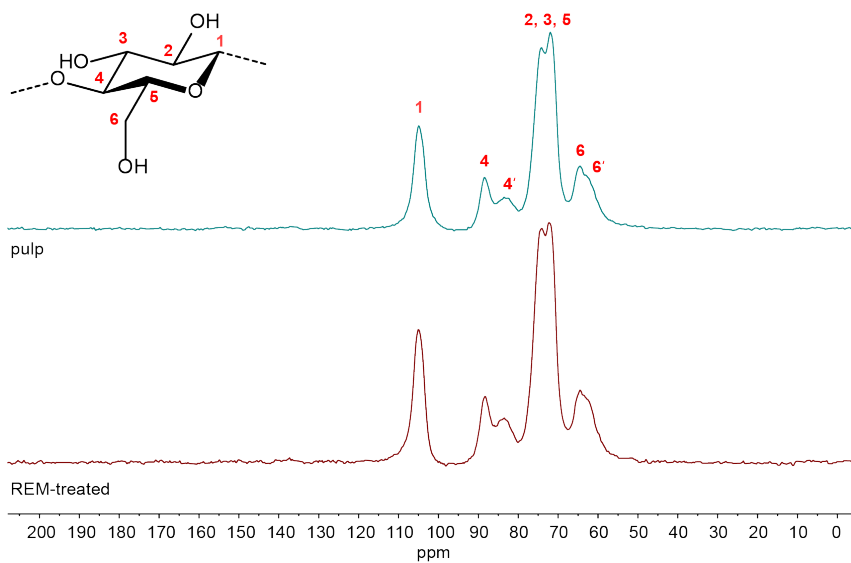
Figure 8.2: ^{13}C-ssNMR spectrum of the starting material pulp (blue line) and the REM-treated CNC sample (red line).
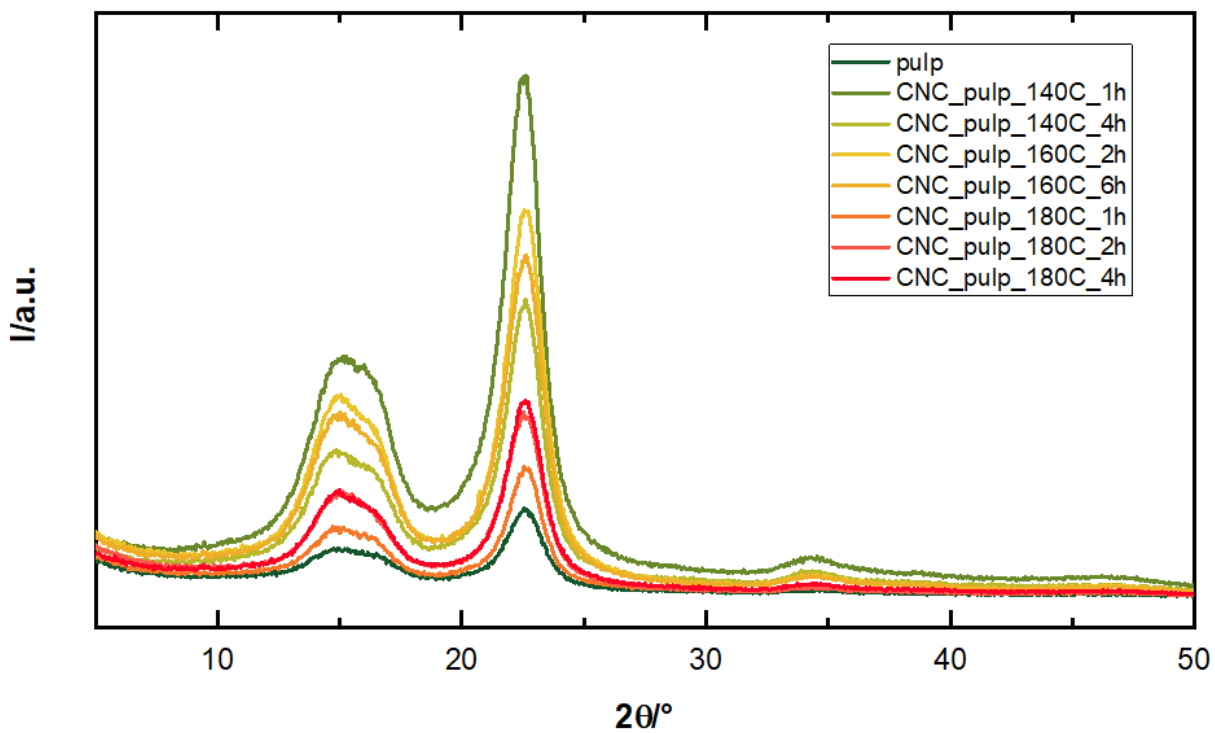
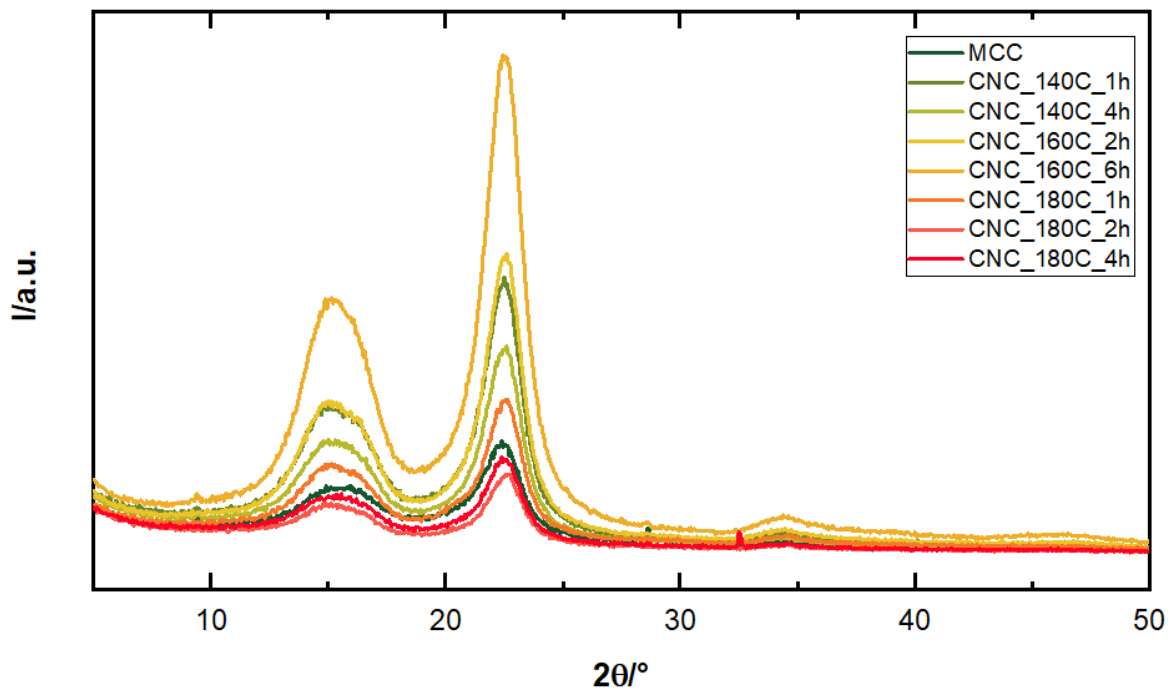**Figure 8.3:** WAXD spectrum of pulp treated in REM1 in varying conditions.

Figure 8.4: WAXD spectrum of SFC treated in REM1 in varying conditions.

Table 8.6: Permeabilities for the tested gases in all fabricated membranes, given in Barrer.

sample	He	H_2	O_2	N_2	CH_4	CO_2
sNC:glu	0.10	0.11	0.10	0.10	0.10	0.09
fNC:bi A	1970	3326	1049	1188	1740	1164
fNC:bi B	19.38	29.68	8.30	9.10	12.80	6.55
fNCbiM1	1.84	1.43	1.23	1.40	1.45	0.59
fNCXbi-A1	1.59	1.54	1.44	1.59	1.39	1.36
fNCXbi-A2	1.59	1.12	1.39	1.65	1.41	1.50
sNC:dbi-2b	2.03	2.95	2.04	1.51	1.50	0.30
sNC:thfi1	1.56	2.06	1.49	1.24	1.19	1.16
sNC:thfi2	0.8	0.67	0.58	0.57	0.55	0.63
CS:pure	0.83	1.55	1.61	1.36	1.34	0.032
CS:glu	0.3	0.83	0.8	0.74	0.73	0.71
CS:thfi	2.34	2.69	1.54	1.12	3.12	3.13
CS:dbi	0.75	1.43	0.44	1.28	1.15	1.24
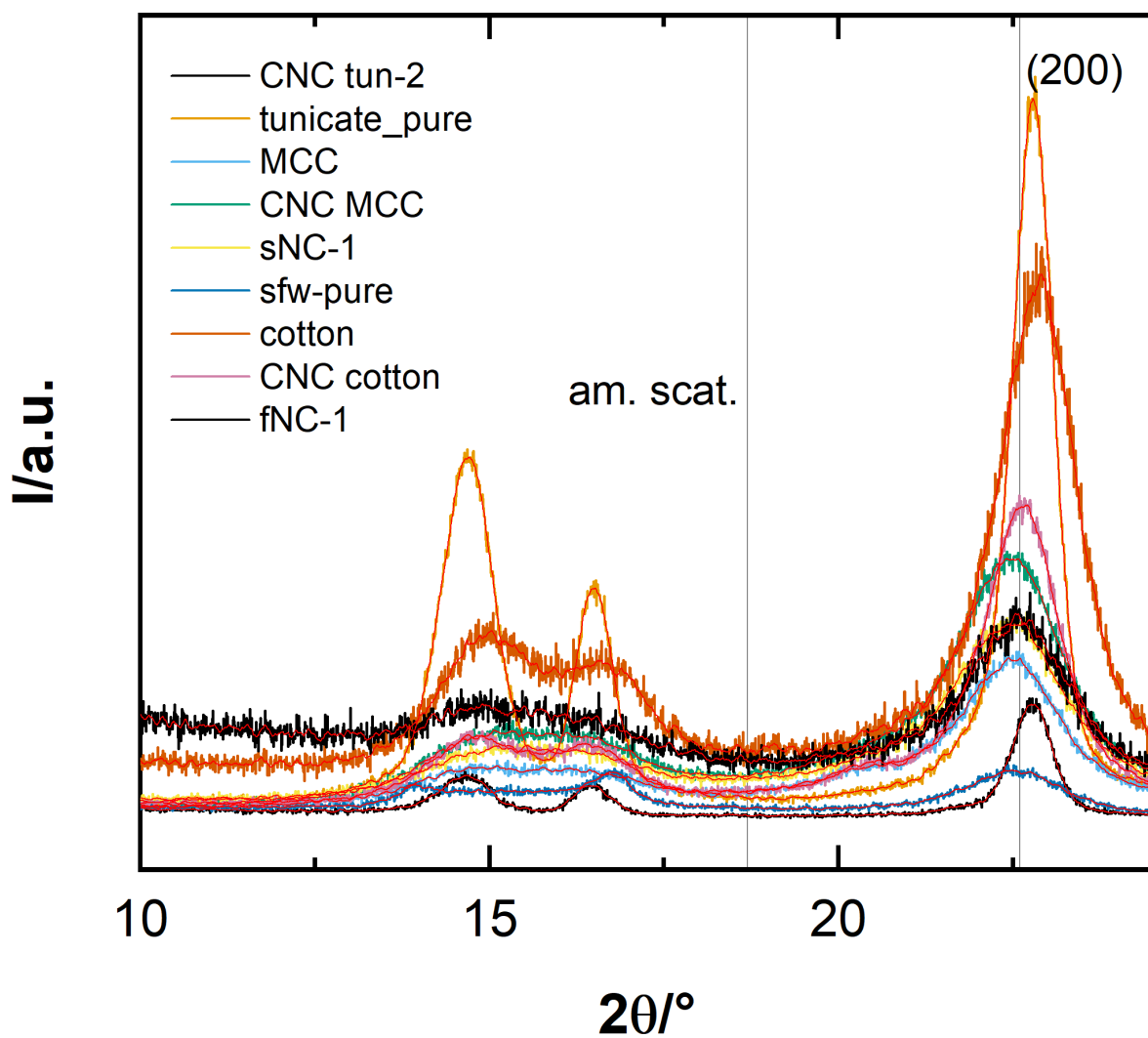
Figure 8.5: XRD spectra with smoothed curve used to determine CrI
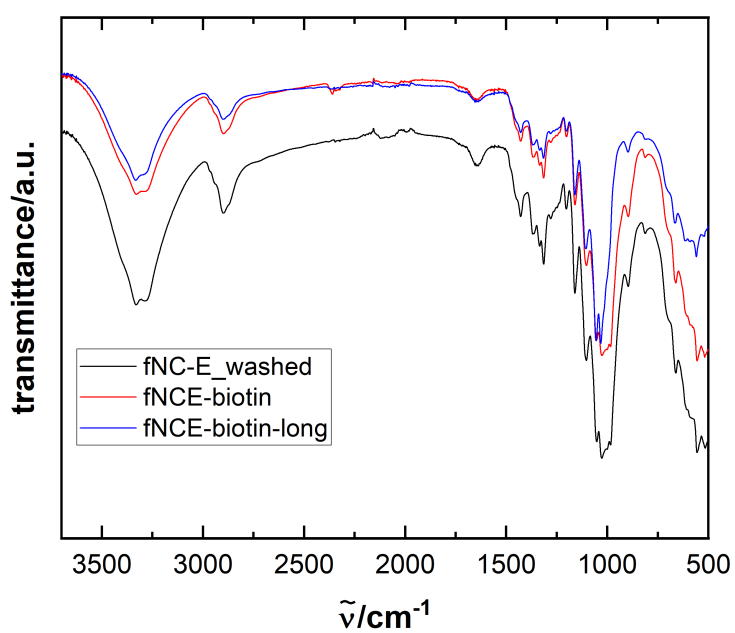
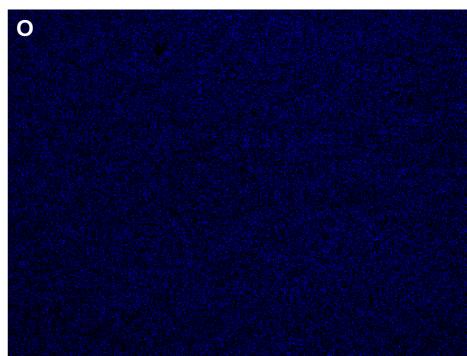**Figure 8.6:** FTIR of CNCs reacted with biotin.

sNC:bi surface

sNC:bi cross section
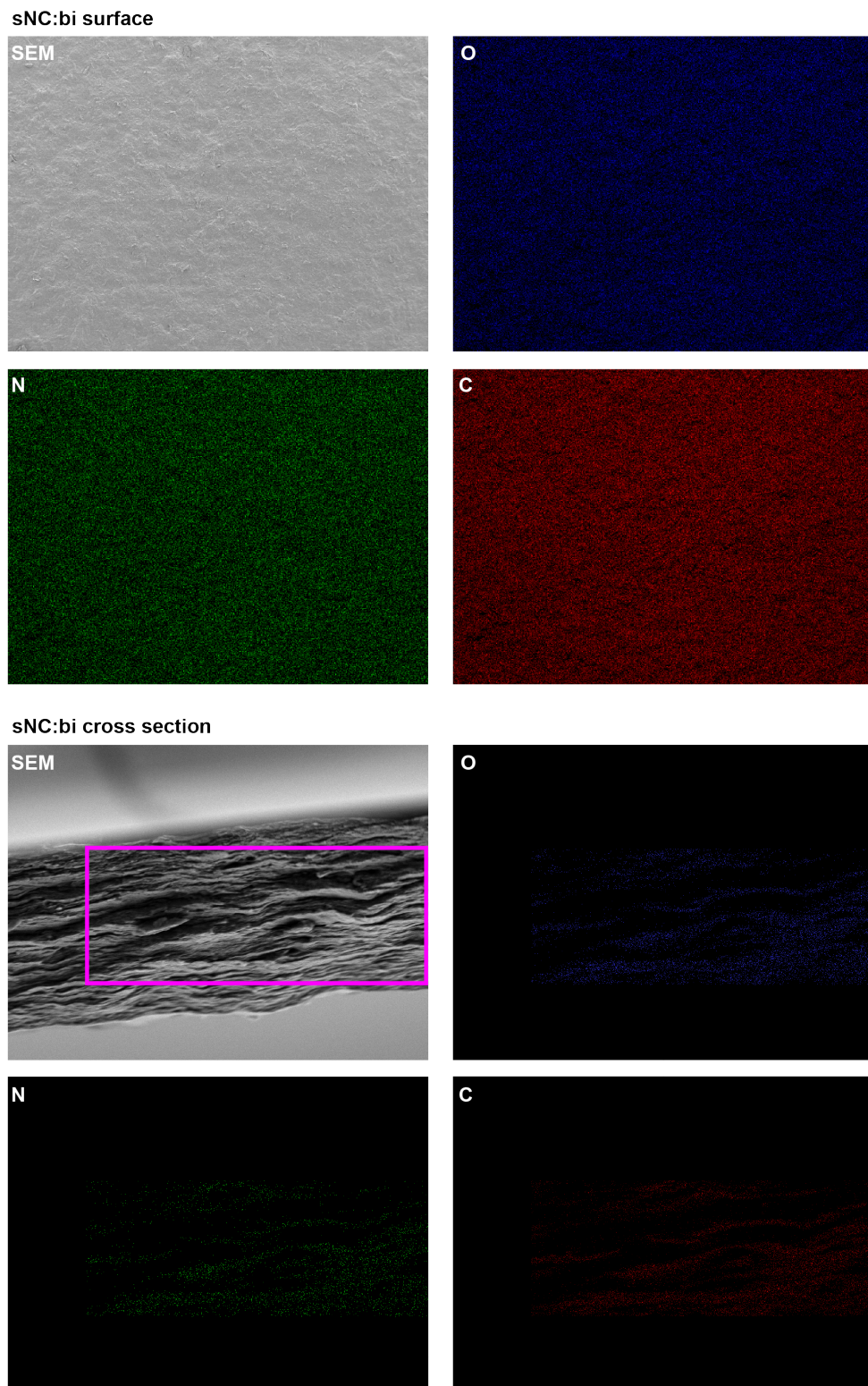
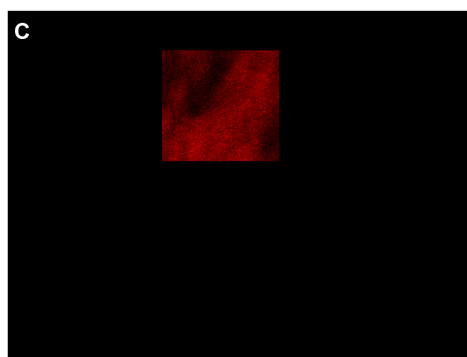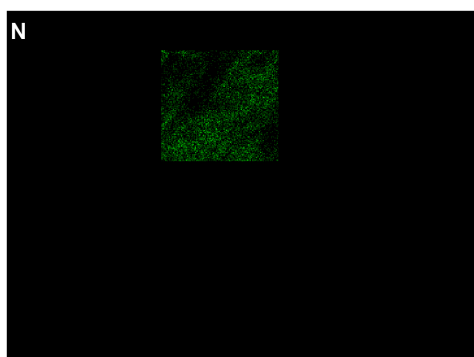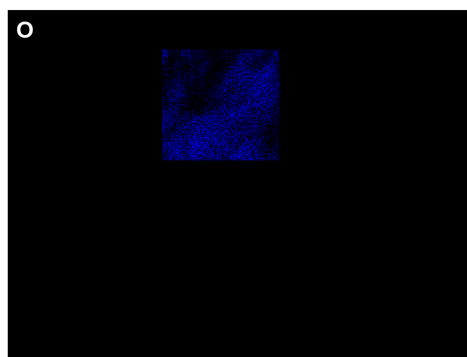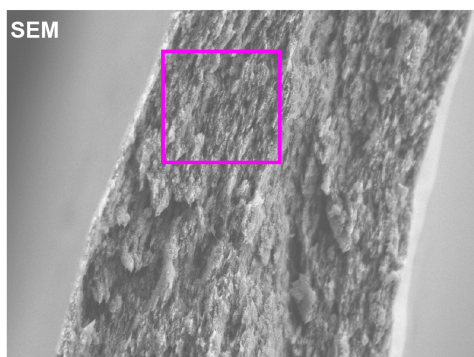**Figure 8.7:** SEM image and EDX maps of sNC:bi surface and cross section.
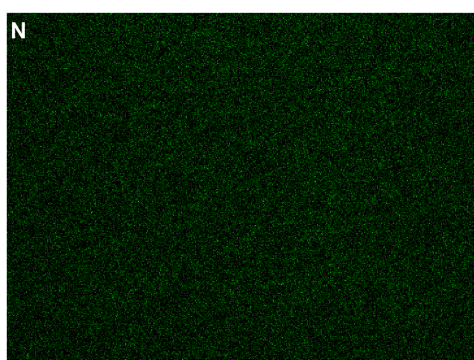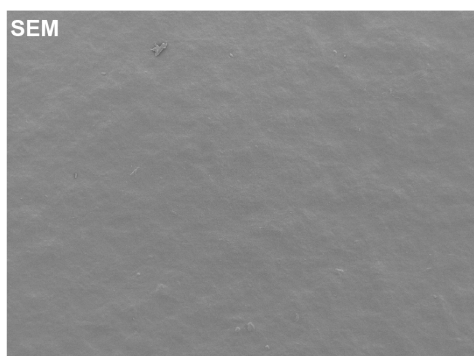
Figure 8.8: SEM image and EDX maps of fNC:bi surface and cross section.